ASSESSMENT OF THE NASA EVOLVE LONG-TERM ORBITAL DEBRIS EVOLUTION MODEL

K.W. Yates
F.M. Jonas

ORION International Technologies, Inc.
6501 Americas Parkway, Suite 200
Albuquerque, NM 87110

February 1995

Final Report

19950418 031

PHILLIPS LABORATORY
Advanced Weapons and Survivability Directorate
AIR FORCE MATERIEL COMMAND
KIRTLAND AIR FORCE BASE, NM 87117-5776

PL-TR--92-1030

This final report was prepared by ORION International Technologies, Inc., Albuquerque, New Mexico, under contract F29601-89-C-0001, Job Order 31080101, with the Phillips Laboratory, Kirtland Air Force Base, New Mexico. The Phillips Laboratory Project Officer-in-Charge was Capt Albert E. Reinhardt (WSC).

This report has been reviewed and is approved for publication.
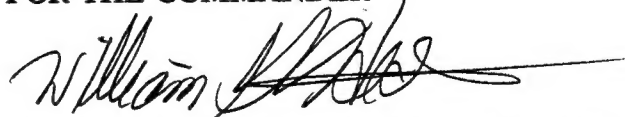
SCOTT R. MAETHNER, Capt, USAF
Project Officer

FOR THE COMMANDER

STEVEN B. DRON, Lt Col, USAF   WILLIAM G. HECKATHORN, Col, USAF
Chief, Space Control   Director, Advanced Weapons
  Technologies Division   and Survivability Directorate

REPORT DOCUMENTATION PAGE

Form Approved
OMB No. 0704-0188

Public reporting burden for this collection of information is estimated to average 1 hour per response, including the time for reviewing instructions, searching existing data sources, gathering and maintaining the data needed, and completing and reviewing the collection of information. Send comments regarding this burden estimate or any other aspect of this collection of information, including suggestions for reducing this burden, to Washington Headquarters Services, Directorate for Information Operations and Reports, 1215 Jefferson Davis Highway, Suite 1204, Arlington, VA 22202-4302, and to the Office of Management and Budget, Paperwork Reduction Project (0704-0188), Washington, DC 20503.

1. AGENCY USE ONLY (Leave blank)	2. REPORT DATE February 1995	3. REPORT TYPE AND DATES COVERED Final · Apr 91 - Jun 92

4. TITLE AND SUBTITLE
ASSESSMENT OF THE NASA EVOLVE LONG-TERM
ORBITAL DEBRIS EVOLUTION MODEL

6. AUTHOR(S)

K. W. Yates, F. M. Jonas

5. FUNDING NUMBERS
C: F29601-89-C-0001
PE: 63215C
PR: 3108
TA: 01
WU: 01

7. PERFORMING ORGANIZATION NAME(S) AND ADDRESS(ES)

ORION International Technologies, Inc.
6501 Americas Parkway, Suite 200
Albuquerque, NM 87110

8. PERFORMING ORGANIZATION REPORT NUMBER

9. SPONSORING / MONITORING AGENCY NAME(S) AND ADDRESS(ES)

Phillips Laboratory
Kirtland AFB, NM 87117-5776

10. SPONSORING / MONITORING AGENCY REPORT NUMBER

PL-TR--92-1030

11. SUPPLEMENTARY NOTES

12a. DISTRIBUTION / AVAILABILITY STATEMENT

Approved for public release; distribution is unlimited.

12b. DISTRIBUTION CODE

13. ABSTRACT *(Maximum 200 words)*

The EVOLVE long-term orbital debris evolution model developed for the NASA Johnson Space Center by Lockheed Engineering and Sciences Company and Systems Planning Corporation is described and evaluated in detail. This computer model calculates the low earth orbit (LEO) debris spatial number density or flux environment as a function of fragment size, altitude, and time. Launched intact objects, introduced from detailed manifest databases, are time-evolved with an analytical orbit propagator. Debris clouds, formed from the application of cloud formation algorithm and breakup model, are time-evolved using a derived phenomenological function. This report describes the overall computer model (e.g., its deterministic and stochastic modes of calculation) and examines the individual submodels used to quantify the debris population in LEO. Model results are compared to observed debris data. Specific recommendations and possible model improvements are cited. Also presented is a sample satellite constellation hazard assessment using EVOLVE.

14. SUBJECT TERMS
Space Debris, Long-Term Debris Model, Orbital Debris Environment, NASA EVOLVE Model

15. NUMBER OF PAGES
162

16. PRICE CODE

17. SECURITY CLASSIFICATION OF REPORT Unclassified	18. SECURITY CLASSIFICATION OF THIS PAGE Unclassified	19. SECURITY CLASSIFICATION OF ABSTRACT Unclassified	20. LIMITATION OF ABSTRACT SAR

NSN 7540-01-280-5500

Standard Form 298 (Rev. 2-89)
Prescribed by ANSI Std. Z39-18
298-102

PREFACE

The author wishes to acknowledge the aid and assistance of the NASA JSC personnel during meetings and discussions with them on their model development. Specifically, the author wishes to thank Mr. Don Kessler of NASA JSC, Dr. Robert Reynolds, Dr. Phillip Anz-Meador, and Dr. Greg Ojakangas of Lockheed Engineering and Sciences Company, Houston, Texas (LESC). Discussions were extremely open and frank, and the NASA insights into the EVOLVE model proved immensely valuable in the ORION analyses. He also would like to thank them for providing the software and the associated EVOLVE documentation that provided the basis of this effort.

Accesion For		
NTIS CRA&I	☑	
DTIC TAB	☐	
Unannounced	☐	
Justification		
By		
Distribution /		
Availability Codes		
Dist	Avail and / or Special	
A-1		

iii/iv

CONTENTS

1.0 INTRODUCTION

This report evaluates qualitatively and quantitatively the National Aeronautics and Space Administration (NASA) EVOLVE models ability to predict the current and future orbital debris environment in low earth orbit (LEO). This effort assesses the approach of the model as well as its capabilities and limitations by examining the analytic and empirical functions used to predict the debris environment. The performance of important integral models will be examined through appropriate sensitivity and uncertainty appraisals.

The near-earth space environment is a natural resource that is sensitive to man's operations in space. The debris created as a result of space activity via launches and orbital breakups is already estimated to be a significant problem to users of the orbital environment. Unless efforts are taken soon to slow the predicted increase in the density of orbital debris, future users will face extreme hazards for their space-based systems. The man-made debris threat is comparable and even exceeds the threat posed by meteoroids in some debris diameter ranges (Ref. 1). As the debris environment increases, collisional cascading between debris fragments threatens to be a self-perpetuating process that could have grave consequences for an active orbiting platform (Ref. 2). The hazards of the environment will impact design and planning considerations for future spacecraft designed to operate in this hostile environment.

Characterizing the man-made debris environment is a crucial first step in assessing potential hazards. Once the environment has been reliably quantified in terms of a flux (in units of impacts/area-time) or spatial density (in units of volume^{-1}), the second step is to determine the probabilities of collision with other orbiting objects. For a space system designer, the third and final step is to determine the damage he can expect to receive given a collision and to determine whether such collision damage exceeds an acceptable limit.

The EVOLVE model was developed at NASA Johnson Space Center (JSC) to address the first step with an emphasis on characterizing the environment in the long term, i.e., over the course of a year or more. It is a semiempirical orbital debris time evolution model incorporating both analytic and empirical submodels to determine the man-made debris environment. The program EVOLVE is the distillation of the debris studies and earlier model development work at NASA JSC (Refs. 3 and 4). This earlier work succeeded in developing a model to predict the debris flux distribution as functions of altitude (h), debris diameter (d), and time (t). Based on the approach of this original model, the EVOLVE was developed to provide environment predictions as functions of d, h, and t using a collection of models developed at NASA and elsewhere to improve predictions. These predictions include an improved spatial density algorithm and improved breakup models describing the number versus mass distributions obtained in a breakup event (Refs. 5-7). A statistical Monte Carlo was added to model the random collision and explosion processes.

1

This effort then assesses the current EVOLVE program to determine its validity, limits of applicability, sensitivity and uncertainty associated with important parameters, and fidelity when compared to actual data.

The functional elements of the program are studied to establish their validity in terms of the current state-of-knowledge on atmospheric/solar effects, breakups via collisions and explosions, traffic models, etc. This report describes each functional element of the EVOLVE model, then presents an independent assessment of the model's assumptions, its validity, and if appropriate, a sensitivity/uncertainty analysis performed on its most important parameters. The goal of this assessment is to assist the Air Force (AF) in the task of developing a long-term model that can do the following:

- Predict future debris environments more accurately at the relevant altitudes and orbit parameters

- Benefit from new AF and non-AF debris measurements

- Accommodate current and future AF space scenarios

Section 2.0 describes the problem of orbital space debris and the impact that contamination of the near earth orbital environment has on current and future space operations. The model computer program is described showing the structure and general approach to introducing intact objects and debris clouds into the environment in either a deterministic or stochastic fashion. Section 3.0 presents an overall assessment of the EVOLVE model approach and methodology. Each of the important submodels that comprise the EVOLVE orbital debris evolution model are then described and assessed in Section 3.0. These submodels are examined in terms of the source models (introduction of intact objects and fragmentation debris into the environment) and the sink models (removal of objects from the environment). Finally, EVOLVE output is compared to data from other models and experimental data to demonstrate its fidelity.

2.0 NASA EVOLVE DEBRIS ENVIRONMENT EVOLUTION MODEL

The EVOLVE model and its basic approach to orbital debris environments is presented in this section. Subsection 2.1 provides the model overview and basic processing philosophy. Subsection 2.2 describes the program structure and modularity. Subsection 2.3 describes handling of intact objects and debris clouds along the two major program processing pathways: deterministic and stochastic.

2.1 MODEL OVERVIEW AND DESCRIPTION

The NASA JSC together with their on-site technical support contractor Lockheed Engineering and Sciences Company (LESC), Houston, Texas, has vigorously pursued research into orbital debris population environment characterization. This research involves projects to model the current and future environment to obtain observational data needed to improve the understanding of the debris environment and to model the hazards expected from the environment. Much emphasis has been placed on developing models that can give an accurate picture of the debris environments both currently and for long-term projections. The first of these research areas, debris environment modeling, has been focused into three primary efforts as follows:

- Detailed environment flux (or spatial density) projections and long-term evolution based on historical space traffic and mission models of proposed future space activity (Program EVOLVE)

- Short- and long-term spatial and temporal characteristics of debris cloud flux (or spatial density) immediately following a fragmentation or breakup of an orbiting object (Program CLOUD or FRGMNT)

- Debris flux magnitude and directionality characteristics relative to a specific orbiting spacecraft (Program FLUX)

This report evaluates the performance of the first of these efforts, program EVOLVE, with its emphasis on long-term modeling of possible future debris environments. The sole intention of EVOLVE is to generate the time-evolved averaged spatial density (or flux) over long-term periods (a year or more). The EVOLVE does not possess the capability to model short-term effects within the environment. Some of the situations which EVOLVE does not model are as follows:

- Localized spatial density enhancement resulting from an on-orbit breakup cloud
- Flux directionality and magnitude effects experienced by a spacecraft surface
- Hanging probability of collision due to a spacecraft moving relative to the average ambient background

3

These effects are built into other numerical codes developed at NASA JSC (Ref. 8).

The prime motivation behind development of the EVOLVE model was to describe the environment in an averaged manner without enormous computational burden, but with sufficient accuracy for many long-term applications. Among these applications are trade studies that are intended to examine possible traffic models and their variations as well as operational and programmatic policies that could affect the future environment. The EVOLVE is not intended to model any specific present or future environment with extremely high accuracy, but is intended to give a reasonable environment result for a specific set of input conditions. Parametric studies of the environment could then be allowed by varying the input conditions. These input conditions include the time range, diameter range and altitude spans characterizing the flux environment and the traffic models. These traffic models (both historical and future) are detailed descriptions of the space activity being added to the environment.

To accurately represent the space environment, a model must deal with two distinctly different classes of objects, the relatively few (~10,000) discretely identifiable intact objects and the numerous (~10^6/event) particles resulting from orbital breakup events (explosions, collisions). Each intact object orbit can be traced individually; the numerous particles from a spacecraft breakup are treated as a propagating cloud or ensemble of objects.

EVOLVE propagates the orbits of intact objects in time using a fast analytical orbital propagator especially designed for low accuracy applications (Ref. 9). This propagator incorporates an atmospheric drag model using a modified Jacchia atmospheric density model (Ref. 10) together with a time-varying solar flux model (Refs. 11 and 12) to estimate orbital decay.

The key concept developed for debris cloud population environment analysis has been to assign the vast number of fragments generated during a breakup event into a manageable number of debris clouds. Each cloud element is placed within a prescribed particle size bin. The spatial density of the relatively few clouds then can be time-evolved rapidly and efficiently using an independently developed analytical flux function. This function is an empirically-derived explicit function of altitude, debris diameter, and time, and implicitly the dynamic solar flux. The cloud objects are assumed to be distributed instantaneously and uniformly throughout each spherical altitude shell in longitude and latitude. This means that the flux function is independent of inclination and right ascension and the localized effects of debris clouds in these dimensions are ignored. Only the altitude dependence (radial dimension) is described by this function.

EVOLVE constructs the environment through a sequential addition of objects contributed from the various sources. This process is done in user-specified time steps so that current conditions can be defined (e.g., the current solar activity level) and reasonably accurate orbital propagation processing can be achieved. The time steps can begin in 1957 (with the launch of the first man-made satellite) and continue to any arbitrary future year. In principle there is

4

no time limit in EVOLVE, but in practice projections to 2010-2020 are typical. All launched intact objects including operational debris along with historical or manifested breakups specified in the input files are processed deterministically; this means that their orbital insertion (launched objects) or occurrence (debris clouds) and characteristics (initial orbital elements, areas, masses, breakup altitude, etc.) are defined specifically by the user. The details of EVOLVE's deterministic processing shall be given in Subsection 2.5.1.

For projected future times, the user may invoke stochastic generation of breakup events as an additional source to the environment. Stochastic processing adds breakup events through a Monte Carlo process using a random number generator and probability functions to determine the occurrence of collisions and explosion events. The fragment clouds created stochastically add to the deterministically-generated base environment. For collisions, the rate of occurrence depends on the magnitude of the local environment's spatial density just prior to the current time step. Therefore, the stochastic collision contribution depends on the deterministic processing baseline as well as the previous stochastic environment contributions. This process represents a feedback mechanism in the EVOLVE model.

Explosions occur independently of the current environmental flux conditions. The availability of explosive objects is specified only within the input files. Thus, the occurrence of explosions determined stochastically relies in part, on the deterministic placement of explosive intact objects into orbit. By using Poisson statistics for both collision and explosion occurrence and calculating the resulting spatial density (or flux) environment, any number of possible future environments may be predicted. The EVOLVE model can then extract statistical means and standard deviations to assign an uncertainty to the possible range in future debris states. Stochastic processing shall be discussed in greater detail in Subsection 2.5.2.

The EVOLVE model outputs the spatial density or flux of objects in the resulting environment. Spatial density results (given as the number of objects per cubic kilometer) are output as functions of time, particle diameter, and altitude above the earth's surface. The results are stored in three-dimensional (3-D) arrays containing spatial density (or flux). This requires the results to be expressed as discrete values and placed into time, particle size, and altitude bins. Flux results are not parameterized as continuous functions as they are in the NASA 90 engineering model (Ref. 13); consequently, the accuracy ultimately depends on how finely divided the parameter bins are made (Subsection 2.3). In EVOLVE, spatial density (given in units of number of objects/kilometers^3) is assumed to be directly proportional to the cross-sectional areal flux (given in units of impacts/meters^2/year) via a constant average orbital velocity of 7.0 km/s for LEO debris objects. EVOLVE results can be output as spatial density or flux with a simple constant conversion factor between them.

2.2 PROGRAM STRUCTURE

The EVOLVE program consists of a driver routine, EVOLVE.FOR, and 25 functions and subroutines all written in standard FORTRAN-77 with versions capable of running on the PC or Digital Equipment Corporation (DEC) VAX computers. The subroutine structure is based around the submodels incorporated into EVOLVE. This modularity facilitates maintenance and allows interchangeability of modules as new data or models become available. The description of those subroutines and their calling interfaces are described in Reference 11.

Figure 1 diagrams the essential structure of the EVOLVE program and its five basic submodels along with each model's important inputs and outputs. The EVOLVE approach to constructing an environment flux entails introducing intact objects or debris clouds into the near-earth space environment through two general source models: the traffic models (for intact object deposition) and the breakup models (for breakup event fragment deposition). Planned operational debris objects (e.g., discarded shrouds, explosive bolts, etc.) introduced during launch are included in the traffic model data. Debris caused by satellite deterioration while on-orbit is not modeled in EVOLVE. The intact objects or clouds (defined as a subset ensemble of fragments from a breakup event) are then subject to sink mechanisms which serve to remove the objects from the environment.

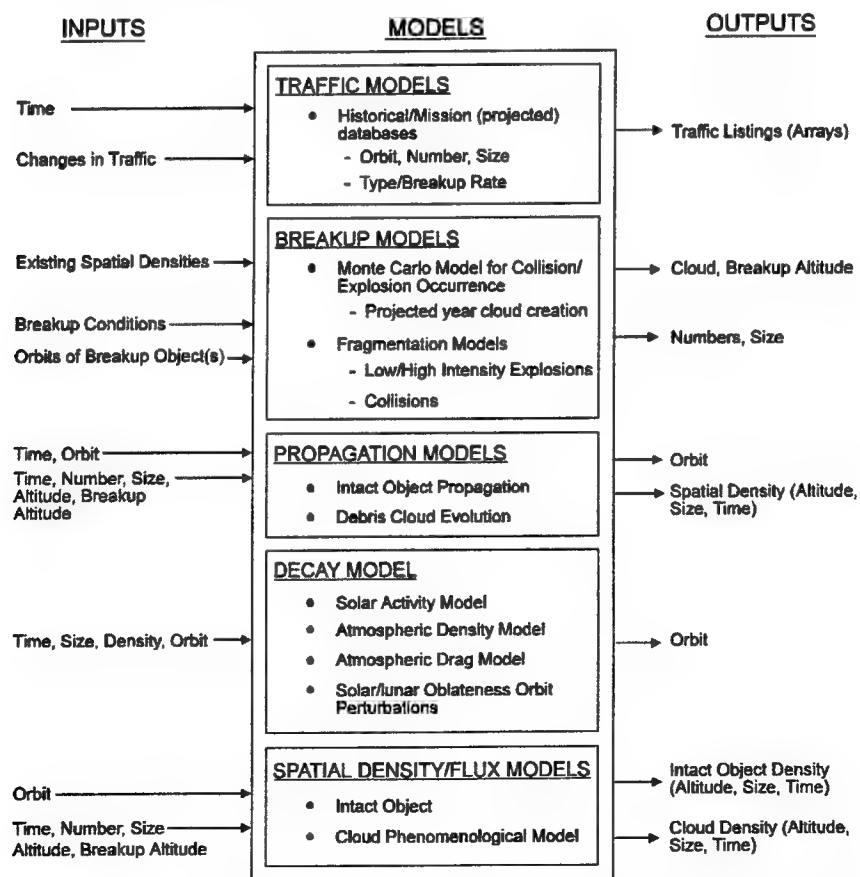| INPUTS	MODELS	OUTPUTS
Time	**TRAFFIC MODELS** • Historical/Mission (projected) databases - Orbit, Number, Size - Type/Breakup Rate	Traffic Listings (Arrays)
Changes in Traffic		
Existing Spatial Densities	**BREAKUP MODELS** • Monte Carlo Model for Collision/ Explosion Occurrence - Projected year cloud creation • Fragmentation Models - Low/High Intensity Explosions - Collisions	Cloud, Breakup Altitude Numbers, Size
Breakup Conditions		
Orbits of Breakup Object(s)		
Time, Orbit	**PROPAGATION MODELS** • Intact Object Propagation • Debris Cloud Evolution	Orbit Spatial Density (Altitude, Size, Time)
Time, Number, Size, Altitude, Breakup Altitude		
Time, Size, Density, Orbit	**DECAY MODEL** • Solar Activity Model • Atmospheric Density Model • Atmospheric Drag Model • Solar/lunar Oblateness Orbit Perturbations	Orbit
Orbit	**SPATIAL DENSITY/FLUX MODELS** • Intact Object • Cloud Phenomenological Model	Intact Object Density (Altitude, Size, Time) Cloud Density (Altitude, Size, Time)
Time, Number, Size Altitude, Breakup Altitude		

Figure 1.   Major EVOLVE submodels (from Refs. 8 and 11).

The only naturally available sink mechanism within the orbital decay model is atmospheric drag (Figure 1) which incorporates a series of separate submodels required to propagate and decay object orbits. These submodels include the solar activity model, the atmospheric density model, solar/lunar orbital perturbation model, and the atmospheric drag/orbital contraction model. Closely associated with the decay model, but distinguished as separate models in this study, are the orbital propagation models. These are the algorithms used to time-evolve or propagate the orbits of objects within the environment. For intact objects, the orbital propagation model is the algorithm used to calculate the initial orbital elements needed to invoke the decay model, where the actual propagation calculations take place using the Mueller decay algorithms (Ref. 9). For debris clouds, the orbital propagation in time is implicit in the flux results obtained from the phenomenological cloud function. In the orbital propagation model certain options are available to the user through flags specified in the traffic models. They are:

- Deorbiting of orbiting rocket stages and payloads after end of mission life
- Collision avoidance
- Stationkeeping

All of these processes affect the duration that an object can remain in orbit. Deorbiting is a man-made policy wherein otherwise useless payloads and rocket bodies are immediately removed by using a small amount of stored residual fuel. Collision avoidance affects the potential growth in the debris environment through collisions by limiting the number of objects capable of collision. Stationkeeping is the process where an active satellite maintains a prescribed orbital element set. The effects of drag and orbital perturbations are actively counteracted by on-board thrusters which periodically adjust the current orbit to maintain the initial orbit throughout the active life of the payload.

The spatial density/flux models block encapsulates the algorithms necessary to convert the presence of intact object orbits and debris clouds in the near-earth environment into the form of a spatial density (number of objects/kilometers^3) or flux (number of impacts/meters^2 - year) (Ref. 7). EVOLVE must calculate spatial density directly for each intact object orbit and then sum these spatial densities to obtain a total spatial density. The phenomenological model used to time-evolve debris clouds provides the debris cloud spatial density contribution to the environment. The output of the debris cloud evolution function is in terms of density (number/kilometers^3) so the contribution from one debris cloud can be added directly to the contributions from other debris clouds and the intact object sum total to obtain a total spatial density for the environment.

As described in the previous subsection, EVOLVE introduces source objects into the environment either deterministically or stochastically. These processes are distinct pathways in EVOLVE and are handled by the driver program EVOLVE.FOR. Figure 2 shows a flowchart of the essential operations conducted by this driver routine. EVOLVE first reads the user-specified inputs in the EVOLVE.DAT file which contains control flags and other initialization information needed to begin processing. EVOLVE.FOR sends processing down
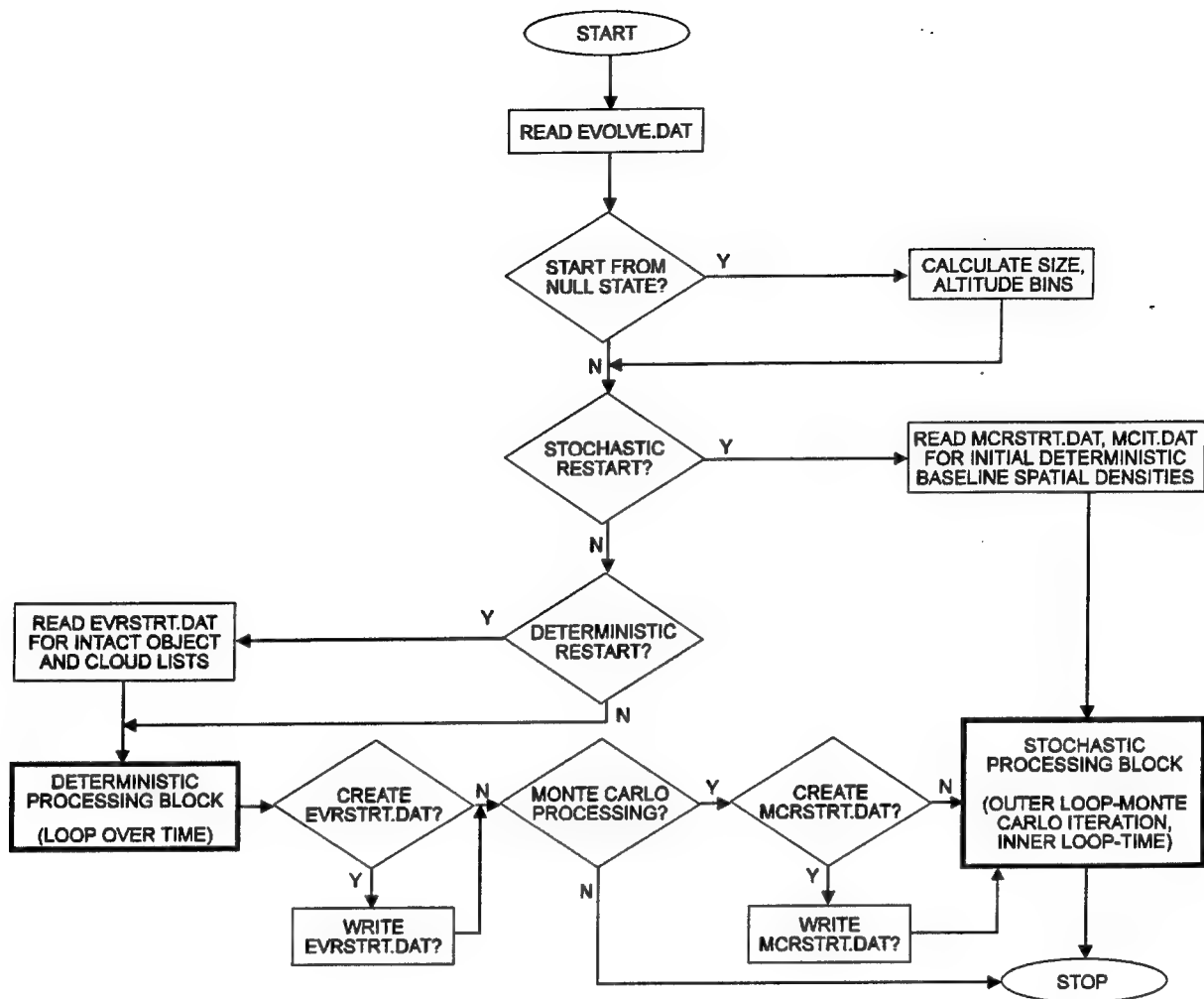
7

Figure 2.   General flow of EVOLVE (from Ref. 11). Bold outlines indicate the deterministic and stochastic processing blocks.

the appropriate pathways depending on the flag conditions set in EVOLVE.DAT. These conditional branches are shown as the conditional boxes diagrammed in Figure 2. The EVOLVE.FOR architecture sets up the information required to initiate the deterministic processing block and/or the stochastic processing block.

If a user starts from the null state (i.e., no prior EVOLVE processing being performed), the program needs to initialize the widths, ranges, and dimensions of the particle diameter and altitude bins which comprise two dimensions of the 3-D array, in which EVOLVE stores its spatial density results. The third dimension, time, is automatically determined by the time range and step size specified by the user in EVOLVE.

8

It then performs, as a minimum, the deterministic processing block shown in Figure 2. If desired, upon completion of the deterministic processing over the entire time range (which may include both historical and future years), the stochastic processing (for future years only) may be invoked to generate statistical future debris environments. Either a deterministic or stochastic restart file may be created upon deterministic loop completion to contain deterministically created baseline intact object/cloud lists or spatial densities.

If a deterministic restart file (EVRSTRT.DAT) is created, the current list of the nondecayed orbits and debris clouds is saved. The spatial densities that the arrays of orbits would produce is not calculated and saved. In this way, a future EVOLVE run can read this file as input and begin processing at the next time step without repeating all prior time step calculations. This is a time-saving feature for the user if the same deterministic baseline is used over a selected range of time steps prior to the time range of interest. For example, the user may process all historical years 1957-1989 and save the list of intact objects and debris clouds current as of the end of 1989 into EVRSTRT.DAT. Using the deterministic restart option, the user may begin processing in 1990 and avoid having to reprocess all previous years input lists.

Unlike the deterministic restart file, the stochastic restart file MCRSTRT.DAT contains time - centered spatial density arrays (i.e., spatial densities averaged to the center of the processing time step) resulting from the baseline deterministically placed intact objects and debris clouds. This baseline spatial density is common to all projected environments, upon which stochastically-introduced debris cloud spatial densities are added to obtain a total environment during each Monte Carlo interaction (trial). The MCRSTRT.DAT contains only the deterministic baseline, and like the deterministic restart file EVRSTRT.DAT, it saves the user the time it takes to calculate the deterministic baseline. For each trial, a separate complete environment is calculated and stored in the Monte Carlo ensemble file MCENSEM.DAT. Each trial will generate a different projected environment so that means and standard deviations for the ensemble of such environments can be analyzed. The Monte Carlo processing requires that the spatial densities be calculated since they are required for modeling the occurrence probability of collisions and explosions (Subsection 3.2.2.1). The description of the deterministic and stochastic processing blocks displayed in Figure 2 shall be fully described in Subsections 2.5.1 and 2.5.2.

The general sequence of events to obtain environment projections using EVOLVE is given in Figure 3. Step 1 is the deterministic processing of all historical data contained in the input files having the DBS file extension. Step 2 is the corresponding deterministic processing of specified future data in the input files having the PRJ file extension. The spatial densities resulting from steps 1 and 2 are stored in MCRSTRT.DAT (if specified). Step 3 is calculated for each Monte Carlo iteration with the total flux environment being the sum of step 3 and the sequential flux result of steps 1 and 2.

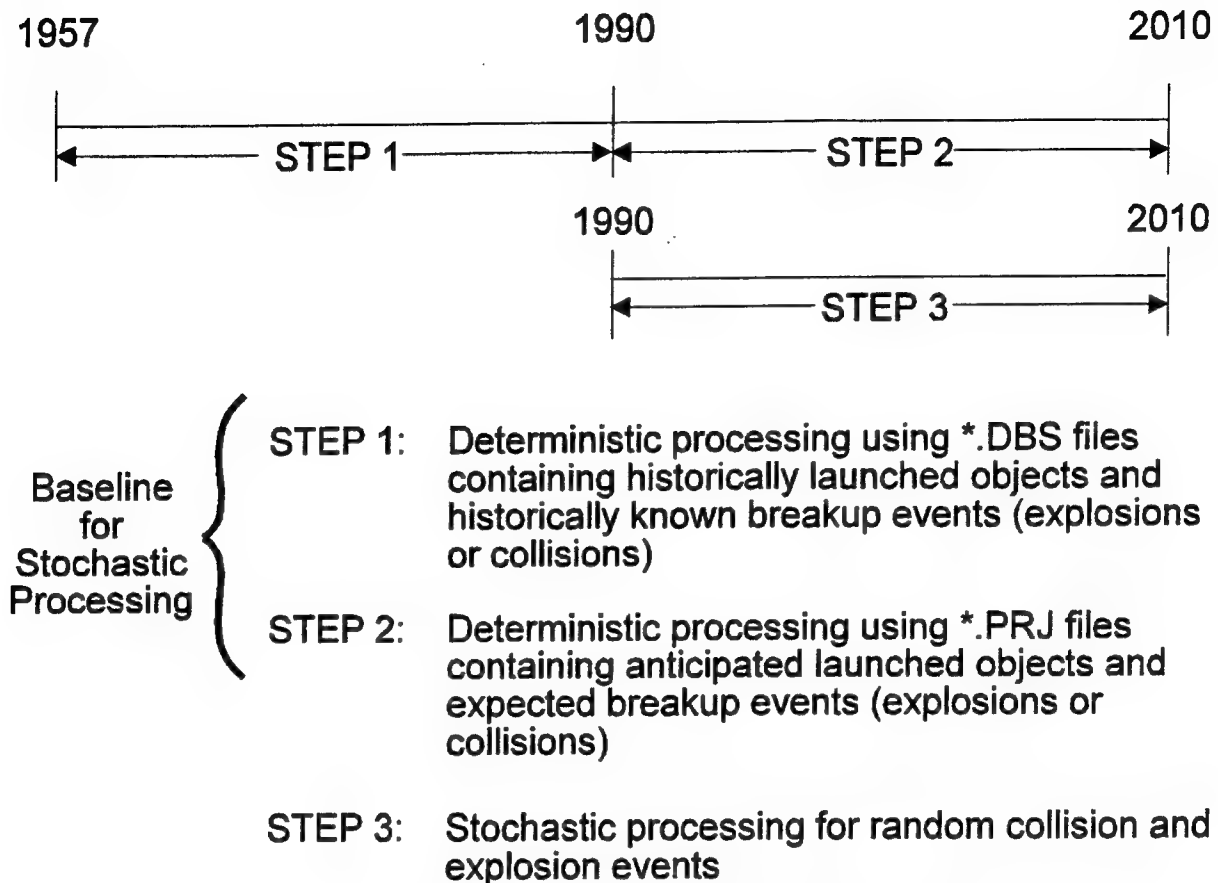Processing sequence to produce environment projections using EVOLVE:

1957   1990   2010

|←———————— STEP 1 ————————→|←———————— STEP 2 ————————→|

                                  1990   2010

                                  |←———————— STEP 3 ————————→|

Baseline
for
Stochastic
Processing
{

STEP 1: Deterministic processing using *.DBS files containing historically launched objects and historically known breakup events (explosions or collisions)

STEP 2: Deterministic processing using *.PRJ files containing anticipated launched objects and expected breakup events (explosions or collisions)

STEP 3: Stochastic processing for random collision and explosion events

Figure 3.   Code description (from Ref. 11).

2.3 PROGRAM PROCESSING

The EVOLVE program is the core processing program of a set of computer databases and programs used to obtain predicted debris environments in terms of flux or spatial density. Figure 4 diagrams the layout of the EVOLVE program together with its input and output files and associated utility postprocessing programs.

The EVOLVE model requires as input the detailed historical and future (mission model) space traffic input files. EVOLVE performs its operations deterministically and/or stochastically, writing the results to the DETDMP.DAT and/or MCENSEM.DAT output files (as specified by the conditions set in EVOLVE.DAT). Two postprocessing computer programs are available (Figure 4) which process the two types of EVOLVE output files programs HISTRCL and MCENSEM.
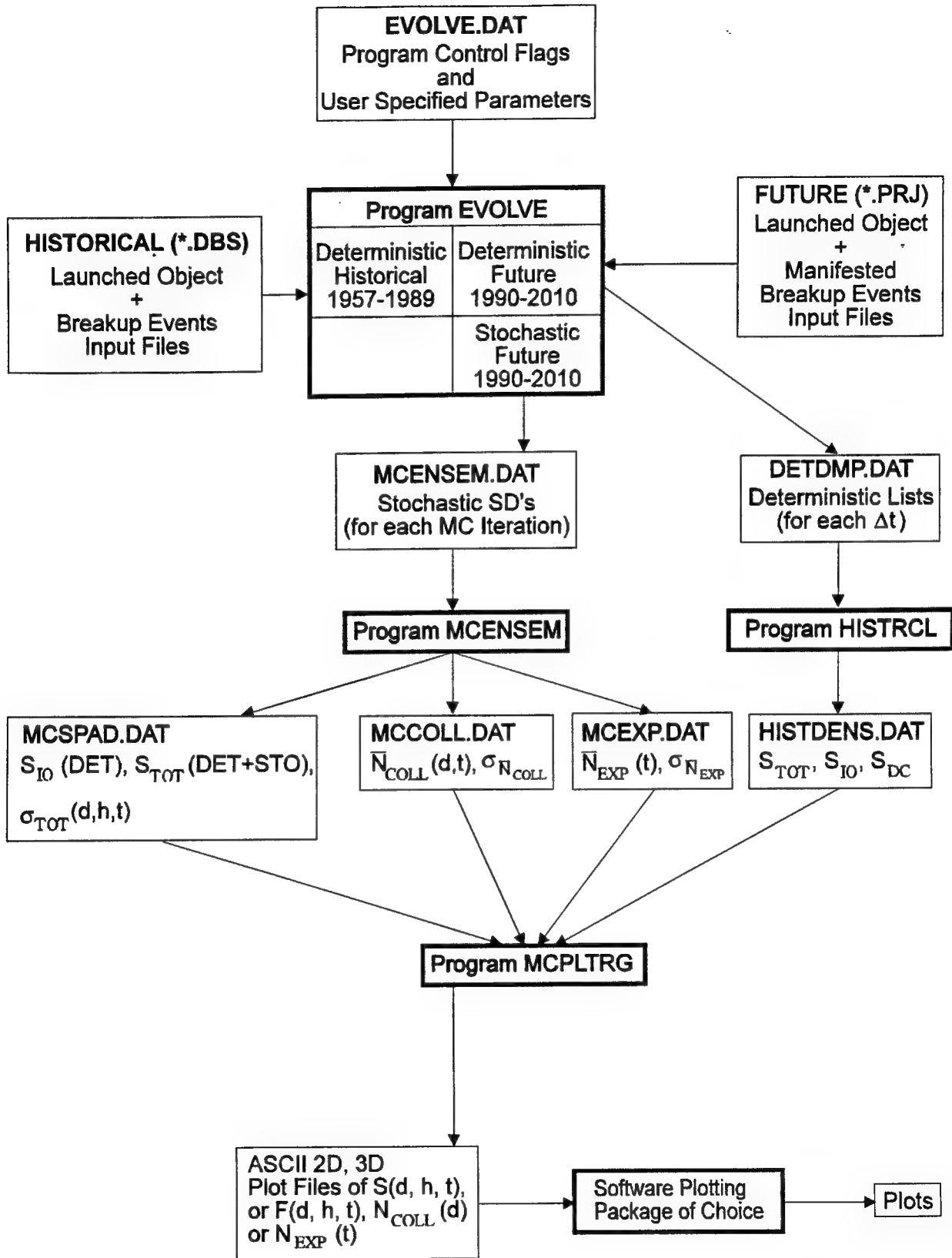
10

Figure 4.   EVOLVE input/output and postprocessing.

Program HISTRCL uses the DETDMP.DAT deterministic output file. It takes the lists of intact objects and debris clouds output at each time step, Δt, in DETDMP.DAT and calculates the total spatial densities as functions of altitude h and debris size d (cumulative and differential), storing the results in the output file HISTDENS.DAT. The intact object and debris cloud spatial densities are also calculated and output to this file. HISTRCL uses the same spatial density model subroutines, SPDENI and SPDENC, used in EVOLVE to calculate spatial densities for intact objects and debris clouds, respectively.

If Monte Carlo processing was performed in EVOLVE, the output file containing the spatial density environment of each Monte Carlo iteration is written to MCENSEM.DAT. The post-processing program MCENSEM reads these spatial density arrays and performs the statistical calculations to obtain the $\pm\sigma$ standard deviations of the mean total spatial density (deterministic and stochastic) along with the variance as functions of d (cumulative and differential), h, and t. These spatial density results are output to MCSPAD.DAT. The MCENSEM program also calculates the mean number of collisions occurring as functions of time and interaction size bins along with the variance, and writes the results to MCCOLL.DAT. Either cumulative or differential distributions using the time and size bins are created. Similarly, the mean number of explosions occurring as a function of time (both cumulative and differential) are written to file MCEXP.DAT.

The plot file generation program MCPLTRG takes as input the HISTDENS.DAT file (if the historical data option is desired) or the three data files, MCSPAD.DAT, MCCOLL.DAT, MCEXP.DAT (if statistical projected data is desired) and generates 2- or 3-D ASCII data plot files suitable as input into any standard plotting package. The MCPLTRG program prompts the user with a wide variety of information including the type of data to generate (e.g., flux versus altitude), the appropriate parameters (d, h, t) to be held fixed, and the output file name. The details of this program and type of plot files available to the user are discussed in Reference 11. The programs MCENSEM, HISTRCL, and MCPLTRG are utility program extensions of the EVOLVE program to produce EVOLVE results in usable, analyzable, format. Almost all EVOLVE results shown throughout this report were obtained using these programs. For more details of these utility programs, the reader is referred to the EVOLVE documentation in (Refs. 11 and 12).

The EVOLVE program driver (EVOLVE.FOR) reads in user-specified initial conditions and program control flags via the file EVOLVE.DAT (Ref. 11). Several user-controllable inputs relating to processing control are specified in this file. There are important user specifications relating to bin characteristics file which are listed in Table 1.

The user has a certain degree of control on the specifications used to bin the spatial density results of EVOLVE. These inputs are important since they determine the ranges over which EVOLVE does its calculations and the resolution of its results. These parameter ranges and bin widths correspond to the three dimensions of the calculated spatial density (or flux): time (t), particle diameter (d), and altitude (h). The diameter may be determined as either cumulative or differential in time. In principle, there is no limitation to the size of the spatial

density arrays; however, there is a practical limit dictated by computer memory and disk space. For example, the PC version of EVOLVE has been limited to use a maximum of 63 time bins, 26 size bins, and 50 altitude bins (81900 total) to accommodate the numerous spatial density arrays found in EVOLVE and its postprocessing routines.

Table 1. Important user specifications in EVOLVE.DAT.

Parameter	Range	Bin Width
Time	t_{start}, t_{end}	Δt (normally Δt = 1 year)
Particle Diameter	$\log_{10}(d_{min,i})$, $\log_{10}(d_{max,i})$ for decade range i	$\left(\dfrac{1}{n_{bins,i}}\right)\left(\log_{10}(d_{max,i}) - \log_{10}(d_{min,i})\right)$
Altitude	h_{min}, n_h	Δh

The 63 time bins using a Δt = 1-yr interval allows a current linear time range of 63 consecutive years. This is a software limitation only and larger time ranges are realizable. For example, larger Δt intervals could be set enlarging the size of the time bins. In EVOLVE, it is recommended that Δt always be set at 1 yr since certain models, such as the solar flux level model in EVOLVE, assume a yearly increment.

The altitude range, like that of time, is specified linearly by the minimum altitude of the range, h_{min}, and by the number of Δh wide altitude bins n_h. The maximum range value is given by $h_{max} = h_{min} + n_h \Delta h$. The spatial density characterized by altitude h_o is just the average over the bin width. For example, assume the specific altitude h_o = 150 km were being characterized in EVOLVE calculations and the user specified h_{min} = 100 km, n_h = 50, and Δh = 38 km. The 150-km altitude would contribute to altitude bin #2 in the 139 to 176-km range, whose linear average is 157 km. This procedure approximates the actual altitude being binned to within the width of an altitude bin. The user can, of course, adjust the bin values and Δh widths to center the bins about any desired altitude. Decreasing the bin width would improve the accuracy of characterizing one particular altitude. The effect of the Δh width on the overall spatial density shall be explored further in Subsection 3.2.1.4.

The particle diameter dependence of spatial density varies over several orders of magnitude; consequently, the diameter bins are specified linearly in logarithmic space to accommodate the entire diameter range. The user has the option to specify one or more decade ranges in logarithmic space and then to specify the number of subintervals within each decade range. The number of decade ranges, n_i, containing $n_{d,i}$ bins/decade is first specified. For each decade range, i, the number of bins $n_{d,i}$ with which to subdivide the range is user-specified as well as the lower and upper limits of the decade expressed in terms of unit powers of 10. For example, the decade range from 0.1 to 100 cm is expressed as -3 to +0 or $\log_{10}(10^{-3})$ -

$\log_{10}(10^0)$ m. The option to specify more than one decade range with a different $n_{d,i}$ value gives the user the versatility of dividing a certain diameter region with finer resolution than other regions. For all purposes in this present assessment, only one decade range with one $n_{d,i}$ value was used for simplicity.

Several models in EVOLVE require mass distributions rather than particle size distributions; at the time the diameter bins are established mass bins are also established via a mass versus diameter analytic relationship m(d) (Subsection 3.2.2). The mass distribution should be considered the more fundamental quantity describing breakup debris characteristics. As will be described in Subsections 3.2.2 and 3.2.3, the number distributions produced in the collision and explosion breakup events are specified in terms of mass rather than diameter, and to produce flux results as functions of diameter a mass/size relationship is required.

2.4 OBJECT MODELING

EVOLVE models two sources of objects contributed to the environment: intact objects (Subsection 2.4.1) and breakup debris clouds (Subsection 2.4.2).

2.4.1 Intact Objects

The debris environment modeled in EVOLVE contains (as one component) intact objects inserted into orbit from launch activity. Active and nonactive satellite payloads, orbital insertion rocket boosters, and operationally-generated debris such as explosive bolts and shrouds comprise a significant contribution to the overall environment and are the main source of large objects for cumulative sizes d >10.0 cm (Subsection 3.4). All intact objects are introduced deterministically through historical and mission model databases read by the MISMOD subroutine in EVOLVE. These databases represent a detailed description of the launched space traffic during any given time. Once launched, the orbits are propagated and a dynamic array list is maintained for each time step in the EVOLVE.FOR driver. The treatment of intact objects in the debris environment shall be discussed fully in the intact object source model assessment of Subsection 3.2.1.

2.4.2 Debris Clouds

On-orbit breakup debris clouds constitute the other environmental component modeled in EVOLVE. A debris cloud is defined as the ensemble of fragments resulting from a collision or explosive breakup, distributed into the proper size bins. The number placed into each size bin is estimated using a number versus size distribution, derived from a number versus mass distribution breakup model dependent upon breakup type. The breakup event is then characterized by a series of subclouds, each corresponding to a diameter bin size. The orbital element dispersion and, consequently, the spatial density of each subcloud depends on the characteristic ejecta velocity model derived from an assumed ejecta velocity (ΔV) model, the breakup altitude of the event, the breakup epoch, and the time after the breakup. The breakup epoch together with the time after breakup are used to calculate the effective time that the

cloud is exposed to the atmospheric drag processes to account for a variable solar flux. The time evolution of each subcloud spatial density is determined for each cloud at each time step in the EVOLVE. FOR driver. This is accomplished with a relatively simple analytical flux function, which is a function of t, d, h, and h_0 (breakup altitude). The treatment of debris clouds is explored in greater detail in the debris cloud source model (Subsection 3.2.2).

2.5 PROCESSING PATHWAYS

The deterministic and stochastic EVOLVE processing pathways are elaborated upon in this section. Subsection 2.5.1 describes the deterministic introduction of intact objects and debris clouds while Subsection 2.5.2 examines the randomized introduction of debris clouds via the stochastic processing algorithm.

2.5.1 Deterministic Processing

The EVOLVE model deterministic processing pathway handles all objects placed into orbit via the input files for historical (DBS extension files) and future (PRJ extension files) years. This includes all launched intact objects (payloads, rocket bodies, and operational debris) and all specified fragmentation event clouds. The details of these objects are discussed in Subsections 3.2.1.1 and 3.2.1.2. The purpose of deterministic processing is to place the objects into the environment from the data files through a time loop ranging over the user-specified time range in user-specified Δt increments read from the EVOLVE.DAT file. At each time step, the orbits (for intact objects) and subclouds (for debris clouds) are propagated using the appropriate model. A dynamic array of intact objects and debris clouds is maintained through the time loop. Figure 5(a) charts the salient procedures in the deterministic processing block while Figure 5(b) diagrams the essential procedures of the stochastic block. These diagrams correspond to the appropriate processing blocks shown in Figure 2. Each major step describes the action of an EVOLVE subroutine labeled in bold script.

In the deterministic process loop, the current level of solar activity S is obtained by SOLACT, to be used as input in the propagation models for intact objects (ORBUPD) and debris clouds (CLDUPD). The MISMOD program performs the operations to read and store the current year's input file lists. The number of intact objects in the dynamic arrays is expanded by the number of intact objects input from these lists. This expanded array of objects is processed in ORBUPD. Likewise, the current number of clouds is updated in similar fashion and the array list of clouds propagated in subroutine CLDUPD. If the user opts to create the MCRSTRT.DAT, the spatial densities for each source is calculated in subroutines SPDENI (intact objects) and SPDENC (debris clouds). Otherwise, the time loop processing continues until the final specified time step is reached.
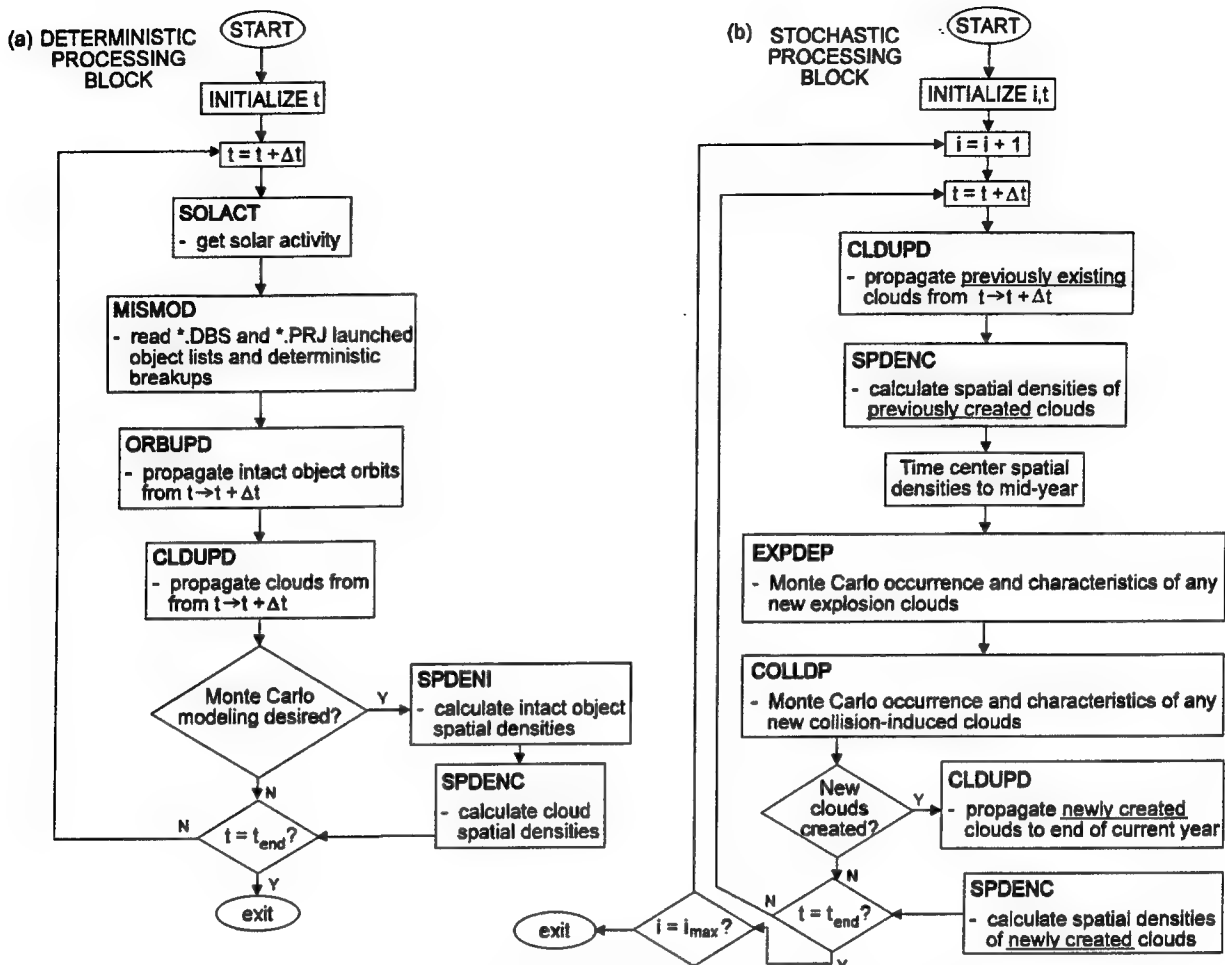
Figure 5.   EVOLVE deterministic and stochastic flow loops (from Ref. 11).

2.5.2 Stochastic Processing

Stochastic processing handles the probabilistic Monte Carlo production of collision and explosion breakup events. The fragment clouds produced in this processing loop are in addition to those specified in deterministic processing. While the environment produced in deterministic processing is exactly reproducible given the same input conditions, the stochastic processing introduces an uncertainty resulting from the probabilistic nature of future breakup events. The occurrence of collisions between two objects in the environment and explosions among potentially explosive objects such as rocket boosters is modeled in Monte Carlo fashion with a random number selection using an assumed Poisson probability distribution. Figure 5(b) diagrams the stochastic processing block contained within the EVOLVE.FOR driver.

This algorithm contains two loops, the outer one for the Monte Carlo iteration, and the inner one for the time loop. During each step of the time loop, previously created stochastic clouds

16

are propagated to the end of the current time step, $t + \Delta t$, at which time the spatial density of the previously created clouds is obtained. These clouds are time-centered for the current time step (i.e., the spatial densities of the clouds evaluated at the end of the time step are averaged with the spatial densities determined for the beginning of the time step). Using the time-centered total spatial densities (deterministic baseline + previously created stochastic clouds), the occurrence and characteristics of any new high intensity explosion (HIE) and low intensity explosion (LIE) debris cloud(s) is determined in EXPDEP. As will be explained in Subsection 3.2.2.1, the spatial densities are required to determine the number of objects within each altitude and size bin capable of exploding. Next, the subroutine COLLDP is called to determine the occurrence and characteristics of any new collision-induced breakup cloud(s). The total time-centered spatial densities are used in COLLDP to obtain the total number of objects within each altitude and size bin. This is used for estimating the collision rates between objects, which is needed for calculating the collision probability (Subsection 3.2.2.1). Explosion and collision clouds produced from the calls to EXPDEP and COLLDP are then propagated to the current end of time step in a second call to CLDUPD. Spatial densities are calculated for the newly established debris clouds and added to the environment before continuing to the next time step.

Once the maximum time range specified by the user is reached, the current Monte Carlo trial is completed and its results are written to MCENSEM.DAT. The Monte Carlo trial counter is incremented and the procedure starts for the next trial. The user specifies a random number seed in EVOLVE.DAT. Thus, a new set of projections may be made by changing this value between EVOLVE runs. The EVOLVE program generates the MCENSEM.DAT file containing a record of each trial's spatial density arrays. To calculate the means and variances of the projected environments, a separate postprocessing computer program called MCENSEM must be run to process the MCENSEM.DAT file.

3.0 EVOLVE PROGRAM ASSESSMENT

3.1 INTACT OBJECT RELATED SOURCE MODELS

Launched objects are the major source of large size debris (d $\geq$ 10.0 cm). Approximately half of the USSPACECOM radar tracked objects in orbit are active payloads, inactive payloads, and operational debris; the rest is fragmentation debris large enough to be detected by the detection threshold (5-10 cm depending on altitude) (Ref. 1). Unlike fragmentation debris, almost all of the launched intact objects are large enough to be regularly tracked by radar. Only very small operational debris such as remnants of explosive bolts are not generally trackable. The intact objects launched at a rate of approximately 300 objects per year represent one source of debris added to the environment that is handled by EVOLVE. Its treatment of intact objects is made in a computationally efficient straightforward analytical manner. Object orbits are individually propagated and a complete accounting is made of their continued presence in the LEO environment governed by atmospheric drag and gravitational perturbations.

Intact objects are directly specified by the user in historical and future mission model data files. These databases are described in Subsections 3.1.1 (historical) and 3.1.2 (future traffic). Subsection 3.1.3 explains the mechanisms to propagate the intact object orbit through a subroutine call to the orbital decay routines. Subsection 3.1.4 closes the discussion of EVOLVE intact object handling by explaining the techniques to convert the presence of intact objects in the environment into a spatial density or flux.

3.1.1 Historical Database

3.1.1.1 Description. For past years of the space age, EVOLVE introduces launched objects as discrete intact objects into the environment from established launch manifests. The historical manifests contain those objects actually launched into orbit from the years 1957-1988 (in the version assessed by ORION). The historical lists can be extended a year at a time as they become available.

Currently, EVOLVE uses as input 33 historical data files labeled with the file extension, *.DBS, covering the years 1957-1989. These lists were provided to ORION by NASA. The 1989 file is a replication of the 1988 list. Only launched payloads, spent rocket boosters, and operational debris known to be associated with the launch are included. The lists contain all information needed by EVOLVE to conduct its deterministic historical processing. These fields are given in Table 2. An asterisk character located in the fifth column of the first field of a record signifies that all subsequent records represent deterministically-introduced debris clouds resulting from known satellite breakups. In this case, the code processes the file information for a debris cloud record. This record contains fields of parameter values such as the type of fragmentation event associated with a cloud. These fields are described in Table 3.

18

Table 2. EVOLVE intact object input file record description.

Data Field	Data
1	International Designator (character)
2	Name or description (character)
3	h_{ao}, initial apogee altitude (km)
4	h_{po}, initial perigee altitude (km)
5	i_o, inclination (deg)
6	Ω_o, initial right ascension of the ascending node (deg)
7	ω_o, initial argument of perigee (deg)
8	A, area (m^2)
9	m, mass (kg)
10	A/m, area/mass ratio (m^2/kg)
11	Stationkeeping duration (yrs)
12	Deorbit flag (0 = no deorbit, 1 = deorbit at end of life)
13	Collision/Explosion event (0 = nonexplosive, 1 = collision, 2 = LIE, 3 = HIE)
14	Collision avoidance (0 = no CA, > 0 = number of years for CA)
15	Minimum size for collision avoidance (mm)
16	Descriptor field
17	Number of objects having this same orbit

Table 3. EVOLVE debris cloud input file record description.

Data Field	Data
1	Cloud name (character)
3-7	Same as in Table 2
9	Breakup type (1 = Collision, 2 = LIE, 3 = HIE)
10	Mass of exploding object or collision target
12	Mass of collision projectile

3.1.1.2 <u>Model Assessment.</u> The historical database is a complete launch record of all historical years between 1957-1988 derived from the USSPACECOM Space Surveillance Center catalog data and other unclassified sources. It represents a complete account of all known launched objects into LEO, geosynchronous orbit (GEO), and other special orbits such as geosynchronous transfer orbits (GTO), Molniya, etc. Unless new information comes to light to add to the manifest, these file lists require no user modification. These files could be easily modified to study "what if" scenarios using EVOLVE. These studies can examine the possible effects of having altered a specific condition in the past and how such a change might have impacted the current and future environments. The orbital elements h_a, h_p, and i

are those prescribed at launch or measured shortly after orbital insertion by radar network sensors.

The only information not included in these data lists is the exact date of orbital insertion. Currently, EVOLVE does need this information since it randomizes the launch date. If the EVOLVE model were concerned with accurately replicating the current (or any past date environment) this might be an issue; however, the long-term and statistical nature of the code makes this unnecessary because actual launch dates are distributed uniformly throughout the year. Whether random or actual launch dates are used is immaterial for most current or future environments.

As a recommendation, it is suggested that actual historical launch dates be used wherever possible to make the model a more robust accounting of actual historical conditions, although for most applications the results would be negligible since these dates are statistically distributed throughout the year. This modification would be simple to implement.

3.1.2 Mission (Traffic) Model Database

3.1.2.1 Description. For projected years, EVOLVE introduces launched objects as discrete intact objects into the environment from a mission model database. The mission model represents a proposed launch manifest identical in format and processing as historically launched objects. This list contains all anticipated launches along with their explicit orbit parameters, mass/size characteristics, etc. The fields contained in these lists are described in Table 2.

Currently, there are 21 files (file extension *.PRJ) that contain projected mission model intact object lists for years 1990-2010. These lists have the same format as the *.DBS files. The only distinction between historical files and projected data files is the file extension. The *.PRJ files, as provided by NASA, contain the Civil Needs Database (US civilian satellites including shuttle launches) appended to the 1988 historical (SATS_88.DBS) data file to approximate the number of objects to be placed in orbit for each future year (Ref. 14). The appended historical data file approximates the contribution from other sources (US Department of Defense [DoD], Soviet, European, and other foreign traffic) since no other valid traffic model is currently provided. Therefore, the *.PRJ files, as they now stand, serve as the predicted data until a more complete mission model that includes Soviet, European launches, etc., can be obtained. Like the historical data files, debris clouds may be introduced to the environment by inclusion in the record file. This allows certain users (e.g., antisatellite system modelers) to manifest a breakup event to examine its long-term effect upon the environment. Treatment of such a debris cloud follows the same deterministic processing pathway as in the historically introduced cloud.

3.1.2.2 Database Assessment. The importance of the traffic model implemented in the projected data files cannot be overstated. The EVOLVE results for projected years depend largely on the behavior of the additional objects and fragmentation events introduced in future

years. The launch rate for a future year is the number of items specified in that year's mission model list; the contents of these projected files dictate the trends modeled in the future environment.

The traffic model defines the deterministic baseline contribution to the future modeled environment. It directly affects the stochastic processing of events by affecting the a priori spatial densities required by the Monte Carlo prediction model for collision and explosion probabilistic occurrences (Subsection 3.2.1). Implementation of the projected mission model via the input lists is the most straightforward approach possible. Adjusting the launch rate or explosion rate means adjusting the respective number of intact objects or explosion events in the input file. The traffic model assumes no explicit traffic growth rate or explosion rate function. It contains the detail and flexibility of incrementing the environment object-by-object but also has the associated problem of defining the traffic model to a detail that makes altering the traffic model a logistical burden to the user. The model allows ready incorporation of alternative mission model data sets. The traffic model approach in EVOLVE is deemed to be the best choice available, but one which can be unwieldy if frequent or major changes are desired.

3.1.3 Intact Object Orbital Propagation Model

EVOLVE processes the intact objects through an algorithm that sets up the conditions required by the orbital propagator and then calls the propagator routine to obtain updated values of the orbital elements. This algorithm, composed of a series of component subroutines, is the intact object orbital propagation model.

Intact objects input into EVOLVE (from the files described in Subsections 3.2.1.1 and 3.2.1.2) are launched into orbit at a current rate of ~300 objects/year. As will be shown in the collision and explosion models for breakup debris generation (Subsections 3.2.2. and 3.2.3), the number of debris fragments, especially small diameter fragments, generated per event can reach millions. Compared to breakup debris, the intact objects comprise only a small number of the total objects in LEO. Thus, the manageable number of intact objects (~2500 are maintained by EVOLVE in orbit through 1989) allows direct calculation of their orbits through analytical orbital mechanics expressions coupled with atmospheric drag and orbital perturbation effects.

3.1.3.1 Description. EVOLVE establishes a time loop in the deterministic processing phase which begins at the user-specified time and loops through the specified Δt increments until a user-specified final time is reached. Currently, EVOLVE is equipped to only handle yearly increments (i.e., Δt is normally set to 1 yr). At each time step within the deterministic processing loop (in the EVOLVE.FOR main program), the data file containing newly launched payloads, rocket bodies, and related operational debris data for the year is read into EVOLVE (via subroutine MISMOD). These objects are added to the end of a list of previously launched intact objects still in orbit as of the beginning of the year. (Deterministically placed debris clouds encountered in the data files are processed differently,

21

as will be discussed within the context of the debris cloud propagation model in Subsection 3.2.4.) Each intact object together with its orbital elements and other record data read from the historical or projected database (Subsections 3.1.1 and 3.1.2) is uniquely identified by the array index variable NORB. The maximum value of NORB at any point during program operation gives the current number of intact objects in orbit.

Once the current year's launched objects are added and NORB is updated, EVOLVE invokes the subroutine ORBUPD containing the intact object orbital propagation model. This model loops through the list of all intact objects (i = 1...NORB) and performs several operations in the following order:

- Determine the time elapsed since launch.

- Determine if the propagation decay routines will be used on this object. The criteria for this are

  - If perigee altitude h_p < 100 km, object orbit is considered decayed and is removed
  - If perigee altitude h_p > 2000 km, object orbit exceeds the limitations of the decay routines and is removed
  - If apogee altitude h_a > 40000 km, h_a is set to 40000 km

- Determine the orbital propagation parameters. These are

  - Semimajor axis (a_i)
  - Eccentricity (e_i)
  - Propagation time step (Δt_i)
  - Absolute propagation times (epoch)

- Determine the sun's right ascension (α) to the ecliptic plane.

- Convert the following quantities from degrees to radians:

  - Inclination (i_i)
  - Argument of perigee (a_i)
  - Right ascension of ascending node (Ω_i)
  - Right ascension of the sun (α)

- Determine the amount of drag for the object. To do so requires calculation of the ballistic coefficient $B_i = C_D(A/m)_i$, where $(A/m)_i$ is the area to mass ratio for the object and C_D is the coefficient of drag (C_D is assumed to be 2.2 for all objects).

- Determine the exospheric temperature (T_∞).

- Invoke the propagation/decay routines (subroutine DECAY). The inputs to DECAY are

  - Semimajor axis, a_i
  - Eccentricity, e_i
  - Inclination, i_i (does not change in DECAY)
  - Argument of perigee, ω_i
  - Right ascension of the ascending node, Ω_i
  - Ballistic coefficient, $B_i = C_D(A/m)_i$
  - Solar right ascension, α
  - Exospheric temperature, T_∞
  - Propagation time step, Δt_i

- Update in subroutine PRECPY the values for Ω_i and ϖ_i using first-order secular perturbations (J_2). The values of a_i, e_i, and i_i from DECAY are used as the inputs.

- See if the new perigee altitude $h_p < 100$ km. Remove all objects for which this condition is true.

A more detailed description of these bulleted algorithm items is provided in Appendix A.

3.1.3.2 <u>Model Assessment</u>. The methodology to update the intact object orbital elements a and e is a straightforward application of the decay routines. The model provides the shell in which to calculate the initial conditions for the call to subroutine DECAY. The assessment of the DECAY routines themselves is given in Subsection 3.3.3.

Updating the argument of perigee (ω) and right ascension of the ascending node (Ω) within ORBUPD is not necessary for most LEO orbits encountered. Any orbit whose apogee altitude $h_a < 14000$ km is subjected only to the atmospheric drag perturbation. (See Subsection 3.3.3 for a description of the DECAY model and orbit types.) The calculations for ω and Ω are only important as initial conditions for the sun/moon perturbations. (Type 2 or 3 orbits as described in Subsection 3.3.3). Type 2 orbits do not have updated values of ω and Ω returned from the DECAY subroutine, therefore the ω, Ω updates are necessary for an accurate calculation of a Type 2 orbit. A Type 3 orbit, however, does return updated versions of ω and Ω from DECAY but the values returned are ignored. Instead, the ω and Ω values are updated in the PRECPY subroutine just after the return from the DECAY routines in ORBUPD.

The algorithm for solar right ascension is of relatively low precision (0.01 deg precision) as stated in Reference 15, but is a simple analytic expression sufficient for the accuracy of the orbital propagation and decay processes utilized in EVOLVE.

3.1.4 Intact Object Spatial Density Model

EVOLVE models the near-earth environment by calculating the spatial number density of orbiting objects located within a spherical shell volume of space about the earth. Intact objects launched into orbit through the input file databases contribute one portion of the total number of objects located in this volume. The majority of objects contributing to the environment are fragmentation debris. The spatial density contribution from breakup debris is discussed in Subsection 3.2.4. This section discusses the spatial density calculations for intact objects and how the radial and latitudinal dependences of the density can be estimated.

3.1.4.1 Description. The spatial density algorithm for intact objects used in EVOLVE is based on an algorithm developed to find the average collision probability between the outer moons of Jupiter (Ref. 7). This reference derives the spatial density expressions and then describes how these may be used to determine the probability of collision between any two objects in a defined volume element. The spatial density (number of objects per unit volume) is defined as the fraction of time that an object spends in a specified volume element along its orbital path. For an earth orbiting satellite, the perigee q, the apogee q', and orbital plane inclination i, define the orbit path. If Δt is the amount of time spent in the volume element ΔU and T is the orbital period then the density is given by

$$S = \frac{\Delta t}{T \Delta U} \tag{1}$$

The simplest volume element ΔU to consider is a thin spherical shell of radius R, and thickness, ΔR, about the center of the earth. A single orbit will contribute to be the spatial densities of a series of one or more ΔR thick shells of varying radii, intersecting the orbit path. If the orbit is circular, the satellite is contained entirely within a single arbitrarily thick shell; the spatial density is just the inverse of the shell volume. The volume of a shell ΔU at inner radius R given a thickness ΔR is

$$\Delta U = \frac{4\pi}{3}[(R + \Delta R)^3 - R^3] \tag{2}$$

Assuming that $\Delta R \ll R$ as would be the case for a narrow altitude band in LEO, this reduces to

$$\Delta U = 4\pi R^2 \Delta R \tag{3}$$

Thus, for circular orbits, the average spatial density in the spherical shell is

$$S = \frac{1}{4\pi R^2 \Delta R} \tag{4}$$

where $\Delta t/T = 1$ (i.e., the object always lies within the shell).

24

The assumption is made that the right ascension of the ascending node and argument of perigee are constantly changing with time due to secular perturbations of the orbit. Because of this perturbation, all values of these two parameters are likely to be considered equal. This is true for all orbits being propagated by the model described in Subsection 3.1.3. The uniform right ascension of the ascending node distribution means spatial density is independent of longitude. The consequence of a secular and uniform change in the argument of perigee will be discussed later in this subsection.

For elliptical orbits, unless either the apogee or perigee lies within the volume element, the object will pass through a volume element twice within one orbital period (Figure 6). The time spent within this shell is then twice the time it takes the object to traverse the radial dimension of the shell. If V_R is the radial component of the orbital velocity V, then

$$\Delta t = \frac{2\Delta R}{V_R} \tag{5}$$
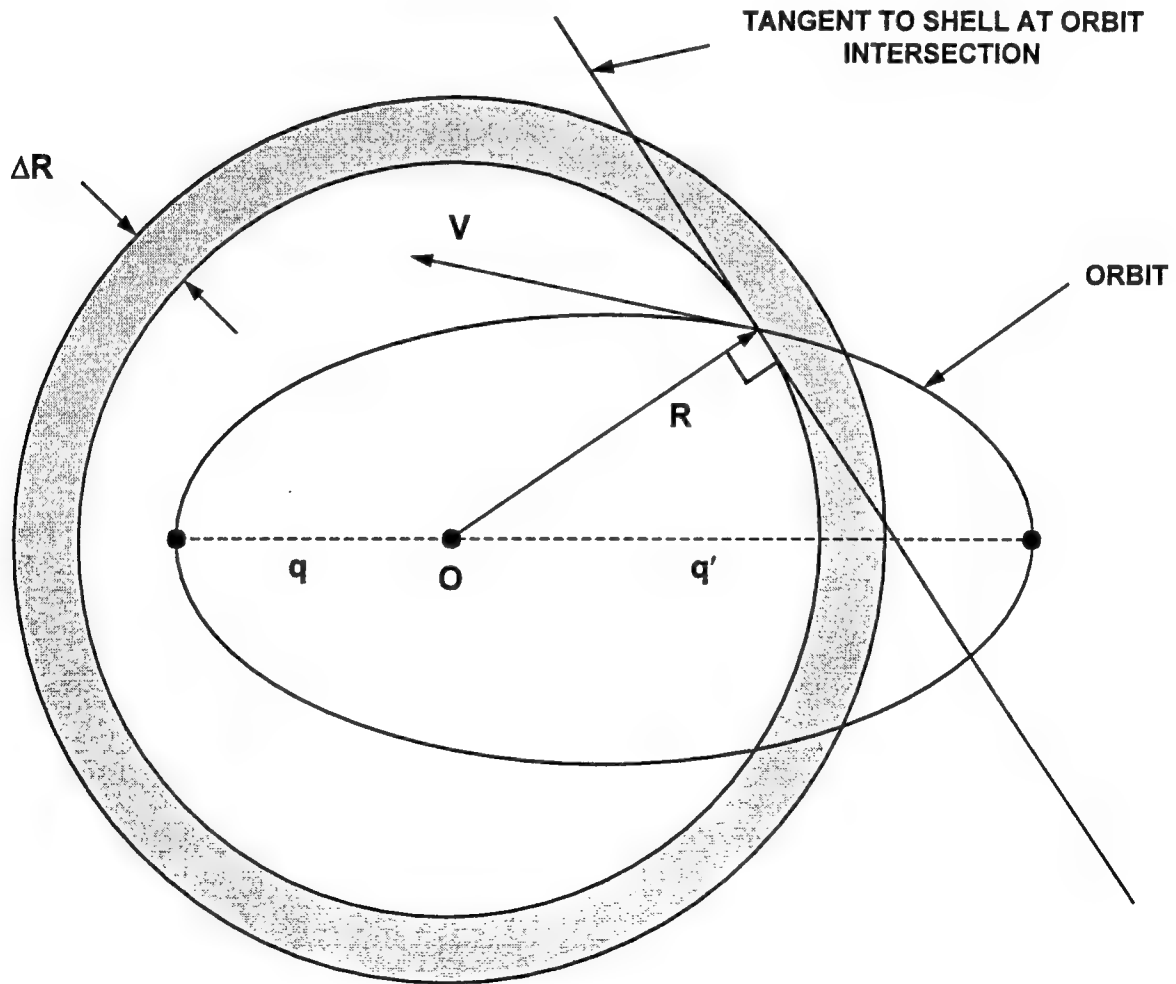
Figure 6.   Diagram showing the relationship between an elliptical orbit and a spherical shell of inner radius R and thickness ΔR.

25

The T and V_R are readily derivable from Keplerian mechanics to yield an expression for the spatial density in terms of the orbital elements, a (semimajor axis), q (perigee), q' (apogee), and radial distance R

$$
S(R) = \begin{cases} \dfrac{1}{4\pi^2 Ra\sqrt{(R-q)(q'-R)}} & \text{for } q \leq R \leq q' \\[2em] 0 & \text{for } R < q \text{ or } R > q' \end{cases} \tag{6}
$$

The details of the derivation may be found in Reference 7.

This expression yields the spatial density averaged over all latitudes in a shell of radius, R, and unit thickness. It represents the total spatial density contributed to that spherical shell volume by a single object. The total spatial density in the shell (which corresponds to an altitude band) is merely a sum of the contributions of all orbits that pierce this unit volume.

The spatial density within a spherical shell can be localized further by considering the latitude dependence that a single orbiting object contributes. If latitude is considered in addition to radius, the density is considered within annulus volume elements ($\Delta U_{\beta\text{-band}}$) centered about Earth's rotational axis. A cross-section of a portion of such a an annular element is show in Figure 7. The latitude dependence originates from both the orbital inclination and the assumed uniform secular perturbation of the argument of perigee over a long period of time. The result is that all points along an orbit eventually sweep out a circular path in the plane of the orbit having inclination, i. Consider the point, P, of the orbit at radius, R, and within the distance ΔR in Figure 8. This ΔR corresponds to the shell thickness of a spherical shell that intersects the orbital plane. Figure 9 shows this orbit in the orbital plane. The secular ω perturbation causes the argument of perigee, ω, to rotate with a constant angular velocity denoted by $\dot\omega$. Keeping P fixed means that the ω rotation will keep point P within R and $R + \Delta R$. If an object's orbital distance was always the constant distance, the spatial density averaged over all latitudes at the radius R would be the inverse of the shell volume, i.e.

$$
S'(R) = \frac{1}{4\pi R^2 \Delta R} \tag{7}
$$

(That is, the object fixed at P always lies within the spherical shell as the argument of perigee precesses.) To determine the latitude dependence of S, the shell is further segmented into volumes as shown in Figure 7. These volumes are slivers of the spherical shell between latitudes β and $\beta + \Delta\beta$. The volume of this element is
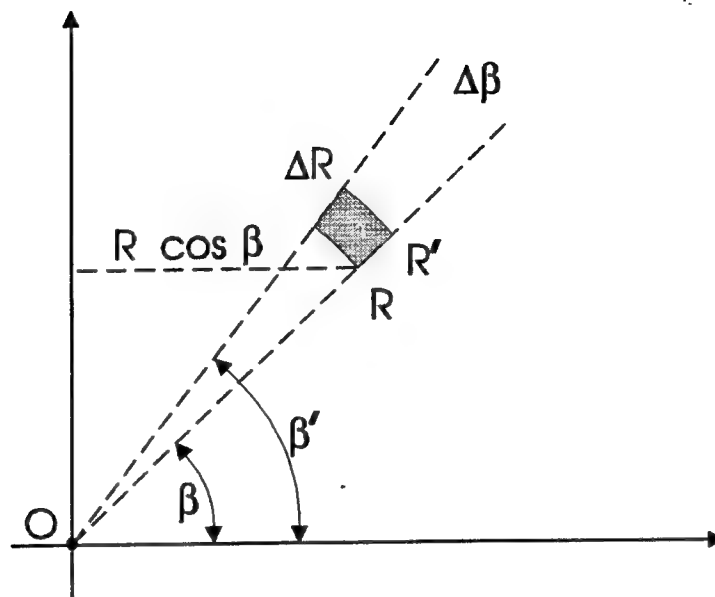
Figure 7.   Diagram showing the cross-section of the latitudinal annulus volume
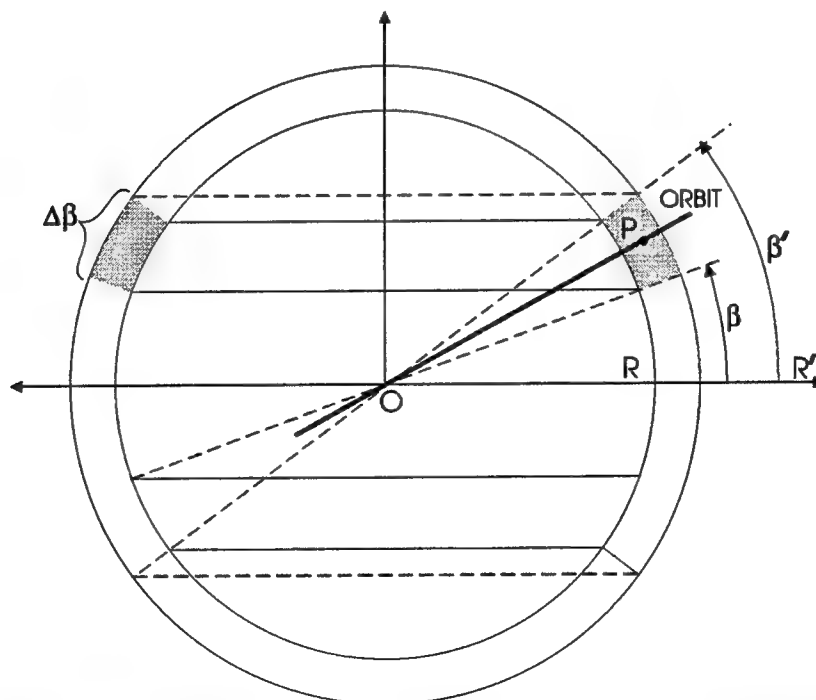element ($\Delta U_{\beta\text{-band}}$).

Figure 8.   Diagram showing an orbit with respect to the equatorial plane and spherical
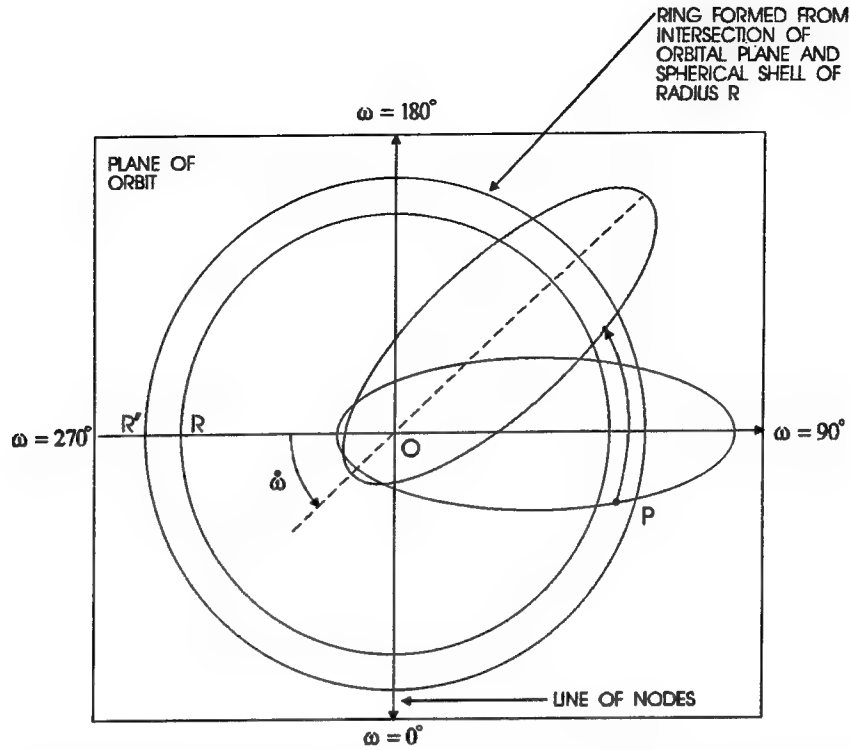shell of inner radius R. The latitudinal annular volume element containing P is
highlighted.

27

Figure 9. Diagram showing the intersection of an elliptical orbit in its orbital plane with a spherical shell of inner radius R and outer radius R+R′.

$$\Delta U_{\beta-band} = 2\pi R^2 \cos\beta \, \Delta\beta \, \Delta R \qquad (8)$$

They form volumetric latitude rings (or bands) about the z-axis (which corresponds to the Earth's axis of rotation). As ω of an orbit at an inclined angle rotates with respect to the equatorial plane, the P sweeps through all accessible latitude bands at a constant distance, R.

The values of latitude, β, which a single inclined orbit traverses, ranges from $0 \le \beta \le i$. Above this latitude there is no spatial density contribution to any latitude band from this object. Since ω is assumed to be uniformly distributed, the circular path created at P will cross all latitude bands up to a maximum latitude, β_{max}, reached when P reaches its maximum vertical distance above or below the equatorial plane. If P is either the perigee or apogee point, this occurs at ω = 90 deg and 270 deg and, in addition, if P is the apogee then β_{max} = i. As a result, P will spend the greatest amount of time in the latitude band specified by β_{max}. The time spent traversing a latitude band, $\Delta\beta$, is given by

$$\Delta t = \frac{2\Delta\beta}{\dot{\omega}\sin\alpha} \qquad (9)$$

28

The value of α is given by spherical geometry as

$$\alpha = \cos^{-1}\left(\frac{\cos i}{\cos \beta}\right) \qquad (10)$$

Therefore, the minimum Δt occurs at $\beta = 0$ where $\sin(\alpha) = \sin(i)$ and the maximum asymptotically approaches infinity as $\beta \to i$. Figure 10 shows the spatial density of a 65 deg inclination orbit at a single altitude (R = constant) for all latitudes 0 deg $< \beta <$ 65 deg. The circular path at radius R caused by ω precession contributes to the spatial density in the volume element $\Delta U_{\beta\text{-band}}$ by the amount

$$S'(R,\beta) = \frac{\Delta t}{T\Delta U_{\beta-\text{band}}} \qquad (11)$$

where the period is given by

$$T = \frac{2\pi}{\dot{\omega}}$$

and $\dot{\omega}$ is the angular velocity.
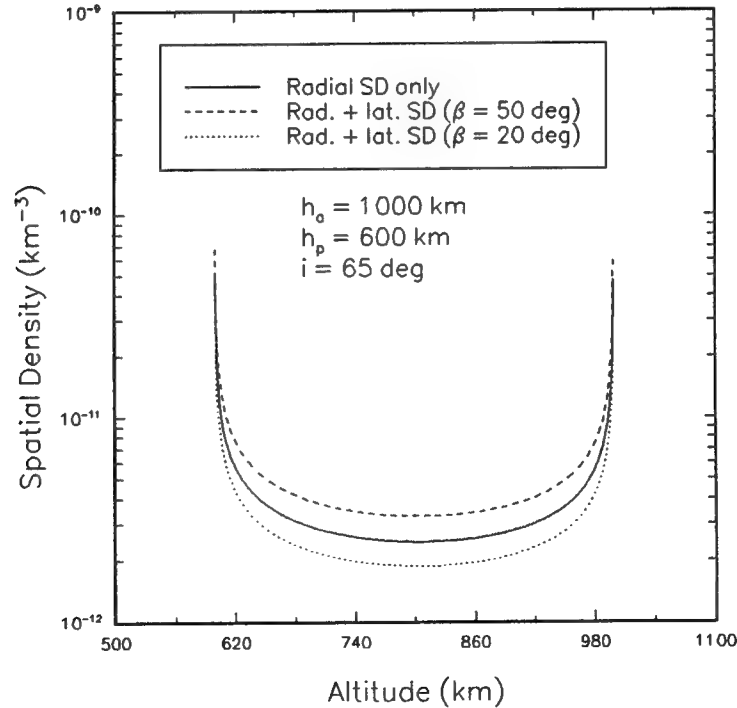
Figure 10.   Spatial density versus altitude for a single orbit (q = 600 km, q' = 1000 km, i = 65 deg).

29

Thus,

$$S'(R, \beta) = \frac{1}{2\pi^2 R^2 \sin\alpha \cos\beta \, \Delta R} \tag{12}$$

is the spatial density at (R, β) given that the object is within R and $R + \Delta R$. This density can be written as a product of the radial dependence and the latitude dependence to give

$$S'(R, \beta) = f(\beta)S'(R) \tag{13}$$

The ratio of the spatial density at latitude β, $S'(R, \beta)$, to the spatial density of the spherical shell at radius R averaged over all latitudes is given by

$$f(\beta) = \frac{S'(R, \beta)}{S'(R)} \tag{14}$$

Even if the object at P does not have unit probability of being within $R + \Delta R$ at all times, but only traverses the ΔR thick shell for a fraction $\Delta t_{\Delta R}$ of its orbital period, the results are the same:

$$f(\beta) = \frac{(\frac{\Delta t_{\Delta R}}{T})S'(R, \beta)}{(\frac{\Delta t_{\Delta R}}{T})S'(R)} = \frac{S'(R, \beta)}{S'(R)} \tag{15}$$

This factor then represents a spatial density enhancement over the purely radial spatial density to account for the latitude dependence. The expression for the spatial density at any (R, β) becomes after some derivation

$$S(R, \beta) = \frac{1}{2\pi^3 Ra\sqrt{(\sin^2 i - \sin^2\beta)(R - q)(q' - R)}} \tag{16}$$

where $q < R < q'$ and $0 < \beta < i$. When $R < q$, $R > q'$, or $\beta > i$, $S(R, \beta) = 0$. Note that this expression is singular at $R = q$, $R = q'$, and $\beta = i$. This problem is overcome by finding the average spatial density over the volume (Ref. 7). These singularities are integrable when the average spatial density of a volume is calculated. The average number of objects found within a finite volume element is

$$\bar{S} = \frac{\int S(R, \beta) \, dU}{\int dU} = \frac{\int\int f(\beta)S(R)R^2 \cos\beta \, dR \, d\beta}{\int\int R^2 \cos\beta \, dR \, d\beta} \tag{17}$$

30

This can be written as two separable integrals:

$$\bar{S}(R, R') = \frac{\int_R^{R'} S(R)R^2 \, dR}{\int_R^{R'} R^2 \, dR} \qquad \text{and} \tag{18}$$

$$\bar{f}(\beta, \beta') = \frac{\int_\beta^{\beta'} f(\beta)\cos\beta \, d\beta}{\int_\beta^{\beta'} \cos\beta \, d\beta} \tag{19}$$

where $R = R' - R$ and $\Delta\beta = \beta' - \beta$. Assuming $\Delta R << R$, defining $\bar{R} = (R + R')/2$ and using the exact volume of a spherical shell given by Equation 2, the radial integral becomes one of the following (depending on orbit position relative to the altitude band $R + \Delta R$):

$$\bar{S}(R, R') = \begin{cases} \dfrac{3\bar{R}}{4\pi^2 a(R'^3 - R^3)}\left[\sin^{-1}\left(\dfrac{2R' - 2a}{q' - q}\right) - \sin^{-1}\left(\dfrac{2R - 2a}{q' - q}\right)\right] & \text{for } R' < q' \text{ and } R > q \\[4mm] \dfrac{3\bar{R}}{4\pi^2 a(R'^3 - R^3)}\left[\dfrac{\pi}{2} - \sin^{-1}\left(\dfrac{2R - 2a}{q' - q}\right)\right] & \text{for } R' \geq q' \text{ and } R \geq q \text{ and } R \leq q' \\[4mm] \dfrac{3\bar{R}}{4\pi^2 a(R'^3 - R^3)}\left[\sin^{-1}\left(\dfrac{2R' - 2a}{q' - q}\right) + \dfrac{\pi}{2}\right] & \text{for } R' \geq q' \text{ and } R' \geq q \text{ and } R \leq q \\[4mm] \dfrac{3\bar{R}}{4\pi^2 a(R'^3 - R^3)} & \text{for } R' \leq q \text{ and } R \geq q' \\[4mm] 0 & \text{for } R' \leq q \text{ or } R \geq q' \end{cases} \tag{20}$$

The six possible orbital orientations with respect to the spherical shell are diagrammed in Figures 11-15 for easier visualization. The six orientations yield five conditions necessary to determine the radial spatial density S(R) relative to the specified ΔR band.
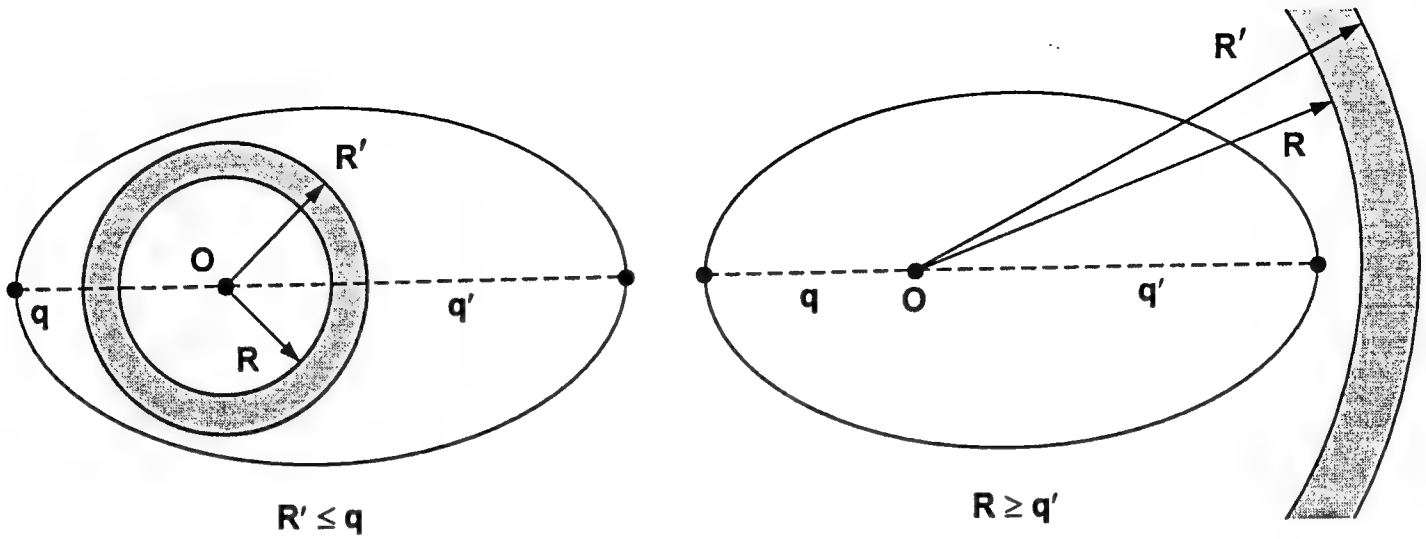
31

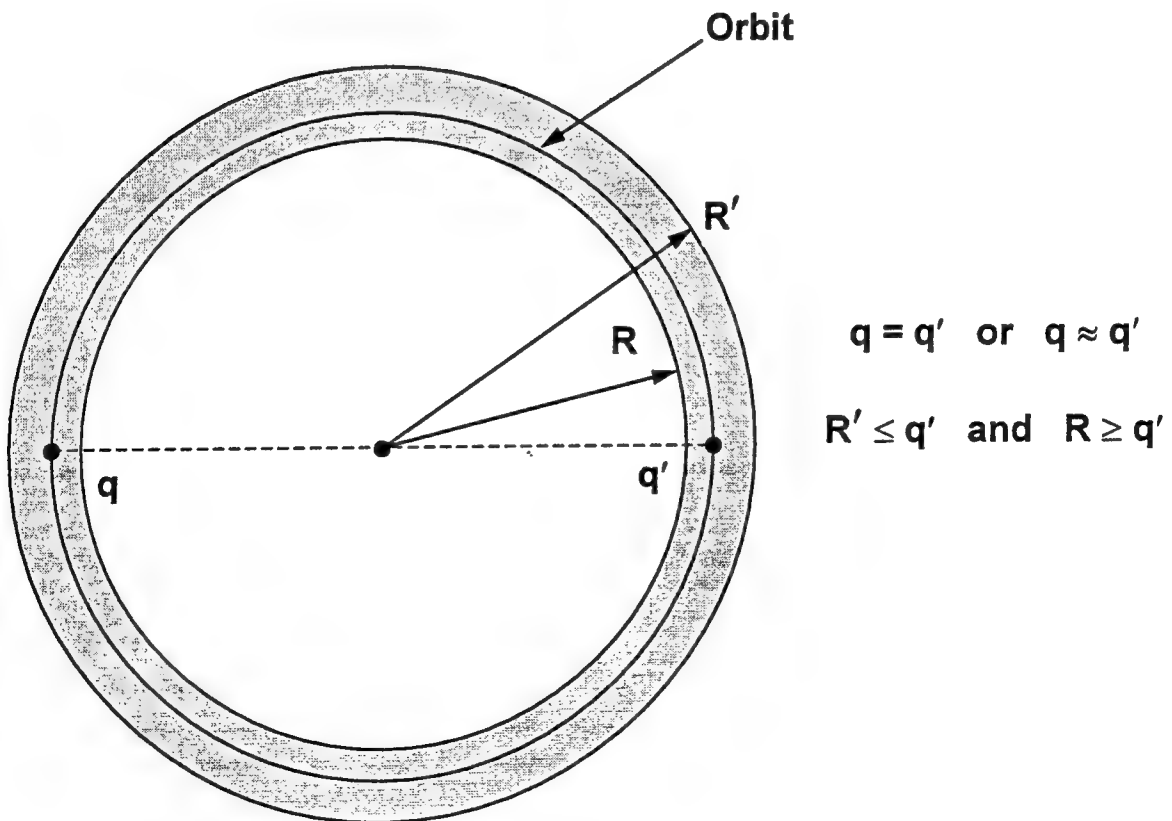Figure 11.   Case 1: Orbit does not intersect spherical shell volume.

$$q = q' \quad \text{or} \quad q \approx q'$$

$$R' \leq q' \quad \text{and} \quad R \geq q'$$

Figure 12.   Case 2: Orbit lies entirely within shell.

$R' \le q'$
and
$R' \ge q$
and
$R \le q$
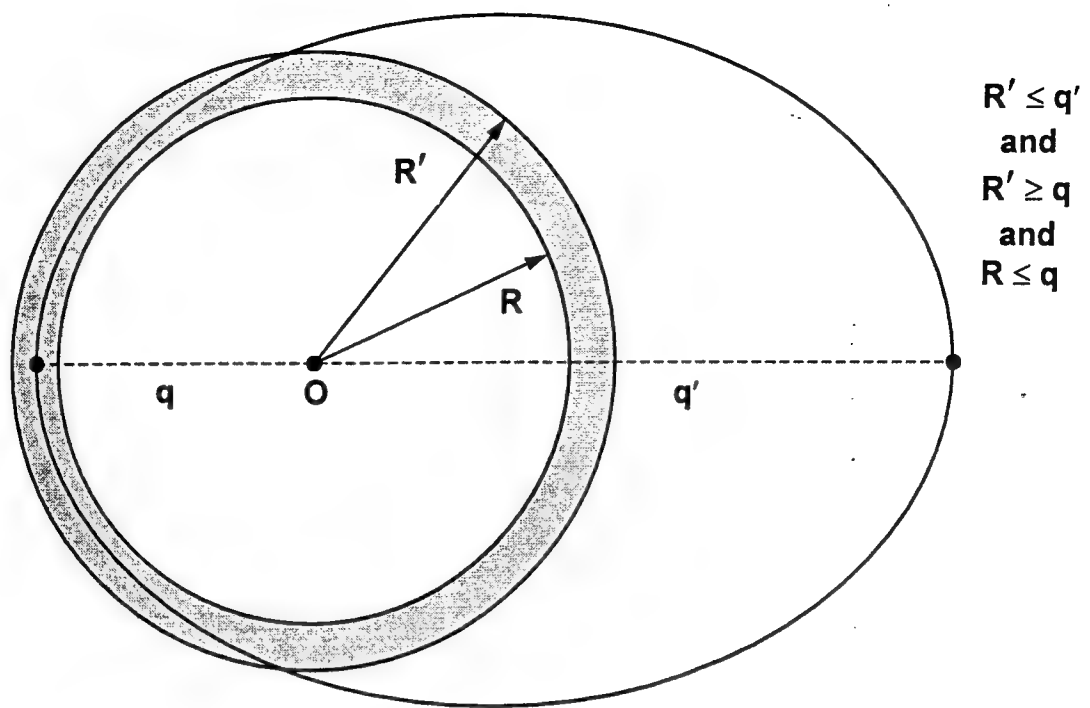
Figure 13.   Case 3:   Orbit perigee, q, lies within shell.

$R' \ge q'$
and
$R \ge q$
and
$R \le q'$
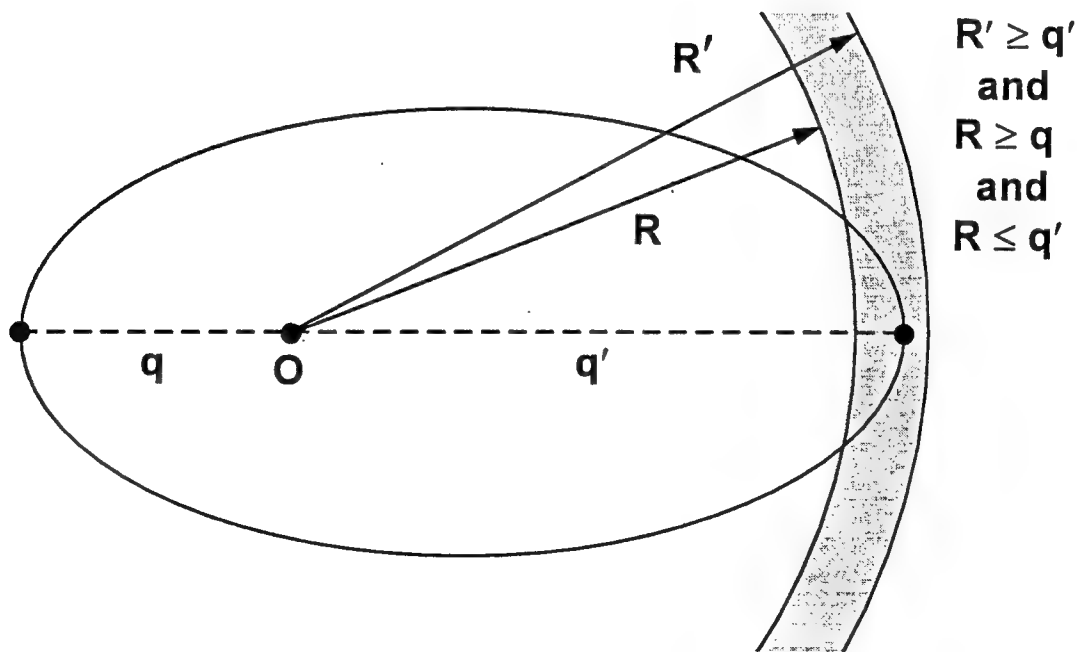
Figure 14.   Case 4:   Orbit apogee, q', lies within shell.

33
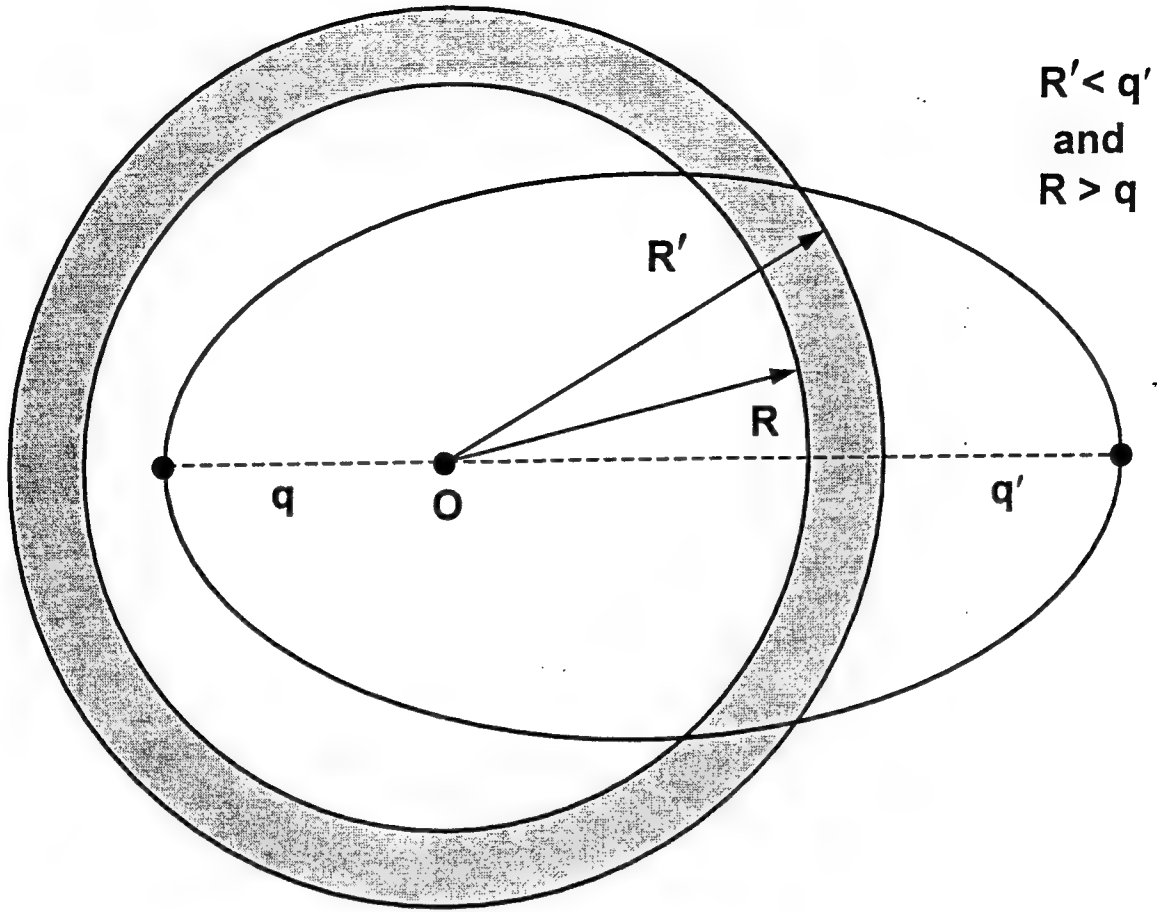
Figure 15. Case 5: Orbit passes through shell, neither apogee or perigee lies within shell.

If the approximate expression for the volume of a spherical shell as given by Equation 3 is used instead, Equation 20 reduces to the spatial density expressions found in Reference 7.

The latitude integral integrates to become

$$
\bar{f}(\beta, \beta') = \begin{cases} \dfrac{2}{\pi(\sin\beta' - \sin\beta)} \left[\sin^{-1}\left(\dfrac{\sin\beta'}{\sin i} \right) - \sin^{-1}\left(\dfrac{\sin\beta}{\sin i} \right) \right] & \text{for } \beta' \leq i \\ 0 & \text{for } \beta > i \end{cases} \tag{21}
$$

3.1.4.2 <u>Model Assessment</u>. The definition of spatial density as given by Equation 1, based on the fraction of an orbital period dwelt by an object in a specified volume, is a straightforward geometrical argument. With the derivations given in the previous subsection, the LEO environment can be subdivided into concentric spherical shell volumes whose spatial density contribution from a specified orbit can be evaluated using Equation 20. These expressions were derived with the assumptions that the secular perturbations to the argument of perigee and right ascension of an orbit average out over a long period of time and, as a result, the longitudinal dependence of that orbit's contribution to the LEO environment may

34

be neglected. Equation 20 gives the latitude averaged spatial density within the entire spherical shell of thickness ΔR. Multiplying Equation 20 by an enhancement factor that depends on the orbital inclination (Eqn. 21), the total spatial density can be approximated in both radial and latitudinal dimensions.

The spatial density model implemented in EVOLVE uses the latitude-averaged radial density expressions of Equation 20 only and does not employ the additional inclination-dependent function of Equation 21 which would give a finer degree of localization to the spatial density calculation. This simplification is justifiable since the spatial density given by the expressions of Equation 20 are sufficient to provide the flux necessary for long-term environment descriptions and collision rate calculations for future collision breakups (see Subsection 3.2.1). EVOLVE is currently designed to only produce an altitude (radial) spatial density dependence in its output flux results. The radial dimension is the only spatial dimension required to model the debris environment for the long-term applications for which EVOLVE was designed; thus, it becomes unnecessary to include the additional latitude localization term. Eliminating the (β, β') flux enhancement term simplifies the computer coding required to determine the spatial densities. It also greatly reduces the computation time since a nested FORTRAN DO-loop would be required to calculate the spatial density over all valid $\Delta\beta$ bins at each ΔR (altitude) bin. Such a nested DO-loop would slow the run time of the model tremendously.

The use of the radial-only expressions in Equation 20 represents the latitude-averaged value of spatial density. This can be observed by integrating Equation 21 with respect to β over the range -90 deg $\leq \beta \leq 90$ deg to yield unity. Figure 16 plots Equation 21 over $0 \leq \beta \leq 90$ deg (the function is symmetric about the y-axis) for an orbit having a perigee altitude $h_p = 500$ km, apogee altitude $h_a = 1000$ km, and an inclination $i = 65$ deg. Clearly the enhancement function (β,β') significantly increases at latitudes near the inclination of a specified orbit. The dwell time of the object is maximum for the latitude band at $\beta = i$. Figure 17 shows Equation 20 plotted for two orbits, each at $i = 65$ deg. The more circular orbit ($q = 500$ km, $q' = 1000$ km) yields a higher spatial density over the altitude range it occupies compared to the more elliptical orbit ($q = 500$ km, $q' = 100$ km). The upper curve in Figure 17 shows the spatial density contribution of a circular orbit in each altitude bin. This represents the maximum spatial density magnitude possible for a single object at each altitude bin and is shown for comparison. Figure 18 compares the spatial density for an $i = 65$ deg elliptical orbit as a function of altitude for the radial-only expressions of Equation 20 with the spatial density enhanced by the inclination dependent term of Equation 21.

This latitude enhanced density was calculated for six latitude bands at $\beta = 1, 20, 30, 50, 60,$ and 64 deg with an assumed latitude bandwidth of $\Delta\beta = 1$ deg. Clearly, the radial only spatial density expression represents the average over all latitudes with the flux enhancement at high latitudes offset by a flux decrease at low latitudes. The spatial density varies by no more than a factor of 3 over the latitude range 0 deg $\leq \beta \leq 0.9$ i deg, where i is the orbital inclination.
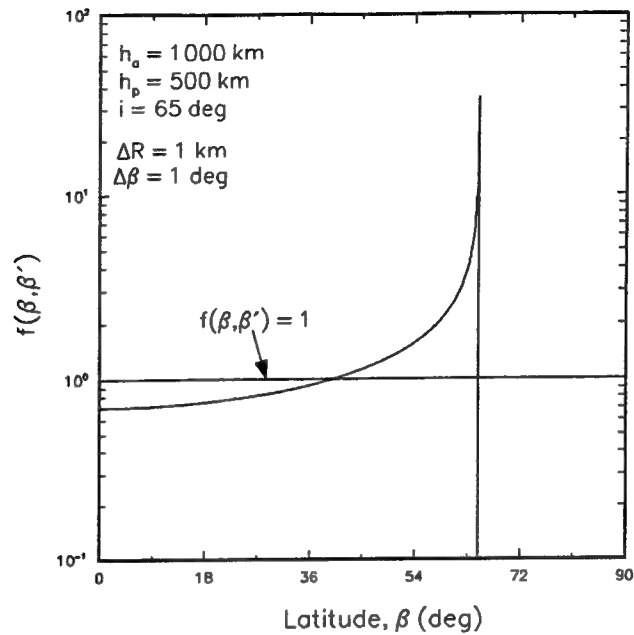
Figure 16.   The latitude flux enhancement term of Equation 21 is plotted for the indicated orbit as a function of β.
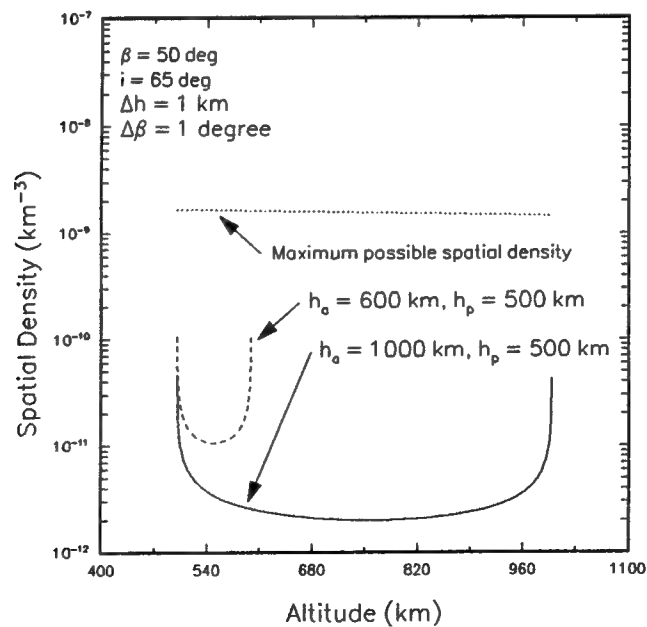

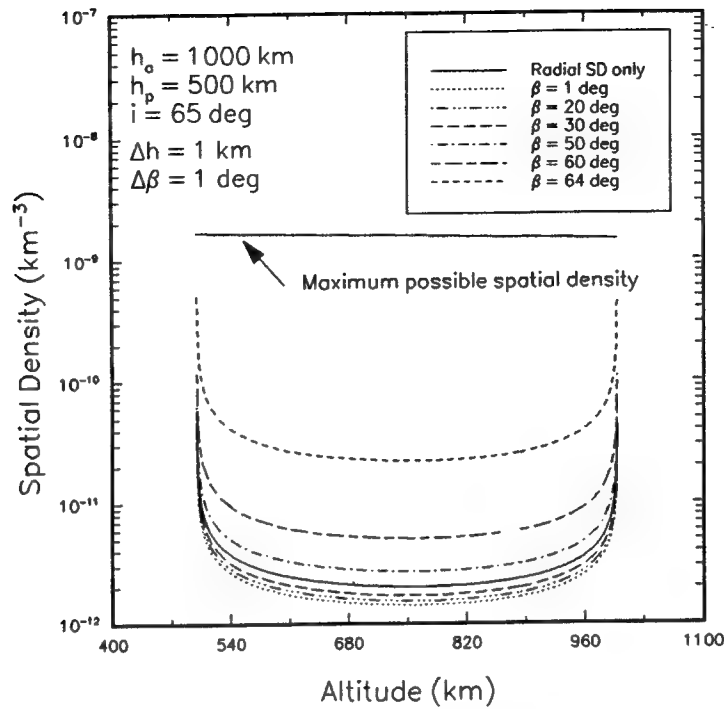Figure 17.   Spatial density versus altitude using Equation 20 for two orbits indicated in the figure.

Figure 18. Spatial density versus altitude for a single orbit using Equation 20 only compared to the latitude enhanced spatial density calculated using Equation 17.

As can be seen in the integrated expressions in Equation 20, there is a dependence of on the width of the altitude bin given by $\Delta h = \Delta R = R' - R$. Since the derivation of Equation 20 assumed that $\Delta R \ll R$, then

$$\frac{\text{Time spent in shell } \Delta R = R' - R}{\text{Volume of shell}} = \frac{f(R, h_p, h_a)}{\frac{4\pi}{3}[(R + \Delta R)^3 - R^3]} \approx \frac{f(R, h_p, h_a)}{4\pi R^2 \Delta R} \quad (22)$$

The function $f(R, h_p, h_a)$ determines the fraction of the fixed orbit contained within the shell. Increasing Δh can either increase or decrease the value of depending on where R is taken. For a single orbit at one specified altitude completely contained within the volume ΔR (with a, R held fixed) the relation is approximately inversely proportional to ΔR, so

$$\bar{S} \propto \frac{1}{\Delta R} \quad (23)$$

Since the orbit is entirely contained within a ΔR thick volume shell, increasing the volume by increasing ΔR (at the fixed altitude R) will simply decrease the spatial density inversely as a function of the dimension of the volume that is increased (i.e., the radial dimension here).

37

3.1.4.3 <u>Sensitivity/Uncertainty Analyses.</u> The spatial density expression given in Equation 20 is parameterized in terms of the altitude bin width ($\Delta R = \Delta h$), a user-specifiable quantity whose value can affect the spatial density estimation. A study was made to quantify the effect and sensitivity of the Δh value chosen by the user on the total flux results calculated by EVOLVE.

The Δh dependence is a mathematical result of the integration of Equation 6 to eliminate the singularities at the apogee and perigee points. Equation 20 is an approximate form of the exact (but considerably more complex) integral and is valid only when $\Delta h \ll R$. This suggests that in the limit as $\Delta h \to 0$, Equation 20 approaches the exact spatial density at the point R, otherwise this expression approximates the spatial density at the average of R and R' (or). Reference 7 found that when $\Delta h \leq 0.1R$, and when represents the true average of the bin boundaries (R and R'), then Equation 20 approximates the exact integral to within 1 percent. It is recommended, then, that the user of EVOLVE minimize the altitude bin width whenever possible. If a large altitude range is being modeled, a larger bin width must be used to cover this range (since the maximum number of altitude bins is limited). The user should be aware of this phenomenon and its consequences when selecting the altitude range and bin widths.

To demonstrate the sensitivity of the Δh value on the total cumulative flux results, EVOLVE was used to obtain flux versus time and flux versus diameter at three altitudes, h = 300 km (Figures 19 and 20), h = 800 km (Figures 21 and 22), and h = 1500 km (Figures 23 and 24). At each altitude, runs were made using bin widths of $\Delta h = 10$, 50, and 200 km and the results were compared for each altitude. The range was selected to center an altitude bin at the altitude h being examined. For example, in the h = 300 km, $\Delta h = 10$ km case, the altitude bin centered at this altitude ranged from 295-305 km. Similarly, for the $\Delta h = 50$ km case, the altitude ranged over 275-325 km, and for the $\Delta h = 200$ km case it ranged over 200-400 km. From examination of the functional form in Equation 20, it can be seen that the selection of Δh also defines the R and R' boundaries of the altitude shell by which the intact object orbits are compared (in the inverse sine terms). A larger shell defined by a larger Δh value encompasses more orbits and increases the time dwelt by objects having orbits which intersect this shell. This increase, however, is moderated by the larger Δh in the denominator of Equation 20. In these runs, the selection of Δh will always affect the calculation of the spatial density contribution of each intact object through Equation 20. Intact objects contribute to the environment only in the diameter regime $d \geq 1.0$ cm.

The flux results shown in Figures 19-24 also include the debris cloud fragments generated from the historical list of known breakup events. Equation 20 is not used in EVOLVE to calculate the environment flux contribution from these clouds; instead, the flux is evaluated at a particular value of h in a phenomenological function described in Subsection 3.2.4. The only source of fragments to the cumulative flux for $d < 1.0$ cm sizes are debris clouds. Figure 20 shows the difference between the $\Delta h = 10$ km and $\Delta h = 200$ km fluxes at the low altitude h = 300 km to be approximately a factor of 3 for $d \leq 0.5$ m. Since this is the region where debris clouds dominate, the observed difference arises from the differences in
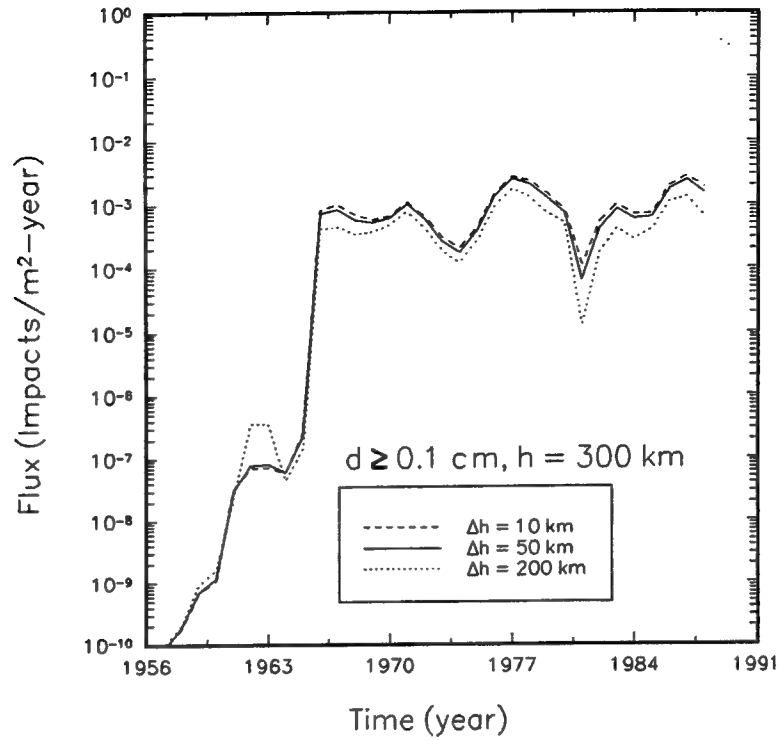
38

Figure 19.   Flux versus time for cumulative d ≥ 0.1 cm fragments at 300 km for three
              different altitude bin widths (Δh = 10, 50, 200 km) using Equation 20.
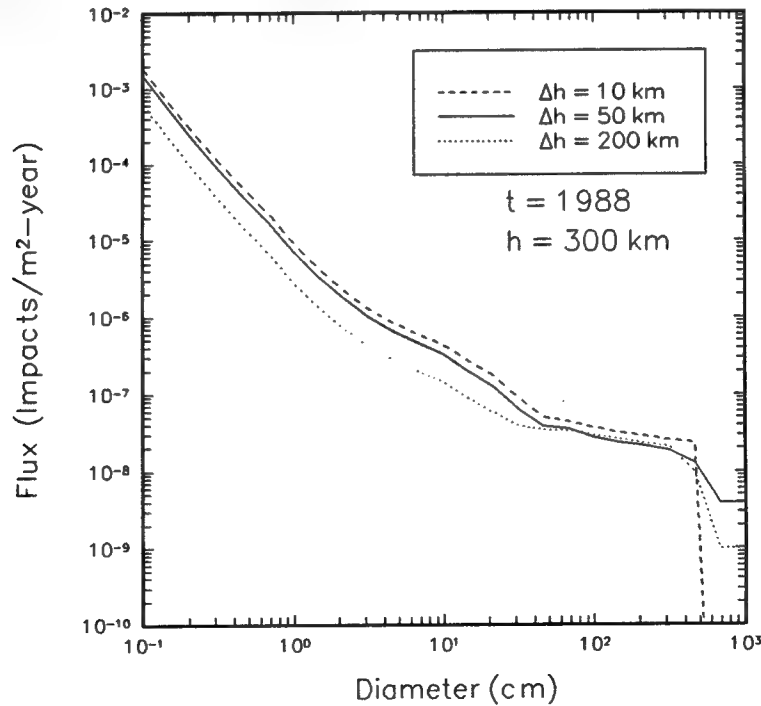

Figure 20.   Flux versus cumulative diameter in 1988 at 300 km for three different altitude
              bin widths (Δh = 10, 50, 200 km) using Equation 20.
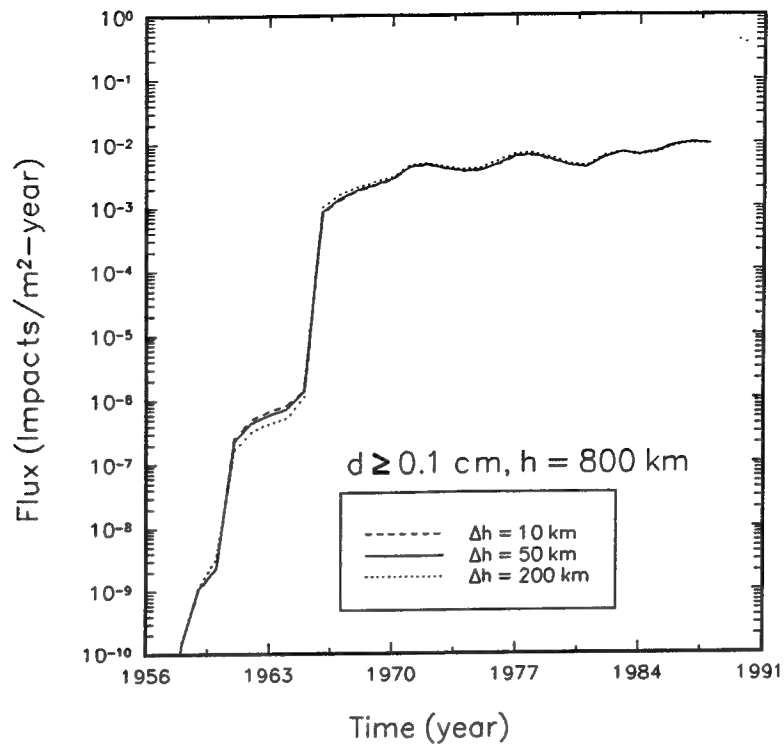
39

Figure 21.   Flux versus time for cumulative d ≥ 0.1 cm fragments at 800 km for three different altitude bin widths (Δh = 10, 50, 200 km) using Equation 20.

Figure 22.   Flux versus cumulative diameter in 1988 at 800 km for three different altitude bin widths (Δh = 10, 50, 200 km) using Equation 20.

Figure 23. Flux versus time for cumulative $d \geq 0.1$ cm fragments at 1500 km for three different altitude bin widths (Δh = 10, 50, 200 km) using Equation 20.
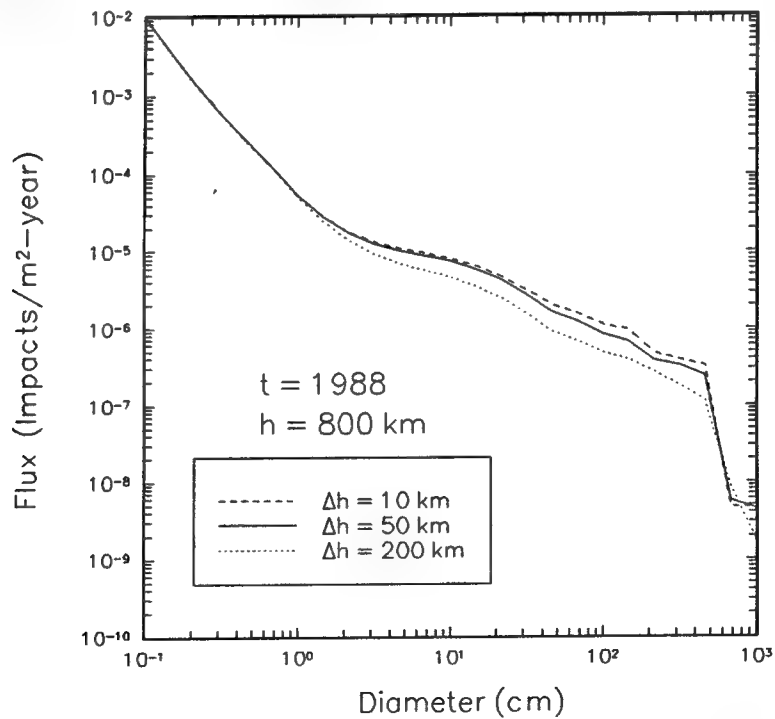

Figure 24. Flux versus cumulative diameter in 1988 at 1500 km for three different altitude bin widths (Δh = 10, 50, 200 km) using Equation 20.
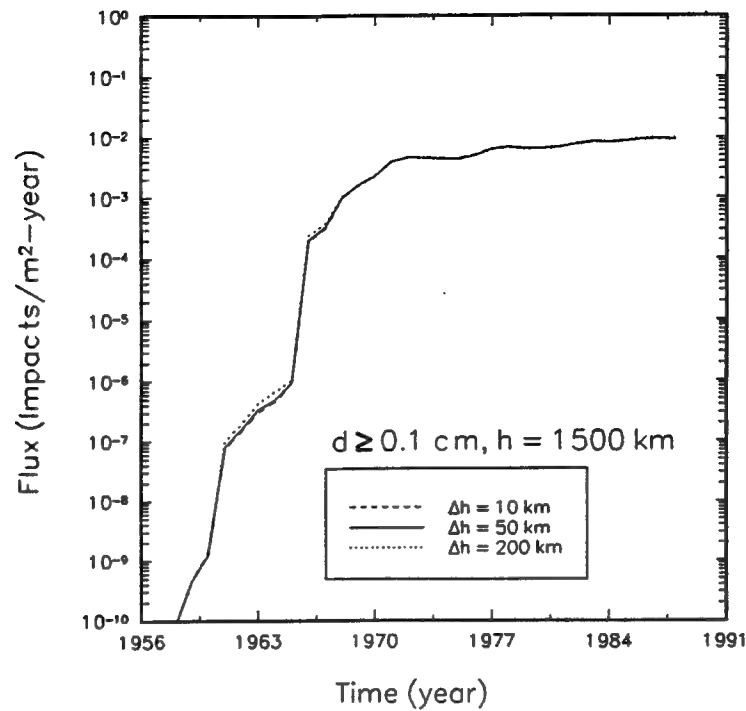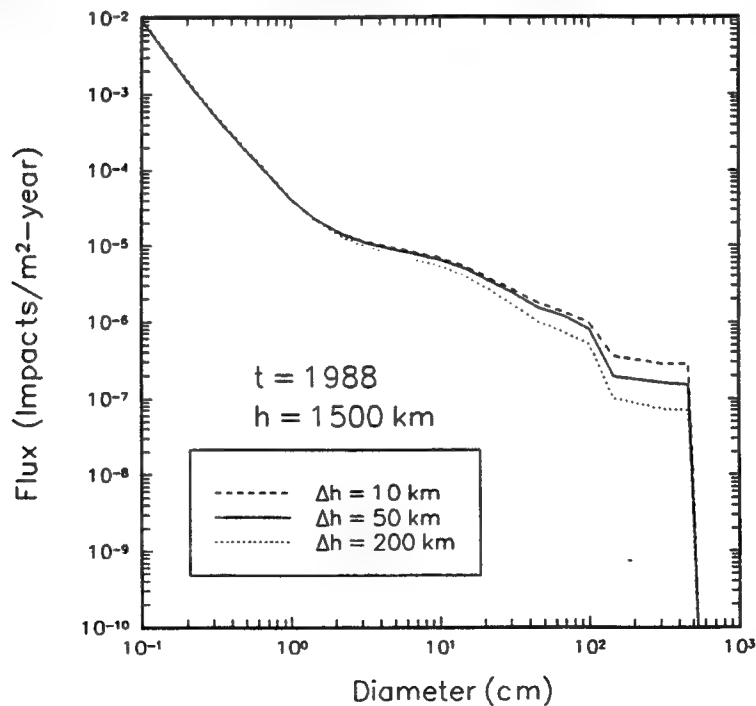
41

the lower boundary of the Δh bin centered at h = 300 km. This lower boundary defines the value of h used in the phenomenological function to determine the flux at h. Most of the historical breakups have occurred at breakup altitudes h_o > 300, so the flux contribution in this size bin will generally decrease with decreasing h.

Thus, the differences in the lower boundary of the altitude resulting from the different Δh values centered about the altitude h cause the differences seen in Figure 20. The opposite effect should occur at higher altitudes. If an altitude h is chosen such that most breakups occur at a lower altitude (i.e., most breakups obey h_o < h), then the slopes of the resultant flux profiles generated by the debris cloud function will cause an increase with decreasing altitude above h_o (i.e., the slopes are negative). The effect is much smaller since the slopes of these profiles on the high side of h_o are much flatter. Figures 22 and 24 show this trend for small sized fragments. (In Figure 24, the Δh = 200 case flux is observed to be marginally larger than the Δh =10 and 50 km cases.)

The flux is sensitive to the Δh value for large sized fragments (d $\geq$ 1.0 cm) where intact objects are the most significant contributors to the environment flux. The calculation of the flux for these objects utilizes Equation 20 directly in EVOLVE. Figures 20, 22, and 24 all show that the flux varies among the three test cases by up to a factor of 5 for the large intact object diameter regime. Generally, the trend shown in these plots is that the smallest bin width yields the largest flux and that the flux decreases with increasing Δh. Equation 20 averages the dwell times of objects having orbits that intersect the Δh range. Most orbits will simply pass through this Δh range, especially if the range is small as it is in these cases. For such orbits, increasing the Δh width will increase the dwell time contributions of these orbits, but not in proportion to the resultant increase of the spherical shell volume defined by Δh. As a result, the flux generally decreases with increasing Δh width. This situation can change, however, if the Δh band lies in an altitude region where a significant number of orbit perigees reside. As was shown in Figure 16, the spatial density contribution of an orbit to an altitude bin can be dramatically increased if that altitude bin includes the orbit perigee or apogee point (or is near these points). Likewise, the flux within a Δh shell can be enhanced if it includes a significant number of circular orbits. The LEO environment is characterized by a relative high concentration of orbital perigee points (for elliptical orbits) and circular orbits at lower altitudes (200-500 km range). This explains the effect seen in Figure 20 for d $\geq$ 0.8 m size objects where the Δh = 200 km case actually exceeds the flux of the Δh = 10 and 50 km bin widths. The 200-km bin width is wide enough to include more of these orbits and orbit segments than either the 10- or 50-km bin can encompass. The same effect could be seen at higher altitudes if the Δh range happened to enclose a large number of orbit apogees, but since LEO elliptical orbits tend to be more widely distributed in altitude, and there are fewer circular orbits at higher altitudes, this effect is generally not observed. (The same effect can also occur at an altitude where a concentration of similar intact object orbits are located, for example as in a satellite constellation.)

This study has demonstrated that there is a definite sensitivity of the EVOLVE flux (or spatial density) results to the Δh width selected by user for the altitude bins. Many factors affect the

error one can expect including the altitude at which the flux results are desired and the orbital characteristics of the objects within the altitude range being examined.

3.2 DEBRIS CLOUD RELATED SOURCE MODELS

A major source of orbital man-made debris in terms of numbers of fragments distributed in the near earth environment is the on-orbit fragmentation of launched intact objects. EVOLVE models this source of debris as debris clouds and this section describes the methodology used to predict and establish a debris cloud associated with each fragmentation event.

Two basic types of fragmentation can occur on-orbit: (1) hypervelocity collision impacts between two orbiting man-made objects or between a meteoritic particle and a man-made object and (2) internal explosions. In addition, there are two types of internal explosions, designated HIE and LIE, that are distinguished in EVOLVE (as will be explained in Subsections 3.2.2 and 3.2.3). As of 14 June 1991, there have been 104 identified breakups of launched payloads and spent orbit-insertion rocket boosters since the first identified breakup on 29 June 1961 when the Transit 4A Ablestar rocket body exploded (Ref. 16). Virtually all breakups have either been explosions resulting from residual fuel in propulsion systems (33 percent of all events) or have been deliberate explosions (40 percent) (Ref. 16). Approximately 25 percent of the fragmentation events have unknown causes. Except for the two known US antisatellite tests (P78 and D180) in the 1980s and a series of suspected Soviet antisatellite tests (e.g., Cosmos 1275), there has been no direct evidence of a collision occurring between two man-made objects, although there is a reasonable probability that a collision has occurred or will occur in the near future (Refs. 7 and 17). Of the 6883 objects catalogued in the USSPACECOM SATCAT on 14 June 1991, 1996 (29 percent) radar-tracked objects are catalogued payloads and spent boosters while 4887 (71 percent) objects are identified as debris (Ref. 16). This represents only those catalogued objects tracked by USSPACECOM space surveillance network (with an estimated minimum detectability resolution of ~5 cm for 400-km altitude objects and ~10 cm at 1000-km altitude). Thus, a large population of objects cannot be measured directly to ascertain their size, mass, and number distributions. This missing population must be modeled using estimated mass and size distributions.

EVOLVE accounts for this population by establishing a debris cloud associated with every breakup event incorporated into the environment. The first step in this process is to determine whether an event has occurred or not. The debris cloud constitutes an ensemble of objects that, once created, is assigned an array element description and maintained in the program array lists. The cloud arrays utilize the same array ranges and widths used to bin intact object size, mass, and altitude density characteristics. In this way, the separate contributions from intact objects and debris clouds can be summed directly to obtain the total environment spatial density. The individuality of each of the vast number of cloud fragments produced per event is lost; instead they are averaged into the far fewer size and altitude bins (arrays) with which EVOLVE does its processing. The distributions yielding the differential number (N) of

43

fragments produced per unit mass (in kilograms) between m and m + Δm is then calculated and used to scale a phenomenological function describing the time evolution of the spatial density of the cloud. (Cumulative distributions can be obtained from these differential distributions.) The breakup is characterized entirely by this cloud flux function once the number of fragments per unit mass is found. Subsection 3.2.2.1 examines the Monte Carlo model used to predict with some uncertainty the probability of occurrence of both types of breakup. Subsection 3.2.2.2 discusses the collision number/mass distribution model while Subsection 3.2.2.3 discusses the equivalent models for two types of explosion breakups. Subsection 3.2.2.4 concludes with a discussion of the flux function characterizing a single debris cloud.

3.2.1 Monte Carlo Model for Explosion/Collision Events

The EVOLVE program introduces fragmentation events into the modeled environment in two ways depending on the processing pathway taken by the user. First, as explained in Subsection 3.1.1.1, the intact object that experiences a collision or explosion may be entered explicitly as a record in the historical or projected mission model input files. The initial conditions necessary to process the object as a debris cloud are included. These are the breakup type (collision, LIE, or HIE), the altitude h_o at which the breakup occurred, object mass, m_{tot}, and projectile mass, m_p, if the event is a collision. When input into EVOLVE in this manner, the event is processed deterministically. The second way in which clouds may be introduced is via a probabilistic Monte Carlo method that predicts the occurrence of an event. The debris clouds formed by either process increment the environment flux independently of each other.

3.2.1.1 Description. The Monte Carlo model places into the environment those debris clouds resulting from a random collision or explosion. The EVOLVE program performs this processing in the stochastic pathway for projected years only (for which there is a statistical uncertainty in the flux level). The Poisson distribution is given by

$$P_n(\lambda) = \frac{\lambda^n}{n!} e^{-\lambda} \tag{24}$$

where λ is the mean number of events in a time interval and n is the actual number of events occurring.

The specified time interval in EVOLVE is usually set at 1 yr. The mean parameter λ determines the probability of occurrence. To determine n, the probabilities are distributed along a number line (Figure 25) that varies from 0 to 1. A random number generator yielding a value between 0 and 1 is used to randomly select a value of n along this unit length number line. If $n \geq 1$ then one or more events will have occurred. Equation 24 depends only on λ, the mean number of occurrences in the time step. Thus, the model performance depends wholly on λ.

44

Number n of collisions or explosions in time interval Δt

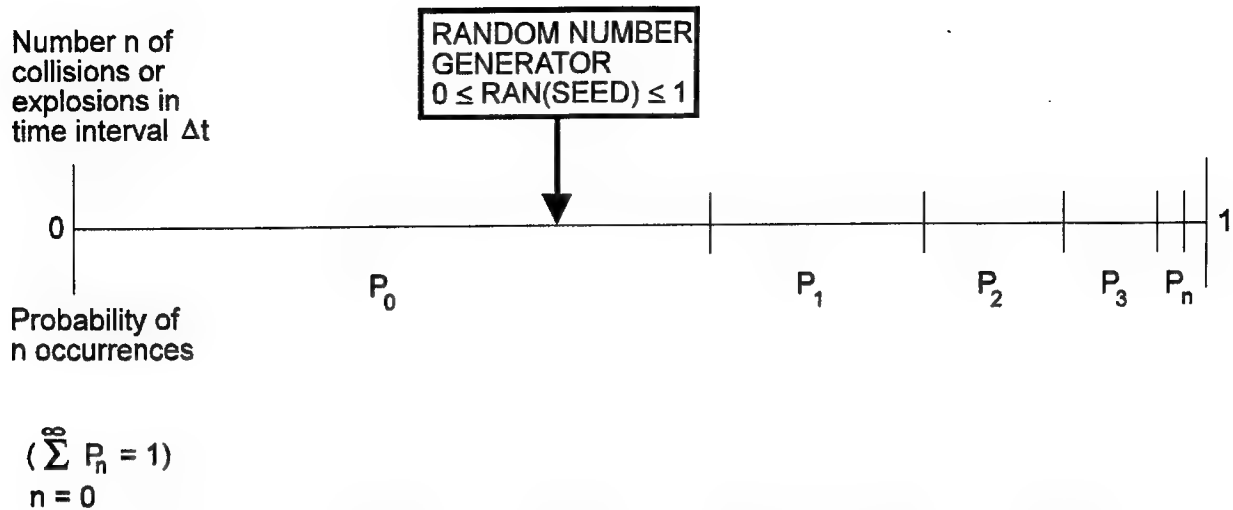Probability of n occurrences

$$\left(\sum_{n=0}^{\infty} P_n = 1\right)$$

Figure 25.   Probability line to determine collision and explosion occurrences.

For collisions, $\lambda = \lambda_{COLL}$ is based on the simple geometrical expression relating the collision rate to the spatial density. Consider a spherical object i having a diameter d_i and cross-sectional area A_i traversing a spherical altitude shell (bin) k having volume ΔU_k. The object has a certain probability of colliding with another object within this volume over an exposure time Δt. The second object j, also assumed spherical in shape, has diameter d_j and cross-sectional area A_j. A collision can occur only when the cross-sectional areas between the two objects touch or overlap as shown in Figure 26. The collision cross section for the interaction pair (i, j) is given by

$$A_c = \frac{\pi}{4}(d_i + d_j)^2 \tag{25}$$

Now, as object i sweeps through shell ΔU_k over a period Δt, the associated collision cross-section area A_c sweeps out a fractional volume of the spherical shell ΔU_k shown in Figure 26, assuming that the relative velocity between the objects is $\bar{V}$

$$V_c = A_c \bar{V} \Delta t \tag{26}$$

The number of objects N_i having diameter d_i within the swept out volume V_c is given by

$$N_i = V_c S_i \tag{27}$$

where S_i is the spatial density of d_i sized objects in ΔU_k volume element. The mean number of collisions in time Δt then is defined as the number of fragments N_i encountering an N_j population of objects with diameter d_j in the volume element ΔU_k
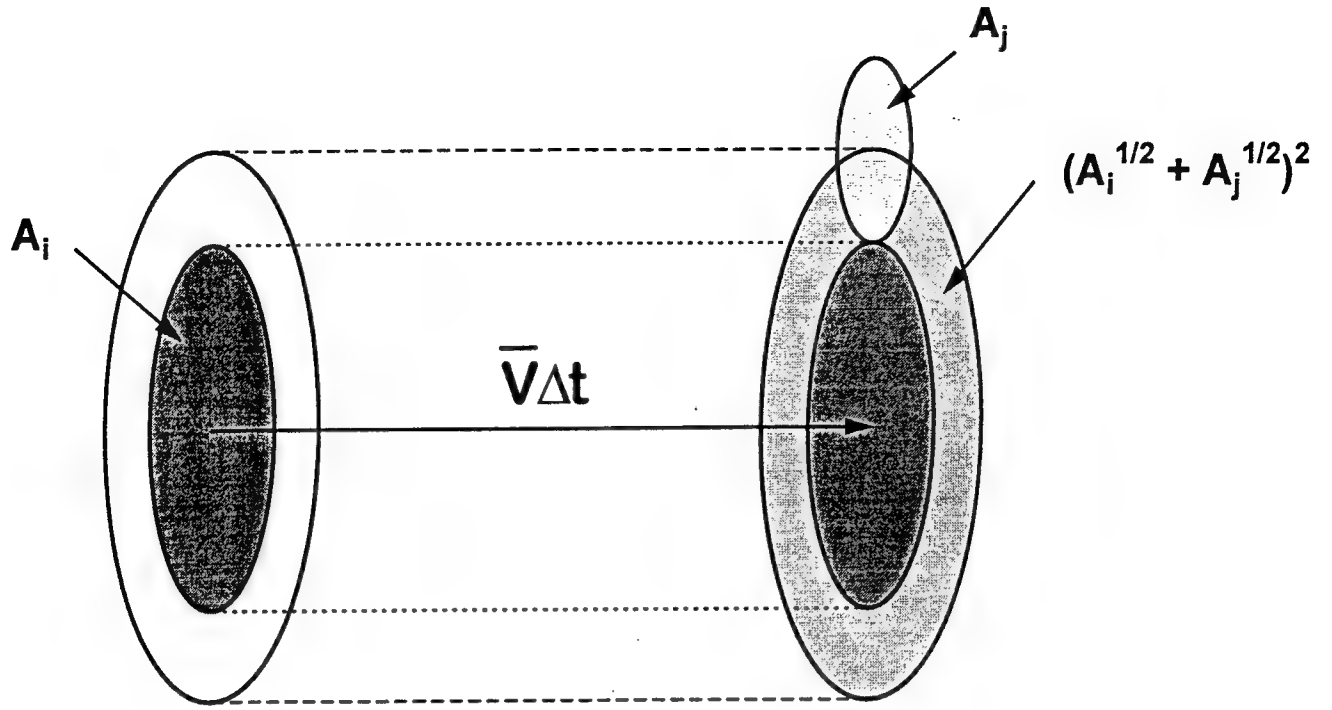
45

Figure 26.   Collision geometry between two fragments having areas A_i and A_j, respectively.

$$N_j = \Delta U_k S_j \qquad (28)$$

The collision rate is given by

$$\lambda_{COLL} = V_c \, \Delta U_k \, S_i \, S_j = \frac{\pi}{4}(d_i + d_j)^2 \, \overline{V} \, \Delta t \, \Delta U_k \, S_i \, S_j \qquad (29)$$

The ambient spatial densities S_i and S_j associated with altitude shell k are the same densities determined using the equations described in Subsection 3.1.4. Equation 29 describes the mean number of collisions between particles in two different size bins in the kth altitude bin. The mean number of collision expression for the collision of two objects within the same size bin is

$$\lambda_{COLL} = V_c \, \Delta U_k \, S_i \, S_j = \frac{\pi}{2}d_i^2 \, \overline{V} \, \Delta t \, \Delta U_k \, S_i \left(S_j - \frac{1}{\Delta U_k} \right) \qquad (30)$$

The $1/\Delta U_k$ term removes the spatial density contribution of the primary object since it cannot collide with itself.

46

During the stochastic processing, EVOLVE scans through all altitude bins at each time step to determine if a collision has occurred in each bin. If it has, then the cloud generation routines are invoked (Subsections 3.2.2, 3.2.3, and 3.2.4).

For explosions, only intact objects tagged as being explosive within the projected mission model traffic lists can explode. The probability of explosion then depends on the availability of explosive objects in the launch manifest lists. Furthermore, the type of explosion depends on the type of object that explodes. EVOLVE distinguishes between two types of explosions which yield different ejecta characteristics. The LIE describes the breakup when the structure is not in direct contact with the explosive (e.g., residual fuel or oxidizer in an otherwise empty tank) or is a result of secondary effects such as shock wave propagation and secondary collisions. The HIE results from the fragmentation of material that is in close contact with the explosive. The fragments will have large kinetic energies associated from this contact. The EVOLVE developers have classified four types of time-dependent explosion probabilities according to the type of intact parent object (all fragmentation debris is assumed nonexplosive). These classifications and their associated explosion probabilities P(E) are given in Table 4. During stochastic processing, when an object flagged as being explosive according to one of the four classes is encountered, a separate array is summed to obtain the product of the spatial and the explosion probability. For this reason, the identity of the type of object and category of explosion is lost. Thus, to compensate for this lost information, the explosion rates are multiplied by a factor representing the percentage of explosion rates historically observed to be LIE or HIE events. This percentage is 28 percent for LIE and 72 percent for HIE events (Ref. 11). The basis for these values is the approximate average observed in the 1980s for these events; however, the historically observed (1961-1989) numbers of explosions derived from the EVOLVE historical (DBS) databases shown in Table 5 suggest that 40 percent is LIE and 60 percent is HIE. Table 5 also indicates that the time-averaged rate from 1961-1989 for LIEs is approximately 1/yr while for HIE it is approximately 2/yr.

Table 4. Classes of explosive objects and associated explosion type and probabilities.

Class	Typical Object	Explosion Type [a]	P(E) [b]
1	Soviet upper stages	LIE	0.014
2	US and other upper stages	LIE	0.210
3	Soviet photoreconnaisance satellites	HIE	0.252
4	Soviet EORSAT satellites	HIE	0.460

[a] LIE represents 28 percent of breakup events, HIE represents72 percent of breakup events.

[b] Probability of objects exploding within first year.

47

Table 5. Number of fragmentation event occurrences as declared in the *.DBS database files.

Year	LIE	HIE	Collisions
1961	1	0	0
1962	1	0	0
1963	1	0	0
1964	1	0	0
1965	4	0	0
1966	3	2	0
1967	0	0	0
1968	0	3	0
1969	3	0	0
1970	1	2	0
1971	0	2	0
1972	0	0	0
1973	2	1	0
1974	0	0	0
1975	3	2	0
1976	1	3	0
1977	3	4	0
1978	2	3	0
1979	0	3	0
1980	1	1	0
1981	1	7	1
1982	0	5	0
1983	0	4	0
1984	1	1	0
1985	3	2	1
1986	1	4	1
1987	1	2	0
1988	0	0	0
1989	0	0	0
TOTAL	34	51	3
AVG.	1.17/yr	1.76/yr	0.10/yr

The expected number of satellites then is calculated from

$$\lambda_{EXP} = C \ S_{EXP} \ P(E) \ \Delta U_k \tag{31}$$

where $P(E)$ is the probability listed in Table 4, $C = 0.28$ for an LIE and 0.72 for an HIE event, ΔU_k is the volume of the kth altitude shell and s_{EXP} represents the spatial density of

48

explosive objects only (summed in a special array separate from the spatial density arrays containing all objects). Thus, the product s_{EXP} and ΔU_k yields the number of explosive objects of that class within the altitude band. The P(E) value represents a constant probability during the first year of mission elapsed time after which P(E) is set to zero and the object becomes nonexplosive. As in the collision processing, the explosion spatial density arrays are scanned at each yearly time step to determine if any objects added to the environment (within a year) have indeed exploded.

3.2.1.2 Model Assessment. The Monte Carlo model is a straightforward application of probability theory. For the Poisson distribution to be valid, it must adhere reasonably close to the following assumptions (Ref. 18):

- Possible to divide time interval of interest into many small subintervals
- Probability of an occurrence remains constant throughout time interval
- Probability of two or more occurrences in a subinterval is small enough to be ignored
- Independence of occurrences within one time interval

Normally a yearly interval is used in EVOLVE, which can easily be subdivided into as small a subinterval as necessary, satisfying the first point. The collision events during a yearly step will add to the environment and particles will be removed by various sink mechanisms. These effects are small compared to the overall population, so over the yearly time step the probability of occurrence should remain constant, satisfying the second point. In the course of a year there are few events, so the probability of simultaneous occurrence is negligible. This satisfies the third assumption.

The independence of the events from one another is assumed in the fourth point. This assumption is true for self-explosions if external factors which could affect the explosion rate (such as continual exposure to sunlight for sun-synchronous satellites) are neglected. The independence assumption is not strictly true for collisions since this rate is dependent on the ambient spatial density created from previous collisions, explosions, and launch activity. The spatial density is sufficiently low so that the probability of a collision is small. The additional probability caused by the added debris originating from collisions in a single year is small enough to be neglected. For these reasons, the Poisson distribution is applicable to use in this model for predicting the occurrence of collisions and explosions.

The methods used to establish the Poisson mean λ_{COLL} or λ_{EXP} for the appropriate breakup event have been assessed as valid approaches. The methodology for collisions is appropriate for the statistical processing of such events and is limited only by the size bin resolution. As the number of size bins available to characterize objects by diameter decreases (for a fixed diameter range), the uncertainty increases in determining the diameter of colliding fragments, leading to a greater uncertainty in the collision probability per interaction pair. Explosive event handling is deemed sufficient for long-term modeling, but it must be recognized that this model depends entirely on the assumptions of explosion frequency built into it. Currently, with lack of a better model, the empirical observations of historical data for on-

49

orbit explosions offer the best source for estimating the λ_{EXP}. The assumed percentage rates are slightly different from the observed percentage rates for the overall database (28/72 LIE/HIE compared to 40/60 for the entire databases). The percentage rates incorporated into EVOLVE are an approximate average of the 1980s rates which have significantly higher proportion of HIE events than does the average obtained using the entire historical database (1957-1988). The 1980s explosion rates are then assumed to continue into 1990s and beyond reflecting the trends of the most recent historical years. Recent historical trends seem to indicate that the rate of explosions is declining and, therefore, the current rates used may be too high. The explosion rates are readily adjustable, however, but would require recompilation of the program. For statistical modeling of future environments using EVOLVE, the assumptions underlying the rates assigned to random explosions are important to the results. Since explosions have comprised approximately 95 percent of the known breakups historically, and it is conceivable that their contribution will be the dominant source of fragments to the environment for years to come, the future overall flux results will be driven by these rates.

The assumption that objects have zero probability of explosion after 1 yr is a significant limitation, since several explosions have been observed to occur for several objects years after launch (e.g., the NIMBUS-6 Delta rocket booster which exploded in 1991 after being launched in 1975). This effect will underestimate the long-term explosion frequency rate. In fact, a survey of the 101 known explosive breakup events through 14 June 1991 reveals that 23 (or 23 percent) of these occurred more than a year after the orbital insertion date.

The flux results shown in Figures 27-31 are typical of the type predictions made by EVOLVE during stochastic processing. In these examples, 10 Monte Carlo trial predictions were made for the period 1990-2010. The mission model deterministic baseline assumed the same intact object traffic launched in 1988 for each projected year appended by the Civil Needs Data Base (Ref. 14) of future civilian launches. No deterministically placed explosions or collisions were specified in the mission model. In Figures 27-31, the deterministic historical and projected baseline is compared to the statistical mean and $\pm\sigma$ bounds for the stochastically placed collision and explosion breakup events. Figures 27 and 28 show the flux variation with time at altitudes of 500 km and 1000 km, respectively, for three cumulative diameter bins. With no deterministic breakup events specified, the deterministic baseline is seen to decrease over future years for the smaller debris (whose only source is from breakups). The Monte Carlo process described in this Subsection adds enough explosion and collision derived debris to maintain (or even slightly increase) the flux level with time. At this altitude, variations due to the solar cycle are clearly observed. The variations significantly reduce at the higher altitude of 1000 km as shown in Figure 28. For 10 Monte Carlo iterations, the statistical uncertainty is approximately a factor of 5 throughout the projected period. Figures 29 and 30 show the cumulative diameter distributions at altitudes of 500 km and 1000 km, respectively. There is an approximate factor of 5 uncertainty throughout most of the diameter range where breakup debris contributes (see Subsections 3.2.2 and 3.2.3). Only in the large diameter regime does the uncertainty begin to vanish. This is where intact objects having no statistical uncertainty dominate. Figure 31 shows the same observed uncertainties distributed
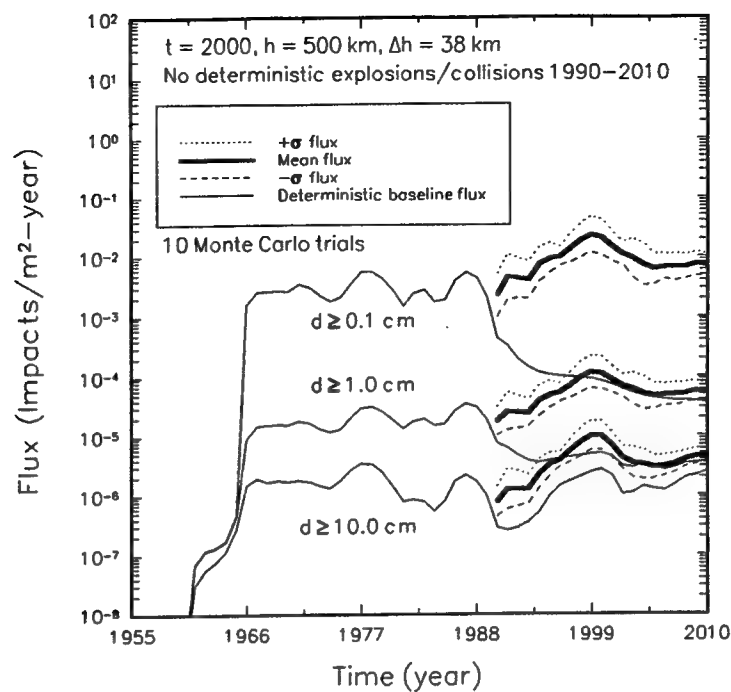
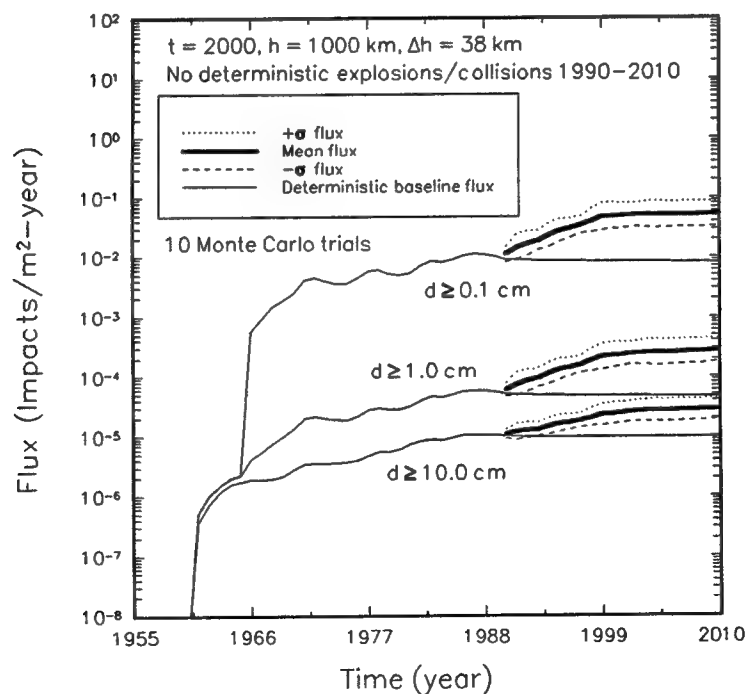Figure 27.   Flux versus time for three cumulative diameters at d ≥ 0.1, 1.0, and 10.0 cm at 500 km.

Figure 28.   Flux versus time for three cumulative diameters at d ≥ 0.1, 1.0, and 10.0 cm at 1000 km.
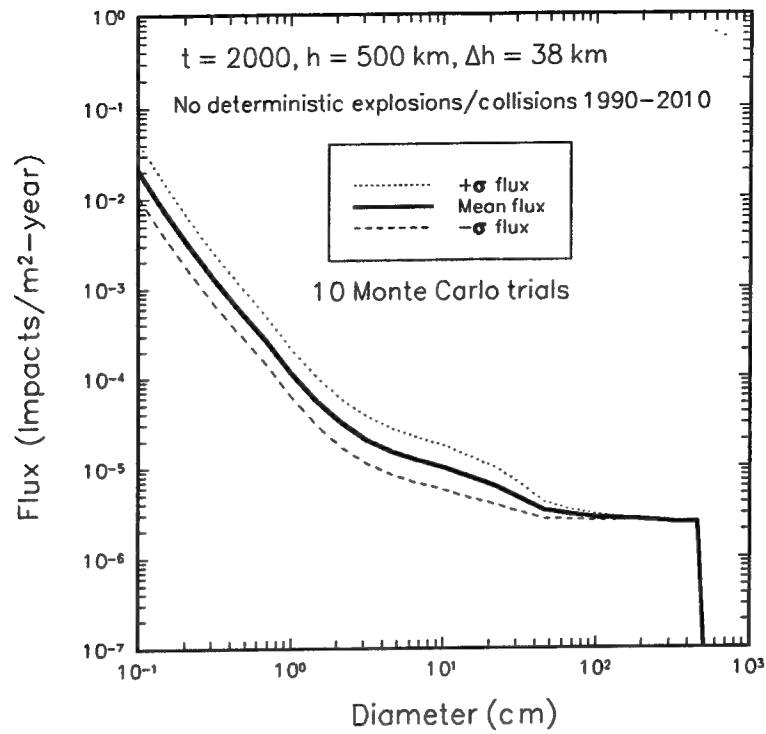
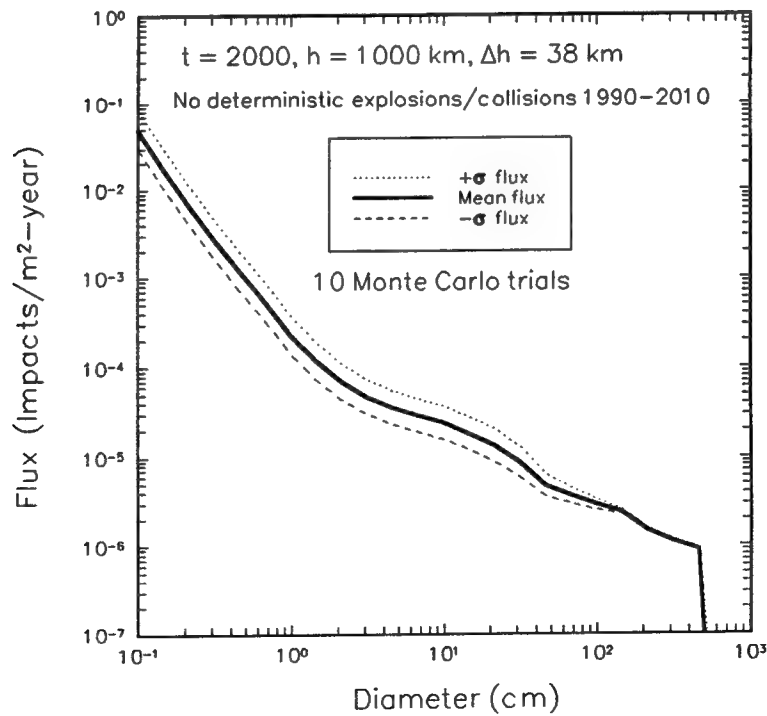Figure 29.   Monte Carlo flux results versus diameter for 500 km in the year 2000.

Figure 30.   Monte Carlo flux results versus diameter at 1000 km in the year 2000.
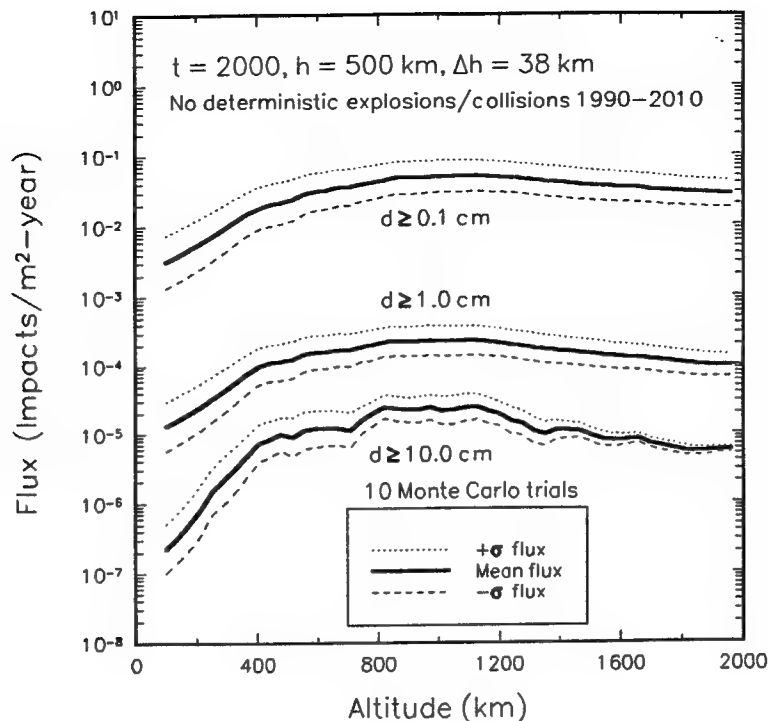
Figure 31.   Monte Carlo flux results versus altitude in the year 2000 for three different cumulative debris sizes.

spatially in altitudes at the year 2000. The decrease in uncertainty for d ≥ 10.0 cm objects as the altitude increases indicates that most of the larger breakup debris fragments (having statistical uncertainty) occupy the lower altitude orbits.

As would be expected in the near term, explosions are the dominate type of breakup predicted to occur. Figure 32 shows the cumulative number of occurrences for both explosions and collisions. The explosion events are shown with statistical error bounds for the same EVOLVE run used to obtain the data of Figures 27-31. There is a wide variance thataccumulates over time. The collision contribution is virtually negligible as shown in Figure 32. No uncertainty bounds are calculated by EVOLVE for this case. These results suggest that the flux level over the time period observed is too small to give rise to a significant collision contribution.

The results in these figures demonstrate the usefulness of EVOLVE as a tool to assess future environments and their statistical uncertainties due to uncertainties in the occurrence of explosions and collisions. The ±σ uncertainty limits determined for a flux at any given time, altitude, and cumulative diameter bin is proportional to where N is the number of Monte Carlo trials. The ±σ values can therefore be reduced by using a larger number of trials in the EVOLVE stochastic processing loop.
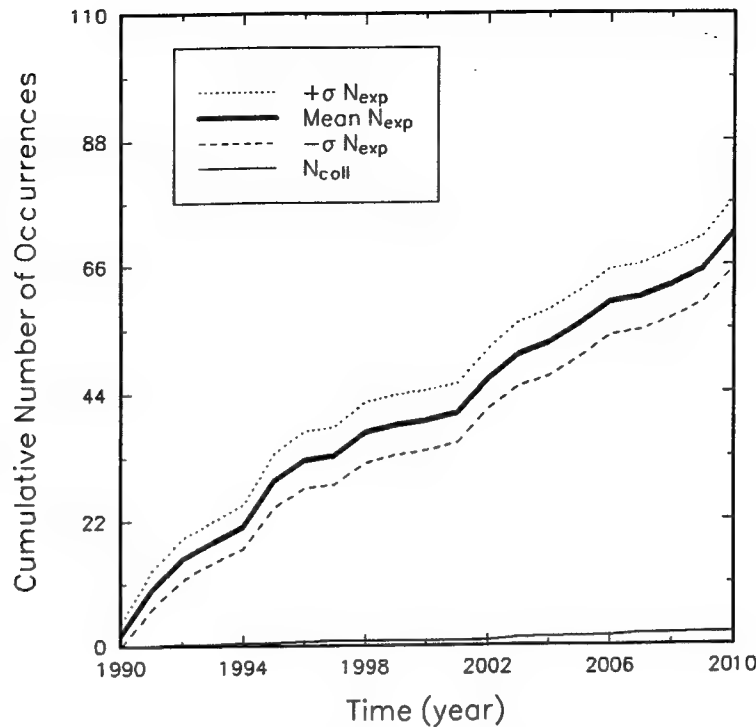
Figure 32.   Cumulative number of predicted explosions N_{exp} and collisions N_{coll} versus time. Statistical uncertainty bounds are shown for N_{exp}.

3.2.2 Collision Fragmentation Model

This subsection describes the cumulative number versus mass distribution model for collision breakup events in EVOLVE. Subsection 3.2.2.1 discusses the model details while Subsections 3.2.2.2 and 3.2.2.3 provide the model assessment and sensitivity/uncertainty analyses of its most important parameters.

3.2.2.1 Description. When a collision between two objects in the environment occurs in EVOLVE, the collision model contained in subroutine COLLDP is invoked to define the characteristics of the cloud. The debris cloud is initially specified by the size distribution of fragments to be placed in the user allotted size bins, the velocity distribution of ejecta fragments, the breakup altitude, and the breakup epoch. The breakup number distribution versus size for collisions is the subject of this section. The other parameters describing the cloud pertain to its spatial extent in altitude and its time evolution (Subsection 3.2.4). The size distribution model is crucial to the performance of the collision contribution of the environment since it specifies the expected number of fragments within each size bin to be added to the environment.

The size distribution model is first determined from an assumed distribution of the number of fragments ejected versus mass. The size bin corresponding to a particular range of masses is obtained from the mass bin distribution calculated in the main EVOLVE.FOR driver using an assumed size versus mass relationship. The mass versus diameter relation is one of the fundamental assumptions incorporated into EVOLVE. Since the breakup model distributions determine mass rather than size, an assumed mass versus diameter distribution must be used to establish a mass bin array to store the breakup cumulative number results.

The characteristic diameter associated with each size bin corresponds one-on-one to a characteristic mass associated with a mass bin. EVOLVE uses the size and mass bins interchangeably where needed. The power law form was assumed to fit the A/m observed in

$$\frac{A}{m} = c_1 d^{-c_2} \tag{32}$$

where c_1 and c_2 are fit constants (Ref. 7). Assuming a circular cross-sectional area for fragments, area can be written

$$A = \pi \left(\frac{d}{2}\right)^2 = \frac{\pi d^2}{4} \tag{33}$$

Equation 32 can be written as

$$m = \frac{A}{c_1} d^{c_2} = \frac{\pi d^{c_2 + 2}}{4 c_1} \tag{34}$$

For an assumed critical mass d_c below which all fragments are assumed to have the density of pure aluminum, $\rho_{Al} = 2699 \ kg/m^3$, the mass relationship takes the simple form

$$m = \rho_{Al} V = \rho_{Al} \left[\frac{4}{3} \pi \left(\frac{d}{2}\right)^3\right] = \left(\frac{\pi \ \rho_{Al}}{6}\right) d^3 \tag{35}$$

Since aluminum is the most common structural material found in orbiting payloads and boosters, the use of aluminum is a reasonable first-order approximation to average density of debris fragments on-orbit. A more detailed study to better approximate the density of debris fragments characterized by size and source would be beneficial and is recommended as an improvement to the model.

Using fit constants $c_1 = 0.01664$ and $c_2 = 0.26$ (Ref. 7), the m(d) distribution becomes

$$m = \begin{cases} 1413.193 \ d^3 & \text{for } d \le d_c \\ 54.315 \ d^{2.26} & \text{for } d > d_c \end{cases} \qquad (36)$$

where

$$d_c = \left(\frac{2c_1 \rho_{Al}}{3}\right) d^{\left(\frac{1}{c_2 - 1}\right)} \approx 0.01 \text{ m} \qquad (37)$$

is the cutoff diameter between the two distributions.

The breakup altitude, h_o, provides the initial point for the collisions. This provides the starting point for the propagation of the fragments into other altitude bins. The event's contribution to the change in spatial density of other altitude bins can then be determined. This will be elaborated upon in Subsection 3.2.4.

In EVOLVE, the collision process is based upon experimental hypervelocity collision data (Ref. 5). The fit to the data uses a power law size distribution incorporating a maximum size cutoff limit of the form

$$N(m \ge M) = aM^{-b} \qquad (38)$$

where N is the cumulative number of fragments greater than or equal to a minimum mass M (i.e., $m \ge M$) and a and b are constants. The cutoff size (and therefore mass) limit means that at some limiting maximum mass, m_{max}, there will only be one fragment created,

$$N(m \ge m_{max}) = a \ m_{max}^{-b} = 1 \qquad (39)$$

Thus,

$$a = m_{max}^b \qquad (40)$$

Since the total mass, m_{tot}, involved in the collision is conserved,

$$m_{tot} = \int_0^{m_{max}} m \left(\frac{dN}{dm}\right) dm = \left(\frac{b}{1-b}\right) m_{max} \qquad (41)$$

56

or

$$m_{max} = \left(\frac{1 - b}{b}\right) m_{tot} \tag{42}$$

Therefore, the expression for N becomes

$$N(m \geq M) = \left(\frac{1 - b}{b}\right)^b \left(\frac{m_{tot}}{M}\right)^b \tag{43}$$

allowing the function to be parameterized in terms of only one constant. Equation 43 gives the cumulative number of particles created for a mass $m \geq M$.

A value for the parameter b (b = 0.7496) was derived (Ref. 3) from two hypervelocity impact tests of small projectiles against a simulated spacecraft wall (Ref. 5). Figure 33 plots this distribution as a function of mass and Figure 34 as a function of diameter over a wide range of respective mass and diameter values. The kink in the diameter curve reflects the m(d) change at d = 0.01 m. To use Equation 43, the total amount of mass (m_{tot}) needs to be found. This is given by

$$m_{tot} = m_e + m_p \tag{44}$$

where m_e is the ejecta mass excavated from the target object and m_p is the projectile mass. An assumption behind Equation 44 is that the projectile is completely destroyed in the collision, so its entire mass contributes to the debris cloud. The larger mass object in a collision is assumed to be the target and the smaller object the projectile. The amount of material excavated is assumed to be proportional to the kinetic energy of the projectile. This is expressed as

$$m_e = A m_p V_i^2 \tag{45}$$

where m_e is the ejecta mass, m_p is the projectile mass, V_i is the relative impact velocity in kilometers, and A is the constant of proportionality. It has been determined that if V_i is expressed in kilometers/second, A is equal to 1 s^2/km^2 (Ref. 19). In EVOLVE, V_i is assumed to be 10 km/s.

EVOLVE recognizes three cases of collision interactions, each yielding a different m_{tot} quantity. The criterion for these cases is the amount of material excavated from the target, m_e:

- $m_e \leq 0.1\ m_t$
  The collision is not catastrophic. The target is not completely destroyed, leaving the residual target intact. The projectile and excavated masses are subject to Equation 43.
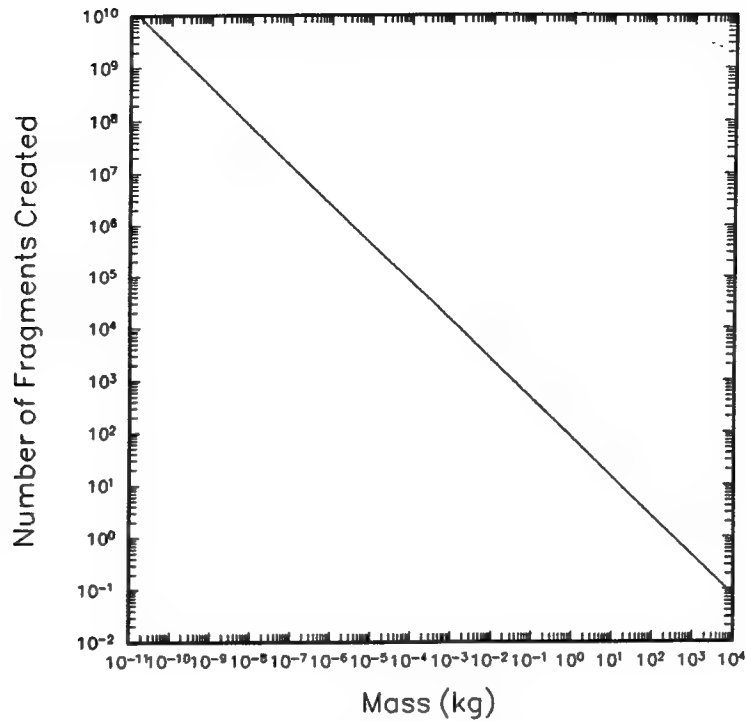
Figure 33.   The cumulative number of fragments produced versus mass for the collision power law distribution.
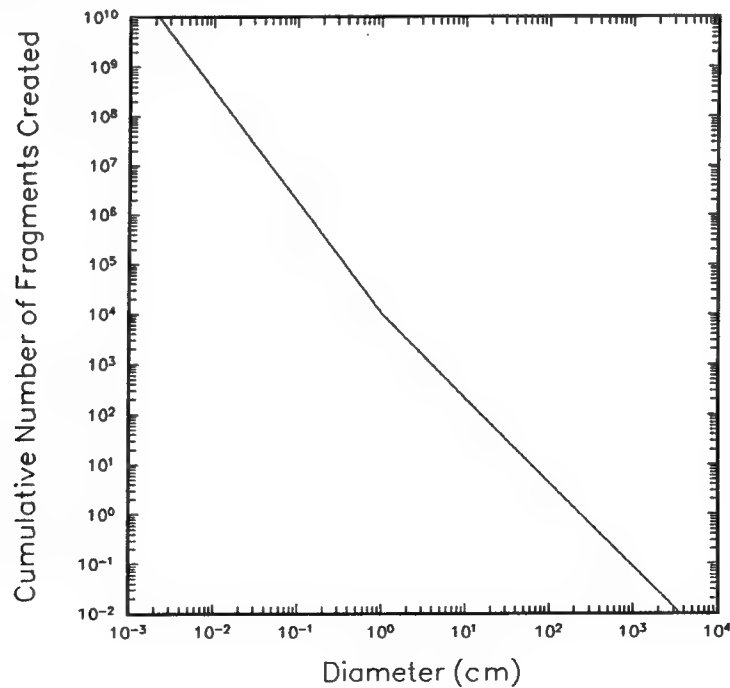

Figure 34.   The cumulative number of fragments produced versus diameter for the collision power law distribution.

58

- **$0.1\,m_t \leq m_e < 0.1\,m_t$**

  The collision is catastrophic. Target is destroyed by a combination of direct hypervelocity impact excavation and resulting shock waves. The fragments are handled by two distributions. The fragments resulting from the collision ($m_{tot} = m_e + m_p$) are treated according to Equation 43 and the fragments from the shock wave ($m_{shock} = m_t - m_e$) are subjected to an LIE as will be explained in Subsection 3.2.3.

- **$m_e \geq 0.1\,m_{tot}$**

  The collision is catastrophic. The target is destroyed through hypervelocity impact. The entire target and projectile masses are subject to Equation 43 to create a single cloud. If $m_e \geq m_t$, m_e is set equal to m_t.

Equation 43 is used for each ith mass bin value m_i and the results stored in a cumulative number distribution array associated with the breakup. Table 6 summarizes the conditions to determine m_{tot} used in Equation 43 for collisions.

Table 6. Estimation of total mass involved in a collision process.

Case	Criterion	m_{tot}	Results
Noncatastrophic	$m_e < 0.1\,m_t$	$m_e + m_p$	One collision cloud, one residual intact object
Catastrophic	$0.1\,m_t \leq m_e < m_t$	$m_e + m_p$ (COLL), $m_t - m_e$ (LIE)	Two clouds, one collision, one LIE
Catastrophic	$m_e \geq m_t$	$m_t + m_p$	One collision cloud

3.2.2.2 Model Assessment. Equation 43 is based on two hypervelocity tests conducted at the NASA Langley Research Center using a light-gas gun to propel a 1.65-g, 0.56-cm-dia steel cylinder at 3.0 km/s and a 0.37-g, 0.56-cm-dia aluminum cylinder at 4.5 km/s into simulated spacecraft walls (Ref. 5). The debris fragments were collected and found to be in the range 10^{-7} - 1 g. This corresponds to a diameter range of 6.4 x 10^{-4} - 0.8 cm using the m(d) relationship. It was reported in Reference 5 that the data fit the power law relationship with a = 7.32, b = 0.80 and a = 4.08, b = 0.84 for the two tests, respectively. The standard deviation for the fit coefficient b is reported to be $\sigma_b = 0.1$ (Refs. 5 and 20). The power law is the best functional form to describe the linear dependence in logarithmic space of the reported data. Later tests have confirmed this dependence (Ref. 6), so this functional form is generally thought to be the best fit given the scarce data available. The expression given by Equation 43 has been scaled by the ejecta mass, m_e, to account for the observation that the number of debris produced by penetration or cratering of a large target by a small projectile follows a power law that is dependent on the amount of ejected mass (Ref. 5). Using these assumptions, and all available data, the relationship used is

$$N = 0.4478 \left(\frac{m}{m_e} \right)^{-0.7496} \tag{46}$$

The coefficient, b observed in the form of Equation 38, was derived from this reanalysis (Ref. 3). In the power law expression of Equation 32, the coefficient b determines the slope of the mass distribution curve while the coefficient a simply shifts the curve along the cumulative number axis. The b coefficient defines the mass-varying relationship, while the coefficient a scales the yield of the number of debris fragments with the total mass m_{tot} available according to Equation 40. It is reasonable to assume the form of Equation 40 for the coefficient a since, for fixed b, the number of fragments created in each size bin would vary proportionally to the mass m_{tot}. Thus, a small mass m_{tot} would yield a smaller number of fragments per size bin than a larger mass, yet the relative slope of the mass distribution would be the same.

The power law distribution of Equation 43 produces a large number of small fragments, as shown in Figures 33 and 34, consistent with the observed data (Ref. 5). The limited amount of data makes certain quantification of the constant b in the model difficult. The value of b is based on just one set of data; more data are definitely required to validate with certainty the assumption of using a power law to describe the mass distribution. Later hypervelocity impact tests do support the value assumed for b, if the power law fit is assumed. Recent lethality tests (from 1988 to 1990) yielded data which suggest that a rounding off of the mass distribution curve occurs for both smaller and larger masses and that a parabolic function best fit these empirical data (Ref. 6). In summary, the mass distribution model for collisions given by Equation 43 is assessed to be a reasonable and valid model given the data from which it is derived, but as more hypervelocity data become available, this model and its assumed functional relationship need to be revisited.

The approach of using three regimes to determine the total mass (m_{tot}) appears to be reasonable, given the large uncertainties associated with hypervelocity impact mechanics. The system of ascribing noncatastrophic and catastrophic regimes to the collision interaction and obtaining m_{tot} as a result is a simple approach but one that is reasonable given the low accuracy and long-term modeling philosophy of the EVOLVE model. All that is needed to describe a debris cloud is the total mass involved in the collision. Studies of hypervelocity impacts into solid structures and basalt (obtained from moon surface cratering, asteroid breakups, and meteroid impact studies) have been applied to hypervelocity impacts into spacecraft structures. At impact velocities of 10 km/s, these studies indicated that the minimum ratio of target mass to projectile mass causing catastrophic breakup is ~115 (Ref. 7). The ratio of the ejected mass (m_e) to the projectile mass (m_p) is also ~115. This is the justification for using Equation 45 to evaluate m_e. Once this quantity is determined, the total mass m_{tot} is just the balance of the target mass m_t and excavated m_e.

3.2.2.3 <u>Sensitivity/Uncertainty Analysis.</u> The mass distribution given by Equation 43 is sensitive to the choice of the coefficient b which determines the slope of the curve. The fit coefficient b = 0.7496 is based on the curve fit to data that spans a mass range of 10^{-7} - 1 g and a diameter range 6.4×10^{-4} - 0.8 cm. Beyond these ranges the power fit curve would be an extrapolation, therefore, the validity far beyond these values becomes more questionable. For fragment diameters of d < 0.1 cm the collision breakup model has the greatest uncertainty. Since EVOLVE is not intended to model below this diameter, this uncertainty will not be important. The large fragment regime is most sensitive to the value of b. Figure 35 shows the effects on both large and small diameter objects of changing the constant b. This Figure shows the cumulative number distribution versus diameter for a collision producing 500 kg of ejecta mass. Five possible values of b are shown (b = b_{min} = 0.5, b = 0.6, b = 0.7496, b = 0.9, and b = 0.999 $\approx b_{max}$). Equation 42 implies that b must lie in the range $0.5 \leq b < 1.0$ for Equation 41 to be valid. The minimum b = 0.5 then is a true minimum while b_{max} asymptotically approaches 1.0. For this case, a change from b = 0.5 to 0.999 produces significant increase in steepness of the slope reducing the larger fragments while dramatically increasing the number of small fragments. In fact, there is an approximate 100 fold increase in the slope for d > 1.0 cm and almost a 1000 fold increase in slope for d < 1.0 cm. The slope changes at d $\approx$ 1.0 cm are a result of the slope discontinuity of the m(d) relationship there.

Figure 36 compares the b = 0.7496 case for three different total masses m_{tot}. These curves scale as

$$\frac{N_1}{N_2} = \left(\frac{m_{tot,\,1}}{m_{tot,\,2}} \right)^b \tag{47}$$

as would be expected taking the ratio of Equation 43 for two different m_{tot} values at fixed b. Figure 36 clearly shows the role that m_{tot} plays in the scaling of the cumulative number of fragments produced.

If the same uncertainties implied in Reference 20 are assumed to apply for Equation 43 with σ_b = 0.1, clearly the uncertainties in b introduce a large uncertainty in the numbers of fragments being estimated in different size regimes. In estimating the errors in the data fit to obtain b, the value of b can change by as much as 50 percent just by using a different error estimation technique (Ref. 6). This rather large uncertainty in b can have tremendous impact on the mass distribution, as demonstrated in Figure 35. It is strongly recommended, therefore, that more hypervelocity impact data be obtained to accurately estimate the value of b. The power law distribution used here currently fits the limited data available well. It is a simple, easy to use relationship but may give incorrect results beyond the supporting data range from which the fit coefficient b is derived.
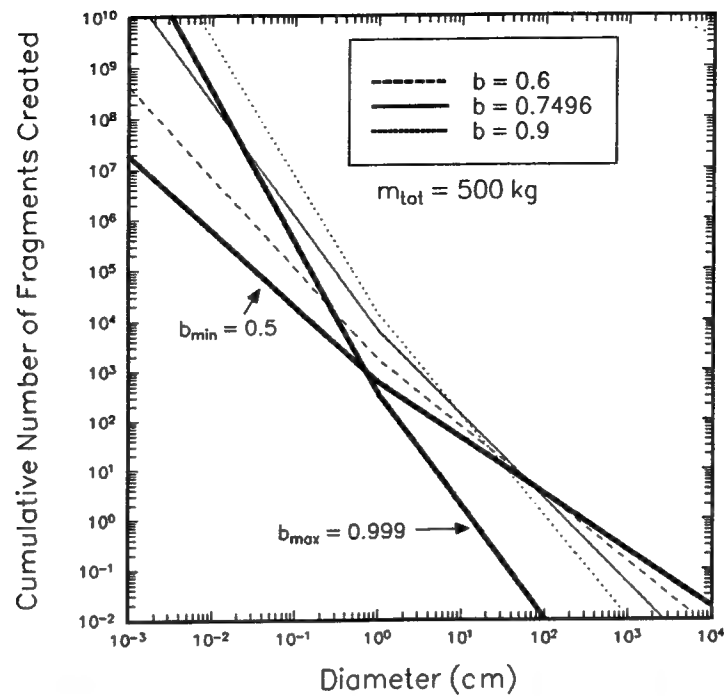
61

Figure 35.   Cumulative number distribution versus diameter using Equation 41 and mass/diameter relation for various selected b coefficient values (0.5 ≤ b < 1.0).
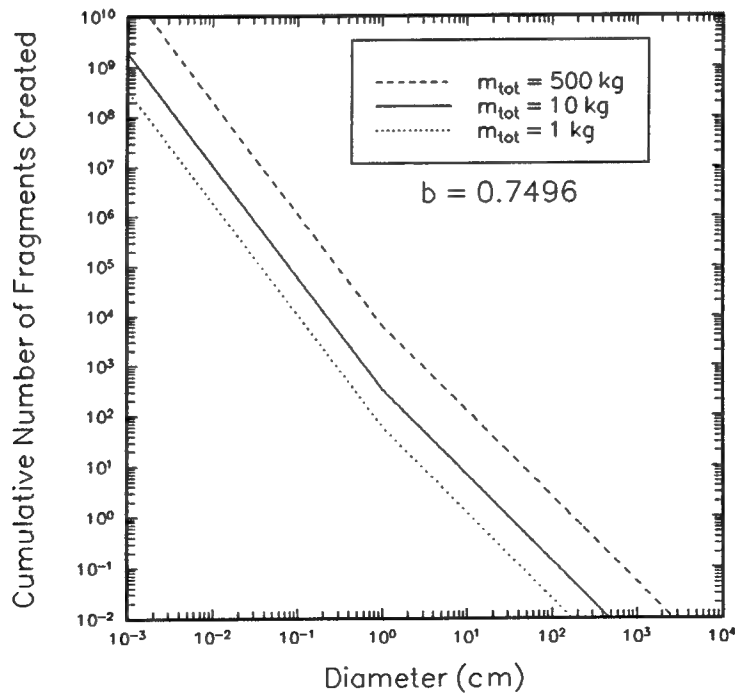

Figure 36.   Cumulative number distribution versus mass using Equation 10 and mass/diameter relationship for three m_{tot} values (1, 10, 500 kg).

3.2.3 Explosion Fragmentation Model

This subsection describes the cumulative number versus mass distribution model for explosion breakup events in EVOLVE. Subsection 3.2.3.1 describes the details of the model. Subsections 3.2.3.2 and 3.2.3.3. give details to the assessment and sensitivity uncertainty of the model.

3.2.3.1 Description.

Unlike collisions, explosion breakups involve just the mass of a single explosive object. Two types of explosions are identified in EVOLVE: LIE and HIE. These explosion classifications differ by their cause, their mass/size distribution, and ejecta velocity characteristics. The LIE generally occurs in rocket bodies and payloads containing residual fuel or other explosive material where the fragmented material is not in close contact with the explosive. A pressure-vessel explosion, a shock wave induced fragmentation caused by a collision, or an HIE in some remote part of the spacecraft structure are examples of the LIE. As was discussed in Subsection 3.2.2.2, the collision model will produce a secondary LIE in the residual target if the mass of the ejecta lies within $0.1\, m_t \leq m_e \leq m_t$. This is termed a catastrophic collision. The LIE type explosions produce a large number of larger fragments. Almost half of all radar-tracked objects by USSPACECOM are attributed to the 34 known LIE as of 1987. When the structure mass is in close contact to the explosive, the explosion is characterized as being high-intensity. The HIE type explosions produce many small fragments that generally cannot be tracked with ground-based radar.

Like the collision mass distribution model, the explosion mass distribution models in EVOLVE are based on limited reported data in Reference 5. The size distribution for LIE events is empirically derived from the experimental data of a single Atlas missile tank fragmentation test. (This very limited data lends a large uncertainty to an empirical model such as described here. Incorporation of additional experimental data is highly recommended to more firmly establish the robustness of this model.) The fragmentation data were fit using an exponential law cumulative distribution of the form

$$N = N_0\, e^{-b\sqrt{M}} \tag{48}$$

The constant N_0 is the total number of fragments with mass larger than M produced and its magnitude will be a function of the exploding parent mass.

Assuming that $N_0 = am_r$, where m_r is a reference mass, then the following is taken as the cumulative mass distribution

$$N(m \geq M) = a\, m_r\, e^{-b\sqrt{M}} \quad \text{for } 0 \leq M \leq m_{max,r} \tag{49}$$

where a and b are constants and $m_{max,r}$ is some maximum mass for which there is only one fragment produced (i.e., at some mass $m > m_{max}$, $N = 1$). This can be expressed using the conservation of mass expression as

63

$$\int_0^{m_{max}} m \left(\frac{dN}{dm}\right) dm = m_r \qquad (50)$$

where m is the mass integration variable.

Now,

$$\frac{dN}{dm} = -\frac{ab}{2} m_r \frac{e^{-b\sqrt{m}}}{\sqrt{m}} \qquad (51)$$

so Equation 50 becomes

$$-\frac{abm_r}{2} \int_0^{m_{max}} e^{-b\sqrt{m}} \sqrt{m}\, dm = m_r \qquad (52)$$

The maximum mass will be some multiple, K_o, of the original mass m_r so that $m_{max} = K_o m_r$:

$$\int_0^{K_o m_r} e^{-b\sqrt{m}}\sqrt{m}\, dm = -\frac{2}{ab} \qquad (53)$$

so

$$a = \frac{2}{b}\left[\int_{K_o m_r}^0 e^{-b\sqrt{m}}\sqrt{m}\, dm\right]^{-1} \qquad (54)$$

When plotted as the number of fragments produced (in log space) versus square root of the fragment mass, the data in Reference 5 indicated a curve essentially having two straight line slopes. For $M^{1/2} \sim 44\ g^{1/2}$ (or M~1936g) the data could be fit to functional form of Equation 48 with one set of coefficients and above this another fit could be obtained using a different set of coefficients. The small mass (<1936 g) curve slope was found to have approximately a 2.7 times steeper slope than the larger mass curve (>1936 g). The results of this two-part curve fit is given in Reference 3 by

64

$$N(m \geq M) = \begin{cases} 1.707 \cdot 10^{-4} \ m_t \ e^{-0.02056\sqrt{M}} & m \geq 1936 \text{ kg} \\ \\ 8.692 \cdot 10^{-4} \ m_t \ e^{-0.05756\sqrt{M}} & m < 1936 \text{ kg} \end{cases} \tag{55}$$

where N is the cumulative number of fragments having mass M (in grams) or larger and m_t is the explosive object mass (in grams). Expressing all masses of Equation 55 in kilograms, the following expressions are obtained

$$N(m \geq M) = \begin{cases} 0.1707 \ m_r \ e^{-0.6514\sqrt{M}} & m \geq 1.936 \text{ kg} \\ \\ 0.8692 \ m_r \ e^{-1.8215\sqrt{M}} & m < 1.936 \text{ kg} \end{cases} \tag{56}$$

This equation is now in the form of Equation 49. The constants a, b are based on explosion data, but they were made to fit NORAD radar-tracked data to account for the unobserved small size population (Ref. 3). All calculations in the LIE model used in EVOLVE assume an arbitrarily chosen 1000-kg for m_r. It fixes the total number of particles available to be distributed from a 1000-kg mass. Equation 54 can be integrated to obtain a in terms of b and $m_{max} = K_o m_r$ in the same manner performed previously with the collision model.

As shown in Reference 11, the expressions in Equation 56 can easily be extended to any arbitrary total mass m_{tot} by scaling the reference mass m_r to the total mass. The m_{tot} value represents the actual mass of the explosive object. By scaling to the 1000-kg reference mass, the same constant in Equation 56 as obtained for the $m_r = 1000$ kg object can be used. The scaling factor is simply a mass ratio of a reference mass m_r to the total mass m_{tot}:

$$f_m = \frac{m_r}{m_{tot}} \tag{57}$$

The equations used to give the LIE cumulative size distribution in EVOLVE now become

$$N(m \geq M) = \begin{cases} 0.1707 \ m_r \ e^{-0.6514(Mf_m)^{0.5}} & \text{for } M \geq \dfrac{1.936}{f_m} \\ \\ 0.8692 \ m_r \ e^{-1.8215(Mf_m)^{0.5}} & \text{for } M < \dfrac{1.936}{f_m} \end{cases} \tag{58}$$

where all masses are expressed in kilograms. Reference 11 shows that the m_r factor properly normalizes this distribution, obtaining a mass range $0 \leq M \leq K_o \ m_{tot}$.

The size distribution of the fragments in an HIE cloud is taken to be of a hybrid nature. The cloud has an LIE exponential law component and an inverse mass law component with 90 percent of the mass following the LIE size distribution and 10 percent following the inverse mass law. The LIE distribution is given by Equation 58. The inverse mass distribution, which contributes to size bins only between 0.1 and 10 cm, is given by the form

$$N(m \geq M) = \frac{a}{M} \tag{59}$$

The expressions used in EVOLVE follow

$$N(m \geq M) = \begin{cases} \dfrac{g_m}{m_s} & \text{for } M \leq m_s \\[3mm] \dfrac{g_m}{M} & \text{for } m_s \leq M \leq m_l \\[3mm] 0 & \text{for } M > m_l \end{cases} \tag{60}$$

where

$$g_m = \frac{m_{tot}}{\ln\left(\dfrac{m_l}{m_s}\right)}$$

is the mass conservation normalization factor, $m_s = 0.1$ cm is the small mass cutoff, $m_l = 10$ cm is the large mass cutoff, and m_{tot} is the total mass of the HIE material.

The version of EVOLVE used in this study is currently set up to assume that $m_{tot} = 1000$ kg for all LIE and $m_{tot} = 6000$ kg for all HIE, regardless of any actual spacecraft mass.

3.2.3.2 Model Assessment. Presently, the EVOLVE code used in this study does not store the mass of the parent satellite involved in an explosion as one of the cloud attributes. The identity of the parent satellite is lost during the spatial density processing for explosion probabilities (Subsection 3.2.2.1); thus, the total masses must be assumed. Significant coding changes in EVOLVE would be required to maintain the identity of explosive object characteristics such as the actual mass. The assumption of constant masses for LIE and HIE events is considered one of the most significant problems for the version of the model used in this assessment. The mass of the fragments could be over or underestimated at any particular time using these assumed total mass values. (Later versions of EVOLVE have overcome this shortcoming.)

The inverse mass relationship of the HIE produces the large number of small fragments in the range 0.1 - 10 cm. In general, this population cannot be directly observed by normal radar surveillance. The effects of mixing 90 percent LIE and 10 percent inverse mass distributions for a 6000-kg object are shown in Figures 37 and 38. Figure 37 displays the cumulative number distribution N versus mass and Figure 38 gives N versus diameter. Also shown for comparison are the pure inverse mass relationship Equation 60 and the pure LIE relationship of Equation 58 for the 6000-kg mass object.

The functional form of inverse mass was chosen to simulate the limited data available based on six HIE tests of thin-walled cylindrical shell structures having thicknesses approximating spacecraft walls (Ref. 5). From these data, the smallest fragment mass produced in any HIE was ~10 mg. This gives an ~2-mm-size fragment diameter using the m(d) relation from EVOLVE. This lower size limit is observed to be independent of the initial mass of the exploding object. Because of the breakup energy available in this type explosion, few large fragments are produced. Much of the explosive energy is used in breakup process producing small fragments. As a result, an assumed 10-cm upper diameter size limit is incorporated in the model; thus, fragments from the 600-kg component of the 6000-kg object (subject to an HIE) are actually distributed from 19 mg to 260 g in mass using the EVOLVE m(d) relation. The remaining 5400 kg of the object structure is treated using the LIE expressions of Equation 58, which provides the larger diameter fragments for HIE events. It should be noted that the 0.1- to 10-cm objects contribute to the environment where observed data are lacking. The 90 percent pure LIE and 10 percent pure HIE breakdown is reasonable since it is intended to model explosions of rocket bodies and other on-orbit structures where only a small portion of the structure is in the vicinity of the explosive (e.g., residual oxidizer or fuel).

3.2.3.3 Sensitivity/Uncertainty Analysis. The LIE mass distribution of Equation 58 as generalized by the form of Equation 49 has been extensively studied (Ref. 6). A series of data obtained from explosion studies were fit to the form given in Equation 49 (Ref. 5). It was found that the scaling coefficient a had a standard deviation (σ_a) that was 31 percent of the nominal mean value , so a = ± 0.31 . Also, the slope coefficient b deviated by as much as 75 percent of its nominal mean value , so b = ± 0.75 . These experiments were performed under controlled conditions, yet a wide variation in a and b were obtained.

The results of on-orbit explosions can be expected to have even a wider variation. The different spacecraft structures, explosive intensity, materials placement and many other real world considerations will increase the spread on the a and b coefficients. The uncertainties in the on-orbit explosions coefficients are assumed to be much larger than that found for the controlled laboratory environment. The values obtained from this analysis are given in Table 7 (Ref. 6).
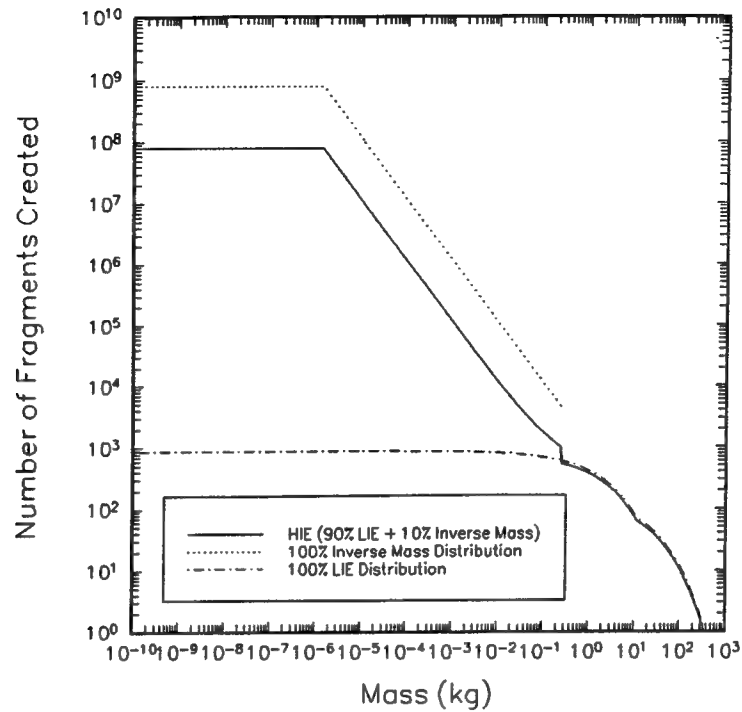
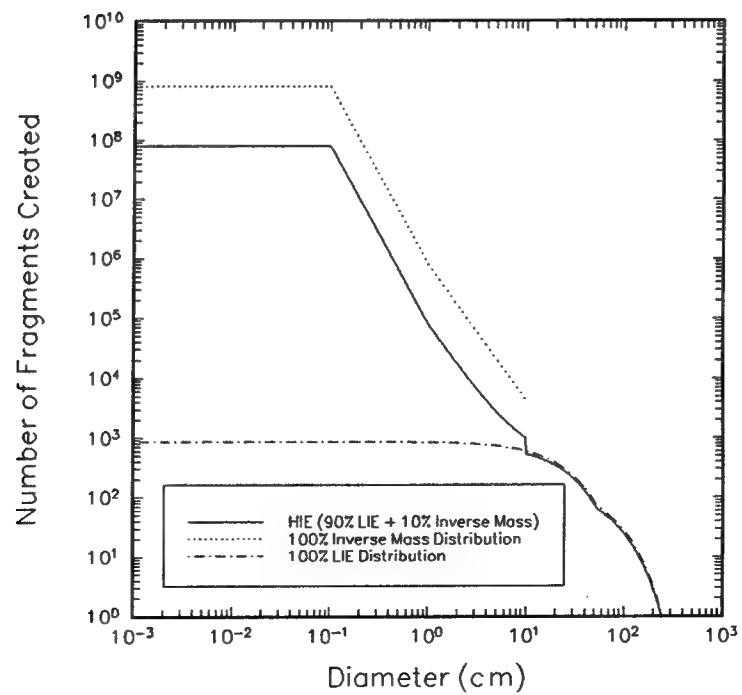**Figure 37.** Cumulative mass distribution for HIE events (solid line) used in EVOLVE.

Figure 38. Cumulative size distribution for HIE events (solid line) used in EVOLVE.

68

Table 7. Coefficient average and ranges for Equation 58.

Coefficient	Average	Lower Limit	Upper Limit
a	5×10^{-4}	1×10^{-4}	1×10^{-3}
b	0.04	0.02	0.06

Using these values, the explosion model can be written as

$$N(m \geq M) = \left(0.5 \begin{array}{c} +0.5 \\ -0.4 \end{array}\right) m_r \ e^{-(1.2649 \pm 0.6325) \sqrt{Mf_m}} \tag{61}$$

where all masses are expressed in kilograms.

The coefficients in Equation 58 indeed lie within the estimated uncertainties given here. Figure 39 shows the curves of Equation 56 plotted versus the mean and $\pm\sigma$ limits of Equation 61 for a reference mass m_r = 1000 kg and total mass m_{tot} = 6000 kg. The $+\sigma$ bound provides the upper bound to the slope, thus, producing the most cumulative number of fragments but with a maximum fragment size just over 1 m. The $-\sigma$ bound exhibits the smallest cumulative number of fragments but with a larger maximum fragment size of ~2.5 m. The results of Equation 58 shown in Figure 40 reflects the overlap between the two cumulative distributions expressed in Equation 58. The slight discontinuity observed in this curve, due to the discontinuity in the m(d) relationship, occurs at

$$d = 0.54 \text{ m where the mass } M = (1.936 \text{ kg})\left(\frac{6000 \text{ kg}}{1000 \text{ kg}}\right) = 11.616 \text{ kg} \tag{62}$$

The EVOLVE function gives a total yield of fragments slightly below the $+\sigma$ values. The maximum fragment size of ~3.0 m, which is larger than that calculated using the $-\sigma$ values, is a result of the summation process between the two cumulative distributions. This analysis shows that there can be a significant uncertainty for one breakup attributed to the uncertainty in the a, b coefficients. In fact, the total yield difference between the $+\sigma$ and $-\sigma$ cases is approximately a factor of 10.

The HIE distribution which contains a 90-percent contribution from the LIE distribution is also affected by the choices of a and b as well as the relative mass m_r. Figures 37 and 38 show the hybrid nature of the HIE distribution. A slight but sudden jump in the cumulative distribution curve occurs at d = 10 cm as a result of the discontinuity between the LIE and inverse mass distributions. The model should provide a continuous distribution since there is no physical basis for a jump at this value. The HIE is fixed by the ratio of the upper and lower mass ranges, m_l and m_s, respectively. The LIE model is more flexible, being defined by the a, b coefficients and the relative mass m_r in the exponential form of Equation 49. The am_r product (or the a coefficient for fixed m_r) can be adjusted to slide the distribution along the y-axis (cumulative number) to nearly coincide with the end point of the inverse mass
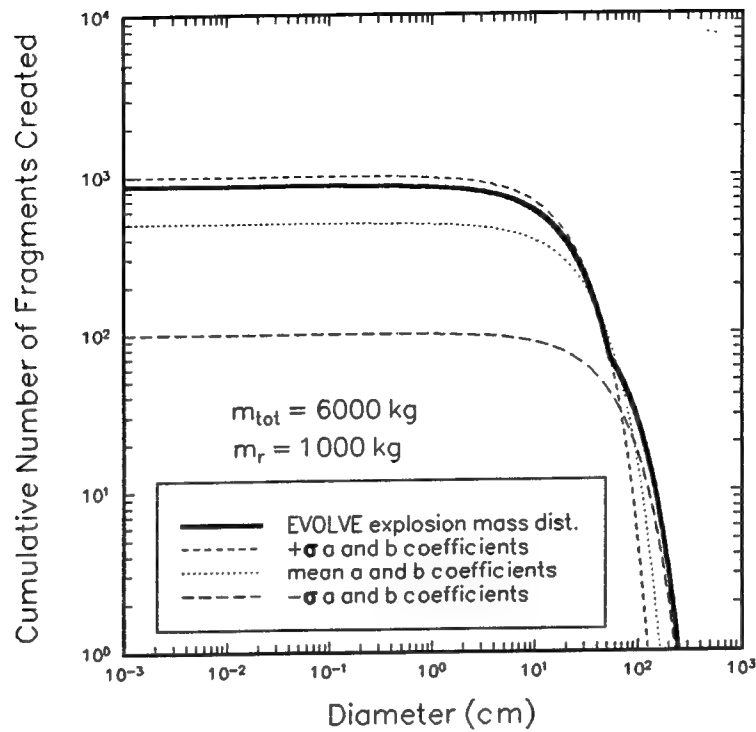
Figure 39. Cumulative diameter distribution for number of LIE fragments created for $\pm \sigma_a$ and $\pm \sigma_b$ coefficients in Equation 61.
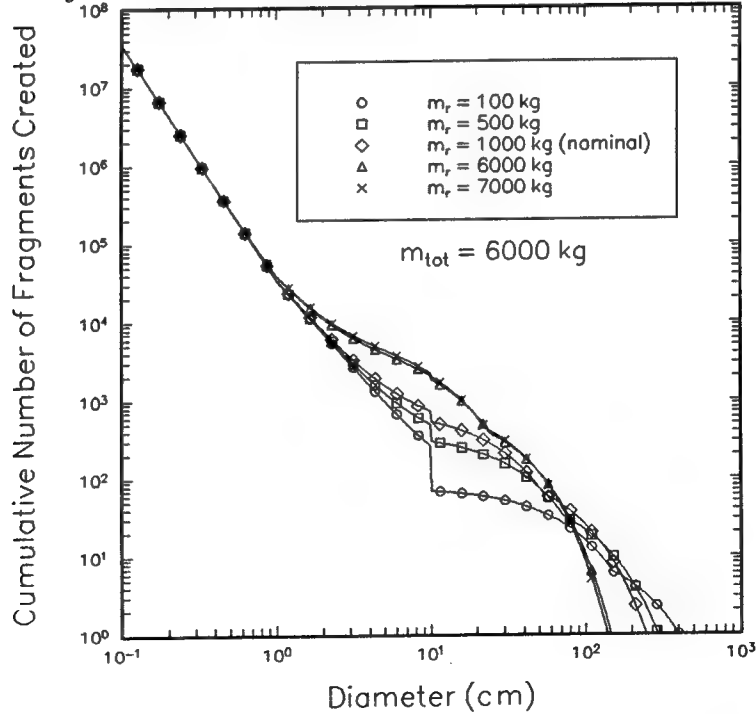

Figure 40. Cumulative number distribution versus diameter for HIE events showing effect of changing reference mass m_r for a fixed mass of 6000 kg.

distribution. Figure 40 demonstrates the effect of varying m_r for a fixed total mass $m_{tot} = 6000$ kg. Clearly, the slope increases as m_r increases (since it is part of the scaling factor f_m in the exponent). Also, the am_r factor is increased. Both effects increase the cumulative number of fragments produced and, if $m_r = m_{tot}$, steepens the slope even further but the effect is relatively insensitive when $m_r > m_{tot}$. The effect becomes dramatic when $m_r << m_{tot}$. Since the m_r factor appears in the exponent and affects the LIE curve slope, the maximum fragment size produced decreases by a factor of ~2.5 (from ~4 to 1.5 cm).

The NASA developers elected to incorporate a simple inverse mass distribution to simulate the results seen in the thin walled cylinder explosion test data (Ref. 5). In contrast, others (Refs. 5 and 6) chose to model the HIE distribution using the same exponential law form, Equation 49, used for LIE events. The HIE distribution merely has different fit coefficient constants (a, b) than the HIE distribution. If the exponential law is applied to model the same distribution range that the inverse mass currently models in EVOLVE, while still retaining the upper and lower size limits, a degree of compatibility and flexibility could be added to the model. This model would be similar in form to the treatment of LIE except that the HIE exponential law component characterizing the fragments in the lower size ranges would have cutoff limits. The coefficients could be chosen to align the LIE and HIE components while giving the appropriate slopes throughout the entire diameter range.

3.2.4 Debris Cloud Propagation/Spatial Density Model

EVOLVE propagates a debris cloud resulting from a collision or explosion in a fundamentally different manner from that of intact objects. Unlike launched intact objects, the EVOLVE program does not individually propagate the larger number of fragments created during a breakup event. Instead, a relatively simple analytical function is used to describe the time evolution of the spatial density of debris fragments within each particle size bin resulting from a single breakup event. As described in Subsection 2.4.2, fragments of a characteristic diameter residing in a single size bin distributed over all altitude bins at a given point in time define a subcloud of the cloud. It is these subclouds which are propagated at each time step over all altitude bins. In the time loops of the EVOLVE.FOR driver (for both deterministic and stochastic processing), a call to the subroutine CLDUPD followed by a call to subroutine SPDENC propagates the individual subclouds of a cloud. This subsection will explain the models contained in CLDUPD and SPDENC which combine both the propagation of clouds with the determination of their spatial density contribution to the environment in one model.

3.2.4.1 Description. The time-evolution of debris subclouds contains a lengthy but straightforward analytical function whose value is dependent directly on five parameters:

- Particle diameter, d (m)
- Altitude, h (km)
- Breakup altitude, h_o (km)

- Elapsed effective time, since breakup, t (yrs)
- Number of fragments in subcloud, N

This analytical function determines the flux contributed to the environment per fragment in units of impacts/meter^2 - year given the above parameters as inputs:

$$f_c(d, h, h_o, t) = f_o\left(\frac{f \cdot g}{f + g} + e\right) \qquad [\text{impacts/m}^2\text{-yr}] \qquad (63)$$

where

$$f = f_1 f_2$$

$$f_1(d, h, h_o) = 10^{\left[(-10.076d + 0.389)\left(\frac{h - h_o'}{h_o}\right)\right]}$$

$$f_2(d, h_o, t) = 10^{\left(-0.33\left(\frac{500}{h_o}\right)^5 d^{c(d)} t^{a(h_o, d)}\right)}$$

$$a(h_o, d) = 1 + h_o\left(1.66 \times 10^{-3}d - 9.61 \times 10^{-4}\right)$$

$$\begin{cases} c(d) = 0.0778 + 22.22d & \text{for } d < 0.01 \text{ m} \\ c(d) = 0.3 & \text{for } d \geq 0.01 \text{ m} \end{cases}$$

$$\begin{cases} f_o(d) = 4 \times 10^{(65.778d - 10.704)} & \text{for } d < 0.01 \text{ m} \\ f_o(d) = 4 \times 10^{(-8.153d^2 + 6.709d - 10.112)} & \text{for } d \geq 0.01 \text{ m} \end{cases}$$

$$g(h, h_o, t) = 6.0 \times 10^{\left[\left(\frac{1200}{h_o}\right)t^{0.8} + 1.2\right]\left(\frac{h - h_o}{h_o}\right)}$$

$$e(d, h, h_o, t) = 0.2 \ f_2 \ 10^{\left(-0.00125(h - h_o)^2\right)}$$

Multiplying Equation 63 by N gives the total cross sectional flux contribution of the debris cloud ($F_c = f_c N$). For surface area flux, divide the cross sectional flux by four.

The complicated analytic expression of Equation 63 is empirically derived from preprocessed curve fits obtained from the results of a numerical code FRGMNT developed at NASA JSC[*] to perform debris cloud evolution studies. Although it is beyond the scope of this report to fully assess this code, a discussion of the model's origin and its major assumptions is crucial to understanding the role these equations play in EVOLVE. Figure diagrams the overall structure of program FRGMNT and shows its major functional subroutines. The FRGMNT program calculates the spatial density of a cloud composed of N_O objects all having the same diameter d_O as functions of altitude and time after breakup. FRGMNT essentially calls two major subroutines in succession: (1) The CLOUD model to determine the initial debris cloud parameters and orbital elements of each individual cloud fragment and (2) the EVOLVE model to determine the time evolution of the individual fragment orbits given the results from CLOUD (DECAY) and to calculate the spatial density as functions of altitude and time (SPAD).

The CLOUD model requires as user-specified initial conditions the number of individual fragments comprising the cloud N_o, the characteristic diameter of all particles d_o, the perigee
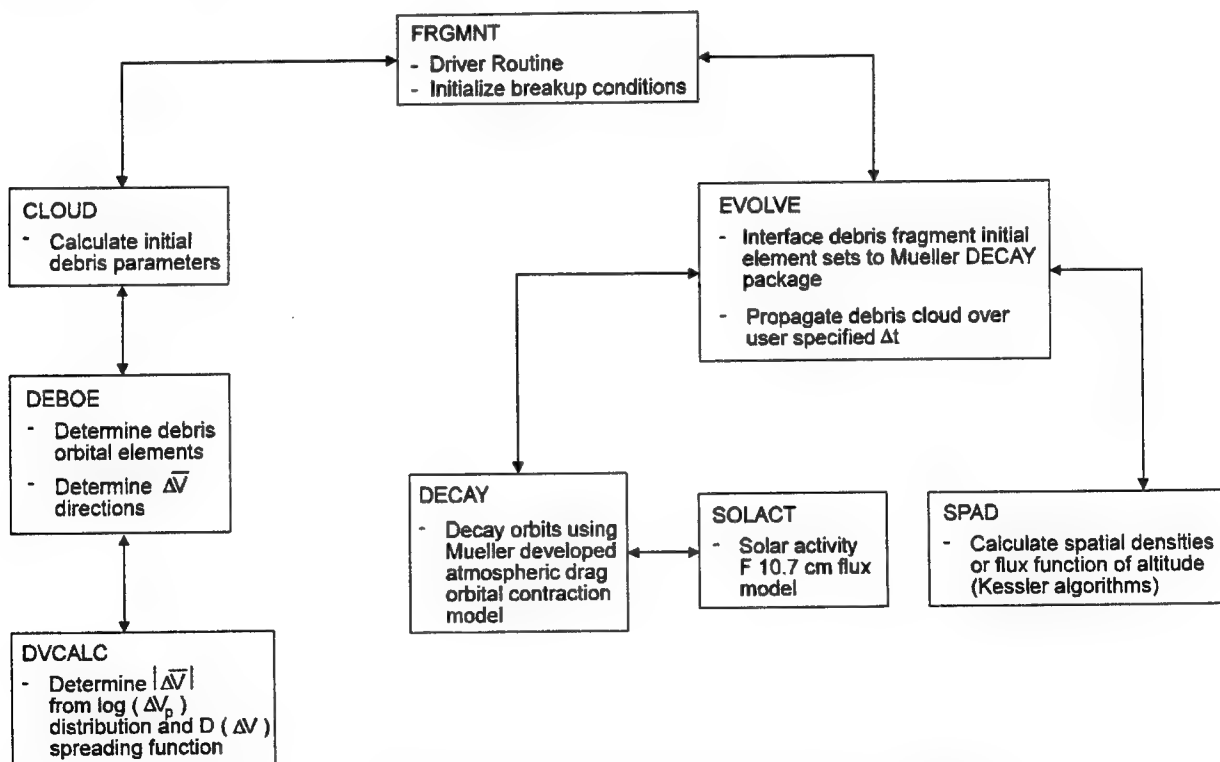

Figure 41. Block diagram of preprocessing code FRGMNT.

[*]Private Communication: P. D. Anz-Meador, 1991.

altitude h_p, apogee altitude h_a, inclination i, right ascension Ω, and argument of perigee ω of the parent satellite orbit. The model invokes the subroutine DEBOE to calculate the debris fragment orbital elements as a function of the imparted ΔV vector oriented by the angular quantities θ and ϕ relative to the initial orbital velocity vector V_o of the parent object at breakup. Currently, the θ and ϕ values are randomly selected yielding an isotropic ejecta direction distribution relative to the center of mass at the breakup point. Clouds are distributed isotropically for both collisions and explosions since the model does not distinguish breakup type. Although an explosion generally distributes its energy isotropically, the location, structure, and materials involved in a spacecraft can cause an asymmetry in the fragment ΔV directions. Assuming that the entire explosive object disintegrating (as is done in EVOLVE), the isotropic direction distribution is valid. For collisions, the assumption of isotropic direction may be unreasonable since significant directionality effects associated with the resultant center of mass motions and momentum transfer are possible. The observed known collision breakups have already observed a degree of directional nonisotropy in the fragments created (Refs. 21 and 22).

DEBOE then invokes the subroutine DVCALC to calculate the velocity magnitude $\Delta V = |\Delta \vec{V}|$. The ΔV magnitude is obtained from a prescribed ΔV distribution as a function of debris diameter. The ΔV distribution chosen for the EVOLVE debris cloud model is based on hypervelocity collision data. Although derived from collision data, the model is applied to all breakup events including explosions. The model incorporated in DVCALC to determine ΔV for a characteristic diameter d is based on a functional form given by Su (Ref. 19) following his analysis of the data obtained from a single hypervelocity test shot of a 0.235 g projectile impacting a target at 3.5 km/s. This form is a quadratic fit in log space and is represented as

$$
\log(\Delta V_p) = \begin{cases} A + B \left[\log\left(\dfrac{d}{d_m} \right) \right]^2 & \text{for } d \geq d_m \\[2em] A & \text{for } d < d_m \end{cases} \tag{64}
$$

where ΔV_p is the most probable $\Delta V = V_{ejecta}/V_{imp}$ for a particle of diameter d, $d_m = C (E_p)^{1/3}$, where E_p is the energy of the projectile, and A, B, C are constants. This expression shows that the ΔV value increases as the projectile kinetic energy increases for a given particle diameter d, although slowly because of the logarithmic function. The ejecta velocity increases as diameter decreases until a limiting value defined by A is reached at the diameter d_m. All fragments with $d < d_m$ are assumed to be given a velocity impulse of $\Delta V_p = 10^A$.

During the 1985 US antisatellite collision test of the P78 "SOLWIND" orbiting satellite with a suborbital projectile, radar measurements of the imparted ΔV velocities were obtained for trackable objects in the diameter range 5 cm < d < 50 cm. These ΔV data are fit to the form

given in Equation 64 to yield the following distribution used in DVCALC for the most probable velocity perturbation ΔV_p

$$
\log_{10}(\Delta V_p) = \begin{cases} 0.875 - 0.0676 \left[\log_{10}\left(\dfrac{d}{d_m} \right) \right]^2 & \text{for } d \geq d_m \\[2em] 0.875 & \text{for } d < d_m \end{cases}
\tag{65}
$$

where

$$
d_m = 1.24836 \times 10^{-9} \sqrt[3]{m_p \, V_{imp}^2} \quad [m]
$$

and m_p is the projectile mass and V_{imp} is the impact velocity (Refs. 23 and 24). Equation 65 gives a single ΔV_p value (in kilometers/second) for each particle diameter. The most probable ΔV_p is equated to the assumed projectile velocity (7.5 km/s) for $d < d_m$. Values of $m_p = 7.5$ kg and $V_{imp} = 10$ km/s were used to generate the curves used for the phenomenological function.

Equation 65 represents a characteristic velocity that can be assigned to each size bin. In reality, there will be a spread of velocities due to the statistical nature of the energy breakup process and to collisional interactions with other particles during and after fragmentation. It has consistently been observed (Ref. 17) in hypervelocity collision experiments that the maximum velocity of ejecta is approximately 1.3 times the projectile velocity (and therefore ΔV_p) (although Su, observes a maximum of 1.67 times the projectile velocity in his analysis) (Ref. 19). The minimum expected ΔV for a fragment in a size bin is assumed to be 0.1 ΔV_p (Refs. 23 and 24).

For each particle diameter, a triangular probability density function $D(\Delta V)$ was applied to the value obtained from Equation 65 to simulate the expected spread in velocity perturbations. This function determines the fraction of debris fragments possessing a particular ΔV value. Now,

$$
D(\Delta V) = 0 \quad \text{for } \Delta V \leq 0.1 \, \Delta V_p \quad \text{and} \quad \Delta V \geq 1.3 \, \Delta V_p
\tag{67}
$$

Also,

$$
\int_{0.1\Delta V_p}^{1.3\Delta V_p} D(\Delta V) \, d(\Delta V) = 1
\tag{68}
$$

75

The triangular function can be written as two linear segments:

$$D(\Delta V) = \begin{cases} m_1 \Delta V + b_1 = D_1(\Delta V) \\ m_2 \Delta V + b_2 = D_2(\Delta V) \end{cases} \tag{69}$$

so

$$D_1(\Delta V_p) = D_2(\Delta V_p) \tag{70}$$

The slopes (m_1 and m_2) and intercepts (b_1 and b_2) can be determined from Equations 67 to 70 to yield

$$D(\Delta V) = \begin{cases} \dfrac{(\Delta V - 0.1\Delta V_p)}{0.54\Delta V_p^2} & \text{for } 0.1\Delta V_p \le \Delta V \le \Delta V_p \\[4mm] \dfrac{(1.3\Delta V - \Delta V_p)}{0.18\Delta V_p^2} & \text{for } \Delta V_p < \Delta V \le 1.3\Delta V_p \end{cases} \tag{71}$$

Equation 71 is plotted in Figure 42 for the value $\Delta V_p = 10^{0.875} = 7.5$ km/s ($d \le d_m$) as used in EVOLVE. Most fragments within each size bin will possess the characteristic peak delta-velocity, ΔV_p, for any given particle diameter. However, fragments can be imparted with velocities $0.1\ \Delta V_p \le \Delta V \le 1.3\ \Delta V_p$ with the frequency probabilities characterized by Equation 71 and shown in Figure 42. The ΔV is selected using a random number generator. The spread of velocities can be observed in Figure 43 as a function of diameter, d, over the range 10^{-7} m $\le$ d $\le 10^3$ m, with an impact velocity of 10 km/s and projectile mass of 17 kg. The solid line represents Equation 65 while the outer curves represent the minimum ($0.1\ \Delta V_p$) and maximum ($1.3\ \Delta V_p$) ejecta velocities possible at each diameter. Again, the number of fragments within any size bin possessing an ejecta velocity within this range is dictated by the distribution of Equation 71.

To determine the sensitivity of Equation 65 on its dependent parameters m_p (projectile mass), and V_{imp} (projectile relative impact velocity), a series of calculations were made holding one parameter constant and varying the other over the reasonable range of values expected for that parameter. Figure 44 shows Equation 65 with m_p = 10 kg and V_{imp} selected for values of 3, 7, 10, and 13 km/s. As expected, from Equations 65 and 66 the variation between the curves becomes larger as d becomes larger. The curves merge at the peak value $\Delta V = 10^{0.875}$ as d$\rightarrow$d$_m$. The maximum variation for this range is a factor of 2 at the maximum expected debris object size (a + d $\approx$ 2 m). Equation 65 is somewhat more sensitive to the projectile mass as seen in Figure 45, where m_p is varied from 1 to 1000 kg for an impact velocity of V_{imp} = 7.0 km/s. The variance at d = 1 m is approximately 1.5 magnitudes. Figures 44 and 45 indicate that the function is more sensitive to the projectile mass than the impact velocity over the reasonable ranges for these parameters.
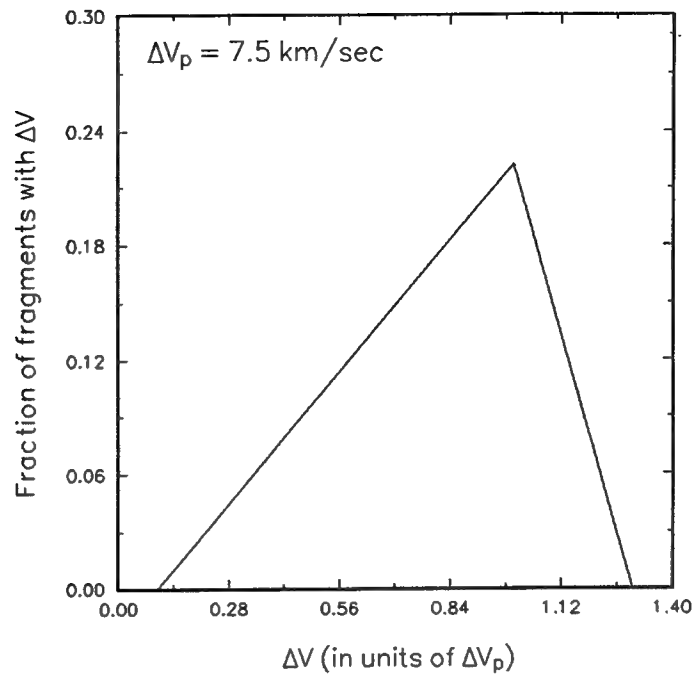
Figure 42. Triangular spreading function applied to the most probable ΔV_p value (assumed here to be 7.5 km/s) designed to spread the fragment velocities within a size bin.
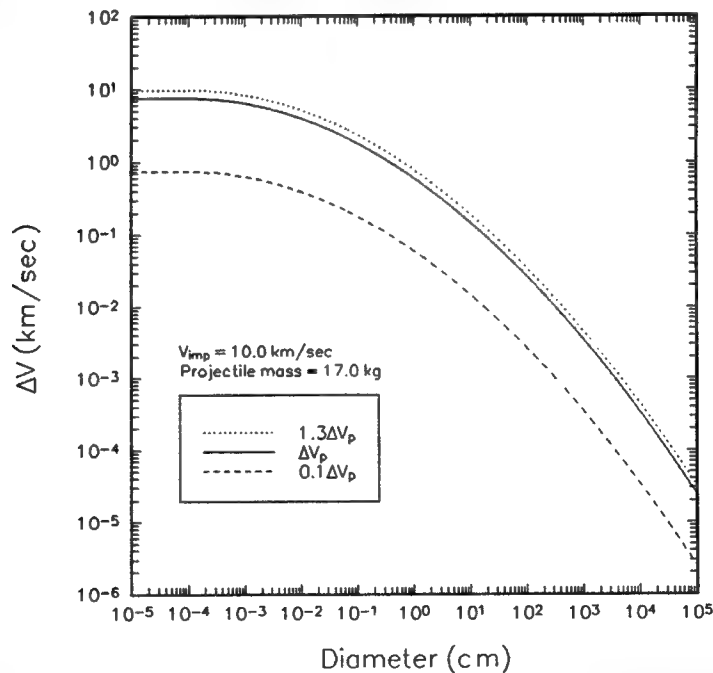

Figure 43. Ejecta ΔV velocity distributions (Eqs. 65 and 71) expected from a hypervelocity impact of a 17-kg projectile at a relative impact velocity of $V_{imp} = 10$ km/s.
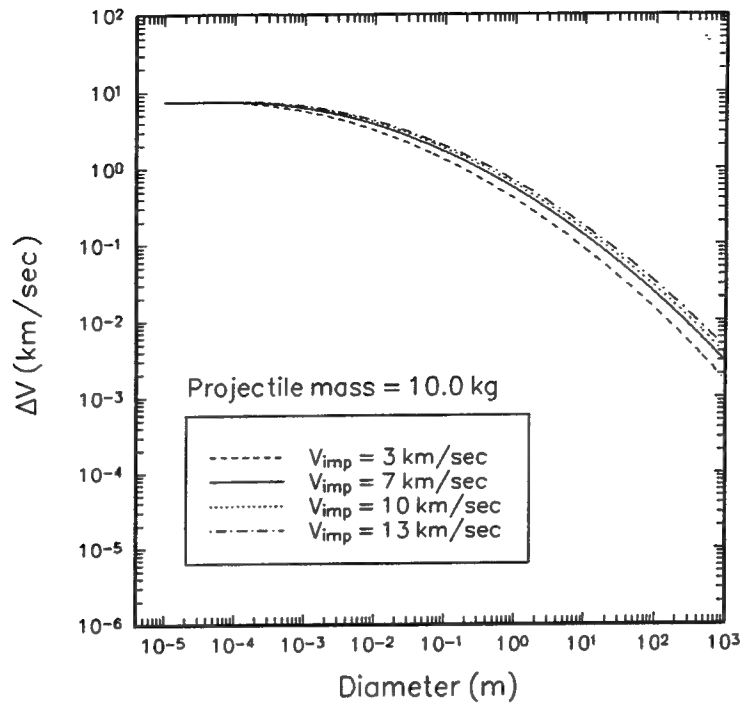
77

Figure 44.   Most probable ΔV_p distributions using Equations 65 and 66 for a projectile mass of 10 kg impacting at four selected impact velocities.
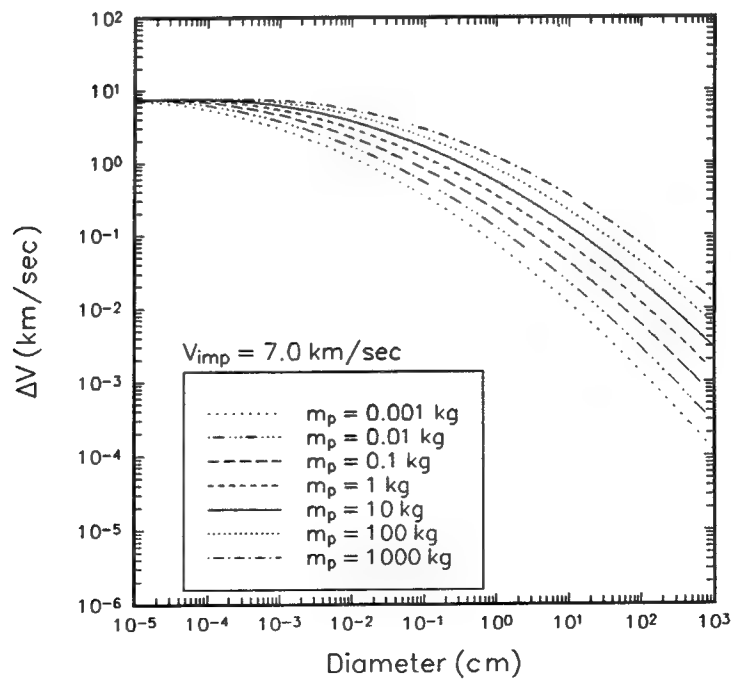

Figure 45.   Most probable ΔV_p distributions using Equations 65 and 66 for a projectile impacting at $V_{imp} = 7.0$ km/s for the seven projectile masses indicated.

78

Equation 65 is used for all three types of breakups (collisions, HIE and LIE) modeled in EVOLVE. The ΔV_p characteristic velocity distribution relies on kinematic parameters that can be associated only with collisions not explosions. Thus, a major weakness of the debris cloud model is the use of the collision ΔV distribution for explosion (both HIE and LIE) events. Explosion events will induce larger ΔV increments into larger size fragments than collisions and this effect can be significant due to the resultant spatial and temporal characteristics of the cloud. The HIE events can transmit tremendous kinetic energy to large fragments yielding an average $\Delta V = 3$ km/s while LIE events tend to yield a much smaller $\Delta V = 100$ m/s. Furthermore, there appears to be no clearly observed dependence of ejecta ΔV on the fragment mass for explosions unlike collisions (Ref. 25). Therefore, it is suggested that a separate model(s) which describes these explosion fragment characteristics be developed and applied to explosion events.

Once $\Delta \overline{V}$ is obtained (i.e., its direction and magnitude have been established), the vector quantity ΔV is vectorially added to the V_o at the breakup altitude h_o to obtain a resultant V_i for fragment i from which the initial orbital elements may be determined.

The N_o fragments of the cloud, each now having a unique set of orbital elements calculated in DEBOE, are now introduced to the EVOLVE module within FRGMNT (not to be confused with the EVOLVE debris environment evolution code). Starting from a specified initial year each fragment orbit is individually propagated over $\Delta t = 1$-yr time intervals using the same orbital propagation and decay routine package used in the EVOLVE program processing of intact objects. This decay model, developed in Reference 9 and based on the analytic equations in Reference 26 shall be described in Subsection 3.3.3. The solar flux, an input to the atmospheric drag model (Subsection 3.3.3), was assumed to be a constant $S = 1.1 \times 10^6$ Jy. This value is approximately the time averaged value of the historically observed flux. The EVOLVE module has since been equipped to call the same SOLACT subroutine used in EVOLVE to determine the yearly constant averaged solar flux (see Subsections 3.3.1 and 3.3.3). The procedure to process the fragment orbits is essentially the same used in EVOLVE to process intact objects. (See Subsection 3.1.3). The SPAD subroutine calculates the flux (in number/m²-yr) resulting from all fragment orbits at the end of the year time interval and stores the results to a data file. The flux (or spatial density) calculation in SPAD uses the same algorithm described in Subsection 3.1.4.

Using program FRGMNT, a matrix of spatial density results were obtained for simulated clouds consisting of $N_o = 1000$ identical sized particles. Clouds were calculated using the following diameter values characteristic fragment sizes: $d = 0.1, 1.0, 10.0,$ and 50.0 cm. For each characteristic fragment size, four breakup altitudes were evaluated along with specified h_a and h_p values. These are tabulated in Table 8. Curves were generated in yearly time steps until either all fragments within the cloud decayed or until 50 yrs had elapsed. Results were output in the form of spatial density profiles like that shown in Figure 46(a) [Ref. 23]. The various cloud densities were then empirically fit to obtain the pheonomenological fit function given in Equation 63. Figure 46(b) shows the corresponding smoothed fit function results for

79

Table 8. Orbital parameters and breakup altitudes used to obtain FRAGMNT results.

Apogee Altitude h_a (km)	Perigee Altitude h_p (km)	Breakup Altitude h_o (km)
2295	595	2090
500	500	500
.960	940	950
1000	1000	1000

Figure 46(a). The actual spatial density curves are reported to have been fitted everywhere to within a factor of 2 (Ref. 23).

The orbital decay process is strongly dependent on the fluctuations of the upper atmospheric density governed in large part by the heating caused by the solar flux. Since the series of curves used to derive Equation 63 were generated using a constant solar flux yielding a constant atmospheric density at a particular altitude, this model cannot support variable solar activity as used in EVOLVE. In an effort to remedy this problem, the NASA modelers developed a technique to account for the solar variability while still maintaining use of Equation 63. Their approach is to estimate the effective time, t_{eff}, that a debris cloud has remained in the environment. This is defined as the integral of the atmospheric density over time divided by a reference atmospheric density ρ_o evaluated at the breakup altitude h_o using the assumed $S = 1.1 \times 10^6$ Jy value. The density is a direct function of the altitude h and exospheric temperature T_∞ (S) which is itself a function of S. This can be written as
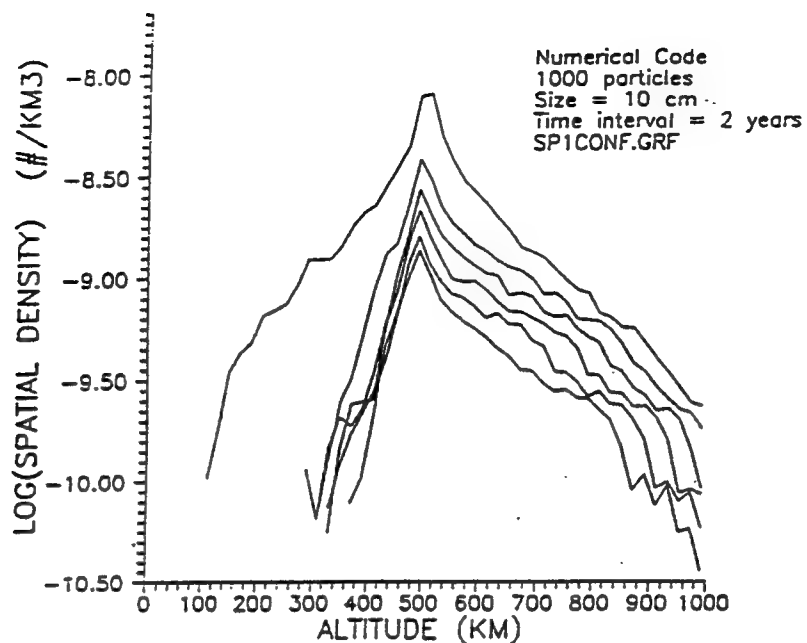
$$t_{eff} = \frac{1}{\rho_o} \int_{t_o}^{t} \rho(h_o, T_\infty[\, S(t') \,]) \, dt' \qquad (72)$$

where t is the breakup time and is the constant atmospheric density, ρ (h_o, T_∞ (S)), evaluated at the breakup altitude h_o for $S = 1.1 \times 10^6$ Jy.
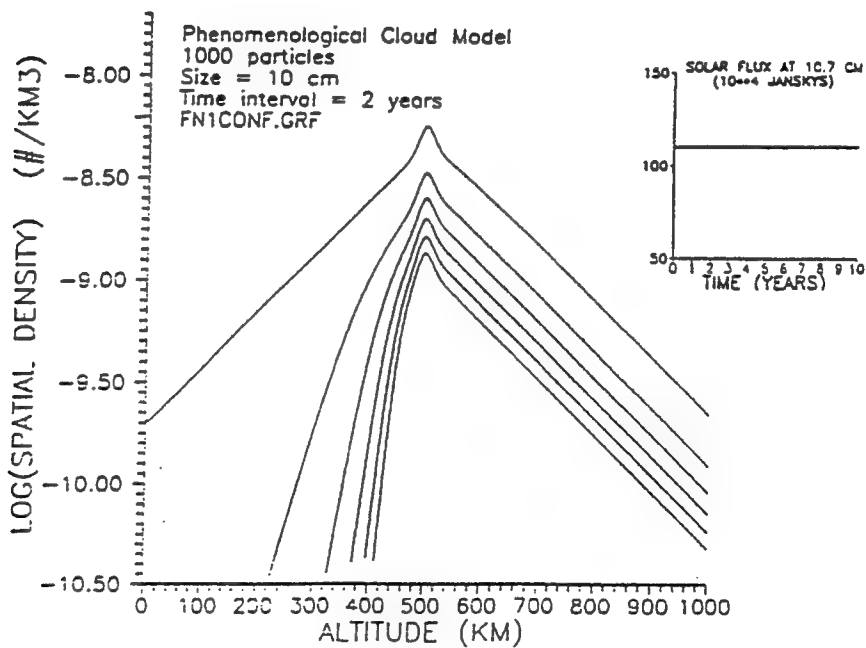
Since the process in time is performed in discrete Δt steps, Equation 72 can be written as

$$t_{eff} = \frac{1}{\rho_o} \left[\sum_{t = t_1}^{t_{curr}} \rho(h_o, T_\infty[\, S(t) \,]) \, \Delta t + \rho(h_o, T_\infty[\, S(t_1) \,]) \, (t_1 - t_o) \right] \qquad (73)$$

where Δt is the time interval (1 yr nominally), t_{curr} is the current epoch at which to

80

(a) Curves generated using the FRGMNT debris evolution code.

(b) Phenomenological function fit curves for corresponding curves in (a).

Figure 46. Spatial density curves (from Ref. 23).

evaluate t_{eff}, and t_1 is the first whole number year time increment after the absolute breakup time t_o (expressed in years). Normally, $t_1 - t_o < \Delta t$. Evaluating Equation 73 is the sole function of the CLDUPD subroutine in EVOLVE. Now, when $t = t_{eff}$ is input into Equation 63, the state of the cloud as if it had undergone actual density fluctuations is approximated. Scaling the time spent in an environment whose density is constant with time according to Equation 73 is assumed to be equivalent to spending the entire time in a variable density environment.

During periods of high solar activity ($S > 1.1 \times 10^6$ Jy, $\rho/\rho_o > 1$), and during periods of low solar activity ($S < 1.1 \times 10^6$ Jy, $\rho/\rho_o < 1$). Figure 47 compares the quantity $(\rho/\rho_o)\Delta t$ by which t_{eff} is incremented to the solar flux S. The flat line for the solar flux represents the $S = 1.10 \times 10^6$ Jy constant level while the flat line for the $(\rho/\rho_o)\Delta t$ quantity represents 1 yr. Clearly, the t_{eff} increment term correlates to the time-dependent change in S as it should. The bottom curve indicates that the effective propagation interval necessary to simulate a large deviation from the constant can be rather large. In 1981, for example, the solar activity level $S = 2.01 \times 10^6$ Jy increasing Δt to 5.14 yr (a net increase of 4.14 yr). Figure 48 shows the elapsed time since breakup, $t_{bu} = t - t_o$ for the normal linear propagation interval ($\Delta t = 1$ yr) versus the effective time, t_{eff}, using Equation 73. The deviations away from the linear increment due to solar flux variability is easily observed.

3.2.4.2 <u>Model Assessment.</u> The phenomenological function given by Equation 63 to characterize the time evolution of the debris subclouds is a novel approach to debris environment modeling which has both advantages and disadvantages that must be weighed carefully. The model is a simple one to use and is readily implemented within the EVOLVE processing framework. Being self-contained within only two subroutines, the model can be easily modified or replaced. The model represents a reasonable approach to modeling the enormous numbers of fragments created in the subclouds of each cloud.

Equation 63 is derived from the set of normalized spatial density profiles of clouds containing 1000 equally-sized fragments with parent orbits given in Table 8. The fit function will most accurately model breakups occurring at or near those orbits upon which the fit function was derived. The functional forms and coefficients were determined to minimize the errors (in a least squares manner) to the spatial density altitude profiles used. Equation 63 represents in one sense the combined, averaged behavior of these debris cloud profiles. Thus, the accuracy of the fit function in modeling a particular breakup event will depend on how comparable the orbital parameters of the parent object are to the breakup orbits specified in Table 8. The data given in Table 8 were selected to model the d, h, h_o, and t dependences of debris clouds originating from a circular or mildly eccentric orbit (e < 0.2) in the LEO environment. The fit function of Equation 63 was derived to model the behavior of such clouds over a reasonable range of breakup altitudes (500-1500 km). The latter three cases of Table 8 specify circular or near circular orbits while the first orbital condition in Table 8 was included to introduce into the fit function some of the resultant spatial density behavior effects characteristic of mildly eccentric orbits (in this case e $\approx$ 0.1). With such orbits being modeled, the breakup radius ($r_o = h_o + R_e$) corresponds approximately to the semi-major axis
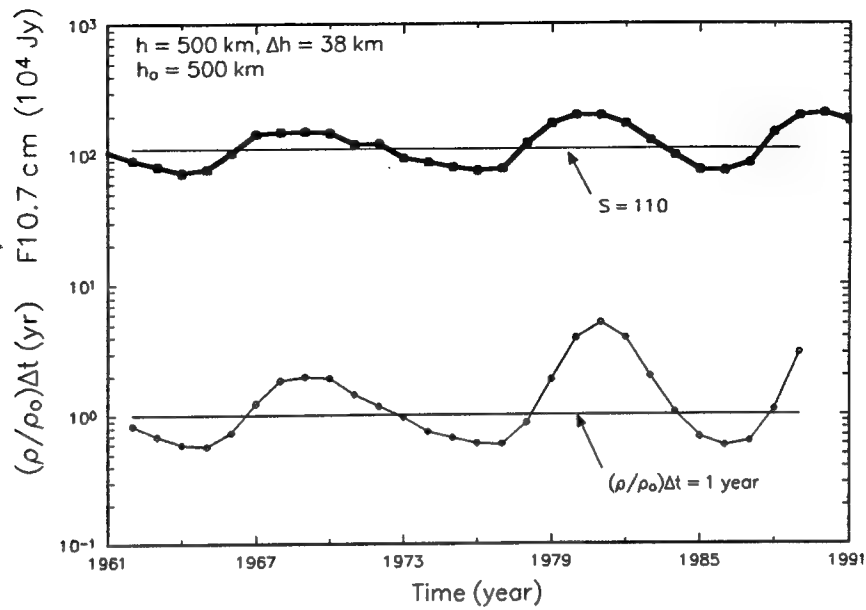
Figure 47. Solar Flux F10.7-cm value form the SOLACT look-up table (Ref. 12) (top) and scaled propagation interval for the phenomenological debris cloud function of Equation 63 (bottom).
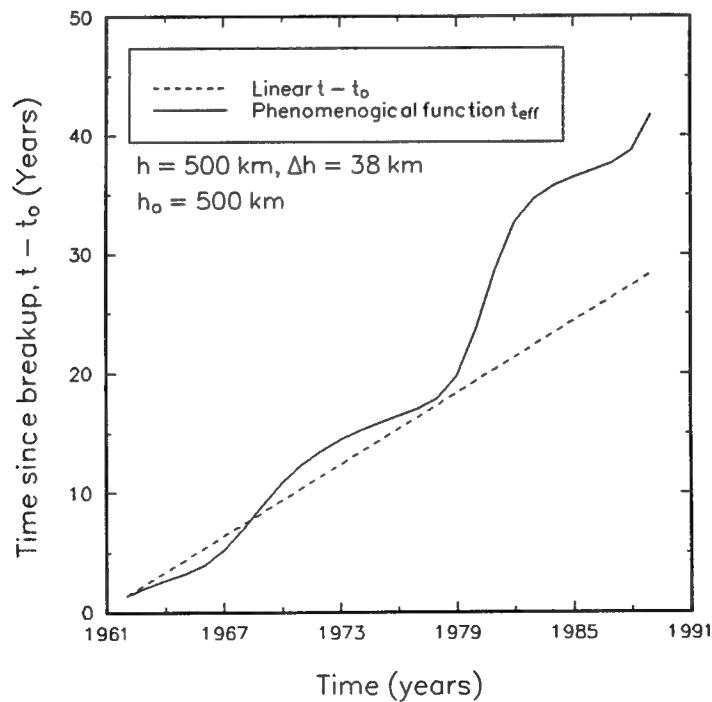

Figure 48. The effective time after a breakup at $h_0 = 500$ km occurring in 1961 (starting at the 1962 yr) versus time.

(a). (For circular orbits, of course, r_o = a.) Wherever an object breaks up along such an orbit, the spatial and temporal characteristics of the resulting cloud will be adequately described by Equation 63. Reference 23 reports that Equation 63 fits the empirically-derived spatial density profiles (calculated in the FRGMNT algorithm) over all d, h, h_o, and t parameters to within a factor of 2. This is remarkable considering the parameter space over which the fits were made and the statistical fluctuations inherent in the FRGMNT-generated curves.

If circular or mildly elliptical orbits are considered, the computational effort saved by using Equation 63 far outweighs the inaccuracies of modeling the spatial cloud densities. To model the individual debris cloud fragments in the same straightforward brute-force manner as intact objects is computationally prohibitive at the present time. The phenomenological function approach for such breakups then is compatible with the EVOLVE design philosophy of being a reasonably accurate yet computationally efficient modeling tool.

A significant drawback to Equation 63 is that this expression, being based largely on the breakup of objects having circular or mildly eccentric orbits, does not account for the highly elliptical orbit whose perigee altitude may reside in the 100- to 2000-km altitude range (e.g., Molniya and GTOs). For large eccentricity orbits, the breakup can occur over a large altitude range with cloud spatial and temporal characteristics far different from that modeled in Equation 63 for circular or mildly elliptical orbits. The spatial extent of fragments ejected from a breakup at the perigee of a GTO would vary significantly from a similar breakup occurring at the same altitude for a circular orbit (or even from a breakup occurring at apogee of the same GTO). The fragments from a GTO breakup will generally take longer to decay than those from a similar circular or mildly elliptical orbit breakup, thus requiring a different time evolution cloud description from that provided by Equation 63. For modeling completeness, it is recommended that the current debris cloud model be expanded to include breakups of objects in high eccentricity orbits (to account especially for possible GTO and Molniya satellite breakups). To best implement such an improvement within the current structure of the EVOLVE debris cloud model would likely entail development of a separate phenomenological function similar to Equation 63, but intended to model breakups of objects having more highly elliptical orbits. The elliptical orbit expression would conceivably be more sophisticated since it would need to parameterize the orbital velocity in terms of the breakup altitude since the orbital velocity will vary considerably with altitude. To select the appropriate phenomenological function, the eccentricity of the orbit of an object undergoing a breakup would have to be evaluated.

Another disadvantage of the fit function approach is that a change in any underlying assumptions used to obtain the spatial density preprocessed clouds would require a readjustment of the fit parameters and/or functional fit forms used to derive the phenomenological function. A new empirical function similar to Equation 63 would have to be reevaluated and incorporated into EVOLVE each time a modification is made. In this regard, EVOLVE is very rigid. As new breakup data become available and as breakup mass and velocity distributions models are continually reassessed, the modifications necessary to update the debris cloud evolution model would become prohibitive.

84

Figures 49-51 show the phenomenological function Equation 63 plotted as a function of its input parameters. Figure 49 shows the altitude dependence of a cloud containing 1000 1.0-cm objects at a breakup altitude of 500 km occurring in the breakup year $t_o = 1991$. The top curve at $t_{eff} = 0$ is the flux altitude distribution at the moment of breakup. The next curve occurs at the $t_{eff} = 1$ year (1992). All succeeding curves are spaced two years apart. The phenomenological function assumes fragments are instantaneously distributed into all altitude bins producing the altitude spatial density dependencies observed in these figures. The spatial density is roughly symmetric about the breakup h_o (a slightly smaller flux is observed toward the lower altitudes). The flux peaks at h_o with a relatively small flux enhancement near h_o; this is primarily due to the fragments that occupy circular or near circular orbits near that of the original orbiting body in an assumed circular orbit. The breakup altitude establishes either the perigee altitude h_p or apogee altitude h_a for all other fragment orbits depending on the resultant velocity of the fragment. In the case where the parent object is assumed to be in a circular orbit at h_o, the breakup altitude h_o becomes the new ejecta orbit's apogee altitude h_a if the imparted ΔV detracts from the original parent orbital velocity. The opposite happens if the imparted ΔV adds to the original parent orbital velocity. In the latter case, the breakup altitude becomes the perigee altitude h_p and the resulting elliptical orbits distribute the object into altitude bins above h_o. The time evolution of the cloud is clearly observed in Figure 49
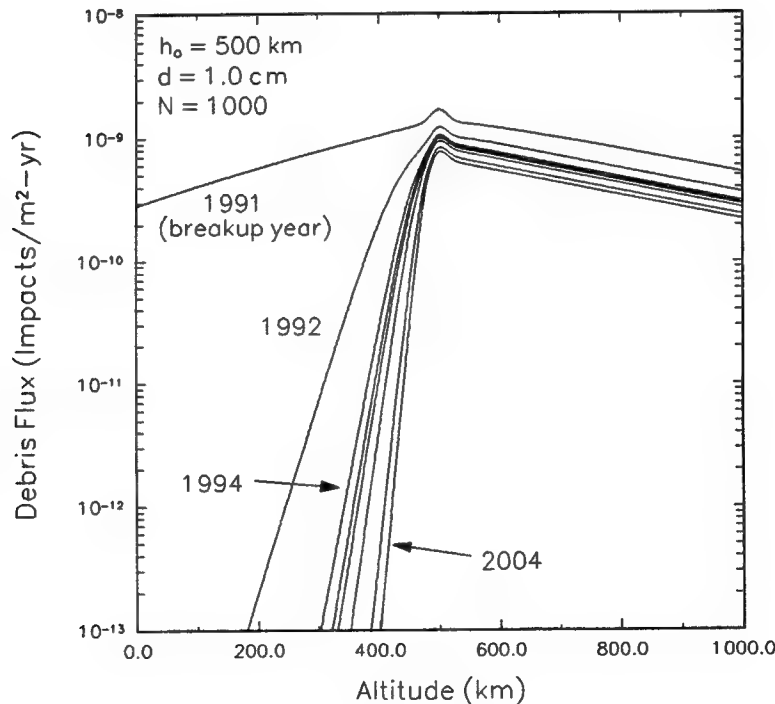

Figure 49.   Flux versus altitude distribution for an assumed breakup at $h_o = 500$ km in 1991. The top curve shows the flux at $t_{eff} = 0$ (t = 1991).
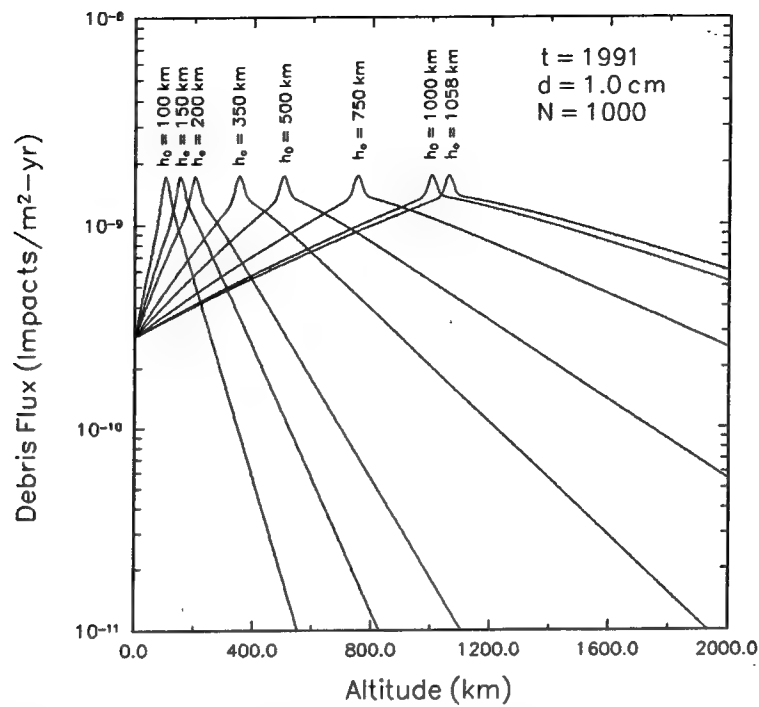
Figure 50. Flux versus altitude distribution for breakups occurring at seven different h_o values in 1991 for d = 1.0 cm fragments.
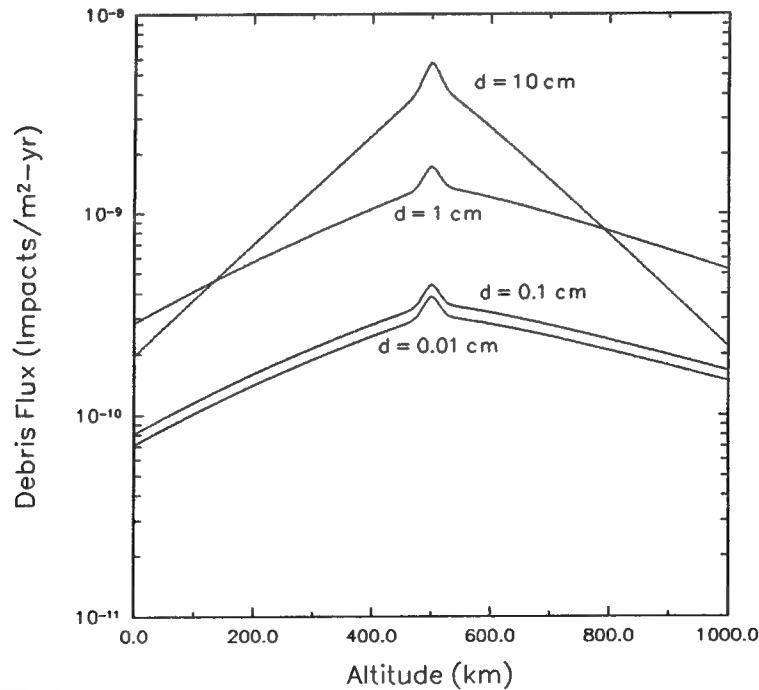

Figure 51. Flux versus altitude for breakup at t = 1991, h_o = 500 km, for four clouds of 1000 particles having diameters d = 0.01, 0.1, 1.0, and 10.0 cm.

with the time sequence starting at the breakup year (1991) and ending in 2004. Virtually all objects ejected into orbits having perigees below the 500-km breakup altitude are removed by atmospheric drag effects, whereas only slight cleansing occurs above 500 km. The nonuniform variation between curves is a manifestation of the periodic solar cycle effects on the upper atmosphere.

Figure 50 shows the results of Equation 63 for seven different breakup altitudes with breakups occurring in 1991. In all cases shown in Figure 44, $t_{eff} = 0$. Figure 50 indicates a consistent narrowing of the spatial distribution curves about the breakup altitude h_o with decreasing h_o. The initial slopes of the curves on the high altitude side of h_o should be reasonably close. There should be only slight differences attributable to variations in net velocities for fragments ejected into elliptical orbits. Imparted ΔV velocities to breakup fragments (spread over the approximate magnitude range 10 m/s $\leq \Delta V \leq$ 130 m/s for 1.0 cm objects) are independent of breakup altitude. The circular orbital velocity at h_o, however, decreases as h_o increases, scaling by the inverse square root of the ratio of the higher altitude to the lower altitude. Therefore, the orbital velocity at $h_o = 100$ km is a slight 1.0672 times that at $h_o = 1000$ km. The overall effect, then, is to cause the resultant velocity vector of ejecta fragments at lower altitudes to be less affected by the ΔV increments added to the orbital velocity. Recalling that Equation 63 approximates a breakup at h_o for a circular or near-circular orbital orientation, the result is that fragments are not ejected into as wide an altitude range at lower breakup altitudes as they are at the higher altitude orbits. The effect has been estimated to be slight for the range of breakup altitudes expected in the LEO environment. For example, if a fragment is ejected with an assumed $\Delta V = 100$ m/s at $h_o = 100$ km, the maximum possible altitude increase (assuming this occurs when the fragment is ejected in the direction of orbital motion) is 341.2 km ($h_a = 441.2$ km), while the same ΔV imparted to a fragment at $h_o = 1000$ km produces a maximum altitude increase of 415.6 km. Thus, the relative increase in spreading due to this phenomenon between $h_o = 100$ km and $h_o = 1000$ km is only ~75 km. The differences in net velocity might explain the slight slope changes among the $h_o = 500$-, 750-, and 1000-km cases in Figure 50; however, this effect is considered too small to cause the dramatic decrease in the curve slopes for breakup altitudes below $h_o = 500$ km. What these slope changes apparently indicate is that Equation 63 does not well represent debris cloud shapes extrapolated beyond the parameter space of the data it is based on in this case, breakups occurring at altitudes less than the 500-km minimum altitude as given by the second scenario in Table 8.

The function of Equation 63 is plotted in Figure 51 versus altitude for four clouds each of a different fragment diameter: $d = 0.01$-, 0.1-, 1.0, and 10.0-cm size particles. Each cloud consists of 1000 particles created in 1991 ($t_{eff} = 0$). The shape of the cloud follows the observed shapes seen in Figures 49 and 50. The curve shapes remain surprisingly constant for the smaller three size cases, varying only in magnitude. Apparently, the function is relatively insensitive for ΔV velocities exceeding ~500 m/s since the width and shape of the curves observed in Figure 51 does not appear to change. The $d = 10$-cm case does show an apparent narrowing due to the smaller imparted ΔV velocities ($\Delta V_p \approx 150$ m/s). Since clouds containing the same number of fragments are shown in Figure 51, the flux magnitude depends

on the dispersal characteristics of the fragments as defined by the imparted ΔV given the fragments. The 10-cm fragments are imparted with a characteristic velocity $\Delta V_p \approx 150$ km/s. Their relatively small ΔV velocities does not distribute the cloud fragments about h_o as widely as the characteristically faster, smaller-sized fragment clouds do; thus, the fragment orbits are more concentrated about h_o. These fragments spend more time in the vicinity of h_o increasing the flux magnitude. As the diameter of the fragments in a cloud is decreased, the imparted characteristic ΔV velocities increases dramatically (Figure 43). The clouds will become flatter with smaller flux magnitudes at all altitudes due to the ejecta fragments becoming more elliptical. The reason the curve slopes among the $d = 1.0, 0.1,$ and 0.01 cm clouds do not change in Figure 51 is not understood.

3.3 ORBITAL DECAY RELATED SINK MODELS

Objects added to the LEO environment through the source models (discussed in Subsections 3.1 and 3.2) do not remain there indefinitely. Objects are affected by a variety of perturbing forces that change their orbital elements; decreasing their net orbital velocity with time. Orbital perturbations include atmospheric drag which contracts both the semimajor axis describing the size of the orbit and the eccentricity describing the orbital shape. The semimajor axis and eccentricity both affect the perigee altitude during which the object experiences the greatest frictional drag force in its orbital course. The orbit loses a certain fraction of its energy during each revolution. The amount lost depends on the atmospheric density at the perigee altitude. Eventually, the orbit decays from the environment.

This section discusses the sink models incorporated into EVOLVE that affect natural orbital decay. Subsection 3.3.1 details the solar radio flux model used to parameterize atmospheric density fluctuations of the upper atmosphere due to solar cycle activity. The value obtained from this model for a given time partly determines the atmospheric density at an orbits' perigee altitude via an atmospheric density model described in Subsection 3.3.2. The atmospheric density at the perigee altitude is the quantity required by the orbital decay model (DECAY) given in Subsection 3.3.3 to determine the orbital element changes to the orbital semimajor axis and eccentricity. The latter is a simplified analytic orbital propagator designed to be reasonably accurate yet computationally efficient (Refs. 9 and 26). The models discussed in this section, together with the propagation algorithms given previously for intact objects (Subsection 3.1.3) and debris clouds (Subsection 3.2.4), provide the natural sink mechanisms for EVOLVE.

Removal of debris through certain operational policies such as deorbit in spacecraft at the end of useful life or collision avoidance can also be modeled in EVOLVE. These sinks were described briefly in the mission model database of Subsection 3.1.2. These active removal mechanisms and their influence on the EVOLVE orbital debris environment predictions are not studied in this report.

3.3.1. Solar Activity Model

3.3.1.1 Description. EVOLVE determines the 10.7-cm wavelength solar flux level at each time step (year) to be used as input into the atmospheric density model for orbital atmospheric drag effects on orbital lifetimes of LEO intact and cloud debris objects. The upper atmospheric temperature and, therefore upper atmospheric density, is directly related to the solar flux level(s). The S value is required to determine the exospheric temperature T_∞ (S) from which the density ρ (h, T_∞) can be calculated. EVOLVE uses a look-up table corresponding to each year between 1956 and 2010 to select this value (in units of 10^4 Janskeys, a Janskey being 10^{-26} W/m^2 - Hz of radiant flux). The S is considered constant throughout the year increment.

The look-up table consists of historically measured S values for the years 1956-1989. They are 12-mo yearly averages of the monthly Herzberg Institute of Astrophysics (Ottawa, Ontario, Canada) Series C observed 10.7 cm solar radio flux levels. The next 8 yrs (1990-1997) are 12-month yearly averages of the 97.5 ($\sim 2\sigma$) percentile best estimate predictions for the remainder of solar cycle 22 obtained by a linear regression fit of the smoothed 10.7-cm values from the previous cycles 1-21. The S values are predicted to be higher than the mean 50-percentile levels to account for an unusually high solar peak to occur during this 11-yr cycle (around 1992). For the projected years starting in 1998, the predicted yearly averages of solar cycle 23 (ending in 2008) are used. These are derived by extrapolations of linear regression fits to the smoothed 10.7-cm values obtained from solar cycles 1-21 (Ref. 27). For the years beyond 2008, solar cycle 23 is repeated indefinitely. Figure 52 shows the solar activity values used in the SOLACT module of EVOLVE along with the 2.5, 50.0, and 97.5 percentile projected values derived from the Marshall Space Flight Center (MSFC) fit data (Ref. 27). The MFSC 2.5 (-2σ), 50.0 (mean) and 97.5 (+2σ) percentile envelope values are compared to National Oceanographic and Atmospheric Administration Space Environment Services Center (NOAA/SESC) data between 1988 and 2008. The 2.5- and 97.5- percentile values represent the lower ($\sim 2\sigma$) and the upper ($\sim 2\sigma$) uncertainty bounds for the solar flux. The SESC data given in Figure 52 are yearly averaged predictions for the remainder of solar cycle 22 obtained from SESC Regression Model predictions of the 10.7-cm flux based on June 1991 observed solar flux and sunspot activity.[*]

3.3.1.2 Model Assessment. The solar flux activity represented by the current SOLACT look-up tables are based on well-established data for historical years and regression predictions based on these historical data for future years. The predicted data have much uncertainty due

---

[*] Private Communication, Sue Greer, National Oceanographic and Atmospheric Administration/Space Environment and Services Center, 1991.

to the inherent difficulty of predicting solar activity. Prediction methods generally rely on extrapolations of observed data as was done here by both the MSFC group and the SESC. This is currently the best method available. The MSFC and SESC predicted values agree remarkably well, as can be observed in Figure 52, lending credence to the selected EVOLVE values. It should be noted that the 1988 and 1989 observed values used by EVOLVE already exceed the 97.5- percentile flux level predictions. The present solar cycle promises to be one of the highest ever recorded.

3.3.2 Atmospheric Density Model

3.3.2.1 Description. The EVOLVE program contains an upper atmospheric density model to estimate the tenuous atmospheric density for the LEO regions above a 100-km altitude. The density is required as input to the succeeding atmospheric drag and orbital contraction model to be discussed in Subsection 3.3.3. The King-Hele drag/orbital contraction expressions (Ref. 26) in that model assume an exponential altitude dependence for density given by

$$\rho(T_\infty, h) = \rho_0(T_\infty, h_0)e^{-\left(\frac{h - h_0}{H}\right)} \qquad (74)$$

where ρ_0 (T_∞, h) is the density calculated at a reference altitude h_0. For the King-Hele expressions in the drag/orbital propagation model, is determined at the perigee altitude $h_0 = h_p$. The scale height constant H is then determined as

$$H = \frac{h - h_0}{\ln\left(\dfrac{\rho}{\rho_0}\right)} \qquad (75)$$

The value of this constant is then used to scale the exponential function used to characterize the atmospheric density in the King-Hele expressions. In EVOLVE, the purpose of the model is to calculate the density (ρ_0). In addition, this model is used to obtain the atmospheric density at the breakup altitude for debris cloud propagation explained in Subsection 3.2.4.

The upper atmospheric density model used in EVOLVE is based on a simplified 1971 Jacchia-Lineberry (J/L) upper atmospheric density model (Ref. 10). As explained in References 9 and 10, the full Jacchia 71 model includes many short-term effects that influence the exospheric temperature T_∞. These effects are as follows:

- Daily variations in solar flux S and the geomagnetic index a_p
- Diurnal bulge producing an atmospheric shape asymmetry
- Semiannual asymmetry effect due to sun-earth orbital distance variations
- Seasonal-latitudinal asymmetry effect due to earth's tilt toward sun

Most of these variations are neglected since the EVOLVE model concern is with long-term effects, on the order of years, and these effects average out. The factor, T_∞, affects the
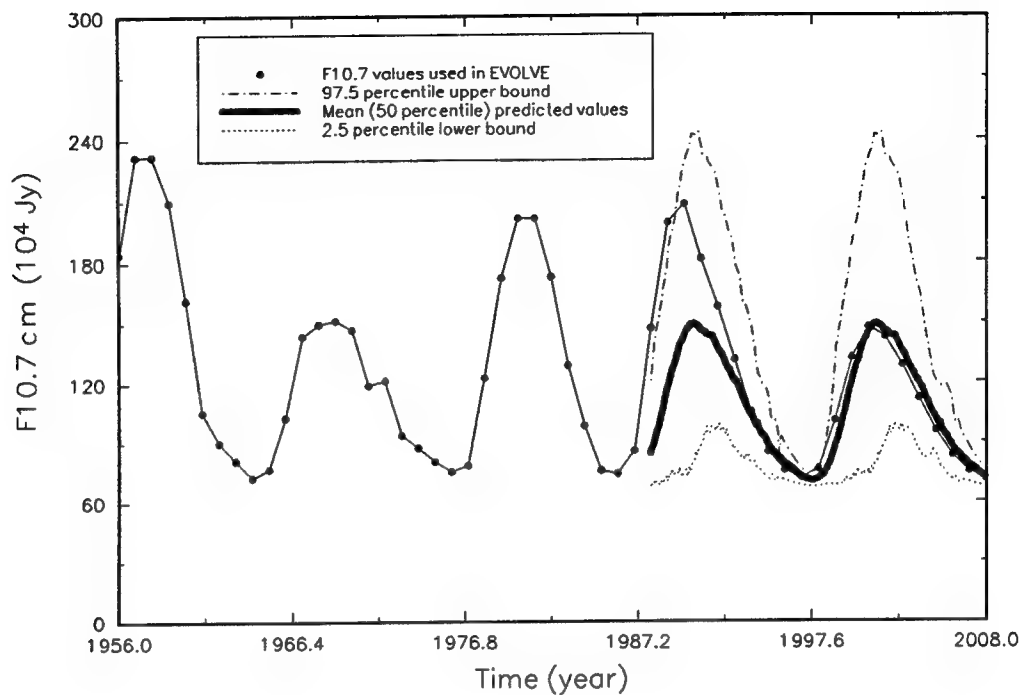
Figure 52.   The F10.7-cm solar ratio flux values used in the EVOLVE solar activity look-up table SOLACT.

density via the solution to complex diffusion equilibrium equations for the various atmospheric constituents. These solutions are modeled by empirical formulae over the valid altitude range 90-2500 km. The Jacchia 71 model tabularizes the numerical integration results of the diffusion equations for each atmospheric constituent. This poses a prohibitive computer storage and computation time requirement. To simplify the Jacchia approach, Lineberry (Ref. 10) made the assumption that the log of the density may be expressed as a truncated Laurent polynomial series in T_∞ and altitude. The coefficients to the series were obtained by fitting the Jacchia tabular results to the Laurent series within layered altitude bands characteristic of the Jacchia model. Lineberry has also simplified the expression for T_∞ so that it is now dependent only on the solar flux S and geomagnetic index a_p. Together, these Lineberry modifications have resulted in a reported fivefold decrease in computation time, yet have retained the model accuracy. The semiannual and seasonal latitudinal effects have been removed. (The semiannual effects are related to the changes in the sun-earth distance and the seasonal-latitudinal effects are related to the seasonal effects of the sun-earth axial orientation.) This model, termed the J/L model, is the atmospheric model incorporated in EVOLVE.

91

The J/L model fits the Jacchia $\rho(T_\infty, h)$ tabular data by using the following truncated Laurent series interpolation function:

$$f(x) = a_1 + a_2 x + \frac{a_3}{x} \tag{76}$$

The density is computed as follows:

$$\rho(T_\infty, h) = 10^3 \, e^\delta \tag{77}$$

where

$$\delta = b_1 + b_2 \bar{h} + \frac{b_3}{\bar{h}}$$

$$\bar{h} = a_1 + a_2 h + \frac{a_3}{h}$$

$$a_i = c_{1j} + c_{2j} T_\infty + \frac{c_{3j}}{T_\infty}$$

Here, δ is the mean vertical profile of ρ, h is a base altitude, h is the geodetic altitude, and b_i, c_{ij} are constants determined from the fit to the Jacchia tables. Hydrogen contribution effects which increases the ρ at high altitudes has been included in this model. This effect becomes significant at altitudes above 500 km. Finally, the exospheric temperature T_∞ used in the model depends only on the solar flux value S as given by the fit relation

$$T_\infty(S) = (432.79 + 3.7516 \, S) + a_p + 100.0(1 - e^{-0.08 a_p}) \tag{78}$$

where the geomagnetic index is itself assumed to be a linear relation of S:

$$a_p(S) = 0.05 \, S + 2.25 \tag{79}$$

3.3.2.2 Model Assessment. The J/L model is a derivative of the well-established Jacchia 71 model, which is considered valid over a wide range of altitudes (90-2500 km). Since ρ is required only for perigee height altitudes in the drag model (Subsection 3.3.3), this model presents no limitations in EVOLVE. (Orbits whose $h_p > 2000$ km are excluded from processing as will be explained in the atmospheric drag model discussion.) The Jacchia 71 model has a reported error of ≤ 10 percent when compared to observed neutral atmospheric density data (Ref. 10). This is reasonably good agreement considering the large uncertainties inherent in modeling such a complex and dynamic phenomenon as the upper atmospheric density. Reference 10 also documented an excellent agreement of ≤ 5 percent between the J/L and full Jacchia models when numerical

comparisons of density results were performed. The modified J/L described here, however, could expect to produce larger errors since the semiannual and seasonal-latitudinal expressions were eliminated. Although both expressions could be easily incorporated into the EVOLVE J/L model, their exclusion is reasonable since the long propagation intervals and lifetimes associated with processing will tend to average out their effects. Exclusion of the daily variations in S and a_p is very reasonable since their effects on ρ are short term and are readily averaged out. The diurnal bulge will also tend to average out over yearly time spans for most LEOs. For some orbits (such as sun-synchronous orbits), however, the diurnal bulge could be significant since the bulge would not change in orientation relative to the orbit with time.

3.3.3 Atmospheric Drag/Orbital Contraction Model

3.3.3.1 Description. Atmospheric drag is by far the most important sink of satellites and debris from the LEO environment. Drag acts to lessen the orbital velocity of an orbit, reducing its semimajor axis in time, and circularizing its shape. Eventually the perigee altitude descends low enough into the denser atmosphere that drag is able to reduce (within one orbital period) the satellite's velocity below orbital velocity and the object falls to earth (or burns up in the atmosphere). At this point the object orbit has decayed and is no longer considered a part of the LEO environment. Besides the atmospheric drag force, other orbital perturbations also act to affect the decayed LEO objects from orbit, but they are secondary in nature. These effects include the three-body-earth/moon/sun gravity perturbations and the geogravitational perturbations (earth oblateness). They generally act to alter orbital orientation, placing the orbit within a denser portion of the atmosphere, whereby drag forces can be more influential. In some cases, these perturbations cause periodic changes in orbit orientation, but over long periods of time their effects average out.

EVOLVE incorporates a model which describes satellite orbit and decay through upper atmospheric drag and orbital perturbations (Ref. 9). Originally designed for collision probability analysis of LEO satellites, where many orbital interactions are averaged over long periods of time, this model estimates the decay process in a global or average manner. The model needs to be fast-running, which rules out any form of numerical integration of orbits in favor of an analytic algorithm. For this reason, the model utilizes previously developed analytic expressions (Ref. 26). The result is a highly efficient model capable of producing the semimajor axis and eccentricity time histories of a wide spectrum of LEO satellite orbits. This subsection shall highlight the salient points in the model and define its limits of validity.

The model is in a self-contained software package of subroutines called DECAY. This package interfaces to the EVOLVE model through a subroutine call. EVOLVE directly invokes these routines to propagate the deterministically introduced intact objects. The FRGMNT code pre-processing of debris cloud fragment orbits, discussed in Subsection 3.2.4, utilizes the same DECAY model to propagate the individual fragment orbits. Thus, the DECAY model results are implicit in the debris cloud phenomenological function time histories.

The DECAY model consists of two distinct submodels whose application depends on the type of orbit being propagated. The first submodel is the atmospheric drag and orbital contraction model for a spherically symmetric density atmosphere with a constant scale height parameter H (Refs. 9 and 26). This model is closely coupled with the atmospheric density model described in Subsection 3.3.2. The second model is the sun/moon/orbital perturbation algorithm. These models are discussed separately at the level of detail necessary to bring forth the essential points.

This DECAY model is perhaps the most numerically complicated and computationally intensive portion of the EVOLVE model. The model is described as a simple but reasonable model intended to characterize satellite decay in some global (average) manner (Ref. 9). It is valid for objects having perigee altitudes of 90 km $\leq h_p \leq$ 2000 km and apogee altitudes of 125 km $\leq h_a \leq$ 40000 km. (The EVOLVE model places further restrictions on the valid ranges to prevent potential numerical processing errors, as discussed in Appendix A.) The parameters listed below are the required input and output parameters:

- Orbital elements describing the orbit

    - Initial perigee altitude h_{po} (updated)
    - Initial apogee altitude h_{ao} (updated)
    - Inclination i
    - Initial argument of perigee ω_o (updated Type 3 orbits only)
    - Initial nodal right ascension Ω_o (updated Type 3 orbits only)

- Initial right ascension of sun λ
- Ballistic coefficient $B = C_D(A/m)$
- Exospheric temperature T_∞
- Propagation interval Δt
- Flag for type of orbit processed

The model distinguishes between three types of orbits according to apogee altitude h_a and orbital lifetime τ_L (which is estimated in DECAY by an approximate analytical function; the true lifetime is obtained by orbital propagation):

- **Type 1**: $h_a \leq$ 14000 km

Orbits affected only by atmospheric drag. They follow the atmospheric decay expressions derived by King-Hele. These orbits are characterized by low apogees where the sun/moon gravitational perturbations are too small to be of any significant effect. Therefore, these perturbations are neglected. Geopotential perturbations (J_2 and higher terms) are neglected because they do not affect the value of the average orbital lifetime that the model seeks to calculate.

The King-Hele derivations are complicated analytic functions calculating the perigee altitude (h_p) and eccentricity (e) time histories (, respectively). They use the initial atmospheric density ρ_p at the h_p of the averaged (osculating) orbit.

Type 1 orbits fall within four subclasses according to eccentricity of the initial orbit and the degree of variation of atmospheric density ρ with altitude via the quantity ae/H:

Normal e (e ≤ 0.2), phase 1, (ae/H) ≥ 3 :
These orbits are generally younger, slightly eccentric orbits (e ≤ 0.02) which have not yet entered phase 2 (see next item below) in their orbital evolution. For reference, these orbits follow Equations 4.44, 4.47, and 4.48 in Reference 26.

Normal e (e ≤ 0.2), phase 2, (ae/H) ≤ 3:
These orbits are those whose eccentricity 0.0 < e < 0.02 is nearly circular but not identically circular. They are generally older orbits in the last stages of circularization. For reference, these orbits follow Equations 4.74, 4.77, 4.80 in Reference 26.

Circular orbits (e = 0):
This case is treated as a separate case to avoid singularities in the normal e expressions above. For reference, these orbits follow Equations 4.84 and 4.88 in Reference 26.

High e (0.2 < e < 0.9):
For reference, these high eccentricity orbits follow the Equations. 4.125, 4.129, and 4.130 in Reference 26. Although DECAY is equipped to process this type orbit, EVOLVE currently does not allow these routines to be exercised because of a software condition to force all orbits with e > 0.2 to be Type 3 orbits:

- **Type 2:** 14000 km < h_a ≤ 40000 km, orbit lifetime τ_L ≥ 4 years

High perigee altitude orbits strongly affected by sun/moon perturbations with lifetimes ≥ 4 yrs. Due to the somewhat periodic variations of perigee with time that these perturbations produce, the decay routines analytically compute the effective perigee altitude density, . The average is simply the time averaged density using the time-dependent semimajor axis, a(t), and eccentricity variations, e(t):

$$\bar{\rho}_p = \frac{1}{\Delta T} \int_0^{\Delta T} \rho(a(t)[1 - e(t)]) \, dt \tag{80}$$

where ΔT is the propagation interval. This value is then used as the density input to the King-Hele expressions.

95

The use of the average density $\bar{\rho}_p$ is required because small changes in h_p induced by the sun/moon perturbations can cause large changes in $\bar{\rho}_p$ due to the exponential nature of the variation in atmospheric density. As discussed in Reference 9, orbits at certain inclinations reach a resonance condition whereby the perigee altitude is either suddenly raised or lowered by a large amount. If h_p is raised, the effects of drag will be lessened and the lifetime may be greatly increased. When these conditions occur, the decay histories become unreliable. The sun/moon affects are coupled with the King-Hele drag equations via $\bar{\rho}_p$ to update e and a.

- **Type 3:** 14000 km $< h_a \leq$ 40000 km, orbit lifetime $\tau_L <$ 4 yrs

High perigee altitude orbits strongly affected by sun/moon perturbations with lifetimes shorter than 4 yrs. Only high eccentricity orbits (e > 0.2) fall in this category. The decay routines treat these orbits semianalytically using a combination of the King-Hele expressions and sun/moon eccentricity variation expressions.

In this case, the lifetime τ_L is too short to allow to be averaged in the same manner as the Type 2 orbit. Therefore, another technique is applied in which the drag equations and sun/moon perturbations are only slightly coupled. This is done by modifying the King-Hele expressions to allow a time-dependent linear variation to h_p and, therefore, the density at perigee over short 60-day time steps. The linear change in h_p is assumed to account for the sun/moon perturbations to e. The perigee altitude changes according to

$$h_p = h_{po} + \dot{q}t \tag{81}$$

and corresponding change in density is

$$\rho_p = \rho_{po} \, e^{-\left(\frac{\dot{q}t}{H}\right)} \tag{82}$$

The linear rate is approximated by the relation

$$\dot{q} = \frac{a_o \left[e(t + \Delta t) - e(t)\right]}{\Delta t} \tag{83}$$

where Δt is the time step (60 days), a_o is the initial semimajor axis and e(t) is the time varying eccentricity. The ρ_p evaluated in this way is input in the King-Hele expressions.

The King-Hele expressions require a value for the ballistic coefficient $(B = C_D(A/m))$ and the exospheric temperature T_∞. Both are assumed constant over the Δt time interval in

which to propagate the orbit. This has important implications for the selection of both values as described in Subsection 3.3.3.3.

3.3.3.2 Model Assessment. The DECAY model, developed for statistical collision probability analyses applications, is sufficiently accurate for the purposes of the EVOLVE model. The long-term modeling goal of EVOLVE has requirements similar to the design goals for which the DECAY routines were developed. The model was designed to be reasonably accurate, averaging out or neglecting many short-term effects not important to long-term processes. It is meant to be fast-running and efficient to allow processing of many environments. The model, which incorporates the King-Hele equations coupled with the simplified sun/moon perturbation expressions, have been compared to the much more sophisticated and well-validated orbital propagators ASOP and DSTROB used at NASA/JSC (Ref. 9). Being full-scale mainframe programs, these propagation codes can include the short-term effects which are neglected in the fast running subroutine DECAY. ASOP and DSTROB are equipped with sophisticated algorithms to estimate orbital drag perturbations and atmospheric density far beyond what is possible in a fast running algorithm such as DECAY. Despite the simplification necessary in DECAY, most of the deviations from ASOP and DSTROB lifetime calculations were <25 percent, with errors up to 50 percent for short-lived orbits. Reference 9 found the greatest errors between DECAY and the full-scale model lifetimes resulted from neglecting the J_2 earth oblateness effect on eccentricity, which affects the observed density at the perigee altitude. The constant atmospheric scale assumption and simplified density model (Subsection 3.3.2) assumptions had a lesser effect on the LEOs. The simplifications of the sun/moon perturbation also had a smaller effect on lifetime estimation than did the J_2 effect. DECAY was found to be less accurate for shorter lifetimes where the perturbation effects which were neglected would be important (since they cannot be averaged out over the short term). Since EVOLVE is a long-term model, the errors with short-term events are not disturbing.

The general consensus is that the 25 percent overall accuracy obtained using DECAY (Ref. 9) is acceptable in light of the long-term modeling goal of EVOLVE. Furthermore, the neglected periodic perturbation effects, the simplified atmospheric density model, and the assumptions associated with the King-Hele analytic expressions are reasonable in the context of EVOLVE.

The main advantage of the DECAY model is its computational speed and efficiency. Being an analytical model, the orbits do not need to be integrated numerically, thus, saving much computational expense. This is especially important when a large number of intact object orbits are involved as in a compounded traffic model or a large number of statistical Monte Carlo environment runs are made.

The DECAY model will handle most orbits presented to it from the input lists in EVOLVE. The DECAY model together with the limitations placed on it in the EVOLVE intact object propagation algorithm discussed in Subsection 3.1.3 limits the type of orbits that can be modeled in EVOLVE. The severest limitation is excluding orbits having $h_p > 2000$ km. The

midaltitude and geosynchronous orbits fall in this category. Objects having $h_p > 2000$ km tend to have long-lived orbits since atmospheric drag is virtually nonexistent at these altitudes. Furthermore, the assumption that h_p is more strongly influenced by the geopotential J_2 term than by third body forces becomes invalid. The Type 1 orbit process would require modification for $h_p > 2000$ km to subject the orbit to the third body gravitational perturbations. The upper limit for h_a at 40000 km poses no real limitations for the EVOLVE model, since there are few objects that occupy both the LEO environment and the deep space regions beyond this limit. Midaltitude or geosynchronous altitude orbit modeling are different problems, which go beyond the intended scope of the EVOLVE model; therefore, their exclusion is not critical.

3.3.3.3 Sensitivity/Uncertainty Analysis. Since the DECAY package propagates orbits and determines the orbital lifetimes of the objects within the LEO environment and, therefore, is essential to the overall spatial density results calculated by EVOLVE, it is instructive to characterize the DECAY lifetime results. First, the sensitivity to different types of orbits and conditions is examined. Next, the uncertainty due to both the ballistic coefficient B and exospheric temperature T_∞ (which is itself a polynomial function of the solar activity S) was estimated to ascertain the uncertainty in the overall flux results attributable to them.

The DECAY results are sensitive to the type orbit being propagated. Orbital orientation determines which orbit type (Subsection 3.3.3.1) is being propagated and, consequently, which portions of the DECAY model are being exercised. Results are calculated using the lifetime analysis code TDECAY which was written to simulate the same intact object orbital debris propagation model encoded in the EVOLVE subroutine ORBUPD (Subsection 3.1.3). Table 9 lists the orbital conditions for 10 test orbits input to TDECAY. They correspond to the same test orbits described in Reference 9 to compare DECAY results to the propagation models DSTROB and ASOP. They are categorized by the four types of orbits listed in Table 9. Three are LEOs of varying h_a and eccentricity e. These orbits fall within Type 1 orbits discussed in Subsection 3.3.3.1. The GTO fall within the Type 2 or 3 orbit category. Results are listed in Table 10 for the DECAY results obtained from Reference 9 as well as two TDECAY cases; one that updates the argument of perigee (ω), nodal right ascension (Ω), and solar right ascension (λ), and one that does not. The latter two cases are meant to compare the effect of updating the ω, Ω, and λ in time as is done in EVOLVE and not updating these values as was done in Reference 9. In all cases the Δt propagations were matched to the reported data.

Table 9. Test orbits for lifetime calculations.

Orbit Type	Case	h_a (km)	h_p (km)	i (deg)	ω (deg)	Ω (deg)	B (m2/kg)	T_∞ (K)	λ (deg)
LEO medium h_a	1	400	150	30	0	0	0.002	1085	0
	2	400	150	0	0	0	0.002	1085	0
LEO high h_a	3	1000	150	30	0	0	0.002	1085	0
	4	1000	150	0	0	0	0.002	1085	0
LEO circular	5	400	400	0	0	0	0.002	1085	0
GTO	6	35799	185	28.6	0	135	0.0162	1048	280
	7	35799	185	28.6	0	180	0.0162	1048	280
	8	35799	185	28.6	0	90	0.0162	1048	280
	9	35799	185	40	0	135	0.0162	1048	280
	10	35799	185	50	0	135	0.0162	1048	280

Table 10. Lifetime calculations for orbits in Table 9.

Case	Δt (days)	Ref. 9 ASOP or DSTROB	Ref. 9 DECAY	Lifetime (Days) TDECAY (1) w/o updating ω, Ω, λ	Lifetime (Days) TDECAY (2) with update of ϖ, Ω, λ
1	2	19.6	24.9	27.8	27.8
2	2	20.5	22.5	24.9	24.9
3	20	106.3	155.1	155.2	155.2
4	20	123.0	139.0	139.2	139.2
5	200	1975.0	1601.0	1209.6	1209.6
6	120	1200.0	1002.0	1002.5	1422.5
7	20	109.0	102.5	102.6	927.3
8	365	>7300.0	>7300.0	5584.5	3735.8
9	120	1080.0	958.0	958.9	261.5
10	120	710.0	787.0	787.5	567.4

Cases 1 and 2 orbits are designed to test the normal, phase 1 orbits of the King-Hele decay expressions. They are LEOs whose h_p descends deep into a region where atmospheric drag effects are important. The orbits decay quickly (within a month), even those with a relatively small ballistic coefficient (B = 0.002 m^2/kg). The inclination difference between Case 1 and 2 is intended to examine the effect the earth's oblateness on both the J_2 effect and atmospheric density by comparing the rigorous model ASOP to DECAY. A significant difference is apparent with the comparison results being 30 percent different. This implies that neglecting earth oblateness effects is important to the lifetime estimation for this type orbit. Large errors for such short lifetimes are not important in the context of the long-term (1 yr or more) modeling of EVOLVE. The lifetimes are too short compared to the yearly time step nominally used in EVOLVE. In principle, there should be no difference between the DECAY value obtained in Reference 9 and TDECAY. There is ~10-percent difference between DECAY and TDECAY observed for the Case 1 orbit. Part of this error may be accounted for by numerical processing differences between the computers in which they were run. The rest of this error cannot be accounted for without further investigation.

The TDECAY(1) and TDECAY(2) results are identical for all Type 1 orbits since the Mueller DECAY routines do not use ω, Ω, and λ for these type orbits.

Cases 3 and 4 orbits represent normal, phase 2, Type 1 orbits. As with the Cases 1 and 2 orbits the large difference to the numerical code ASOP is attributed to neglected J_2 effects and the non-symmetrically shaped atmosphere. When inclination i = 0 deg as in the Case 4 orbit the oblateness effect is eliminated and the results agree more closely. The differences between the reported DECAY results and that calculated by TDECAY are minimal machine-dependent differences.

Case 5 shows the results for LEO circular orbits having long lifetimes. The error compared to ASOP results is primarily caused by density model differences, neglect of the J_2 perturbations in DECAY, and assumed constant scale height. A large unexplainable error (~30 percent difference) occurs between the DECAY values of Reference 9 and that calculated by TDECAY. Nothing could be found to explain this result and further investigation is merited.

Cases 6 to 10 represent different orbital plane orientations of the same GTO. They test the high eccentricity King-Hele expressions coupled with sun/moon perturbations to the perigee altitude processed for Type 2 and 3 orbits. EVOLVE processes only Type 3 orbits and TDECAY processes the orbit as Type 3 if e > 0.2. Since e = 0.69 for these orbits, all are classified as Type 3. The sun/moon perturbations cause variations in eccentricity which, in turn, causes fluctuations in the perigee altitude h_p. Small changes in this altitude can lead to large changes in the lifetime. This phenemenon is caused by large variations in the atmospheric density as h_p changes location within the exponentially-varying density characteristic of the upper atmosphere. These h_p fluctuations are somewhat periodic in nature due to the periodic relative motion of the sun and moon which are assumed to move in the

earth's ecliptic plane. High-order effects not modeled include sun/moon orbit eccentricities, the moon's apsidal line (argument of perigee) secular motion, the moon's secular nodal regression (right ascension) on the ecliptic plane, and the 5.1-deg inclination of the moon's orbital plane with respect to the ecliptic.

Cases 6 to 8 vary the right ascension of the ascending node to orientate the orbit plane relative to the sun and moon. Dramatic effects are observed in the lifetime between the three cases examined. The short lifetime is a result of a resonance condition that occurs at certain inclinations characteristic of the sun/moon perturbations. The result can either cause a rapid increase or decrease in the h_p value. If h_p is decreased, then h_p can be situated deep in the upper atmosphere where drag quickly decays the orbit. Case 8, which differs from Case 7 only by $\Omega = 90$ deg, forces a much higher average h_p over time, causing the orbit to be much longer lived. Cases 9 and 10 are similar to Case 7 except for a change in inclination. The sun/moon perturbations are sensitive to resonant conditions occurring at different inclinations and the effect is observed in the comparisons between Cases 7, 9, and 10. The lifetimes for Case 9 and 10 are significantly longer than that of Case 7 where a resonance appears that forces the h_p quickly below the 100-km upper atmosphere limit. The agreement is good between the Reference 9 DECAY values and those obtained from TDECAY (except for the long lifetime of Case 8 where TDECAY calculates an approximate 24-percent difference, again unexplainable). The TDECAY(2) differs from the other estimated lifetimes because of the ω, Ω, and λ parameter updates at each time step. With the orbital plane orientation continually changing from the apsidal and nodal regression effects, the sun/moon perturbation effects will change with each new orbital orientation. The actual effects are almost impossible to systematically predict. The regression effects are noticeable in the lifetime values shown in Table 10.

The TDECAY package was used to test the sensitivity of calculated orbital lifetimes derived from the Mueller DECAY routines as functions of the solar activity S, ballistic coefficient $B = C_D(A/m)$, and the orbital propagation interval Δt. This study was performed using the same 10 orbit cases described in Table 10. In all calculations, the ω, Ω, and λ values were held fixed at their initial values.

Figure 53 shows the lifetime (in days) versus the F10.7-cm solar flux (in units of 10^4 Janskeys). A constant $B = 0.05$ m^2/kg and $\Delta t = 1$ yr was assumed in the calculations. The solar flux value is varied over 10 selected values ranging over $70 \leq S \leq 260$. The lifetimes were calculated using a constant S value throughout the lifetime calculations. The ballistic coefficient was held fixed at $B = 0.05$ m^2/kg and the propagation interval was held fixed at $\Delta t = 1$ yr. The standard low eccentricity ($e < 0.2$) LEO satellites exhibited an expected decrease in the lifetime with increasing solar flux as shown in the Case 1 orbits. Cases 1 to 4 orbits had a low $h_p = 150$ km to begin with; this is well within the LEO region where drag is appreciable. The elliptical orbit circularizes quickly (i.e.,), and once this happens τ_L is insensitive to S. The observed slight decrease in τ_L with increasing S for Cases 1 to 4 is primarily the effect of S on circularizing the orbit. The Case 5 circular orbit is at an altitude where S significantly affects τ_L by almost an order of magnitude over the S range. The

101

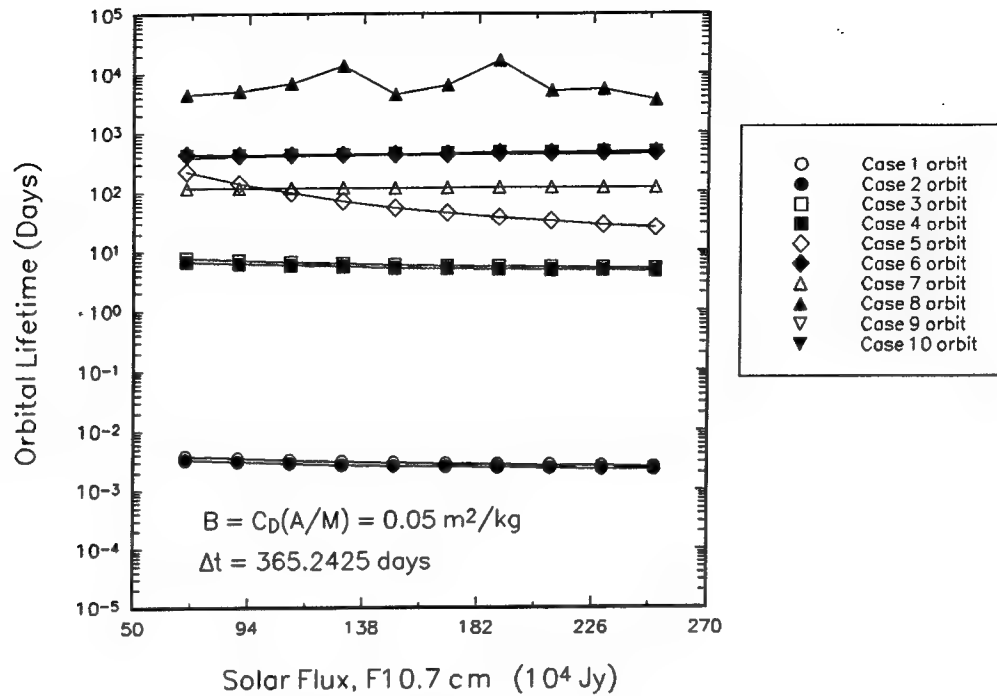Figure 53. Program TDECAY results of lifetime versus solar flux for the 10 orbit cases described in Table 9.

lifetime decreases from ~120 to ~13 days. The GTOs described by Cases 6-10 orbits show surprising results. The curves all show a slight increase in τ_L with an increase in S. Furthermore, they are all relatively insensitive to S over the range of S examined. This is possible since the sun/moon perturbations, which can increase the h_p altitude over time, interacts with the drag perturbation in such a way as to increase the h_p for larger S values. This effect is consistent for all five observed GTOs.

The ballistic coefficient effects on τ_L for the 10 orbit cases are shown in Figure 54. The EVOLVE solar activity values were assumed for one year intervals ($\Delta t = 1$ yr). The EVOLVE variable solar activity table was assumed and a propagation interval of $\Delta t = 1$ yr was used. The first five LEO cases, which only use the King-Hele orbital contraction expressions, are well behaved linear inverse dependences in logarithmic space with the lifetime decreasing for increasing B (implying a power law dependence of τ_L or B). As shown by the steep slopes of these curves, the lifetime is quite sensitive to B for LEO circular or low eccentricity orbits. The high eccentricity, high h_a orbits (Cases 6-10) exhibit unpredictable behavior for $B < 0.1$ m²/kg with some τ_L values increasing, some decreasing, and some remaining relatively constant. Above $B = 0.1$ m²/kg all five cases steadily converge to the same linear curve having the same slope as those calculated for Cases 1-5. This shows that for some very large values of B the drag perturbations at the perigee altitude are large enough to quickly lower the h_a value below the 14000-km limit, below which the King-Hele drag expressions are only used to estimate τ_L. The results shown in Figure 54 are consistent with expected
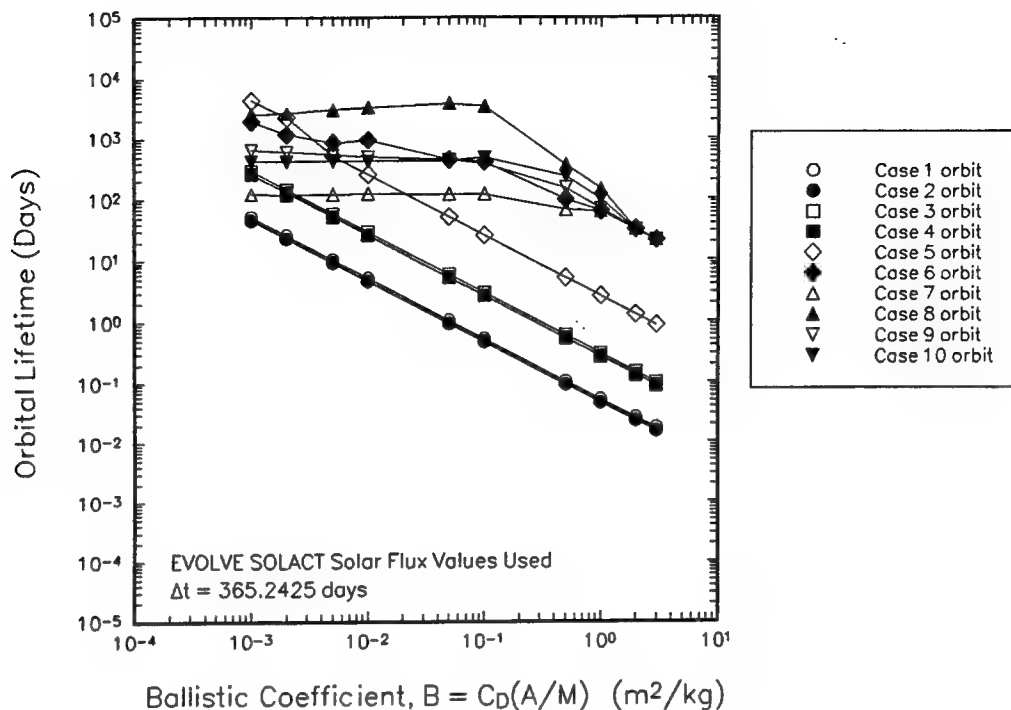
102

Figure 54. Program TDECAY results showing orbital lifetime versus ballistic coefficient B for 10 orbit types given in Table 9.

behavior using DECAY.

During this study, a dependence on the propagation interval Δt was noticed in some τ_L calculations. The Δt is one input to the Mueller DECAY routines and this parameter was varied over a range of user-selected Δt values to generate the curves shown in Figure 55. In principle, propagating an orbit using the drag-only perturbation expressions of King-Hele over a single 20-day step should yield the same results as two sequential 10-day steps. Figure 55 shows that the Cases 1 to 5 King-Hele only orbits are relatively insensitive to Δt. Not until Δt reaches approximately 100 or more days does a slight increase in τ_L become apparent. The GTOs are insensitive to Δt until $\Delta t \sim 10$ days whenever a significant increase or decrease (depending on orbit) takes place in the calculated lifetime τ_L. This effect seems to peak around $\Delta t = 100$ days. The specific cause of the effect is not known but is probably a numerical phenomenon in the sun/moon perturbation calculations occurring when the orbit is propagated at larger time steps. Although a numerical problem of unknown origin in the sun/moon perturbation algorithms is the most likely cause, the effect may be partly attributable to the sensitivity of these calculations to the initial orbital orientation (as was indicated by the resonance conditions of the GTOs in Table 10). The large time interval mayplace the orbital orientation into a slightly different orientation than when shorter time intervals are used. Although the exact cause of this effect is poorly understood, the effect is still there and a user of the DECAY routines should be aware of its implications.

103
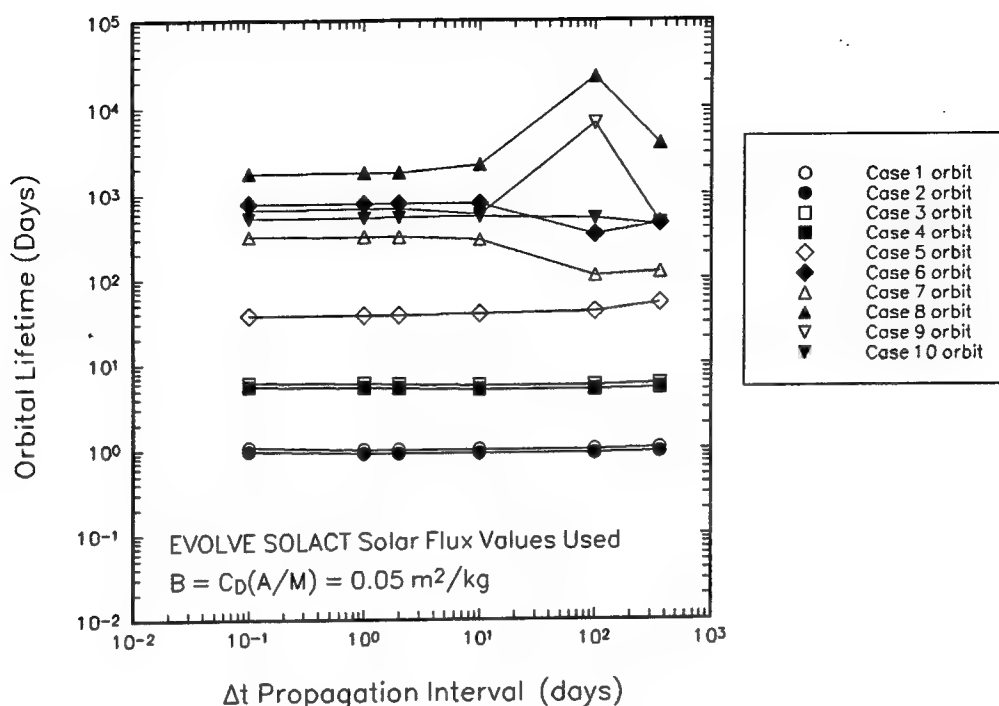
Figure 55. Program TDECAY results showing orbital lifetime versus input propagation interval Δt for the 10 orbit types given in Table 9.

To examine the orbital lifetimes and nature of the intact objects being deployed from the actual EVOLVE input lists, a program (TAOM) was written to read the lists and subject each object to the DECAY routines in yearly time steps (as is done in EVOLVE). The launch date was held fixed at the beginning of the launch year for all objects. The EVOLVE solar activity look-up table was used to determine S required for the exosphere temperature T_∞ calculation. The T_∞ is input directly into DECAY.

The ballistic coefficient required by the DECAY package was determined in the same manner used in EVOLVE. The values of cross-sectional area A and mass m are obtained from the input files with an assumed coefficient of drag $C_D = 2.2$. In this program, as in EVOLVE, if A/m > 100 m²/kg then the A/m ratio is multiplied by 1.5. This factor helps to account for the effect that appendages such as antennae, solar panels, and thrust nozzles will have on A/m for the largest objects (which will generally be satellite payloads or boosters). The minimum value of A/m is 0.005 so that if A/m < 0.005 m²/kg then A/m is set to 0.005 m²/kg. This corresponds to a minimum $B_{min} = 0.011$ m²/kg. The launched object was then propagated in time until it decayed, whereupon the lifetime was recorded.

For each historical input file (years 1957-1989) the percentage of objects falling within the time ranges shown in Table 11 was calculated. For each input list, approximately half the objects would decay within 1 yr. Only 10-15 percent of the objects launched each year

104

Table 11. Analyses of intact object lifetimes from EVOLVE DBS files.

Percent of objects exhibiting lifetime range (years)

Year	Mean A/m (m²/kg)	σ_A/m (m²/kg)	Mean B (m²/kg)	σ_B (m²/kg)	0-1	1-5	5-10	10-50	50-100	100-200	200-500	500-1000	1000-5000	>5000	SKIPPED
1957	0.01349	0.00737	0.02969	0.01820	100.0	0.00	0.00	0.00	0.00	0.00	0.00	0.00	0.00	0.00	0.00
1958	0.04123	0.06946	0.09071	0.15281	55.56	0.00	11.11	0.00	0.00	11.11	0.00	0.00	11.11	11.11	0.00
1959	0.04368	0.09273	0.09611	0.20401	42.86	7.14	0.00	21.43	7.14	0.00	14.29	0.00	0.00	0.00	7.14
1960	0.30371	1.52536	0.66817	3.35579	43.24	5.41	13.51	13.51	5.41	8.11	0.00	2.70	2.70	5.41	0.00
1961	0.07858	1.15379	0.17288	2.53834	65.71	2.86	2.86	5.71	5.71	0.00	2.86	5.71	2.86	0.00	5.71
1962	0.04326	0.85231	0.09517	1.87509	65.63	2.34	5.47	8.59	1.56	2.34	1.56	0.78	3.13	3.13	5.47
1963	0.05695	0.89935	0.12528	1.97967	58.87	6.45	4.03	7.26	0.81	3.23	2.42	0.81	0.81	5.65	9.68
1964	0.09346	0.90815	0.20562	1.99794	63.83	8.51	1.06	4.79	0.53	3.19	6.38	3.72	3.72	2.13	2.13
1965	0.04854	0.72240	0.10679	1.58929	55.48	8.64	1.66	9.30	2.66	1.33	3.65	2.33	3.65	8.64	2.66
1966	0.07937	0.96545	0.17461	2.12399	65.34	5.05	1.08	7.94	2.89	1.08	2.89	2.53	2.53	2.17	6.50
1967	0.04047	0.93076	0.08903	2.04768	60.91	5.86	1.63	8.14	2.61	2.61	2.28	2.93	0.98	3.26	8.79
1968	0.03596	0.97607	0.07911	2.14735	64.96	6.20	1.09	7.30	1.46	2.19	1.46	3.28	1.46	4.38	6.20
1969	0.02573	1.04235	0.05662	2.29318	65.84	4.94	1.23	7.41	2.47	0.82	2.47	2.47	2.47	2.88	7.00
1970	0.03667	0.96040	0.08067	2.11289	57.20	7.38	4.43	11.44	2.95	2.21	1.85	2.58	2.21	6.64	1.11
1971	0.07034	0.91947	0.15474	2.02283	54.04	4.35	9.01	10.25	2.17	2.48	2.48	2.48	3.42	8.39	0.93
1972	0.04649	0.96386	0.10229	2.12049	56.27	5.42	6.44	9.49	1.69	2.37	2.37	2.71	3.39	8.81	1.02
1973	0.04224	0.95327	0.09293	2.09718	62.75	7.19	4.25	5.56	1.63	0.98	1.63	1.96	1.63	10.46	1.96
1974	0.04977	0.96460	0.10950	2.12211	57.65	12.05	4.89	2.28	0.65	2.61	2.61	2.93	1.63	8.79	3.58
1975	0.04582	0.88977	0.10081	1.95749	52.46	16.94	3.83	1.91	0.82	2.19	3.28	3.01	1.95	8.47	4.37
1976	0.04838	0.87259	0.10644	1.91969	50.39	19.64	1.81	3.36	0.78	2.07	2.58	3.36	2.73	8.53	4.91
1977	0.05228	0.90122	0.11503	1.98268	52.63	20.78	1.11	4.71	0.55	1.11	1.94	4.71	2.58	6.37	3.32
1978	0.04300	0.91917	0.09459	2.02218	49.86	12.46	0.85	8.22	1.98	0.57	3.40	3.68	2.77	11.61	4.25
1979	0.04439	1.01395	0.09765	2.23069	60.13	9.30	1.00	7.64	1.66	0.00	2.33	2.66	3.12	6.31	6.98
1980	0.04333	0.99546	0.09533	2.19001	59.93	11.40	1.63	3.91	0.98	0.98	0.98	3.26	1.99	6.31	4.56
1981	0.02966	0.93248	0.06525	2.05145	49.29	15.38	4.27	4.84	2.85	0.28	3.42	2.28	2.28	10.10	4.56
1982	0.03161	0.97138	0.06954	2.13703	54.28	9.73	3.83	4.13	3.24	2.36	1.77	2.95	2.65	10.54	8.55
1983	0.03414	0.93856	0.07510	2.06483	46.34	11.65	7.59	5.42	3.52	2.44	1.90	2.17	2.17	6.49	9.49
1984	0.02995	0.94663	0.06588	2.08258	49.21	13.61	3.93	1.83	2.62	2.09	0.52	3.40	3.14	7.32	13.61
1985	0.03213	0.95434	0.07068	2.09955	44.74	18.06	3.50	4.31	2.16	1.62	1.35	2.43	2.96	6.02	11.59
1986	0.02912	1.03035	0.06407	2.26677	45.51	14.74	1.60	3.53	3.21	2.56	1.60	2.56	3.53	7.28	9.29
1987	0.02622	1.04479	0.05769	2.29854	52.22	7.28	0.63	3.16	4.43	2.53	1.27	3.48	4.11	11.86	12.66
1988	0.04197	1.04793	0.09233	2.30546	49.85	12.23	1.22	3.67	3.06	2.14	0.61	2.75	3.36	8.23	15.29
1989	0.04086	1.02901	0.08989	2.26381	51.76	11.47	1.76	2.94	2.35	2.94	0.59	2.65	3.24	5.81	14.71
TOTAL	0.05221	0.89077	0.11486	1.95969	56.51	9.23	3.40	6.18	2.32	2.20	2.39	2.58	2.76	5.59	6.0

105

exhibit orbital lifetimes exceeding 200 yrs. The conclusion is that much of the intact object traffic characterized by relatively large areas and low masses tends to be launched into low altitudes where atmospheric drag is significant, and decay occurs quickly. The category labeled SKIPPED indicates those objects whose initial orbital parameters exceeded the limitations for acceptable orbits in EVOLVE. Table 11 also provides the mean and standard deviations of the A, m, A/m, and B values found in each year's list. The result averaged over all objects in all lists between 1957-1989 was B = 0.115 m^2/kg with a large standard deviation of σ_B = 1.960 m^2/kg.

The uncertainty of the solar activity level S and ballistic coefficient B each contributes an uncertainty to the overall environment spatial density or flux calculated by EVOLVE. The uncertainties in each parameter fold into the final EVOLVE flux results via the orbital decay model. The ±2σ (2.5 and 97.5 percentile values) bounds on S were estimated in the discussion concerning the solar activity model of Subsection 3.3.1. The effective ±σ bounds on B were calculated in the study discussed above involving the characterization of intact objects input into EVOLVE. In separate EVOLVE processing runs the flux results were obtained using the bounding values.

The solar flux determines the exospheric temperature as discussed in Subsection 3.3.2. Thus, the projected uncertainty in this parameter can have a significant effect on the overallEVOLVE modeled flux environment. Flux results were obtained by implementing the ±2σ values (Ref. 27) as given in Subsection 3.3.1 for future years (1990-2010). The historically measured flux values are assumed to be exact (the measurement uncertainties are neglected). A nominal 3 HIE/ 1 LIE per year traffic model using the 1988 launch rates is assumed (one collision occurs in 1995).

The results are shown in Figures 56-60. Figures 56 and 57 show expected trends in flux variations with the solid line indicating the nominal solar activity (SOLACT) model used in EVOLVE. The nominal values lie within the ±2σ values as expected. The mean (50 percentile) value is shown for comparison. The sharp dips at 1991 and 2002 for the h = 500 km case are results of the peaks in solar flux at these years. Figure 57 shows the much reduced influence of the upper atmosphere (and therefore S) on the flux at the higher altitude h = 1000 km. During peaks in solar flux, the uncertainty in the flux at lower altitudes can be two orders of magnitude or more as shown in Figure 56. Figure 58 indicates an approximate factor of 5 difference between the ±2σ cases over most of the object diameter range for h = 500 and t = 2000 (a moderate solar flux level year). During a peak solar year this uncertainty can quadruple. At 1000 km, the flux is virtually nil as shown in Figure 59 due to the much smaller influence from the upper atmosphere. Figure 60 clearly shows the uncertainty due to S increases with decreasing altitude being almost an order of magnitude for h = 100 km for d ≥ 0.1 cm at t = 2000. This figure also indicates that the upper atmosphere begins to influence orbits via drag at ~900 km. From these figures it can clearly be observed that future flux environments have significant uncertainties resulting form the uncertainties in solar activity S.
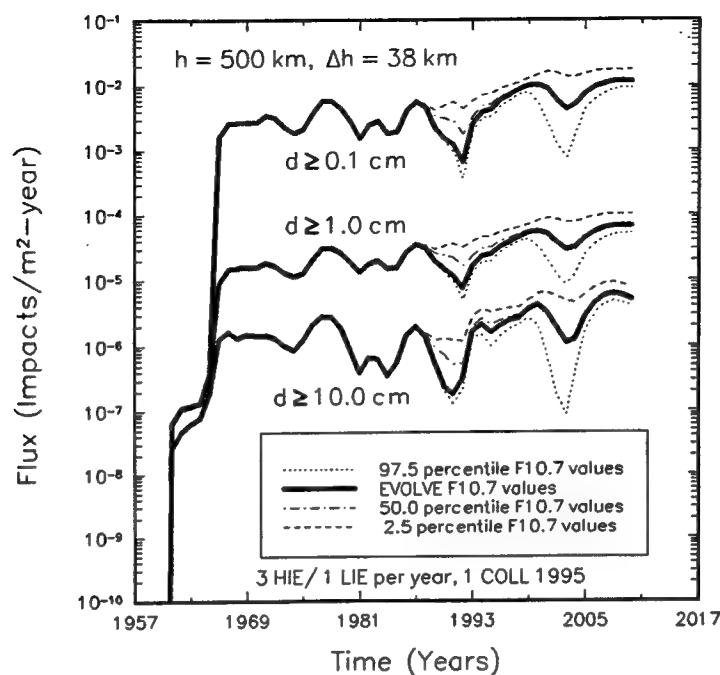
106

Figure 56.   Flux versus time at 500 km for three cumulative diameters, comparing
EVOLVE solar F10.7 cm table values with predicted 2.5, 50.0, and 97.5
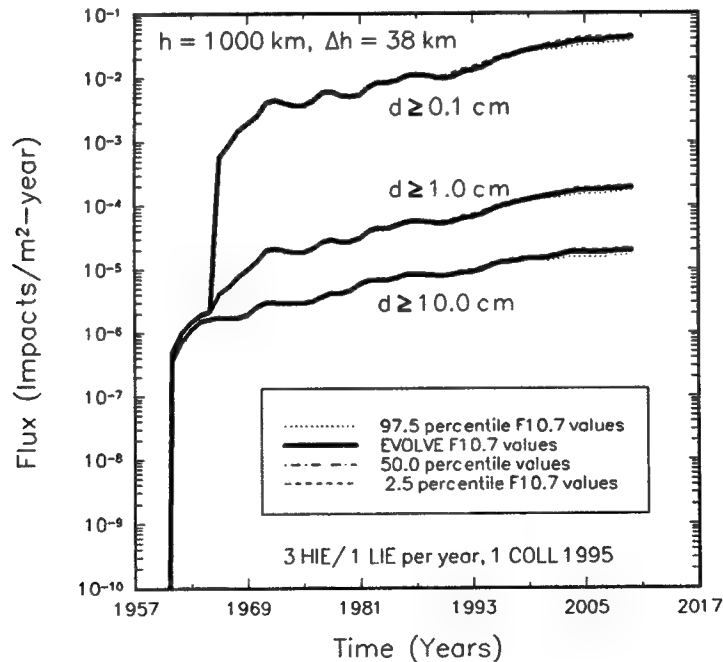percentile values.

Figure 57.   Flux versus time at 1000 km for three cumulative diameters, comparing
EVOLVE solar F10.7 cm table values with predicted 2.5, 50.0, and 97.5
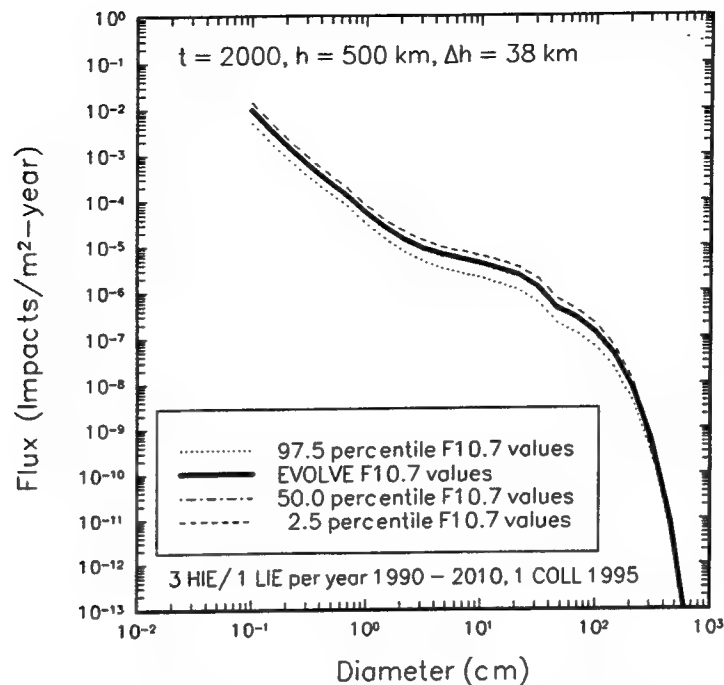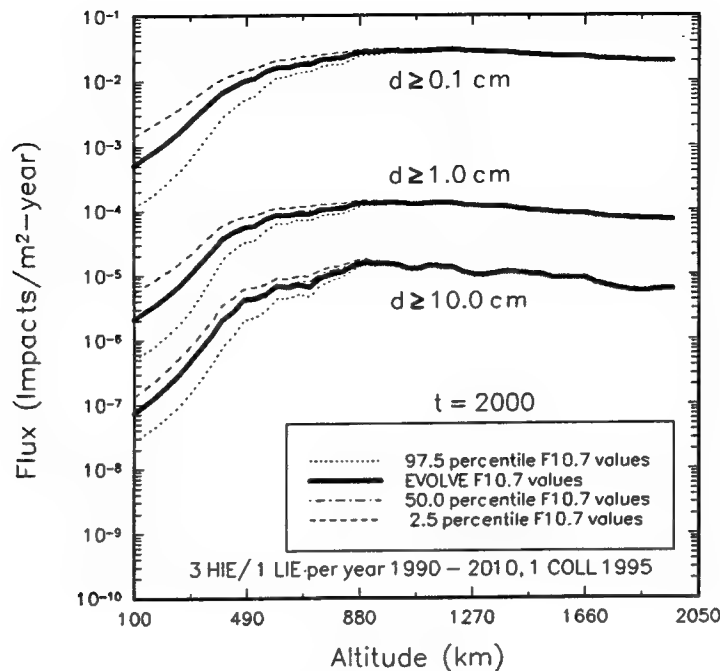percentile values.

107

Figure 58. Flux versus fragment size at 500 km in the year 2000, comparing EVOLVE solar F10.7 cm table values with predicated 2.5, 50.0, and 97.5 percentile values.
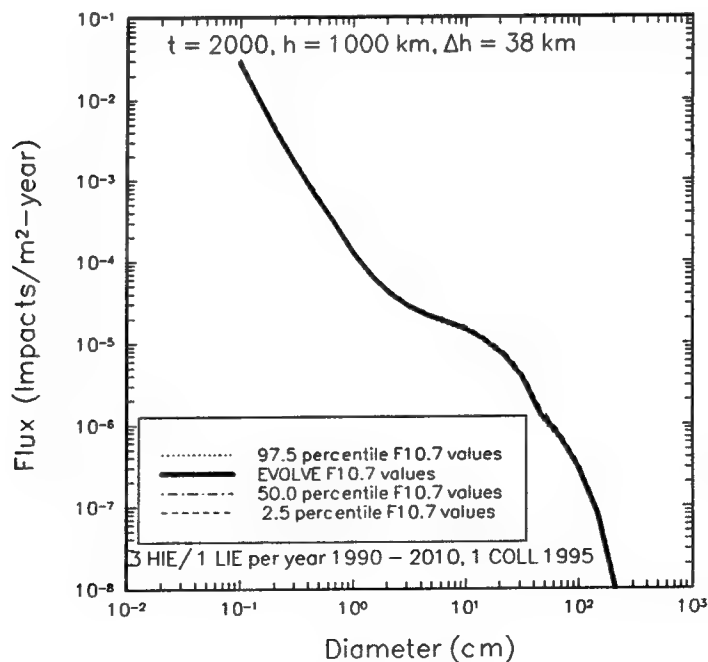
Figure 59. Flux versus fragment size at 1000 km in the year 2000, comparing EVOLVE solar F10.7 cm table values with predicated 2.5, 50.0, and 97.5 percentile values.

108

Figure 60.   Flux versus altitude in 2000 for three cumulative diameters, EVOLVE solar
F10.7 cm table values with predicated 2.5, 50.0, and 97.5 percentile values.

The flux sensitivity to B was obtained by assuming that $+\sigma_B = 2.075$ m²/kg and
$-\sigma_B = 0.011$ m²/kg. These values were input into the EVOLVE by setting B to the
appropriate constant value just prior to the call to the DECAY package in subroutine
ORBUPD. Thus, all objects processed by DECAY are assigned the same constant B. The
results are shown in Figures 61-65 as functions of time (Figure 61 at h = 500, d ≥ 0.1 cm and
Figure 62 at h = 1000, d ≥ 0.1 cm), diameter (Figure 63 at h = 500 km, t = 2000 and Figure
64 at h = 1000 km, t = 2000), and altitude (Figure 65 at t = 2000, d ≥ 0.1 cm). The
EVOLVE runs considered only launched intact objects since only they invoke the DECAY
routines in EVOLVE and there is no equivalent way to introduce variational changes in the
phenomenological function (Eq. 63) for debris clouds. All figures show that the $-\sigma_B$ values
tend to yield the higher fluxes, as expected, and the $+\sigma_B$ values yielded the lower values. The
time curves (Figs. 61 and 62) show the general expected trend with the 11-yr cycle solar flux
as indicated by the dips in flux for the $+\sigma_B = 2.075$ m²/kg case where the environment will be
cleansed of many objects. The $-\sigma_B = 0.011$ m²/kg value shows a much smaller but still
discernible similar trend. The solid line shows results using the actual B values using the
A/m values read from the input lists.

In general, the curves lie within the $\pm\sigma$ bounds but there is an overall tendency toward the
smaller B values. During periods of high solar activity, the relative flux difference between
$\pm\sigma_B$ values increases (up to 2 orders of magnitude or more difference possible as shown in
Figure 61). During quiet solar periods, the difference decreases (factor of 3 difference). The

109
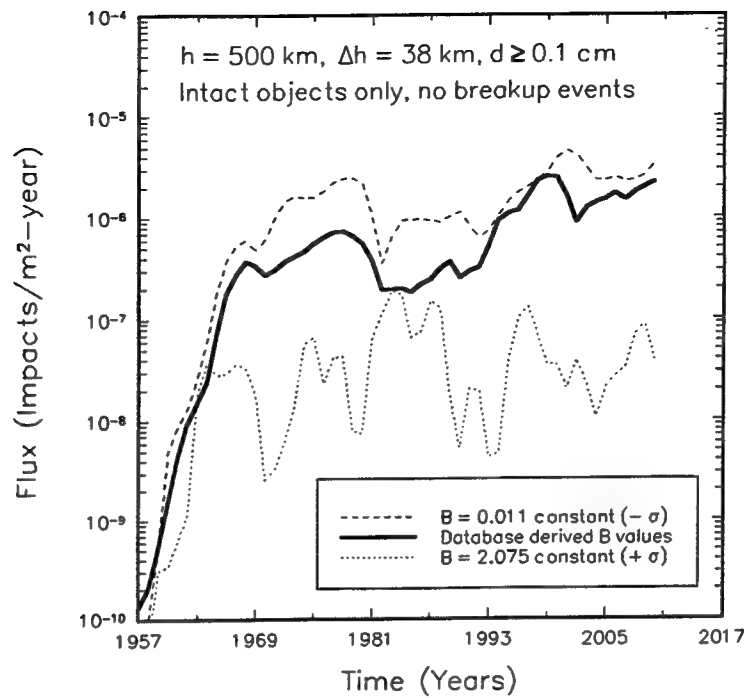
Figure 61. Flux versus time at 500 km and d ≥ 0.1 cm for intact objects only compared to the flux obtained using a constant B for all orbits in EVOLVE.
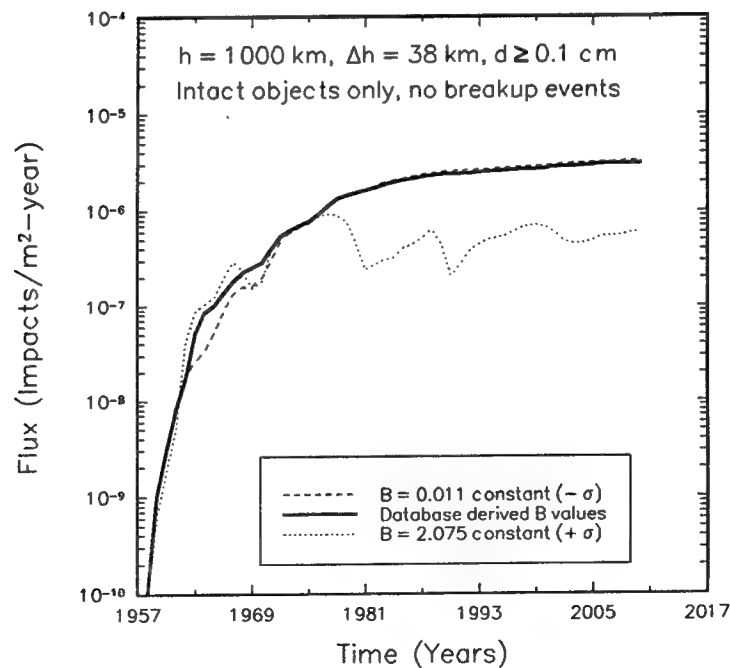
Figure 62. Flux versus time at 1000 km and d ≥ 0.1 cm for intact objects only compared to the flux obtained using a constant B for all orbits in EVOLVE.
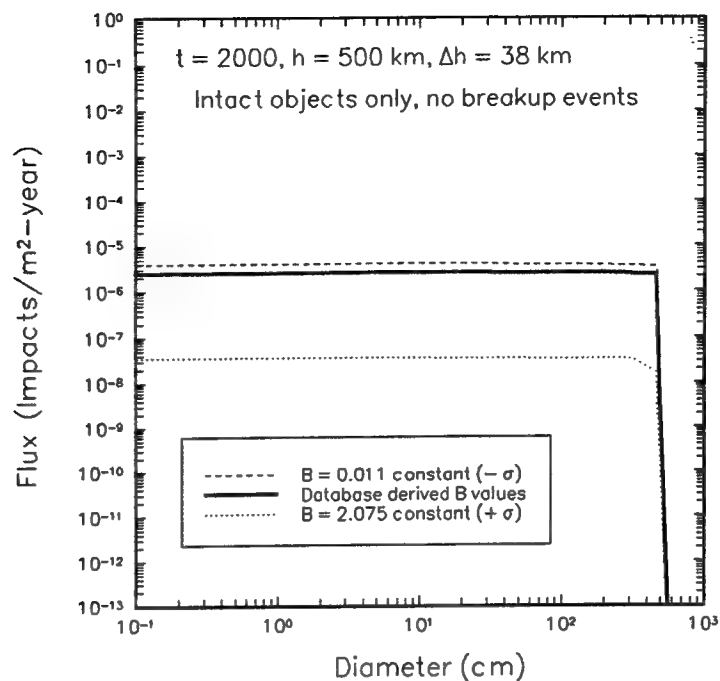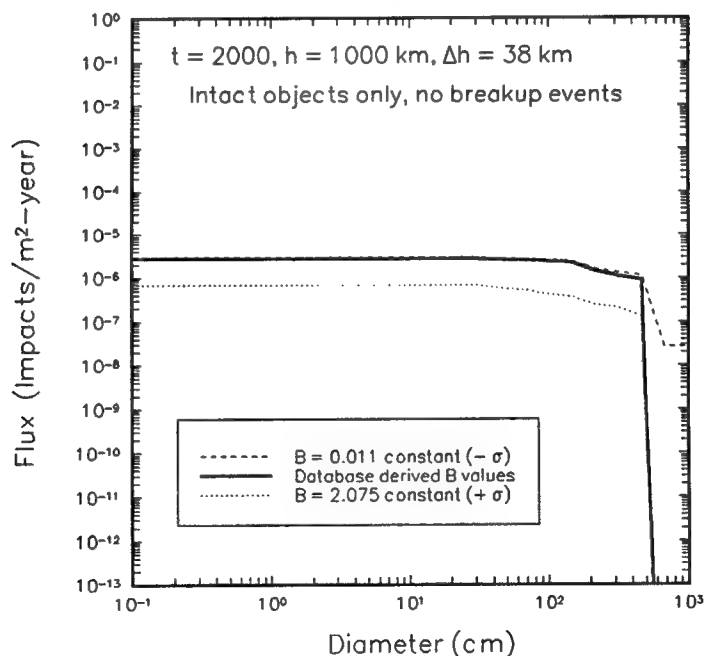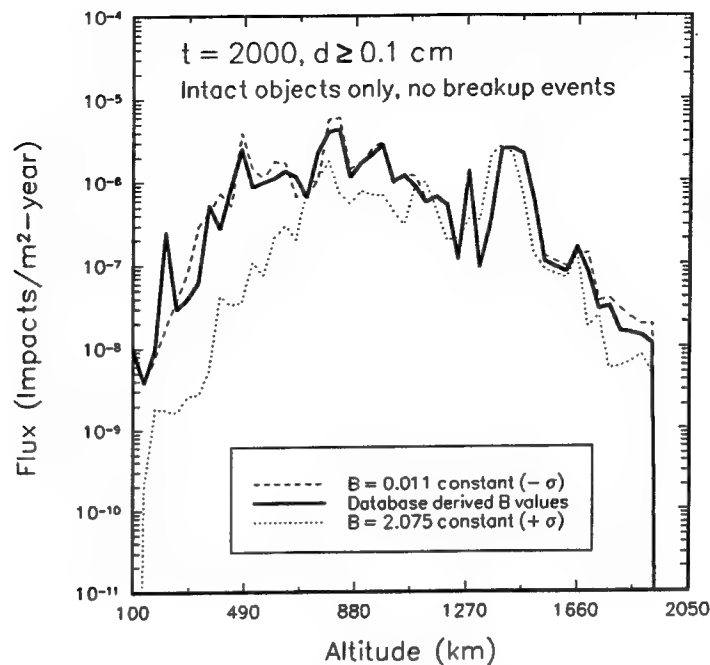
110

Figure 63.   Intact object only flux versus cumulative diameter at 500 km and in the year 2000 compared to the flux obtained using a constant B for all orbits in EVOLVE.

Figure 64.   Flux versus cumulative diameter at 1000 km and in the year 2000 for intact objects only compared to the flux obtained using a constant B for all orbits in EVOLVE.

111

Figure 65. Flux versus altitude in 2000 and for cumulative diameter d ≥ 0.1 cm intact objects only compared to the flux obtained using a constant B for all orbits in EVOLVE.

lower altitude (500 km) case naturally experiences a more dramatic effect due to its proximity to the variable upper reaches of the atmosphere (Figs. 61 and 63). The lower limit $-\sigma_B = 0.011$ m²/kg is hardly affected at h = 1000 km (Fig. 62). The cause of the unexpected inverted flux curves between 1964 and 1970 for the h = 1000 km case (Fig. 62) is not certain, but it may reflect the fact that during this period a significant amount of traffic was launched having apogee altitudes (h_a) slightly above 1000-km. With the $+\sigma_B$ values, these object orbits began to descend more quickly through the vicinity of the 1000-km altitude band, thus, increasing the flux here. With launches in later years, the altitude distribution began to be spread more widely.

Figures 63 and 64 show the cumulative flux as functions of diameter for h = 500 and 1000 km, respectively. They show that the intact objects contribute relatively few objects to the environment as shown by the steep rise and then the sudden leveling off of the cumulative distribution curves. Again, the correlation among $-\sigma_B$, $+\sigma_B$ and the B values derived from database shows the expected trends. Figure 65 displays the altitude distribution. The wider differences observed at the lower altitudes (h < 500 km) is an indication of the cleansing of low altitude low eccentricity orbits from the environment while the widening difference at high altitudes (h > 1700 km) is the result circularization of the high eccentricity orbits resulting from the varying B values. It is possible that the midaltitude region may actually

experience a higher flux for a higher B. Circularization of high eccentricity orbits having low h_p values will take place causing the apogee altitudes h_a of these orbits to begin occupying the midaltitude regions. This effect is observed near the 1000-km altitude in Figure 65. Clearly,the uncertainty in B has profound affects on the uncertainty of the EVOLVE flux results. Although not shown here, the same assumptions will apply to the uncertainty in debris clouds. The large uncertainty in B with the combined intact object and debris cloud fluxes may be as significant to the overall uncertainty as the solar flux value was shown to be in Figures 56-60.

3.4 COMPARISON TO OBSERVED DATA

For past years (1957-1989), EVOLVE incrementally constructs the man-made orbital debris environment from known historical sources (launched objects and breakups) as explained in Subsections 3.1.1 and 3.1.2. For historical years, the EVOLVE model should reasonably simulate observed data and other validated debris models if the underlying models and assumptions built into EVOLVE are valid. The historical year flux results rely only on the deterministic processing phase in EVOLVE. Assuming that the historical launch manifests and observed collision and explosion events along with their associated data (initial orbital elements, masses, etc.) are accurate and represent a complete historical record of actual past events, then the uncertainties in the EVOLVE results depend only on the breakup debris cloud models and atmospheric density/drag/orbital contraction models. EVOLVE was not designed to exactly replicate any specific observed data set or other model, but, instead, be a reasonably robust model to generate a predicted environment based on the current knowledge in breakup modeling and atmospheric density/drag modeling.

A comparison of the EVOLVE flux results was made with available radar and optical measurements obtained from various sources. EVOLVE was run with input conditions to match as closely as possible the existing conditions under which the measurements were taken. These conditions include epoch time (within a year), altitude span, and diameter range. Table 12 summarizes the EVOLVE run conditions and observations made about each comparison. No comparison was made to data for particle sizes below 0.1 cm since EVOLVE insufficiently models this diameter region (described in Subsections 3.2.2 and 3.2.3).

Figure 66 plots an altitude distribution of flux using USSPACECOM SATCAT catalogued objects radar tracked by the Space Surveillance Network (SSN) as of 1 January 1990. These data have a relatively "soft" sensitivity limit of 8-cm-dia objects below which objects cannot be reliably tracked. This limit increases with altitude and at h = 2000 km the limit is ~50 cm (Ref. 28). The EVOLVE results compare reasonably to up to ~1000 km. Although slightly higher in magnitude through this region, the general shape of the curve is well-represented, indicating that the atmosphere decay model produces a decay rate comparable to the apparent observed rate. There are significant discrepancies in the flux magnitude beyond 1000 km,

113

Table 12. Historical EVOLVE Results Compared to Observed Data.

Available Data/Model	EVOLVE Run Conditions	Observations/Comments
USSPACECOM SSN radar data 100 km≤ h ≤ 2000 km January 1990	t = 1957 - 1989 d ≥ 10 cm diameter bin 100 km ≤ h ≤ 2000 km, 50 altitude bins, Δh = 38 km 26 size values 7 decades, 10^{-6} - 10^{3} cm, 26 bins/decade	Good agreement; EVOLVE fills gaps in environment; radar data loses sensitivity to minimum detectable size with h
NASA TM-100471 model i = 30 °, t = 1989, h = 500 km, S = 198.8	t = 1957 - 1989 50 altitude bins, h = 100 km, Δh = 19 km 26 size values 8 decades, 10^{-5} - 10^{3} cm, 25 bins/decade, 8 runs	Good agreement; except for small particle sizes d ≤ 0.1 cm
Goldstone radar data (JPL) 1989, 562- 589 km	t = 1957 - 1988 1 altitude bin, h = 562 km, Δh = 27 km 26 size values 1 decade, 0.1 - 1 cm, 25 bins/decade	Fair agreement; ~ order of magnitude
Arecibo radar data (JPL), 1989, 200-100 km All data reported in 1 alt. bin Δh = 800 km	t = 1957 - 1988 1 altitude bin, h = 200 km, Δh = 800 km 25 size values 2 decades, 0.1 - 10 cm, 12 bins/decade	Fair agreement; within order of magnitude
GEODSS optical data 1989, 500 - 1100 km Data reported in 3 alt. bins, Δh = 200 km	t = 1957 - 1988 1 altitude bin, h = 500 km, Δh = 70 km 25 size bins 2 decades, 10 - 1000 cm, 12 bins/decade	Fair agreement; order of magnitude within scope of intact orbits where uncertainty is least
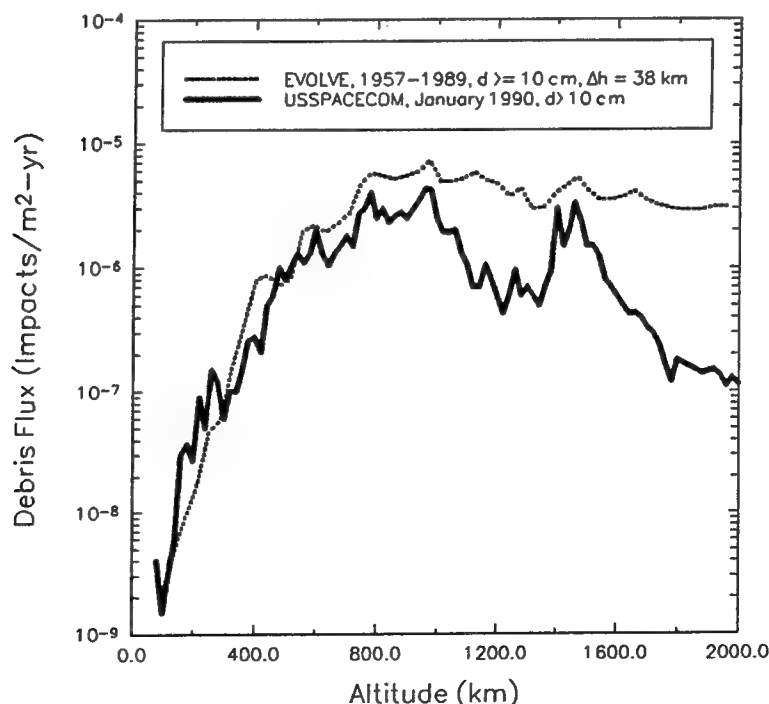
Figure 66.   Comparison of flux versus altitude for USSPACECOM satellite catalogued radar observation data and equivalent EVOLVE flux results.

114

attributable in part to the decreasing sensitivity with altitude of the minimum detectable object size. If such objects cannot be detected, they cannot possibly contribute to the observed environment. Except for the strong peak at ~1400- to 1500-km altitude, the flux decreases steadily starting at 1000 km. Most LEO object orbits are nearly circular or mildly elliptical with semimajor axes below 1000 km implying that their spatial contributions will be primarily below object 1000 km. As altitude increases the debris and intact spatial density will tend to decrease. The flux enhancement near 1400 km is a result of several known breakups occurring from satellites near this altitude. A large number of fragments resulted that could be detected at this altitude producing the observed peak. In interpreting these plots, the user should be aware that a peak in the altitude distribution can occur either from a large number of near circular orbits in the vicinity of the altitude being examined or from a concentration of elliptical orbits having nearly the same eccentricity.

Other factors exist which may explain the observed differences between the measured and EVOLVE modeled populations. These include differences and uncertainties in the modeled ballistic coefficients and orbital propagation/decay rates (preventing comparable decay rates to what is observed), inadequate altitude profile modeling of elliptical orbits (a previously identified problem with the this version of EVOLVE as shown in Section 3.2.4.2), and the assumptions used in constructing the fragment distribution initial conditions in the EVOLVE breakup model. For example, explosions are assumed to disintegrate the total mass of the exploding object, producing a larger population of fragments $d \geq 10$ cm than what would occur if some or all of these objects just partially exploded. Observed on-orbit events seem to suggest that generally only part of the parent object's mass is fragmented (Refs. 17, 25). This may account, in part, for the larger modeled population over measured population seen in Figure 66.

In Figure 67, the EVOLVE results for 1989 and $d \geq 10.0$ cm are compared to the results using the NASA 90 engineering flux model (Ref. 13). The uncertainly bounds for this diameter regime at all altitudes is shown to be a factor of 2-4, placing the EVOLVE results within the upper bound of this uncertainty limit (Ref. 13). The NASA 90 model is an analytical phenomenological function based on a series of flux versus altitude USSPACECOM radar data similar to that plotted in Figure 66. As expected, the smoothed function model curve shown in Figure 67 agrees well with the flux magnitude of the USSPACECOM data shown in Figure 66; therefore, this smoothed curve falls below the EVOLVE output by approximately the same amount. Unlike the data on which it is based, the NASA 90 flux levels off at ~900 km and does not adequately reproduce the peak and valley structure of the observed altitude distribution.

Comparisons were made for flux versus size using data from two dedicated radar and one optical measurement programs. Figure 68 shows the radar observations performed in 1989 on 0.2- to 0.5- cm-dia objects at the Goldstone radar site in an altitude range of 562-589 km (Ref. 29). Figure 69 shows the flux observed for 0.5- to 2.0-cm sized objects in an
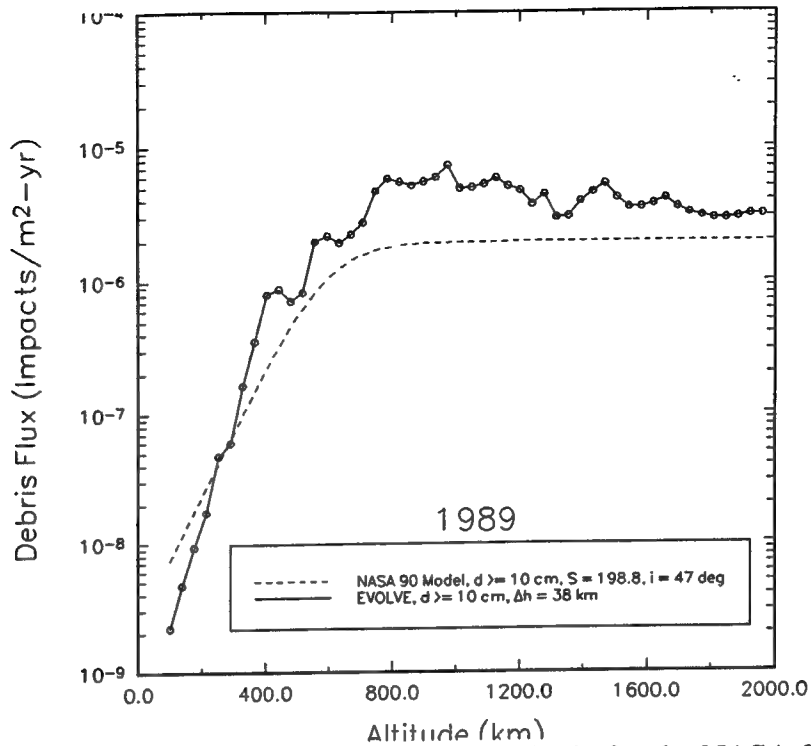
Figure 67. Figure 61. Comparison of flux versus altitude for the NASA 90 engineering flux model (Ref. 13) with the corresponding EVOLVE output.
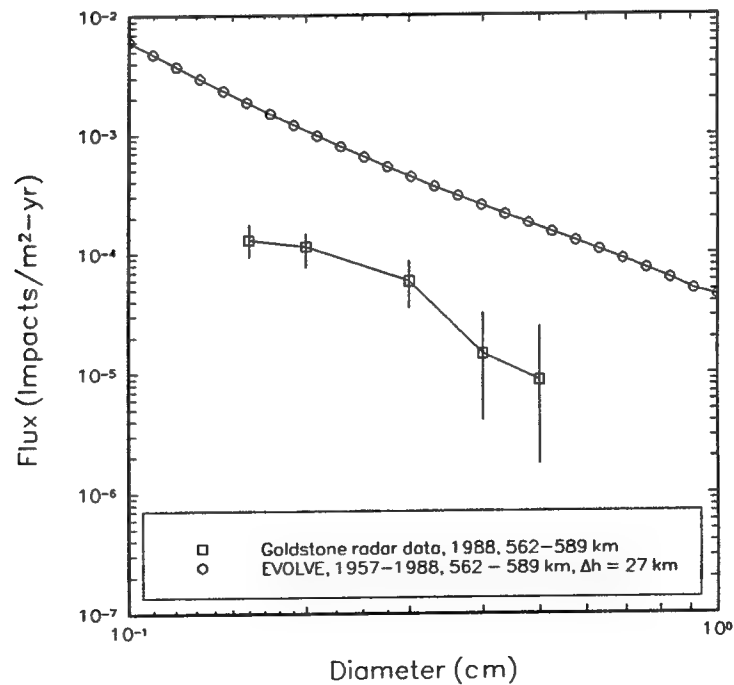

Figure 68. Comparison of flux versus diameter for the Goldstone radar debris flux measurement (Ref. 29) with corresponding EVOLVE flux results.
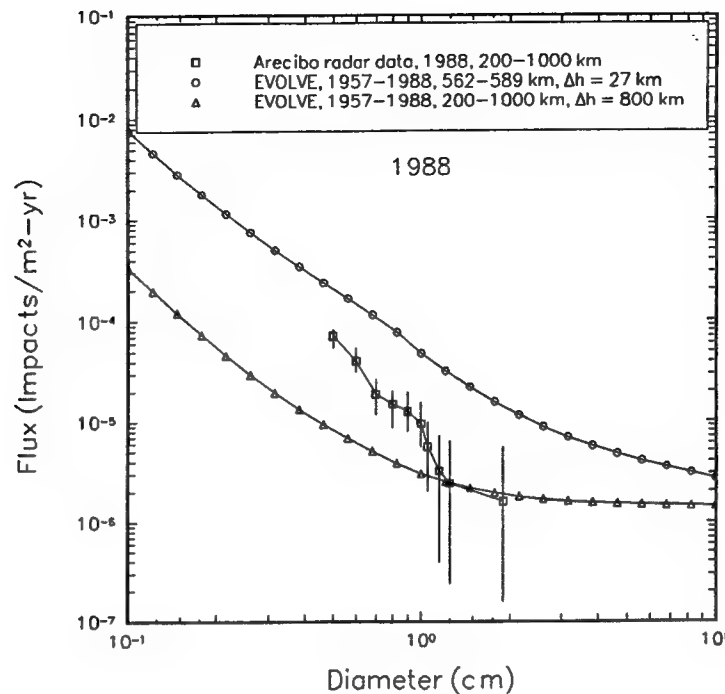
116

Figure 69. Comparison of flux versus diameter for the Arecibo radar debris flux measurement (Ref. 29) with corresponding EVOLVE flux results.

altitude range of 200-1000 km using the Arecibo radar site in Puerto Rico (Ref. 29). The EVOLVE calculations overestimate the flux by approximately an order of magnitude for the 0.2- to 0.5-cm range of the Goldstone radar data shown in Figure 68. The Goldstone data are shown with its statistical error bars (for 14.5 hrs observation), and although the EVOLVE results fall outside of the statistical uncertainty of these data, other uncertainties involved with both the observed data and with the EVOLVE results are not accounted for here. The order of magnitude difference probably lies within the overall uncertainty of both sets of data. The Arecibo data in Figure 69 show slightly better agreement to the EVOLVE results (within an order of magnitude for most points). The error bars represent the statistical uncertainties in the measurement data. The EVOLVE results are calculated using two different Δh bin widths ($\Delta h = 27$ km centered at 575 km and $\Delta h = 800$ km centered at 600 km). The reasons the difference seen between these calculations is explained in Subsection 3.1.4.3. Again, considering the uncertainties involved in both sets of results, the agreement is considered reasonable. All radar observations must estimate object diameter from the observed radar cross section (RCS) signature and there is known to be considerable uncertainty in this value (Ref. 30).

Figure 70 shows some optical measurement of larger sized fragments (10-120 cm) in the 500- to 700-km altitude range using the Ground-based Electro-Optical Deep Space Surveillance System (GEODSS) telescope sites at Socorro, New Mexico, Maui, Hawaii, and the island of Diego Garcia in the Indian Ocean (Ref. 31). The data here represent 80.9 hrs of
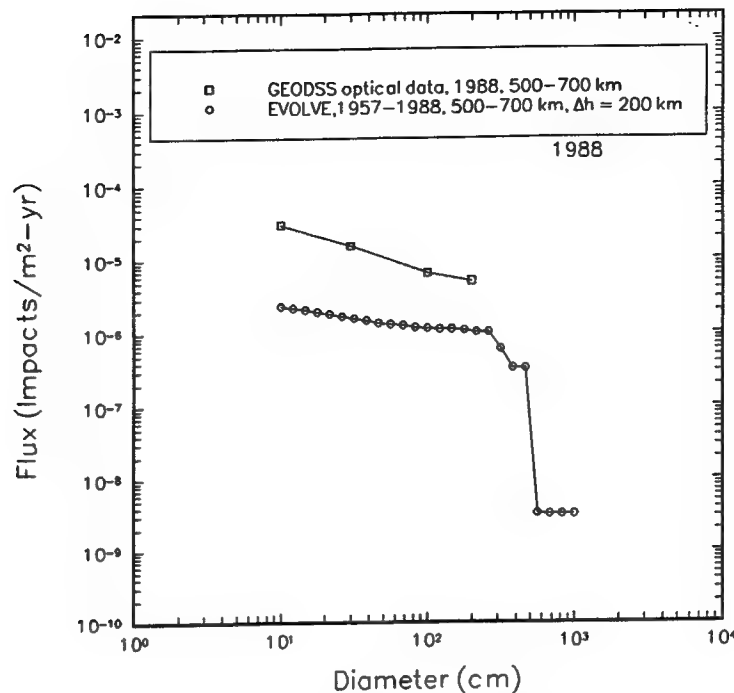
117

Figure 70.   Comparison of flux versus diameter for the GEODSS optical debris flux
measurements with the EVOLVE flux results (Ref. 31).

viewing time. The EVOLVE results agree to the optically observed results to within an order
of magnitude. The size of objects observed with the GEODSS telescopes is related to the
reflectivity or albedo of the objects, a quantity whose observed value has considerable
uncertainty (Refs. 31 and 32). The debris size is derived from an assumed albedo of 0.05 for
the data given in Figure 70. The choice of the mean albedo can significantly affect the
estimated size of fragments observed. Albedo values ranging from 0.003 to 0.8 were
observed in the GEODSS measurements (Ref. 31). In fact, an increase in the mean albedo by
a factor of 10 leads to a diameter decrease of a factor of 3. With such uncertainty, the
comparison of EVOLVE results to the GEODSS data seems reasonable.

The NASA 90 engineering model diameter results are compared to EVOLVE model results in
Figure 71. The agreement is good with the EVOLVE model predictions being only a factor
of 2-5 larger than that of the engineering model throughout most of the size range. The
diameter range below 0.1 cm is shown to illustrate the fact that the EVOLVE model cannot
model this size region due to insufficient source terms. Only the collision model is capable of
contributing fragments below 0.1-cm diameter. EVOLVE is currently not equipped to
supplythe missing population of particles in the small size regimes coming from such sources
as solid rocket exhaust.

The close comparisons to observed data given in Figures 60-71 have helped to establish the
ability of EVOLVE to model the environment. Unlike the NASA 90 engineering model
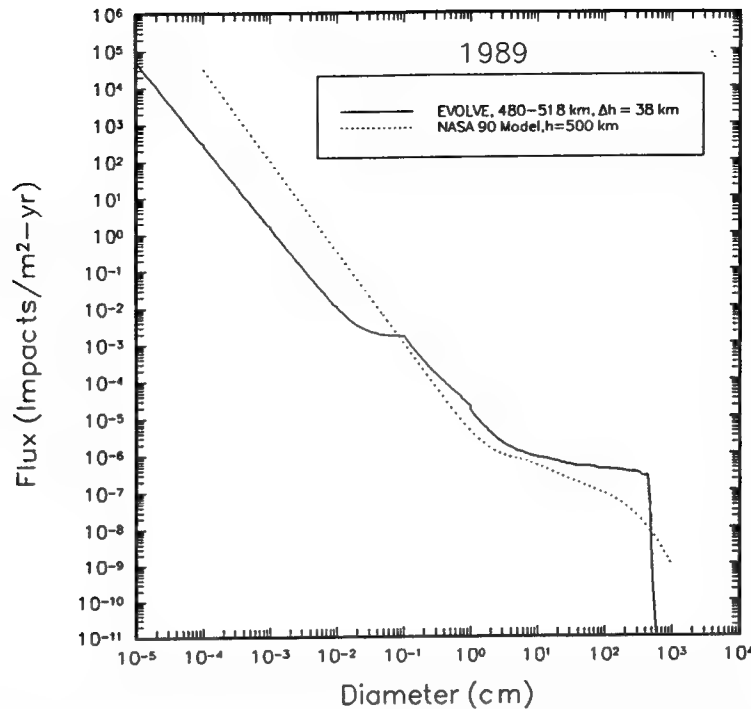
118

Figure 71. Comparison of flux versus diameter for the NASA 90 engineering flux model (in 1989, h = 500 km) (Ref. 13).

which is derived with the corresponding EVOLVE flux model results from curve fits to the same available data (USSPACECOM radar data and GEODSS optical data) and with the exception of the implied fitted mass distribution functions derived from some on-orbit breakups (Subsections 3.2.2 and 3.2.3), the EVOLVE model is independent of any data sources of observed environment data. Instead, the environment is reconstructed in EVOLVE solely on the basis of the interaction between source models which add to the environment and sink terms which remove objects from the environment. Thus, the reasonably close comparison of the modeled environment and the measured environment shown in Figures 60-65 has served to enhance the confidence and fidelity of the EVOLVE flux results obtained.

119

4.0 CONCLUSIONS

The EVOLVE debris environment time evolution model developed by NASA JSC has been assessed. The model represents an integrated ensemble of modularized submodels working together to develop a long-term spatial density or flux description of the LEO environment as functions of fragment size d, altitude h, and time t. The general design approach is to construct the environment by introducing man-made objects in yearly increments of time and propagating their orbits until they are determined to have decayed from the environment.

The model is intended to give a reasonable environment picture in the long-term (a year or more). Effects that occur on a time scale shorter than a year are generally not modeled in EVOLVE. The dynamic environment state is simply the net sum of source terms and sink terms current at any defined time step. The sum of intact objects inserted into orbit and on-orbit fragmentation events comprise the source terms. The objects present in the environment are continually being removed by atmospheric drag and orbital perturbations acting as sink terms. The model has been assessed in terms of the sources (intact objects and debris clouds) and sinks (atmospheric drag and orbital perturbations).

The model is completely analytic and therefore computationally efficient. No numerical integration or sophisticated numerical techniques are used in any submodel comprising EVOLVE. This is accomplished at the expense of achieving higher accuracy since the submodels incorporate many assumptions and simplifications not found in more rigorous models. In nearly all cases, these assumptions are deemed justifiable in view of the environment modeling goal of EVOLVE.

4.1 INTACT OBJECTS

All intact objects are deterministically introduced into the environment. This means that the model user specifies the discrete initial conditions necessary to allow the orbital propagation software to process its future orbital states. The same applies to deterministic breakup events (explosions or collisions) that are forced to occur. The manifest of launched intact objects and deterministic clouds together constitute a traffic model. A traffic model presents a detailed description of the orbital type and number of objects being placed into the environment . The user has great flexibility in defining the constituency and traffic rate characteristics of his EVOLVE inputs. Programmatic or operational options, such as deorbiting spacecraft, collision avoidance, and stationkeeping which may affect the environment are included. The flexibility represented by the traffic models is considered the greatest strength of the EVOLVE model over a simple empirical model like the NASA developed engineering flux model (Ref. 13). The latter model is held fixed to the data on which it is based. Extrapolations beyond these bounds greatly increase the model uncertainty. No such limitations exist for the EVOLVE model. Traffic rates are not tied to some analytic rate functions; instead, they are exactly defined by the traffic lists. EVOLVE generates the environment using an amassed raw database of intact object mass distribution

traffic, breakup models (based on fits to observed fragmentation events), ejecta velocity distribution models, and probability collision/explosion rates. Discrepancies between data and EVOLVE predictions can be attributed to uncertainties in both the measurements and EVOLVE submodel assumptions and simplifications.

Once input into the environment, EVOLVE propagates the intact objects individually using a reasonably accurate propagation model especially designed for long-term modeling applications. This methodology is the brute-force approach. The individual treatment of intact objects is computationally tractable because of the relatively small number of objects involved (<10000 objects over any near-term time interval) and the analytic nature of the propagation model derived by Mueller using King-Hele derived expressions (Refs. 9 and 26).

The orbital decay routines are assessed as being ideally suited for the long-term modeling application of EVOLVE. They are trimmed of many short-term and periodic effects not needed for long-term modeling. The orbital propagation model classifies the orbit being processed into one of three classes to adequately apply the correct mixture of atmospheric drag and sun/moon orbital perturbation effects. Most low apogee altitude orbits ($h_a < 14000$ km) are adequately described by the pure analytic King-Hele drag perturbations. The periapsis and right ascension of orbits are also perturbed by the J_2 gravitational harmonic term but only after the drag-induced King-Hele/Mueller orbital contraction expressions have been applied. Perturbations resulting from higher-order gravitational terms, earth oblateness effects on atmospheric density, and scale height are neglected. These effects are generally short-term and periodic and, therefore, their influences average out. Higher apogee orbits are assumed influenced by sun/moon perturbations only. The sun/moon perturbations themselves are simplified by neglecting higher order and periodic effects. The Mueller propagation and decay routines have been compared to full-scale accurate models and found to be reasonably accurate with <25 percent error for most orbits (Ref. 9). The accuracy worsens for shorter lifetime orbits, but this poses no problem for the long-term modeling in EVOLVE. Thus, the accuracy of the orbital decay model is sufficient for the EVOLVE long-term modeling. The rather large errors in the lifetime estimates average out over the long time spans (one or more years) in which the model is valid.

The decay of intact object orbits is strongly influenced by the external effects of the solar flux heating of the upper atmosphere and the ballistic coefficient characterizing the effect of drag. The Mueller DECAY routines assume that the solar flux and ballistic coefficients remain constant over the year propagation intervals. This is a reasonable assumption for an averaging model. The variable solar flux model installed in EVOLVE is comprised of a look-up table of both historical and projected yearly F10.7 cm radio flux values, S. This suggests that the Δt propagation increments (a user-selectable option for EVOLVE processing) should always be kept to 1 yr. Regression analysis for projected values yielded the 2.5 and 97.5 percentile ($\pm 2\sigma$) uncertainty values for S (Ref. 27). Based on these reported uncertainties, an estimate of the EVOLVE flux uncertainty was obtained. The flux uncertainty due to S variability was found to range from a factor of 5 up to two orders of

magnitude depending on the solar cycle. As expected, the uncertainty in S presents a significant uncertainty only for the lower altitudes (h $\leq$ 900 km) which continually increases as altitude is decreased.

The ballistic coefficient B = C_D(A/m) is a highly uncertain term for most objects which the DECAY routines must process. This uncertainty will directly fold into the EVOLVE flux uncertainty. The intact object ballistic coefficient distribution from all EVOLVE historical input files yielded an average value of B = 0.115 m²/kg with a large standard deviation of σ_B = 1.960 m²/kg. (The standard deviation derived here is skewed by the presence of a few objects having exceedingly large area to mass ratios; consequently, it may not be entirely representative of the true deviation of B values expected for debris fragments. This approach is conservative, however.) The B values came directly from the known size dimensions and masses of launched objects found, in the historical manifest lists. Values of B assigned to debris fragments are generally much more uncertain due to the uncertainty inherent in knowing the size, shape, and mass of individual fragments. Estimates of the EVOLVE uncertainty in the intact object flux resulting from the assumed uncertainty in B show that B can have a dramatic effect on the environment prediction. Depending on the ambient solar flux level and altitude, the flux uncertainties due to uncertainties in B were estimated to range anywhere from a factor of 5 to more than two orders of magnitude. The flux uncertainty is greater at lower altitudes where atmospheric drag which depends on B has a greater effect on the orbit. Even at h = 1000 km, there was an order of magnitude uncertainty attributed to B. This uncertainty arises from the cleansing at 1000-km altitude of objects having elliptical orbits with apogee altitudes $h_a \geq$ 1000 km and perigee altitudes (h_p) low enough to be influenced significantly by drag.

The EVOLVE model characterizes the presence of intact objects in the environment by a calculation of the spatial density within prescribed spherical shell volumes located in the LEO region. Using the assumption that the spatial density from an orbit in the defined volume is related to the fraction of time spent within that volume, a spatial density model has been developed to characterize the environment as a function of altitude only. The assumption that the spatial density depends only on the radial dimension (i.e., altitude) has been shown in this assessment to be reasonable. Latitude (inclination) and longitude dependences have been neglected. The latitude dependent effects were shown in this study to be rather small for most latitudes. For an orbit at inclination i, the spatial density algorithm incorporating latitude (β) dependence did not differ from its radial-dependent only counterpart by more than a factor of 3 over the latitude range 0 deg $\leq \beta \leq$ 0.9 i deg. Only when $\beta \approx$ i did the results vary significantly. The radial only expressions yield the approximate spatial density S averaged over all latitudes. These expressions are integrated form which overcomes singularities at the perigee and apogee points in an orbit and involves a Δh altitude bin width term. The sensitivity of the bin width on the spatial density results has been shown to be small for reasonable values of Δh, but the user should be aware of its possible consequences on the spatial density results.

4.2 DEBRIS CLOUDS

Debris clouds contribute the largest number of objects to the LEO environment. They also are the only source of fragments modeled for sizes $d \leq 1.0$ cm in EVOLVE. Debris clouds originate from three modeled causes: hypervelocity collisions, LIEs, and HIEs. A debris cloud is the ensemble of fragments created during an on-orbit fragmentation event distributed into all user-specified size bins by which the user wishes to express the EVOLVE flux output. Each size bin defines a subcloud containing N objects whose number is derived from an assumed cumulative number versus mass distribution for the appropriate fragmentation type. All fragments lying within the diameter range represented by the size bin are assumed to have the characteristic (average) diameter associated with the size bin. The subcloud is evolved in time using a phenomenological model empirically derived from preprocessed curve fits to the flux results of a cloud containing objects all of equal size. The preprocessing code FRGMNT was used to generate and time-evolve such clouds. Curve fits to the flux versus altitude distributions were performed to obtain the phenomenological fit function used in EVOLVE to characterize the time evolution of debris cloud spatial densities. The initial orbital elements of each cloud fragment at the time and altitude of breakup were determined from an assumed ΔV velocity distribution to yield imparted ΔV magnitudes. The ΔV directions were assumed isotropic. The ΔV velocity magnitude distribution provides the most probable ΔV for the size fragment being ejected. The ΔV distribution is derived from hypervelocity collision test data and is applied equally to collision and explosion events.

The EVOLVE model treatment of debris clouds has been assessed to be both a major strength and a major weakness of the model. The concept of evolving the debris cloud via a phenomenological function is a novel approach to simplify the overhead and computation that would be otherwise required to process each fragment individually. The computational burden is reduced tremendously, allowing EVOLVE to rapidly and efficiently time evolve the debris cloud contribution to the environment. The model is normalized to represent the spatial and temporal behavior of one fragment; the behavior of any size subcloud containing N objects can be readily found by scaling the phenomenological function by the number of fragments in the subcloud. The number of fragments, N, for the particular subcloud being evolved in time is derived from a breakup model in EVOLVE itself, independent of the phenomenological function. The drawback is that the phenomenological function cannot be easily modified to integrate possible new assumptions or models relating to the ΔV distribution applied to breakup fragments, the $D(\Delta V)$ spreading function, or the directionality assigned to the ΔV of fragments at breakup. These models, which can have tremendous impact on the time-evolution characteristics of a debris cloud, cannot be directly altered in EVOLVE since they are implicit in the functional forms and fit coefficients of the phenomenological function. As potential new or better models become available extensive preprocessing and fitting of new spatial density curves would be required before integration into EVOLVE could be accomplished.

The phenomenological function is considered valid for hypervelocity collisions but its applicability to explosions is questionable because the same ΔV distribution used to

characterize hypervelocity collision is used to describe either LIE or HIE breakup events. This assumption is poor for four reasons. First, the model derived for collisions predicts relatively low velocities for larger fragments characteristic of collision ejecta whereas fragments from explosion, especially HIE, have relatively high ΔV velocities. The HIE ejecta velocities can be higher by one or more orders of magnitude for larger sized fragments. Second the velocity distribution can be directionally nonisotropic in an explosion event. Third, explosions fragments do not have a clear-cut dependence on fragment size like that of collision ejecta. Fourth, the collision ΔV model based empirically on observed hypervelocity collision data applied to explosions does not satisfactorily address the basic momentum, energy, and mass balances for such events. The velocity distribution assumed for explosions needs reexamination.

The functional dependences of the cloud evolution model are reasonable, being a fit to the calculated spatial density curves to within a reported factor of 2 over all diameter, altitude, and times. In addition the function has been parameterized as a function of breakup altitude, h_o (Ref. 23). Results show that the function gives the maximum spatial density at h_o decreasing in a predictable fashion at altitudes away from h_o. The time evolution of the debris cloud has been modeled, taking into account the solar flux variability in a unique way. Rather than incorporating an explicit solar flux dependence into the phenomenological function by fitting curves over a wide range of solar flux level S, the solar dependence is accounted for implicitly through calculation of an effective time in the environment. By adjusting the propagation interval to be the ratio of the atmospheric density at the current year's solar flux to the density as $S = 1.1 \times 10^6$ Janskeys, the effective solar activity trends have been shown to be reproduced.

The number of fragments produced per subcloud in a debris cloud are generated using one of three cumulative number versus mass distributions depending on breakup type. These breakup models are crucial to the EVOLVE model fidelity since they determine the number contribution of cloud debris to the environment spatial density. Hypervelocity collisions are modeled using a fit to a power law distribution. The number distribution is sensitive to the total amount of mass available for fragmentation as well as the slope coefficient (b) of the distribution. The slope coefficient b is determined from limited hypervelocity impact data. The numbers of objects produced in a collision is least sensitive to variations in the fit parameter near $d = 1.0$ cm becoming increasingly sensitive for smaller ($d << 60.0$ cm) and larger ($d >> 60.0$ cm) objects. A small b value produces a shallower slope and a proportionately larger number of fragments. Likewise, a steeper slope increases the relative number of smaller fragments. The slope has been shown to be extremely sensitive to the selected value of b. Further data should be obtained to reduce the uncertainty in the collision breakup number distribution.

The methodology to estimate the total amount of ejecta mass involved in the collision distribution is simple, but sufficient, in view of the large unknowns associated with hypervelocity impact mechanisms. The ejecta mass is assumed proportional to the projectile kinetic energy. If the ejecta mass is > 10 percent of the target mass, the residual target mass

is assumed to experience an LIE breakup caused by shock waves and secondary impacts resulting from the collision. This is a valid model assumption intended to simulate the expected hypervelocity breakup in a realistic way.

Explosion cumulative number distributions are likewise fit to a limited database. The LIE obeys an exponential law distribution whose basis is a single ground-based explosion test. The LIE has an effective size cutoff at $d = 1.0$ cm. The exponential law form consists of a two-part function, each part dependent on two fit coefficients (a, b). The function is normalized to a 1000-kg relative mass so that the same function with the same coefficients can be used to describe the number distribution for any total mass. The uncertainty has been estimated for the (a, b) fit coefficients. The overall uncertainty in maximum yield in the cumulative number due to the uncertainty in the fit coefficients was found to be approximately a factor of 10. Like the collision distribution, the fit uncertainties can be reduced with more abundant quality data.

The HIE cumulative number distribution is a mixture of an LIE distribution (90-percent contribution) coupled with an inverse mass distribution (10-percent contribution). The proportions of each component are intended to model the situation where a small portion (10 percent) of a spacecraft, exposed directly to the explosive (e.g., residual fuel), experiences the HIE while the rest of the spacecraft undergoes secondary breakup via an LIE. The inverse mass distribution is valid only over 0.1 cm $< d < 10.0$ cm and is designed to contribute the large population of small fragments, up to a minimum diameter, characteristically observed in ground-based HIE experiments. The HIE distribution experiences a slight discontinuity between the inverse mass and LIE components, which can be eliminated by an adjustment of the reference mass parameter used to normalize the function. Since the inverse mass distribution presents an inflexible model to describe the distribution for these size fragments, an exponential law distribution similar to the LIE might better serve to describe this distribution. An LIE-type exponential law distribution has been used to describe the behavior of HIE fragments elsewhere (Ref. 5).

A major feature of the EVOLVE model is the ability to produce a statistical study of future debris environments based on the statistical uncertainty in the occurrence of collisions and explosions. The random occurrences of collisions and explosions is based on entirely different processes but for the purposes of modeling their occurrence, a standard Monte Carlo technique is applied to both processes in similar fashion. The occurrence of breakup events depends on assumed probabilities of each breakup type occurring over a specified time interval. Poisson statistics are used to model the probability of occurrence. The probabilities for collisions between two distinct particles are dynamic in the sense that they depend on the spatial density of each particle size within an altitude band. As the ambient spatial density of objects increases so does the collision probability. Explosions depend simply on the number of intact explosive objects inserted deterministically from the traffic model. The explosion rate is determined from preset assumed probabilities based on historical experience.

In summary, EVOLVE has significant limitations to the ranges over which it is intended to operate. The sum of the contributions from collision and explosion breakup models do not sufficiently populate the environment below d = 0.1 cm to account for all sources of debris. Explosions contribute nothing below 0.1 cm. The only source of fragments in EVOLVE below this diameter is collision fragments resulting from the power law function with no lower limit. Sources of small fragment debris below 0.1 cm, such as solid rocket motor effluent, are not modeled in EVOLVE. The EVOLVE model is limited by the type of orbits which can be processed. Any LEO whose perigee altitude lies within $100 \leq h_p \leq 2000$ km and apogee altitude $h_a \leq 40000$ km ($h_a > 40000$ km is automatically set to 40000 km) can be modeled. Thus, the EVOLVE program cannot model most midaltitude (e.g., circular) or any geosynchronous satellite orbits. These limitations are not stringent limitations for orbital debris environment modeling for most user applications.

The EVOLVE model assessed in this study has been shown to contain certain model components with demonstrated reasonably large uncertainties which may make the actual model results too suspect to be used as a validated, rigorous operational AF tool for detailed analysis of the long-term time-evolved debris environment. The model uncertainties are not so overwhelming, however, so as to make this model useless as a tool for estimating the debris environment at any historical or future point in time. This model represents an early developmental analysis code to provide reasonable predictions of the debris environment population with assumptions incorporated either to cover areas where little or no data exists (e.g. the number distributions in explosion or collision breakup events) or to make the model computationally efficient (e.g. the phenomenological debris cloud model). There is definitely room for improvement and additional data in several of the models. Thus, it is the conclusion of this study that the EVOLVE model assessed for this study (an early developmental version supplied by NASA/JSC) does not adequately meet AF requirements for a validated long-term model without further improvements.

Nevertheless, this model does contain the necessary framework to meet AF requirements if it is incorporated with properly validated and improved breakup and propagation models and a revised treatment of debris cloud modeling. The EVOLVE model already contains the essential source/sink models with which to portray the environment in an averaged manner as a function of the most important parameters (time, spatial distribution in altitude, and size distribution). Furthermore, the model has the valuable capability of performing probabilistic Monte Carlo studies of future debris environment states and generate statistical uncertainties of the environment due to the probabilistic occurrences of future collision and explosive breakups. The modularity of the program facilitates model changes and provides an excellent test-bed for evaluating new traffic, breakup, and orbital propagation/decay models applicable to debris modeling. The modeling philosophy behind EVOLVE is to estimate the environment from the viewpoint of the source terms contributing debris to the environment (primarily launches, on-orbit explosions, and hypervelocity collisions) and then time-evolving the fragments using sink models (such as atmospheric drag orbital contraction model) to decay the LEO debris population with time. In this regard, the model is successful and it is

recommended that this model be considered as a candidate model for AF long-term modeling efforts.

4.3 RECOMMENDATIONS

There are some areas in the EVOLVE model assessed in this study where future improvement work is recommended. This report assessed the EVOLVE model as it was developed through May 1991. Being a model still under development at NASA/JSC, it should be noted that some of the recommendations presented here will have already been addressed by the time this assessment report is completed and released. The known improvements made to date will be noted parenthetically with the recommendation. The recommendations are as follows:

- Obtain new or develop improved projected traffic model data to implement into the PRJ input files. The EVOLVE model ultimately is only as good as the detailed traffic being sent into the orbital environment. For the EVOLVE model to be a realistic tool for predicting future environments, detailed mission models that include not only US civilian launches like that found in the US Civil Needs Data Base (Ref. 14), but also the proposed traffic from DoD programs and foreign sources (Soviet and non-Soviet must be incorporated).

- Reevaluate the debris cloud evolution model phenomenological function derivation so that it can facilitate model changes in the assumed velocity distribution, velocity spreading function, and/or velocity directionality distribution. Currently, those functions are implicit in the FRGMNT curves with which the phenomenological function was fit. Using FRGMNT, series of curves were parameterized in terms of diameter d. Each size value determined the most probable ejecta velocity ΔV_p and spreading function $D(\Delta V)$, and the curve results returned contained the ΔV_p and $D(\Delta V)$ implicitly. Instead, it is suggested that a series of curves be generated for fixed values of ΔV_p distributed by a spreading function and a phenomenological function derived from fits to these curves. By parameterizing the function in terms of a characteristic velocity for each size d rather than by the size d itself (which is needed in the DEBOE subroutine of FRGMNT to calculate ΔV_p), the velocity distribution and its associated spreading function may be isolated as separate models which require the size as input. Like the cumulative mass distribution breakup models, they may be installed in EVOLVE as subroutines that can be modified easily or replaced with new improved models. This flexibility can further the utility of EVOLVE as a test-bed for possible new velocity distribution models as more data become available.

- Develop separate velocity distribution models for LIE and HIE events, separate from the collision events. The current EVOLVE model assumes the same ΔV_p and $D(V)$

127

distributions (derived from hypervelocity collision data) for all three types of breakup events.

- Improve handling of explosive objects by retaining identity and orbital information of potentially explosive objects in the Monte Carlo modeling of future explosions. In this way the type of explosion could be determined from the objects type (e.g., a Soviet EORSAT), and the 28-percent LIE and 72-percent HIE frequency breakdown assumption can be discarded. Since the identity of explosion events would be retained, the program can keep track of LIE and HIE occurrence rates and debris clouds separately. (Improvement has been made in later EVOLVE versions.)

- Remove assumption of all LIE events involving a 1000-kg total mass parent object and an HIE event involving a 6000-kg mass parent object. This can readily be done if the identity of the exploding object is maintained in the item above. (Improvement has been made in later EVOLVE versions.)

- Represent the uncertainty in the a and b coefficients in the collision and explosion mass distribution models by a spread distribution. The spread in the coefficient could then be drawn randomly from a distribution which represents the uncertainty spread in the coefficients (which can result, in part, from uncertainties in knowing structure specific parameters). These randomly drawn coefficients would then be used in the distribution functions.

- Incorporate new breakup cumulative mass distribution models as new data and models become available. There is ongoing interest in the debris community to establish a better database for such distributions. On-orbit breakup event fragment observations and ground-based collision and explosion tests should better quantify the existing models. Upcoming hypervelocity tests such as the FRGITS and SLAM tests being conducted by the Defense Nuclear Agency should add to the available database and reduce the large uncertainties involved. The breakup models are easily installed in EVOLVE.

- Include the effects of solid rocket motor effluent (Al_2O_3 particles) and meteoroids to account for the small size debris population. At present, these are expected to be the largest contributors to the population below d < 0.1 cm not currently accounted for in EVOLVE. Their inclusion would enhance the utility and robustness of the EVOLVE model to characterize the total debris environment.

- Allow the launch data known for all historical objects in the historical database to determine the orbital insertion epoch for each object. Currently, EVOLVE randomizes all launch date which is satisfactory in a statistical sense. This improvement would make the EVOLVE model more robust. (Improvement has been made in later EVOLVE versions.)

REFERENCES

1. Kessler, D.J., "Orbital Debris Environment for Spacecraft in Low Earth Orbit," AIAA 90-1353, April 1990.

2. Kessler, D.J. and Cour-Palais, B.G., "Collision Frequency of Artificial Satellites: The Creation of a Debris Belt," J. of Geophysical Research, 83, A6, June 1, 1978.

3. Su, S.Y. and Kessler, D.J., "Contribution of Explosion and Future Collision Fragments to the Orbital Debris Environment," Advances in Space Research, 5, 2, pp. 25-34, 1985.

4. Su, S.Y., "Orbital Debris Environment Resulting from Future Activities in Space," Advances in Space Research 6,7, pp. 109-117, 1986.

5. Bess, T.D., "Mass Distribution of Orbiting Man-made Space Debris," TN D-8108, National Aeronautics and Space Administration, Johnson Space Center, Houston, TX, December 1975.

6. McKnight, D. S., "Determination of Breakup Initial Conditions," J. of Spacecraft, 28, 4, pp. 470-477, 1991.

7. Kessler, D.J., "Derivation of the Collision Probability between Orbiting Objects: The Lifetimes of Jupiter's Outer Moons," Icarus 48, pp. 39-40, 1981.

8. Reynolds, R.C., "A Review of Orbital Debris Environment Modeling at NASA/JSC," AIAA-90-1355, April 16-19, 1990.

9. Mueller, A.C., The Decay of the Low Earth Satellite for the Orbital Debris Study J.O. 69-067, Rept. 17520, Lockheed Engineering and Management Services Company, Houston, TX, December 1981.

10. Mueller, A.C., Jacchia-Lineberry Upper Density Model, NASA JSC-18507, October 1982.

11. Reynolds, R.C. Documentation of Program EVOLVE: A Numerical Model to Compute Projections of the Man-made Orbital Debris Environment, System Planning Corp. Report OD91-002-U-CSP, System Planning Corp., Houston, TX, 15 February 1991.

12. Reynolds, R.C. Documented EVOLVE Source Code Listing (Draft), System Planning Corp. Report OD91-002-U-CSP, System Planning Corp., Houston, TX, 15 February 1991.

13. Kessler, D.J., Reynolds, R.C., and Anz-Meador, P.D., <u>Orbital Debris Environment for Spacecraft Designed to Operate in Low Earth Orbit</u>, TM 100471, NASA Johnson Space Center, Houston, TX, April 1989.

14. Version 3.0, Civil Needs Database, 1988.

15. "Low Precision Formulas for the Sun's Coordinates and the Equation of Time," 1991 Astronomical Almanac, pg. C24.

16. McKnight, D.S., ed., <u>Orbital Debris Monitor</u>, 4, 3, July 1, 1991.

17. Johnson, N.L., "History and Consequences of On-orbit Breakups," <u>Advances in Space Research</u>, 5, 2, pp. 11-20, 1985.

18. Harnett, D.L., <u>Introduction to Statistical Methods</u>, 2nd Edition, Addison-Wesley Publishing Co., 1975.

19. Su, S.Y., "The Velocity Distribution of Collisional Fragments and its Effect on Future Space Debris Environment," <u>Advances in Space Research</u>, 10, 3/4, pp. 389-392, 1990.

20. Bess, T.D., <u>Size Distribution of Fragment Debris Produced by Simulated Meteroid Impact on Spacecraft Walls</u>, SP-379, NASA Johnson Space Center, Houston, TX, 1975.

21. Badhwar, G.D. and Anz-Meador, P.D., "On-orbit Breakup Characteristics," <u>AIAA-90-1359</u>, April 1990.

22. Benz, F.J., Bishop, C.V., Eck, M.B., "Explosive Fragmentation of Orbiting Propellant Tanks," <u>Orbital Debris from Upper-Stage Breakup</u>, <u>AIAA Progress in Astronautics and Aeronautics</u>, Loftus, J.P., Jr., ed. vol.. 121, P. 107, 1989.

23. Ojakangas, G.W., Anz-Meador, P.D., and Reynolds, R.C., "Orbital Debris Environment," AIAA Space Programs and Technologies conference, <u>AIAA 90-3863</u>, September 25-29, 1990.

24. Reynolds, R.C., "Review of Current Activities to Model and Measure the Orbital Debris Environment in Low-Earth Orbit," <u>Advances in Space Research</u>, 10, 3/4, pp. 359-371, 1990.

25. Johnson, N.L. and McKnight, D.S., <u>Artificial Space Debris</u>, Orbit Book Company, Malabar, Florida, 1987.

26. King-Hele, D., <u>Theory of Satellite Orbits in an Atmosphere</u>, Butterworths, London, 1964.

27. Hopson, G.D. "Solar Activity Inputs for Upper Atmospheric Models Used in Program to Estimate Spacecraft Orbital Lifetime," Memo EL01 (28-88), NASA Marshall Space Flight Center, Huntsville, AL, February 18, 1988.

28. Knowles, S.H., "Orbital Elements Determination for Breakup and Debris," J. of Spacecraft, 28, 5, pp. 587-591 Sept. - Oct. 1991.

29. Thompson, T.W., and Goldstein, R., "Radar Measurements of Small Debris: Arecibo and Goldstone Radars," AIAA-90-1342, April 1990.

30. Badhwar, G.D. and Anz-Meador, P.D., "Relocation of Radar Cross Section to the Geometric Size of Orbital Debris," AIAA-90-1347, April 1990.

32. Henize, K.G., and Stanley, J.F., "Optional Observations of Space Debris," AIAA-90-1340, April 1990.

32. Potter, A.E. and Heinze, K.G., and Talent, D.L., "Albedo Estimates for Debris," Orbital Debris From Upper-Stage Breakup, AIAA Progress in Astronautics and Aeronautics, Loftus, J.P. Jr., ed., Vol. 121, p. 147, 1989.

APPENDIX A

INTACT OBJECT ORBITAL PROPAGATION MODEL ALGORITHM

The intact object orbital debris model discussed in Subsection 3.1.3 summarized the EVOLVE program steps used to propagate the ith intact object during deterministic processing. This appendix details the steps taken to process intact object orbits. Each numbered item corresponds to the bulleted items in Subsection 3.1.3.1.

1. For the ith object the time elapsed (in years) since launch is determined. The elapsed time, $\Delta t_{launch,i}$, represents the fraction of the current year in which to subject the object to the propagation and decay routines (Subsection 3.3.3). This fraction is calculated using the following expression:

$$\Delta t_{launch,\,i} = t + \Delta t_{step} - \left(t_{launch,\,i} + t_{sk,\,i}\right) \tag{A-1}$$

where t is the current year being considered, Δt_{step} is the time step duration relative to t being considered (currently EVOLVE expects this to be a full year, so $\Delta t_{step} = 1$), $t_{launch,\,i}$ is the launch date epoch for object i in terms of the year it was launched and a decimal fraction thereof (e.g., if object i is launched in mid 1989, then $t_{launch,i} = 1989.5$), and $t_{sk,i}$ is the duration of stationkeeping (in fractional yrs) for object i relative to $t_{launch,i}$.

Stationkeeping extends the launch date beyond the actual launch date. EVOLVE keeps such an object maintained in the list where it continues to contribute to the environment, but does not subject the object to the propagation and decay routines (discussed in Subsection 3.3.3), until the elapsed stationkeeping is over. If $\Delta t_{launch,i} > 0$ and $t_{sk,i} > 0$, the launched object's stationkeeping duration begins and ends within the current year. Equation A-1 is used to evaluate the proper time duration to the end of the current year. If $\Delta t_{launch,i} < 0$ and $t_{sk,i} > 0$, the launched object's stationkeeping extends beyond the current year. If this is the case, it is noted and the orbital parameters are left unchanged. If $\Delta t_{sk,i} = 0$, no stationkeeping is assumed and object is immediately subject to orbital propagation and decay processing. EVOLVE also allows objects to be deorbited if the launched object has a deorbit flag set when read from the databases. If $\Delta t_{launch,i} > 0$ and the deorbiting flag is set (i.e., IDEORB(i) > 0), the object list flag (ISCR(i)) is set to zero and the propagation/decay processing skipped. This is incorrect as it now stands since a mission lifetime is not specified for the object during which its presence will contribute to the environment. Instead, the object is deorbited and removed from the list as soon as it is launched. The stationkeeping and deorbiting features were a recent addition by the NASA developers

and they had not yet been tested.[*] These features are currently not used, with the stationkeeping and deorbit flags usually set to zero in the input manifest lists.

2. The next step in the model is to determine if the perigee altitude for object i, $h_{p,i}$ meets certain conditions for further processing. If $h_{p,i} < h_{min}$, where currently $h_{min} = 100$ km, the object is assumed to have decayed. This value is reasonable since this is the approximate upper boundary of the atmosphere, below which the atmospheric density and atmospheric drag dramatically increases. This minimum value also avoids potential numeric problems in the orbital decay routine (Refs. A-1 and A-2). EVOLVE also removes all objects from the propagation list if $h_{p,i} > 2000$ km to avoid potential numeric problems in the decay software. For the same reason, the object is removed from the list if the apogee altitude $h_{a,i} > 40000$ km. In summary, intact objects are only processed through the propagation/decay routines if

$$100 \text{ km} \leq h_{p,i} \leq 2000 \text{ km}$$
$$h_{a,i} \leq 40000 \text{ km}$$

If $h_{a,i} > 40000$ km, then $h_{a,i}$ is set to 40000 km.

If these conditions are met, the list maintenance flag ISCR(i) is set and processing continues.

3. The orbital propagation routines are now begun here. The initial semimajor axis, a_i, and eccentricity, e_i, are determined from the apogee and perigee altitudes for object i

$$a_i = \frac{h_{a,i} + h_{p,i}}{2} + R_e \qquad (A-2)$$

$$e_i = 1 - \frac{(h_{p,i} + R_e)}{a_i} \qquad (A-3)$$

where $R_e = 6378.145$ km is the average radius of the earth. The time increment over which to propagate the object starting at the beginning of the current year time step is

$$\Delta t_i = 365.2425 \cdot \min(\Delta t_{launch}, \Delta t_{step}) \quad \text{[days]} \qquad (A-4)$$

If an object was launched in a prior year, the propagation begins at the current year t and extends to the end of the current year $t + \Delta t_{step}$ (giving an elapsed time of Δt_{step}). If an object was launched during the current year, the propagation begins at $t + \Delta t_{launch}$

---

[*]Anz-Meador, P.D., private communication, 1991.

and extends to $t + \Delta t_{step}$ giving an elapsed time of $\Delta t_{step} - \Delta t_{launch}$. The epoch at which to calculate the propagated orbital elements is then calculated using USSPACECOM two-line element transmission format (T-format). The T-format for epoch is a decimal number of the form

$$yyddd.dddddd$$

where y indicates the year digit and d indicates a day digit. These epoch conversions are:

$$t_{epoch} = \begin{cases} (t - 1900) \cdot 1000 + \Delta t_{step} \cdot 365.2425 - \Delta t_i & \text{for } t \leq 1999 \\ (t - 2000) \cdot 1000 + \Delta t_{step} \cdot 365.2425 - \Delta t_i & \text{for } t > 2000 \end{cases} \qquad \text{(A-5)}$$

4. The decay routines require the apparent right ascension of the sun as viewed from the earth's equatorial plane. This quantity gives the sun's nadir position on the fixed sphere of the earth throughout a single year. The right ascension is used to calculate sun/moon perturbations on the eccentricity of an orbit. The right ascension, calculated in subroutine RA_S, is based on a low precision formula (Ref. A-3)

$$\alpha = \tan^{-1}(\cos(\epsilon) \tan(\lambda)) \qquad \text{[deg]} \qquad \text{(A-6)}$$

where ϵ is the obliquity of the ecliptic and λ is the ecliptic longitude. These quantities are determined by

$$\epsilon = 23.439° - 0.0000004° \, n \qquad \text{(A-7)}$$

$$\lambda = L + 1.915° \, \sin(g) + 0.020° \, \sin(2g) \qquad \text{(A-8)}$$

where n is the number of Julian calendar days from January 1, 2000, L is the mean longitude of the sun, and g is the mean anomaly. L and g are given by

$$L = 280.460° + 0.9856474 \, n \qquad \text{(A-9)}$$

$$g = 357.528° + 0.9856003 \, n \qquad \text{(A-10)}$$

The mean longitude and mean anomaly must be placed in the range 0 to 360 deg for these expressions to be valid. The quantity n is given as

$$n = JD - 2451545.0 \qquad \text{(A-11)}$$

134

where JD is the Julian date for t_{epoch}. The JD is calculated in subroutine JULDY, (Ref. A-2). The precision of the apparent coordinates of the sun given by the provided formulas (Eqs. A-6 to A-10) is 0.01 deg (Ref. A-3). Thus, it can be assumed that α is accurate to within 0.01 deg.

5. Certain angular quantities required by the decay routines are converted from degrees to radians. These are the inclination i_i, the argument of perigee ω_i, the right ascension of the ascending node Ω_i, and the right ascension of the sun α. The drag routines require the ballistic coefficient $B = C_D \cdot (A/M)_i$ where $(A/M)_i$ is the area to mass ratio of the intact object i read from the data file and $C_D = 2.2$ is the coefficient of drag (assumed the same constant for all objects). The exospheric temperature, T_∞, is calculated in subroutine TINF10 based on the current year's F10.7 cm solar flux constant derived from a look-up table in subroutine SOLACT. The current values of a_i, e_i, and i_i are stored before the propagation routines are invoked.

6. The orbital propagation and atmospheric drag/decay routines are now called via subroutine DECAY which requires 10 parameters as inputs. These are listed as follows:

> a_i - initial semimajor axis for orbit i
> e_i - initial eccentricity for orbit i
> i_i - inclination for orbit i (does not change in DECAY)
> ω_i - argument of perigee for orbit i
> Ω_i - right ascension of the ascending node for orbit i
> $B_i = C_D(A/M)_i$ - (ballistic coefficient/coefficient of drag x area/mass ratio for
> object i)
> α - right ascension of the sun
> T_∞ - exospheric temperature
> Δt_i - time period to propagate orbit i

The tenth parameter is an integer flag, IMARK, which allows the decay software to determine the type of orbit (Ref. A-4). If IMARK = 0, the decay routines automatically classify orbit type, whereas if the eccentricity $e_i > 0.2$ the orbit is forced to use the Type 3 orbit. The DECAY model is described in Subsection 3.3.1.3. Upon returning to ORBUPD, the DECAY routines have "propagated" the orbital parameters a_i, e_i, and i_i by returning the modified values which are now current at the end of the year $(t + \Delta t_{step})$. The updated values are now simply averaged with the original values of a_i, e_i, and i_i (prior to the call to DECAY) to obtain $\bar{a}_i$, $\bar{e}_i$, and $\bar{i}_i$. It should be noted that, although averaged, the DECAY package does not alter the inclination which remains constant through all calculations.

7. The averaged values $\bar{a}_i$, $\bar{e}_i$, and $\bar{i}_i$ are used as input to the subroutine PRECPY which calculates the orbital precession of the right ascension of the ascending node, Ω_i, and the argument of perigee ω_i. These are secular orbit perturbations caused by the J_2

second harmonic term in the earth's gravitational potential resulting from the earth's oblateness. Based on King-Hele (Ref. A-5), these perturbations are

$$\dot{\omega}_i = \frac{3}{4} J_2 n_i \left(\frac{R_e}{P_i}\right)^2 (5 \cos^2 (\bar{i}_i) - 1) \cdot \left(\frac{180°}{\pi}\right) \cdot \left(\frac{31556952}{year}\right) \quad [°/yr] \qquad (A-12)$$

$$\dot{\Omega}_i = -\frac{3}{2} J_2 n_i \left(\frac{R_e}{P_i}\right)^2 \cos^2 (\bar{i}_i) \cdot \left(\frac{180°}{\pi}\right) \cdot \left(\frac{31556952}{year}\right) \quad [°/yr] \qquad (A-13)$$

where $J_2 = 1.08264 \times 10^{-3}$ is the oblateness second harmonic term,

$$n_i = \sqrt{\frac{\mu}{\bar{a}_i^3}}$$

is the mean motion, $R_e = 6378.145$ km is the earth's mean radius, and $\bar{i}_i$ average orbital inclination. The change in the Ω and ω over the period is added to the old Ω and ω values to obtain updated values:

$$\Omega_i = \Omega_i + \dot{\Omega}_i \frac{\Delta t_i}{365.2425} \qquad (A-15)$$

$$\omega_i = \omega_i + \dot{\omega}_i \frac{\Delta t_i}{365.2425} \qquad (A-16)$$

It should be noted that the secular orbit perturbation calculations are performed outside the DECAY package routines in the subroutine ORBUPD.

8. The next step is to compare the current perigee altitude against the value of $h_{min} = 100$ km. If $h_{p,i} < 100$ km, the ISCR(i) flag is set to zero to indicate that the object be removed from the object list since it has decayed. Steps 1 through 8 are repeated until the current maximum number of orbits has been reached.

9. The final step in the intact object orbital propagation model is to loop one final time through all orbits i = 1 ... NORB removing all objects whose ISCR(i) flag has been set to zero. The result is a compacted list of objects that remain in orbit at the end of the current year time step. The processing exits ORBUPD where the main program readies for the succeeding year's processing.

Steps 1-9 are repeated for each time step of the deterministic time loop in EVOLVE.

APPENDIX A REFERENCES

A-1.   Reynolds, R.C. <u>Documentation of Program EVOLVE: A Numerical Model to Compute Projections of the Man-made Orbital Debris Environment</u>, System Planning Corp. Report OD91-002-U-CSP, System Planning Corp., Houston, TX, 15 February 1991.

A-2.   Reynolds, R.C. <u>Documented EVOLVE Source Code Listing (Draft)</u>, System Planning Corp. Report OD91-002-U-CSP, System Planning Corp., Houston, TX, 15 February 1991.

A-3.   "Low Precision Formulas for the Sun's Coordinates and the Equation of Time", 1991 Astronomical Almanac, pg. C24.

A-4.   Mueller, A.C., <u>The Decay of the Low Earth Satellite for the Orbital Debris Study J.O. 69-067</u>, Rept. 17520, Lockheed Engineering and Management Services Company, Houston, TX, December 1981.

A-5.   King-Hele, D., <u>Theory of Satellite Orbits in an Atmosphere</u>, Butterworths, London, 1964.

APPENDIX B

SATELLITE CONSTELLATION HAZARD ASSESSMENT USING EVOLVE

A study was made to evaluate the feasibility of using the EVOLVE code results for probability of collision studies for a prescribed satellite constellation. Specifically, a top-level collision probability study of two possible satellite constellations within the background LEO debris environment was conducted to demonstrate the use of EVOLVE flux output as a means of determining the hazard to a particular satellite. The output of EVOLVE is spatial density converted to flux (in units of impacts/meter^2-year) via a constant relative velocity of 7.0 km/s. This output is obtained in the form of 3-D arrays storing the flux in a small set of altitude bins h, cumulative size (diameter) bins d, and tagged by time t (as discussed in Subsection 2.3). The deposition of intact objects and breakup fragments is assumed to be distributed instantaneously and uniformly about the earth (Subsection 3.2.4). The volume used to determine the radially (altitude) dependent spatial density (or flux) is the volume of this thin spherical shell (Subsection 3.1.4). The flux can easily be examined in any of the three dimensions (d, h, t), but perhaps the time dependence of F(d, h, t) for a fixed h_o, d_o is of most interest to the system designer desiring to know the probability of impact that his/her spacecraft has with the debris environment.

The probability of collision calculations used in this study utilizes the EVOLVE flux F(d, h, t) in a relatively straightforward manner. The cumulative number of impacts on a randomly oriented surface of area A over a period of exposure time $t_{exp} = t_f - t_i$ in the environment is given by

$$N = \int_{t_i}^{t_f} A \cdot F(d_o, h_o, t) \, dt = A \sum_{t = t_i}^{t_f} F(d_o, h_o, t)\Delta t \qquad \text{(B-1)}$$

where $\Delta t = 1$ yr for EVOLVE results. The probability that exactly n impacts will occur is given by a Poisson distribution

$$P_n = \frac{N^n}{n!} e^{-N} \qquad \text{(B-2)}$$

The probability then depends on the exposure time t_{exp} used to calculate N which is generally the time since satellite deposition into orbit. The total probability of collision for an entire constellation is obtained by summing the individual satellite collision probabilities.

EVOLVE provides only the average flux of particles for a specific (d, h, t) combination. It does not calculate the cumulative N or P_n; instead, postprocessing software was written to prepare the data presented in this analysis. Two programs, CPROB.FOR and TOT.FOR, were

written to generate ASCII files containing the flux versus N and P_n values necessary for input to a separate plotting package.

Results for two possible constellation architectures (described in the sections below) have been obtained using EVOLVE to calculate flux. "Small" and "large" constellations, referring to the number of satellites deployed, were developed as inputs to the EVOLVE code. Three scenarios (A, B, C) were run for each constellation.

The "small" constellation architecture consists of the following:

- 60 total satellites deployed
- All circular orbits
- Three altitude layers:
  - 16 satellites of 700 km, i = 45 deg
  - 32 satellites of 1600 km, i = 90 deg
  - 12 satellites at h_a = 2500 km, h_p = 500 km, i = 0 deg (4 satellites) and i = 90 deg (8 satellites)
- Launch rate: 1993-1998: 10 satellites/year
- 10-yr stationkeeping upon deployment
- Each satellite has 10-m^2 area, 450-kg mass
- Each satellite launched with Titan IV booster (17.671 m^2, 12000 kg) and 4 bolts   (4.3 x 10^{-4} m, 0.01 kg ea.)
- Constellation satellites and rocket bodies do not explode
- Deployment Schedule in Table B-1

Table B-1. "Small" constellation deployment schedule.
Number Deployed

Year	Type 1 (400 km)	Type 2 (1600 km)	Type 3 (2500 km)
1993	4	6	-
1994	4	6	-
1995	-	8	2
1996	-	8	2
1997	4	2	4
1998	4	2	4
TOTAL	16	32	12

Three scenarios, designated A, B, or C, were run for this constellation:

A.   Deployed architecture with three high-intensity explosions (HIE), one low intensity explosion (LIE) per year induced, one collision in 1995 (between 500-kg target and 1-kg projectile)

139

B.   Architecture deployed, but not further future collisions or explosions

C.   No architecture deployed; normal launch activity.

The "large" constellation architecture consists of the following:

- 1000 total satellites deployed
- All circular orbits at i = 89 deg
- Three altitude layers:
  - 340 satellites at 400 km altitude
  - 330 satellites at 450 km altitude
  - 330 satellites at 500 km altitude
- Launch rate: 1993-1999: 30 satellites/year
                   2000-2010: 50 satellites/year
                   2011-2015: 48 satellites/year
- 7-yr stationkeeping upon dep loyment
- Each satellite has 1-m^2 area, 80-kg mass
- Each satellite launched with Titan IV booster (17.671 m^2, 12000 kg) and 4 bolts   (4.3 x 10^{-4} m, 0.01 kg ea.)
- Constellation satellites do not explode
- Deployment Schedule in Table B-2

Three scenarios, designated A, B, or C, were run for this constellation:

A.   Deployed architecture with three HIE and one LIE per year induced, two collisions (in 1995 between 500 kg and 1 kg objects, in 2011 between 850 kg and 1 kg objects)

B.   Architecture deployed, but not further future collisions or explosions

C.   No architecture deployed; normal launch activity.

The flux versus time results are shown in Figures B-1 and B-2 for scenarios A and B, respectively, for both constellations. (Scenario C is virtually identical to scenario A for both constellations and is not shown for clarity.) The small constellation flux was calculated at the mean altitude h = 1550 km (Δh = 1850) while the large constellation flux was determined at h = 450 km (Δh = 150 km). The altitudes were selected to determine the average debris environments in which the two constellations are exposed. The Δh widths were chosen to ensure inclusion of the stationkept intact constellation satellite orbits within the volume defined by Δh. Satellites launched early in deployment for the large architecture will begin decaying from their stationkept orbit as soon as the 7-yr stationkeeping duration ends. This means that some satellites will likely exit the volume defined by Δh before the year 2019. Their orbits will fall below 375 km (lower limit of the volume used to calculate the spatial

Table B-2. "Large" constellation deployment schedule.
Number Deployed

YEAR	Type 1 (400 km)	Type 2 (450 km)	Type 3 (500 km)
1993	10	10	10
1994	10	10	10
1995	10	10	10
1996	10	10	10
1997	10	10	10
1998	10	10	10
1999	10	10	10
2000	20	20	10
2001	20	10	20
2002	10	20	20
2003	20	20	10
2004	20	10	20
2005	10	20	20
2006	20	20	10
2007	20	10	20
2008	10	20	20
2009	20	20	10
2010	20	10	20
2011	16	16	16
2012	16	16	16
2013	16	16	16
2014	16	16	16
2015	16	16	16
TOTAL	340	330	330

density) into the denser atmosphere where drag decay will proceed quickly. The cumulative probability results presented here assume that all satellites remain within the specified volume through the specified time range. This is true for the small constellation where the stationkeeping duration exceeds the year 2010 for all constellation satellites.

The flux level changes dramatically when explosions and collisions are turned off for future years especially at low altitudes as shown in Figure B-2. Here, the atmospheric density is large enough to cleanse much of the debris through drag effects. Also, the periodic solar activity effect on atmospheric density becomes very pronounced at the lower altitude (as seen in the large constellation case of Fig. B-2).

For each scenario, plots of the cumulative number of impacts Equation B-1 that a single constellation satellite would experience in the environment as a function of the projected year are shown in Figures B-3 to B-8. For each scenario, results were obtained for cumulative

diameter sizes of d ≥ 0.1 cm, d ≥ 1.0 cm, and d ≥ 10.0 cm. The increased cumulative number of collisions for future three-HIE/one-LIE rate case (scenario A) over the case where future collisions/explosions are turned off (scenario B) is clearly evident for both constellations. The difference between scenarios A and C (which gives the contribution of the constellation intact satellites) was observed to be negligible except for the large constellation d ≥ 10.0 cm size bin where the contribution from the large number of 1.0-diameter satellites becomes noticeable in deployed constellation case. The small number of satellites deployed in the small constellation has a negligible effect on the environment.

The small constellation satellite shows a greater risk to collision (for all sizes) than the large constellation satellite. Primarily, this is due to the much larger exposure area assumed for the small constellation satellite (10 m^2 compared to 1 m^2).

Figures B-9 to B-14 show the cumulative probabilities of collision for the three diameter sizes for both constellations that a "test" satellite having the cross-sectional area indicated will experience assuming the test satellite is exposed to the environment starting in 1993 (the first year of deployment for both constellations). The sums of all curves (n = 0 to ∞) add to unit probability. The probabilities of collision with d ≥ 0.1-cm objects for a single satellite is very low but increases with exposure time to the environment. The curves indicate that a collision with a d ≥ 0.1-cm object is more likely than no collision after about 7 yrs for the smaller constellation.

The net results for both constellations are shown in Figures B-15 (small constellation) and B-16 (large constellation) which give the overall hazard assessment of the constellation in terms of impact with debris fragments having the indicated cumulative diameters. These curves were obtained using Equation 1 for the deployed satellites and the corresponding deployment schedule to obtain t_{exp} for each projected year. Equation B-1 is multiplied by the number of satellites deployed during that projected year n_j and the total is obtained by summing all projected year contributions

where j = 1993-1998 for the small constellation and j = 1993-2015 for the large constellation. The assumption is made that no constellation satellites decay from orbit over the time ranges examined (1993-2010 for the small constellation and 1993-2019 for the large constellation).

Figure B-15 indicates that the small constellation can expect to experience at least one collision with a 1.0-cm or larger object shortly after the year 2010 (17 yrs after initial deployment) while Figure B-16 shows the large constellation has a smaller probability of collision (five times less likely) for the same size object. Again the cross-sectional area difference between the constellation satellites is the factor primarily responsible here.

142
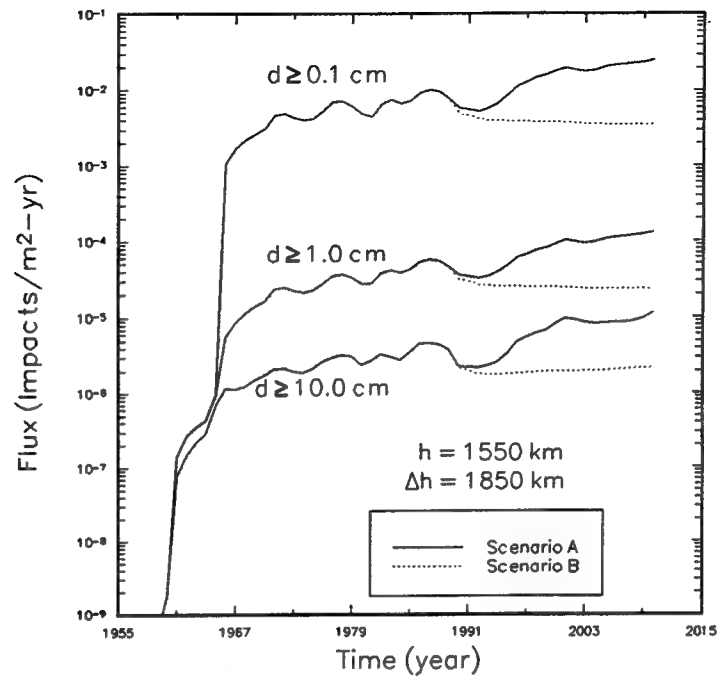
Figure B-1.   Flux for the "small" constellation deployed with the normal three-HIE/one-LIE per year rate (scenario A) compared to no future explosions or collisions (scenario B).
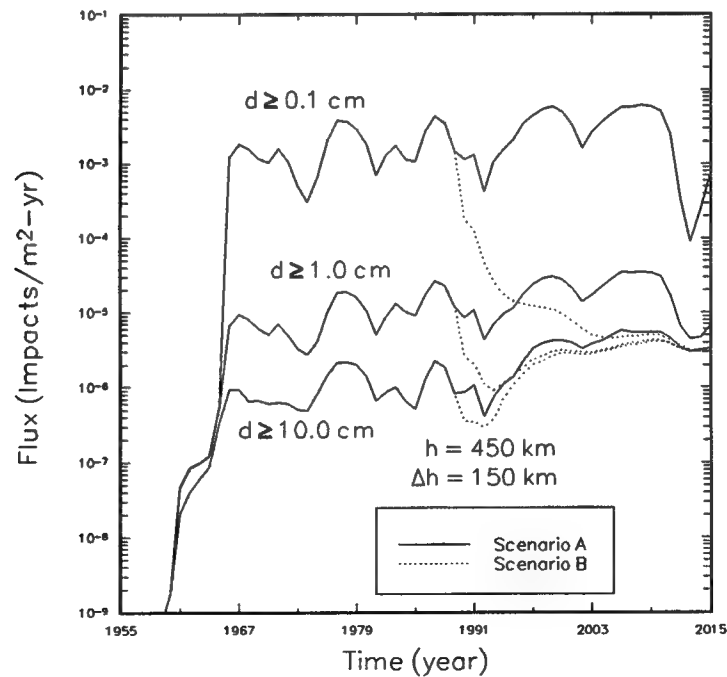
Figure B-2.   Flux for the "large" constellation deployed with the normal three-HIE/one-LIE per year rate (scenario A) compared to no future explosions or collisions (scenario B).

143
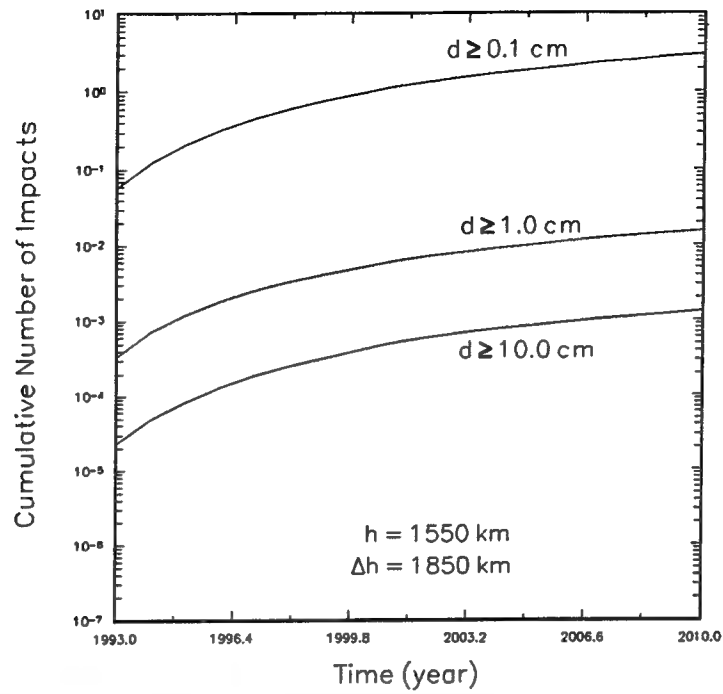
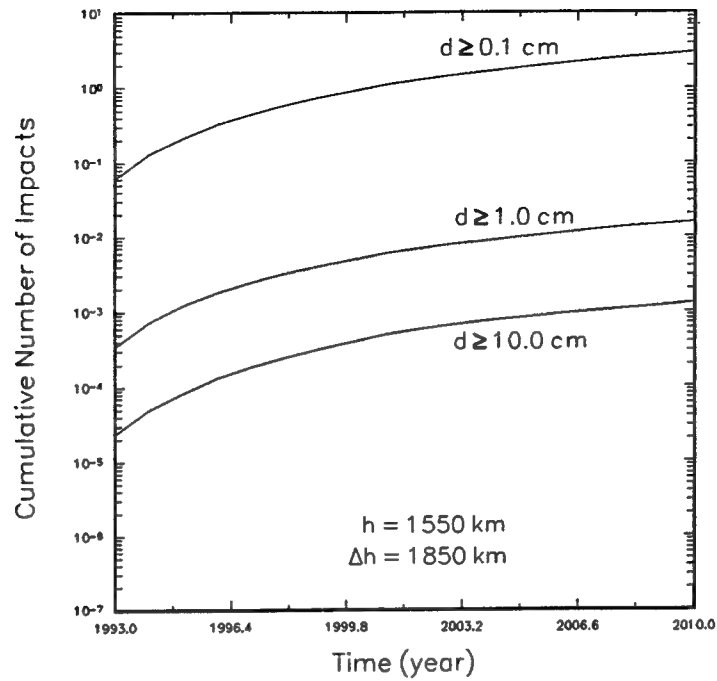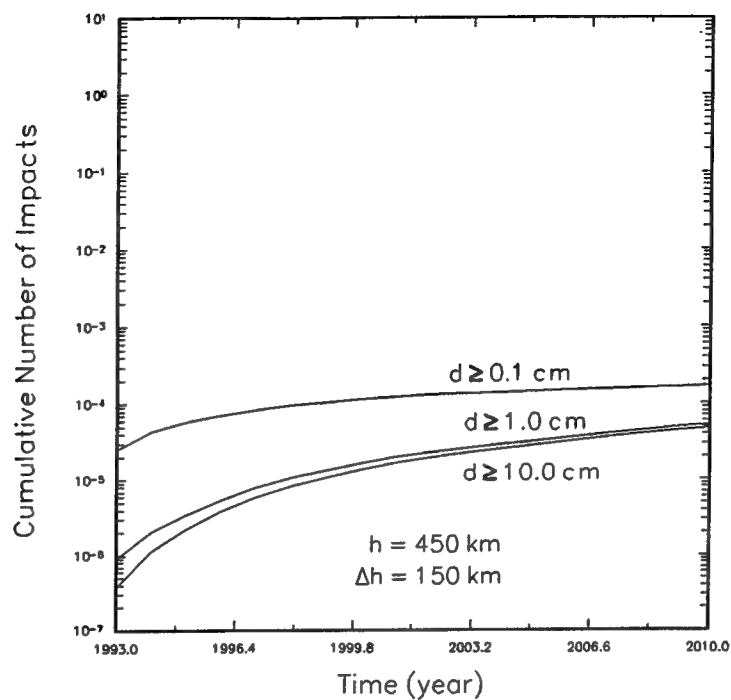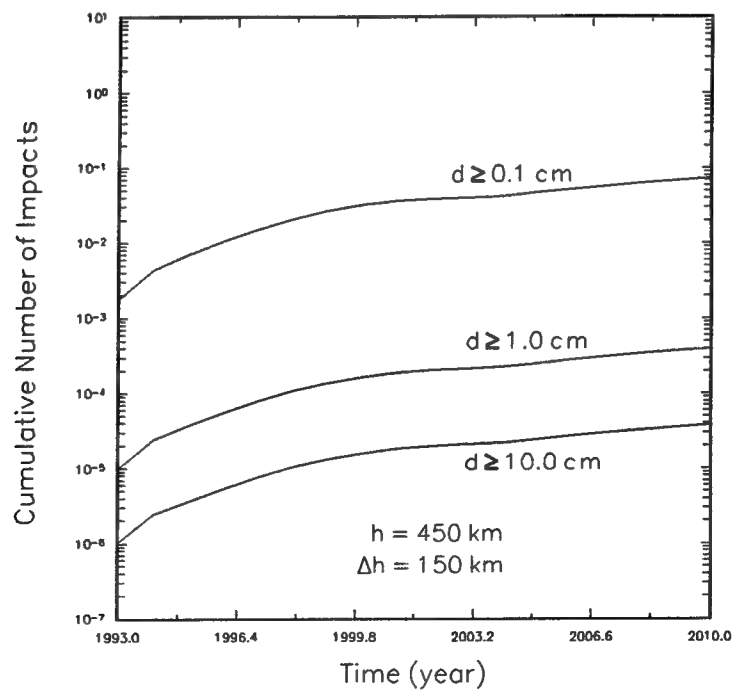Figure B-3. Cumulative number of impacts experienced by a 10 m² area satellite in an environment containing the "small" architecture for scenario A.
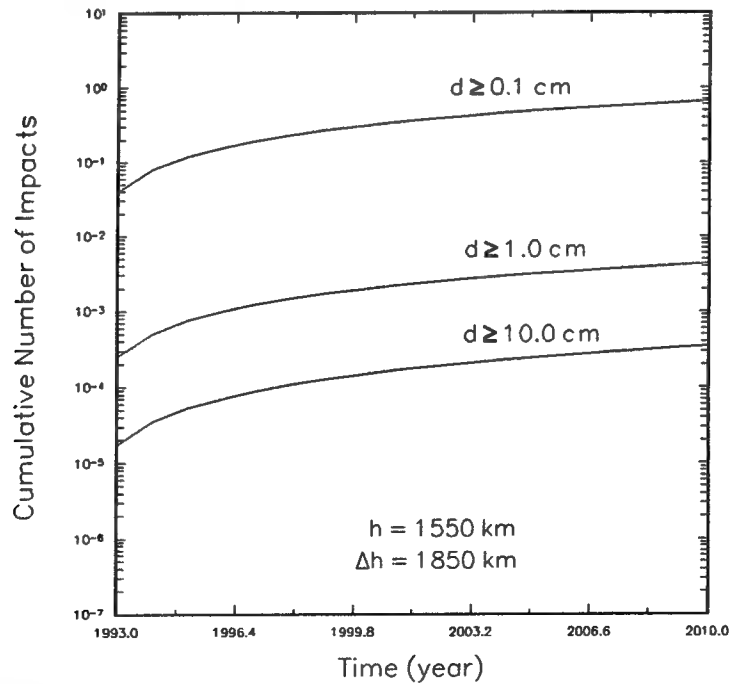
Figure B-4. Cumulative number of impacts experienceed by a 10 m² area satellite in an environment containing the "small" architecture for scenario B.

144

Figure B-5. Cumulative number of impacts experienceed by a 10 m² area satellite in a background environment (no constellation deployment) for scenario C.
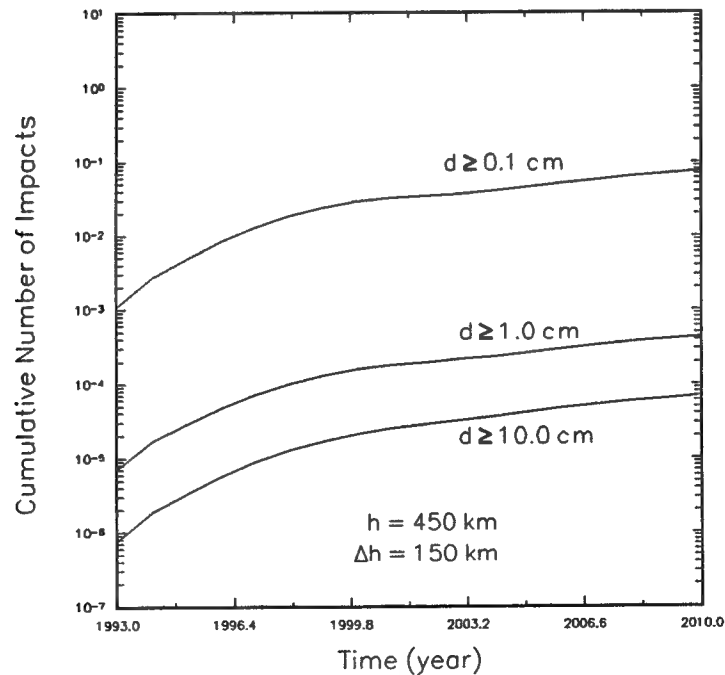
Figure B-6. Cumulative number of impacts experienced by a 1 m² area satellite in an environment containing the "large" architecture for scenario A.

145

Figure B-7. Cumulative number of impacts experienced by a 1 m² area satellite in an environment containing the "large" architecture for scenario B.

Figure B-8. Cumulative number of impacts experienced by a 1 m² area satellite in a background environment (no constellation deployment) for scenario C.
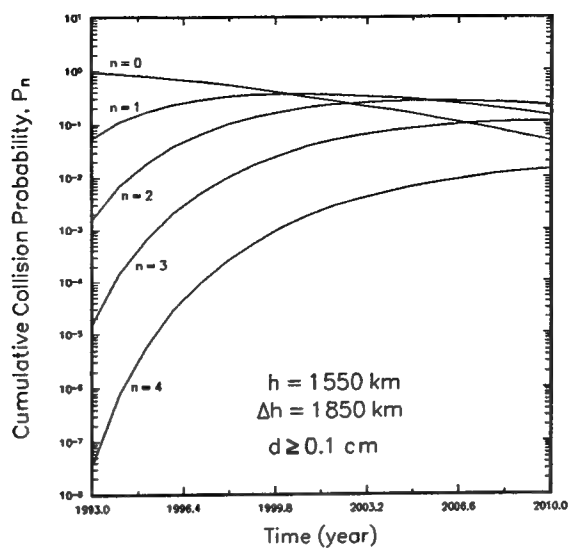
(a) P_n versus time for $d \geq 0.1$ cm
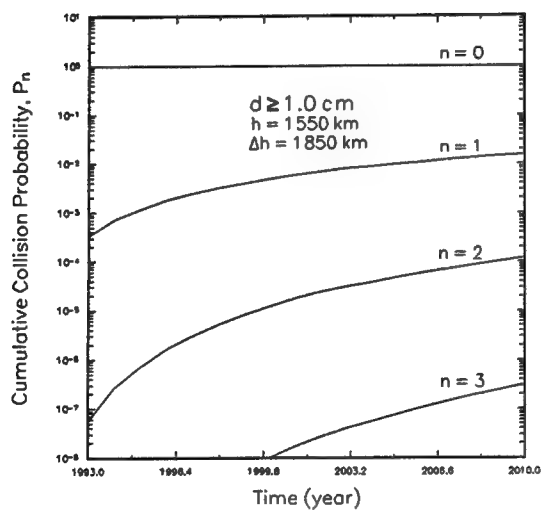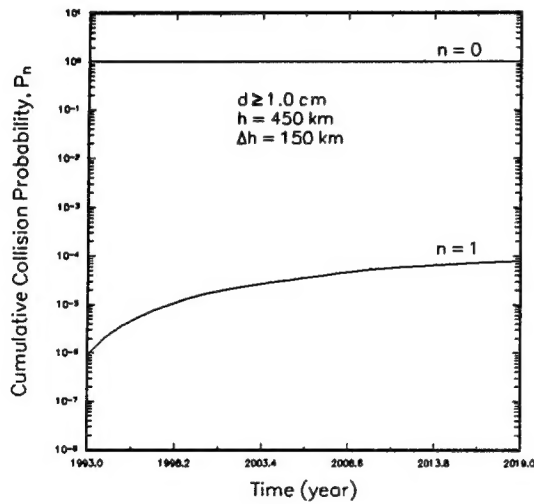

(b) P_n versus time for $d \geq 1.0$ cm
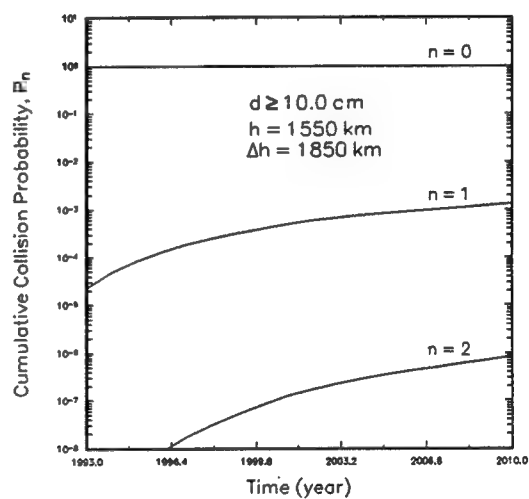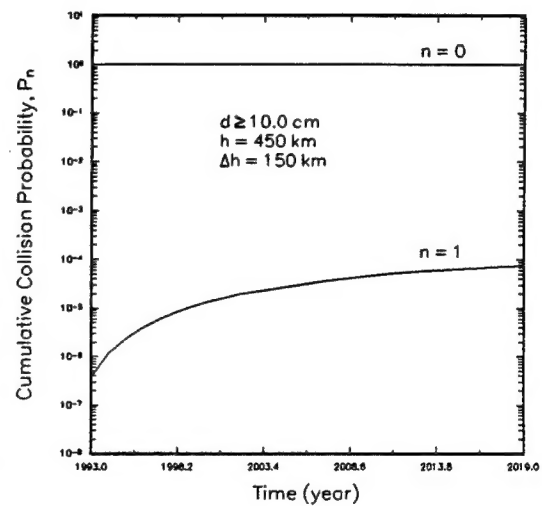
(c) P_n versus time for $d \geq 10.0$ cm

Figure B-9.   Cumulative probabilities of impact versus time for three cumulative diameter size cases for a 10-m^2 satellite in scenario A.

147
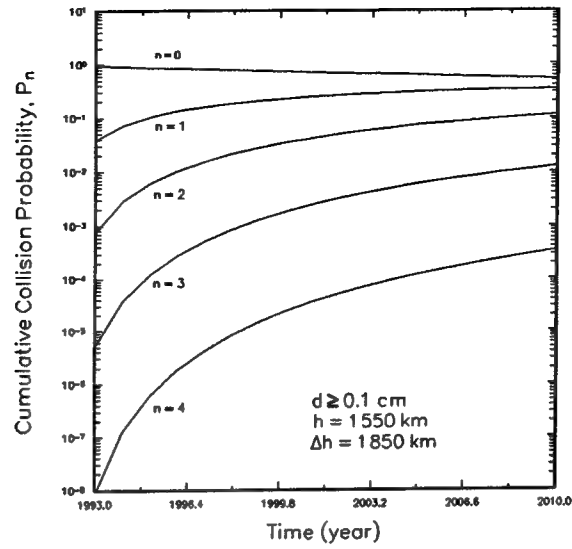
(a) P_n versus time for $d \geq 0.1$ cm
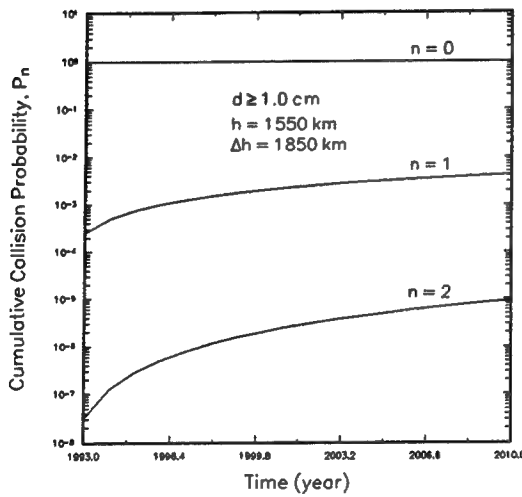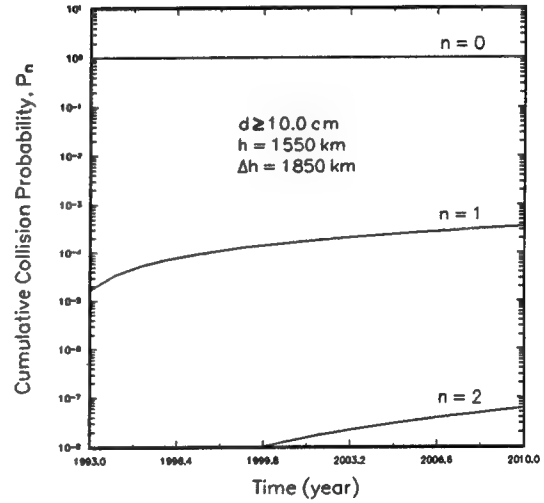
(b) P_n versus time for $d \geq 1.0$ cm   (c) P_n versus time for $d \geq 10.0$ cm

Figure B-10. Cumulative probabilities of impact versus time for three cumulative diameter size cases for a 10 m^2 satellite in scenario B.

148
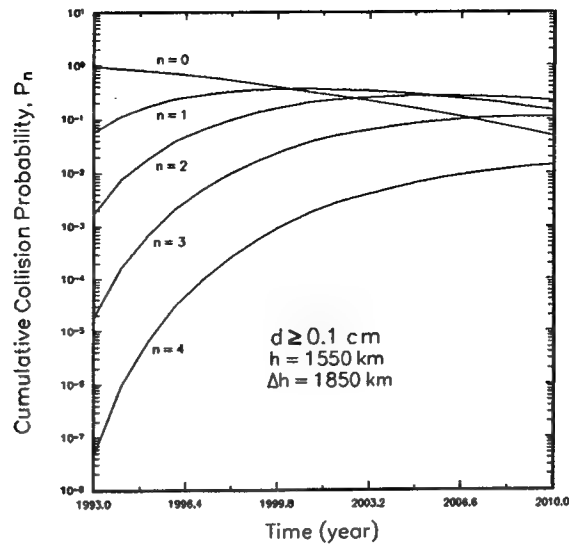
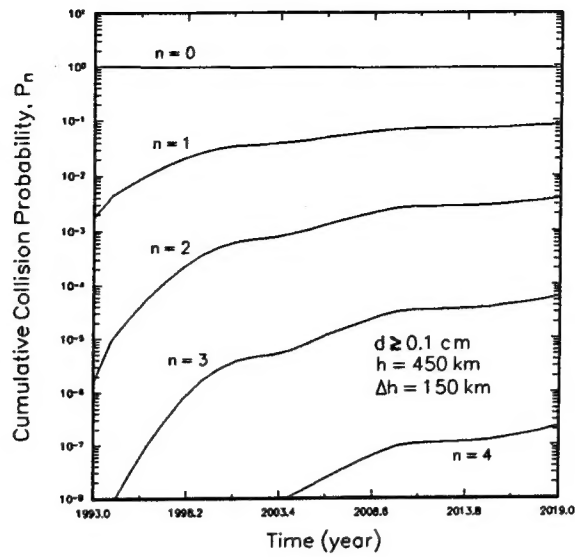(a) P_n versus time for $d \geq 0.1$ cm
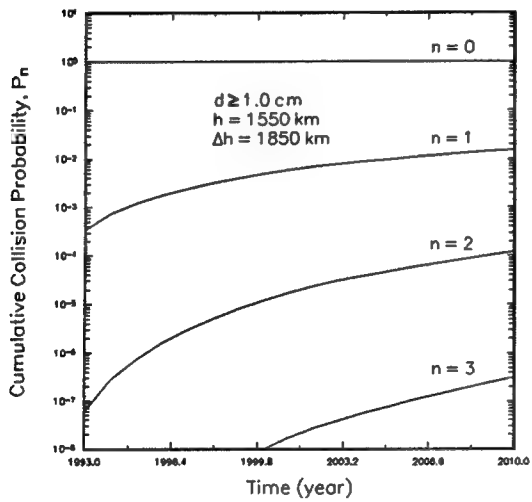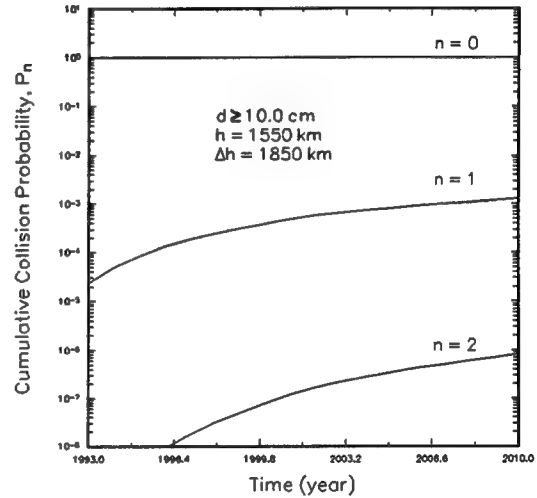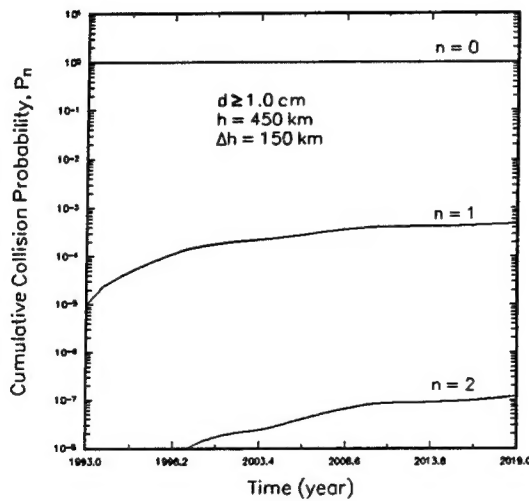

(b) P_n versus time for $d \geq 1.0$ cm   (c) P_n versus time for $d \geq 10.0$ cm

Figure B-11. Cumulative probabilities of impact versus time for three cumulative diameter
size cases for a 10 m² satellite in scenario C.

149
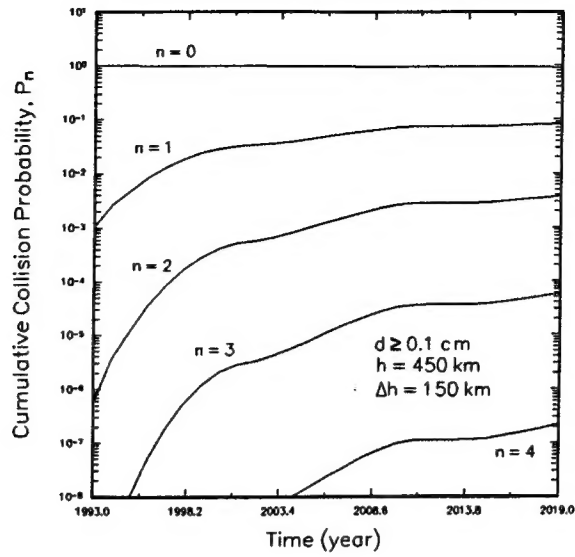
(a) P_n versus time for $d \geq 0.1$ cm

(b) P_n versus time for $d \geq 1.0$ cm

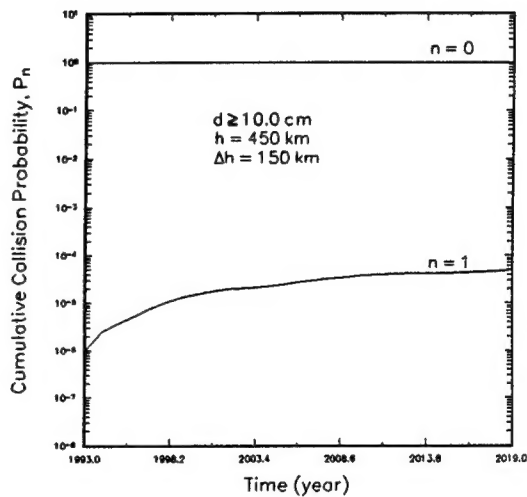(c) P_n versus time for $d \geq 10.0$ cm

Figure B-12. Cumulative probabilities of impact versus time for three cumulative diameter size cases for a 1 m^2 satellite in scenario A.

150
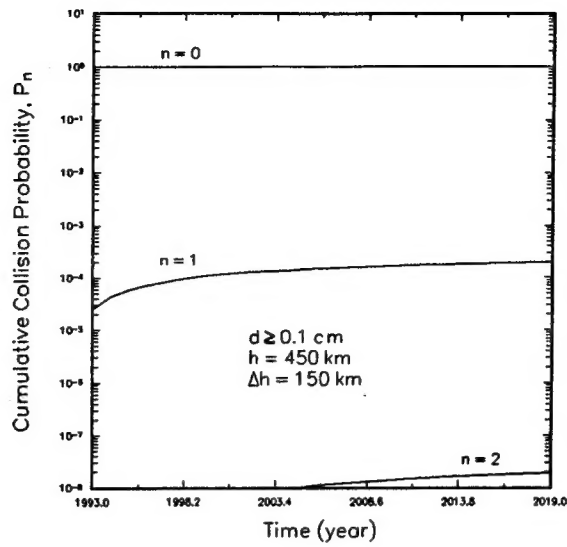
(a) P_n versus time for $d \geq 0.1$ cm

(b) P_n versus time for $d \geq 1.0$ cm   (c) P_n versus time for $d \geq 10.0$ cm

Figure B-13. Cumulative probabilities of impact versus time for three cumulative diameter size cases for a 1 m^2 satellite in scenario B.

151

(a) P_n versus time for $d \geq 0.1$ cm

(b) P_n versus time or $d \geq 1.0$ cm

(c) P_n versus time for $d \geq 10.0$ cm

Figure B-14.   Cumulative probabilities of impact versus time for three cumulative diameter size cases for a 1 m^2 satellite in scenario C.
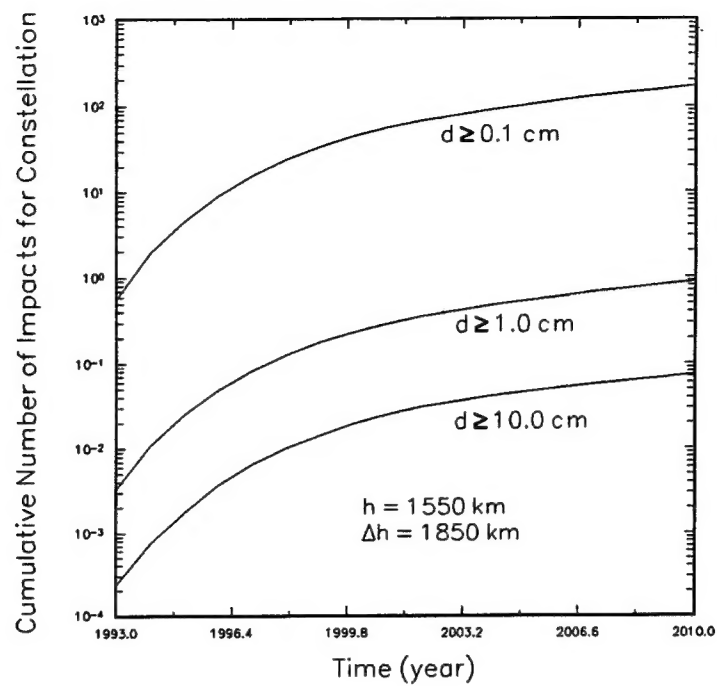
152

Figure B-15. Total cumulative number of impacts experienced by the "small" constellation assuming scenario A rates for three cumulative diameter d values.
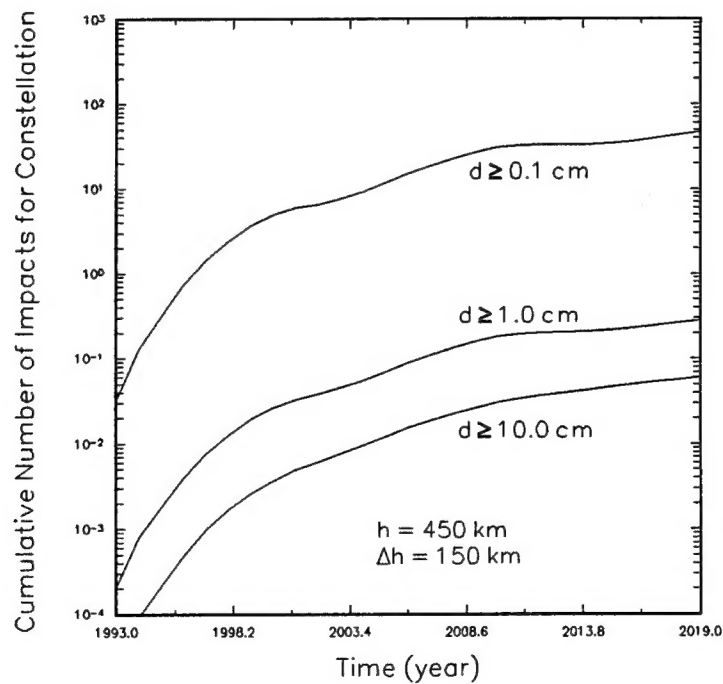

Figure B-16. Total cumulative number of impacts experienced by the "large" constellation assuming scenario A rates for three cumulative diameter d values.

153/154